Structure and Rheology of Polymer Mixtures at the Boundary between Soft Solid and Viscous Liquid Behaviors – from Fundamental Studies to Application

by

Ying Liu

A dissertation submitted in partial fulfillment
of the requirements for the degree of
Doctor of Philosophy
(Macromolecular Science and Engineering)
in the University of Michigan
2022

Doctoral Committee:

Professor Ronald G. Larson, Chair
Professor Zhan Chen
Professor Jinsang Kim
Professor Peter Ma

Ying Liu

liuying@umich.edu

ORCID iD: 0000-0002-4297-1185

Dedication

This work is sincerely dedicated to my beloved family: my mother, father, grandfather, and significant other Xinghui Song.

Acknowledgements

As my 22 years of education coming to an end, I would like to take this opportunity to express my most sincere gratitude to my mentors, colleagues, family and friends.

First, I thank my advisor Prof. Ronald Larson for his exceptional guidance and instructive advice during my pursuit of Ph.D. His unfailing passion for research is very inspiring to me. The continued support and rigorous suggestion he patiently provided helped me develop professionally as an independent researcher and tapped my potential to fulfill this dissertation work. These learnings not only secure me a dream job at 3M, but also will benefit me throughout my future career. I am honored to be supervised by him both in research and in life. Along with that, I am grateful for my dissertation committee members: Prof. Jinsang Kim, Prof. Zhan Chen and Prof. Peter Ma for their core courses lectures, detailed feedback, and helpful discussion. I would also like to thank my diverse collaborators in Dow Chemical Company: Kurt Koppi, Rocky Zhu, Stanley Yee, and Jon Degroot for guiding the 3D Printing project; in Mechanical Department at the University of Michigan: Prof. Albert Shih, Dr. Matthew Hildner, James Lorenz and William Van den Bogert for printing the materials; and in Anton Paar Company: Abhishek Shetty for rheological measurements.

Second, I want to thank the sources that funded my doctorate research and support my living: National Science Foundation Grants (No. DMR 1707640 and No. DMR 2100513), Dow Chemical Company University Project Initiatives, PPG fellowship, Rackham School - Teh-Hsun Lee Award scholarship, as well as other various university and industrial fellowships.

Third, I want to extend my heartfelt thanks to the graduated and current Larson Group members, visiting scholars and undergraduates: Prof. Sabina Wilkanowicz, Prof. Wende Tian, Prof. Yifan Zhang, Prof. Wenlin Zhang, Dr. Ali Salehi, Dr. Weizhong Zou, Dr. Ryan Hall, Dr. Yufei Wei, Dr. Nisha Hollingsworth, Dr. Alyssa Travitz, Dr. Grace Tan, Dr. Mohsen Ghasemi, Dr. Rongbin Li, Erin Xu, Yezhi Jin, Yuanding Huang, Dr. Yanan Gong, Christina Rice, Chaohang Xu, Conor Harris, Anukta Datta, Srinivasa Tanmay Velidanda, Futianyi Wang, Huiling Li, Boyao Wen, Erdem Ozdemir, Samuel Ogunwale, Omkar Roy, as well as Dr. Tianyu Liu, Keara Saud, Dr.

Peng-Kai Kao and Dr. Mahesh Ganesan from Solomon Group for making the research environment friendly and my social life outside the lab colorful and unforgettable. In the past few years, we have created numerous good times and loving memories, especially during COVID lock-down. As an international student in a foreign country, this group is truly my “family” in Ann Arbor, providing me a sense of belonging. I also have learned a lot from conversations and collaborations with each one of you, and I wish everyone the best of the luck in the future.

Last but not the least, I am thankful to my family and partner Xinghui Song, who always support me along the way. Their encouragement and love have motivated me to be a better self without fear. Without their uplifting inspiration and unfailing support, this thesis paper would not be possible. At the same time, my wholehearted appreciation goes to everyone who has been there for me whenever I desperately needed them during my Ph.D. journey.

Table of Contents

List of Tables

List of Figures

List of Equations

Abstract

This thesis presents results for two polymeric systems with liquid-to-solid transitions, i.e., oppositely charged polyelectrolytes in water with salt that can form a gel and polydimethylsiloxane (PDMS)-particle suspensions that exhibit yield stress in 3D printing applications. The phase behavior of oppositely charged polyelectrolytes in water with salt is studied using proton and carbon quantitative nuclear magnetic resonance (H NMR, C NMR) spectroscopy, thermogravimetric analysis (TGA), conductivity, and silver chloride titration. The linear rheology of the coacervate phase formed by these mixtures is studied with an emphasis on time-salt superposition and the emergence of a low-frequency plateau in storage modulus. For the PDMS-based suspensions, rheology is used as an indicator of success in 3D printing applications.

A protocol is developed for quantifying the compositions of both supernatant and coacervate phases using a combination of H NMR, C NMR, TGA, conductivity, and titration. With these methods, the phase diagrams of polyacrylic acid /poly (diallyl dimethylammonium chloride) (i.e., PAA/PDADMAC) in potassium chloride at different pH values are generated experimentally. We find that with increasing salt concentration, the coacervate phase volume initially increases and then quickly drops to zero at the critical salt concentration, and we quantify the concentrations of both polyelectrolytes in both phases for some compositions. At low pH, we also find a novel phase separation re-entry at high salt concentration, probably related to the solubility of PAA as a function of pH and salt, implying strong non-electrostatic driving forces for coacervation at low pH.

The linear viscoelasticity of coacervates is reviewed, with a focus on time-temperature/salt/pH/hydration superpositions. A variety of polyelectrolyte pairs show successful time-salt superposition, with master curves similar to those for neutral polymers. However, in some cases, a solid-like, as opposed to a fluid-like, response is observed at low frequencies, especially at low salt concentrations. Some coacervates seem to fit the “sticky diffusion” theory reasonably well, wherein relaxation is controlled by the breakage rate of ion pairs; the dependence of the “sticker” lifetime on salt concentration has been explored but is not well understood as yet.

Direct ink writing additive manufacturing with a static mixer and fine-tip nozzle is studied by printing PDMS mixed either with fumed silica or as a two-part commercial liquid silicon rubber (LSR) mixed with polyethylene glycol (PEG). We assess their printability by printing a hollow slump cone, whose print quality is correlated with rheological measurements, including 1) a shear rate up-ramp followed by a down-ramp in shear rate, 2) creep tests at a series of increasing stresses, and 3) oscillatory shear with increasing amplitude well into the nonlinear regime. The PDMS-fumed silica mixtures fail to print even at the highest fumed silica loading used (9 wt.%), while LSR-PEG with 4 or 6 wt.% PEG prints very well even with low Shore hardness LSR. These large differences in printability of two classes of PDMS materials correlate poorly with rheological behavior in many of the above tests. The exceptions are the apparent yield stress during a down-ramp in shear rate following a previous up-ramp to the maximum shear rate of 1000 s^{-1}, which is similar to the highest shear rate in the print nozzle, the stress at the crossover of the apparent G' and G'' curves in a strain amplitude sweep, and the stress at which irreversible flow becomes dominant in a stress sweep. These results indicate that the printability of the materials considered here depends strongly on both their yield stress and their ability to rebuild structure and yield stress quickly after experiencing the high shear rates characterizing their emergence from a narrow nozzle tip.

Chapter 1
Introduction and Background

1.1 Literature Review

1.1.1 Polyelectrolyte (PE) with Its Applications

Polymers, or long-chain molecules, appear in plastics, rubbers, fibers, and even components of the human body. Neutral polymers have been quite well understood in terms of their equilibrium structure, dynamics, and nonlinear mechanical behavior. However, for oppositely charged polyelectrolytes, or charged polymers, there has been some experimental work on thermodynamic and rheological behaviors [1-3] but understanding is still mostly qualitative. Considering the increasing attention gained recently by their various applications such as biomaterials [4-12], photovoltaic cells [13-20], fuel cells [21-23], super-tough transparent materials [24], nanocomposite assemblies [25], selective patterning [26], enzyme-active coatings [27], drug delivery [28-29], sensor fabrication [30], microencapsulation [31], underwater adhesives [32], self-assembled structures in biological fields [33], and others [34], it is time that the gap in quantitative understanding of PE system is addressed.

1.1.2 Quantitative Theories for PE Phase Behavior Predication

This gap motivated the study of PE phase behavior. For over 60 years, the only theory for the phase behavior, of oppositely charged polyelectrolytes was the Voorn-Overbeek (V-O) Theory [35]. The theory predicts that when polyelectrolytes with opposite charges are mixed with a salt solution whose concentration is below a critical value, the polymers associate with each other and phase separate into two phases at equilibrium: a coacervate phase, dense in polymer, and a supernatant phase, containing salt ions but little polymer [36] (see Figure 1-1). The ratio of volume fractions of the two phases, which helps define the system phase behavior, is easily tunable by

modifying many physicochemical parameters including salt concentration, salt identity, pH value, the chain length of the polyelectrolytes, charge regulation and ionic bond strength.

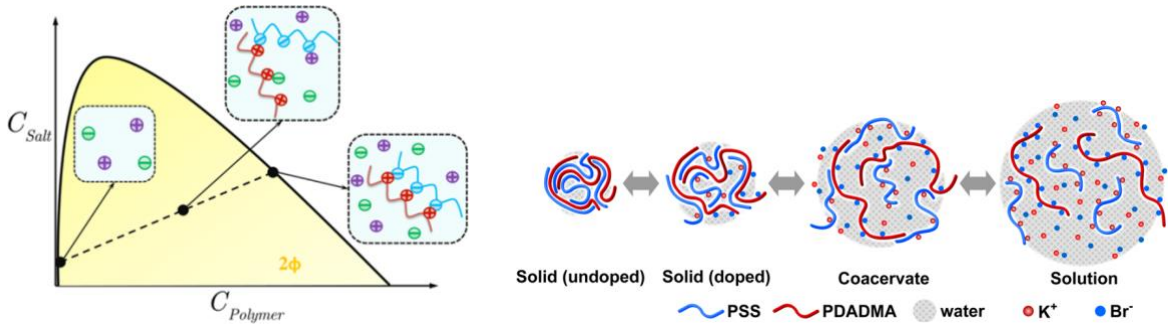

Figure 1-1. (Left) Typical polyelectrolyte phase diagram. (Right) Illustration of polyelectrolyte complexes. Poly (styrene sulfonate) (PSS, a strong polyanion), and poly (diallyldimethylammonium chloride) (PDADMAC, a strong polycation) are mixed in water, with KBr salt gradually added into the mixture [36].

Although the dominant theory has been the V-O Theory [35], which predicted the coacervate phase behavior of strong polyelectrolytes. However, factors such as the effects of ion-pairing, counterion condensation, and charge regulation, were neglected by the V-O theory. Modifications of the V-O Theory have emerged recently, however, including the promising theory proposed by Salehi and Larson [37] which accounts for the three above-mentioned effects. Nevertheless, before this new theory can be of any value, a systematic experimental dataset with a focus on weak polyelectrolytes is needed to validate the model.

To fulfill this end, a general protocol has been developed in the phase behavior study (Chapter 2), using a combination of analytical methods, for the quantification of strong and weak oppositely charged polyelectrolytes under various pH, salinity, and polymer concentrations. To be more specific, quantitative proton and carbon Nuclear Magnetic Resonance (NMR), thermogravimetric analysis (TGA), conductometry, and titration techniques were used for accurately measuring the composition of oppositely charged polyelectrolyte complexation, specifically for PSS and PDADMAC in KBr solution (PSS/PDADMAC/KBr), and poly(acrylic acid) (PAA, a weak polyanion) and PDADMAC in KCl solution (PAA/PDADMAC/KCl).

1.1.3 Rheology Studies of PE Complexation

As the understanding of the phase behavior of oppositely charged polyelectrolytes deepens, further investigation was underway stepping into one of the mysterious fields remaining in polymer science – the dynamics, and rheology of coacervates.

As mentioned above, despite the wide variety of applications and growing interest in their thermodynamics and rheology, coacervates still remain relatively poorly understood, due to the lack of quantitative theories to capture its zero-shear viscosity and relaxation time dependence on molecular weight, and on concentrations of polymers and salt. The best-known theory for the rheology of coacervates is the 'sticky diffusion' model [38] for associating polymers, but its applications to coacervate rheology have been limited due to the daunting complexity of coacervates. An encouraging discovery in the past decade, however, that has shed light on coacervate rheology is time-salt superposition, which was first found in multiple polyelectrolyte chemistries by Cohen Stuart et al. [39-40], where the linear rheology curves of coacervates with different salt concentrations can be shifted horizontally and/or vertically and superposed onto a master curve. Recent studies have proposed relationships or scaling laws between the salt concentration and shift factor but with different conclusions [40-41]. After compared the R^2 values for fitting the available data reported in the literature to 1) the square root relationship and 2) the linear relationship, one cannot conclude one relationship is better than the other [42] (Chapter 3). Hence, a systematic experimental study is needed to dig deeper into the principle of time-salt superposition using rheology methods, to obtain the relationship between salt concentration and shift factors for time-salt superposition and to reveal the relaxation mechanism of the coacervate. Factors, such as salt identity, chain length of the polymers, polymer concentration, pH value, salinity, and temperature, which influence the coacervation or phase separation process may also have impacts on the coacervate rheology behavior. It is essential to study of time-salt superposition in polyelectrolyte complexes, such as PSS/PDADMAC/KBr and PAA/PDADMAC/KCl coacervates, with an emphasis on the low-frequency plateau observed, on top of the quantitative understanding of their phase behavior. (Chapter 4)

1.1.4 Other Polymer Rheology and 3D Printing Applications

The continuous study of PE coacervate (PEC) rheology provided more insightful experiments to the field of PEC rheology and guidance for development of future theory as well as material applications. The prevalence of three-dimensional (3D) printing techniques, or additive manufacturing, has been growing rapidly for the past decade. 3D printing uses a variety of polymeric materials to perform customized printed products. Being a relatively new technology, however, the relationship between the materials' printability and their rheological characterization still remains unclear. With a wide range of material options including silicones, polyurethanes, celluloses, polyolefins and others, Dow is uniquely positioned to capitalize on the next growth spurt of 3D printing as it transitions to functional prototyping and manufacturing, targeting materials include reinforced polydimethylsiloxane (PDMS). To decipher this mysterious field, collaborating with Dow Chemical Company, investigation into the definition of yield stress both on rheometer and on 3D printer were underway. (Chapter 5)

1.2 Research Contributions

Noted that Chapter 3 and 4 are joint work with another graduate student Huiling Li, both published in Journal of Rheology; and chapter 5 is joint work with another Ph.D. student Matthew Hildner.

1.3 Reference

[1] Fu, J.; Schlenoff, J. B. (2016) Driving Forces for Oppositely Charged Polyion Association in Aqueous Solutions: Enthalpic, Entropic, but Not Electrostatic. J. Am. Chem. Soc., 138, 980−990.

[2] Priftis, D.; Laugel, N.; Tirrell, M. (2012) Thermodynamic Characterization of Polypeptide Complex Coacervation. Langmuir, 28, 15947−15957.

[3] Vitorazi, L.; Ould-Moussa, N.; Sekar, S.; Fresnais, J.; Loh, W.; Chapel, J.-P.; Berret, J.-F. (2014) Evidence of a Two-Step Process and Pathway Dependency in the Thermodynamics of Poly-(Diallyldimethylammonium Chloride)/Poly(Sodium Acrylate) Complexation. Soft Matter, 10, 9496−9505.

[4] Chluba, J.; Voegel J.C.; Decher G.; Erbacher P.; Schaaf P.; Ogier J. (2001) Peptide hormone covalently bound to polyelectrolytes and embedded into multilayer architectures conserving full biological activity. Biomacromolecules 2:800.

[5] Mendelsohn J. D.; Yang S. Y.; Hiller J. A.; Hochbaum A. I.; Rubner M. F. (2003) Rational design of cytophilic and cytophobic polyelectrolyte multilayer thin films. Biomacromolecules 4:96.

[6] Izumrudov V. A.; Kharlampieva E.; Sukhishvili S. A. (2005) Multilayers of a globular protein and a weak polyacid: role of polyacid ionization in growth and decomposition in salt solutions. Biomacromolecules 6:1782.

[7] Lvov Y.; Caruso F. (2001) Biocolloids with orderd urease multilayers shells as enzymatic reactors. Anal. Chem. 73:4212.

[8] Thierry B.; Kujawa P.; Tkaczyk C.; Winnik F. M.; Bilodeau L.; Tabrizian M. (2005) Delivery platform for hydrophobic drugs: prodrug approach combined with self-assembled multilayers. J. Am. Chem. Soc. 127:1626.

[9] Jessel N.; Atalar F.; Lavalle P.; Mutterer J.; Decher G.; Schaaf P.; Voegel J.C.; Ogier J. (2003) Bioactive coatings based on a polyelectrolyte multilayer architecture functionalized by embedded proteins. Adv. Mater. 15:692.

[10] Benkirane-Jessel N.; Lavalle P.; Hubsch E.; Holl V.; Senger B.; Haikel Y.; Voegel J.C.; Ogier J.; Schaaf P (2005) Short-time tuning of the biological activity of functionalized polyelectrolyte multilayers. Adv. Funct. Mater. 15:648.

[11] Sun Y.; Zhang X.; Sun C.; Wang B.; Shen J. (1996) Fabrication of ultrathin film containing bienzyme of glucose oxidase and glucoamylase based on electrostatic interaction and its potential application as a maltose sensor. Macromol. Chem. Phys. 197:147.

[12] Tang Z.; Wang Y.; Podsiadlo P.; Kotov N. A. (2006) Biomedical applications of layer-by-layer assembly: from biomimetics to tissue engineering. Adv. Mater. 18:3203.

[13] Durstock M. F.; Spry R. J.; Baur J. W.; Taylor B. E.; Chiang L. Y. (2003) Investigation of electrostatic self-assembly as a mean to fabricate and interfacially modify polymer-based photovoltaic devices. J. Appl. Phys. 94:3253.

[14] Li H.; Li Y.; Zhai J.; Cui G.; Liu H.; Xiao S.; Liu Y.; Lu F.; Jiang L.; Zhu D. (2003) Photocurrent generation in multilayer self-assembly films fabricated from water-soluble poly (phenylene vinylene). Chem. Eur. J. 9:6031.

[15] Pradhan B.; Bandyopadhyay A.; Pal A. J. (2004) Molecular level control of donar/acceptor heterostructures in organic photovoltaic devices. Appl. Phys. Lett. 85:663.

[16] Lowman G. M.; Hammond P. T. (2005) Solid-state dye-sensitized solar cells combining a porous TiO2 film and layer-by-layer composite electrolyte. Small 1:1070.

[17] Liang Z.; Dzienis K. L.; Xu J.; Wang Q. (2006) Covalent layer-by-layer assembly of conjugated polymers and CdSe nanoparticles: multilayer structure and photovoltaic properties. Adv. Funct. Mater. 16:542.

[18] Man K. Y. K.; Wong H. L.; Chan W. K.; Djurisic A. B.; Beach E.; Rozeveld S. (2006) Use of Ruthenium-containing conjugated polymer as a photosensitizer in photovoltaic devices fabricated by a layer-by-layer deposition process. Langmuir 22:3368.

[19] Mwaura J. K.; Pinto M. R.; Witker D.; Ananthakrishnan N.; Schanze K. S.; Reynolds J. R. (2005) Photovotaic cells based on sequentially adsorbed multilayers of conjugated poly(p-phenylene ethylnylenes) and a water-soluble fullerene derivative. Langmuir 21:10119.

[20] Wang S.; Li C.; Chen F.; Shi G. (2007) Layer-by-layer deposited multilayer films of water soluble polythiophene derivative and gold nanoparticle exhibiting photoresponsive properties. Nanotechnology 18:185707.

[21] Farhat T. R.; Hammond P. T. (2005) Designing a new generation of proton-exchange membrane using layer-by-layer deposition of polyelectrolytes. Adv. Funct. Mater. 15:945.

[22] Phillips A. K.; Moore R. B. (2006) Mechanical and transport property modifications of perfluorosulfonate ionomer membranes prepared with mixed organic and inorganic counterions. J. Polym. Sci: Part B 44:2267.

[23] Xi J.; Wu Z.; Teng X.; Zhao Y.; Chen L.; Qiu X. (2008) Self-assembled polyelectrolyte multilayer modified Nafion membrane with suppressed vanadium ion crossover for vanadium redox flow batteries. J. Mater. Chem. 18:1232.

[24] Podsiadlo P.; Kaushik A. K.; Arruda E. M.; Waas A. M.; Shim B. S.; Xu J.; Nandivata H.; Pumplin B. G.; Lahann J.; Ramamoorthy A.; Kotov N. A. (2007) Ultrastrong and stiff layered polymer nanocomposites. Science 318:80.

[25] Andres. C. M.; Larraza, I.; Corrales, T.; Kotov, N.A. (2012) Nanocomposite Microcontainers. Adv. Mat. 24:4597.

[26] Hammond, P. T.; Whitesides, G. M. (1995) Formation of polymer microstructures by selective deposition of polyion multilayers using patterned self-assembled monolayers as a template. Macromolecules 28:7569.

[27] Onda, M.; Lvov, Y.; Ariga, K.; Kunitake, T. (1996) Sequential actions of glucose oxidase and peroxidase in molecular films assembled by layer-by-layer alternate adsorption Biotechnol. Bioeng. 51:163.

[28] Wohl, B.M.; Engbersen, J.F.J. (2012) Responsive layer-by-layer materials for drug delivery J. Controlled Release 158:2.

[29] De Koker, S.; De Cock, L.J.; Rivera-Gill, P.; Parak, W.J.; Velty, A.Z.; Vervaet, C.; Remon, J.P.; Grooten, J.; De Gist, B.G. (2011) Polymeric multilayer capsules delivering biotherapeutics. Adv. Drug Delivery Rev. 63:748.

[30] Sun, Y.; Zhang, X.; Sun, C.; Wang, B.; Shen, J. (1996) Effects of pH on the supramolecular structure of polymeric molecular deposition films. Macromol. Chem. Phys. 197:147.

[31] Piacentini E. (2013) Food Research International 53, 362.

[32] Brenna M. J. (2017) Biomaterials 124, 116.

[33] Van der Kooij H. (2012) Langmuir 28, 14180.

[34] Liu, Y.; Winter H. H.; and Perry S. L. (2017) Linear viscoelasticity of complex coacervates. Adv. Coll. Interf. Sci. Matter 239, 46-60.

[35] Overbeek, J. T. G.; Voorn M.J. (1957) Phase separation in polyelectrolyte solutions. Theory of complex coacervation J. Cell. Compar. Physl., 49:7.

[36] Wang, Q.; Schlenoff, J. B. (2014) The Polyelectrolyte Complex/coacervate Continuum. Macromolecules 47 (9), 3108–3116.

[37] Salehi, A.; Larson, R. G. (2016) A Molecular Thermodynamic Model of Complexation in Mixtures of Oppositely Charged Polyelectrolytes with Explicit Account of Charge Association/Dissociation. Macromolecules 49, 24, 9706-9719.

[38] Rubinstein, M.; and Semenov A. N. (2001) Dynamics of entangled solutions of associating polymers. Macromolecules 34, 1058−1068.

[39] Spruijt, E.; Sprakel J.; Lemmers M.; Cohen Stuart M. A.; and van der Gucht J. (2010) Relaxation Dynamics at Different Time Scales in Electrostatic Complexes: Time-Salt Superposition. Physical Review Letters 105, 208301.

[40] Spruijt, E.; Cohen Stuart M. A.; and Van Der Gucht L. (2013) Linear Viscoelasticity of Polyelectrolyte Complex Coacervates. Macromolecules 46, 1633-1641.

[41] Yang, M.; Shi J., and Schlenoff J. B. (2019) Control of Dynamics in Polyelectrolyte Complexes by Temperature and Salt. Macromolecules 52, 1930−1941.

[42] Larson, R.; Liu Y. and Li H. (2021) Linear viscoelasticity and time-temperature-salt and other superpositions in polyelectrolyte coacervates. Journal of Rheology 65, 77.

Chapter 2

Development of Analytical Measurements for Quantifying the Compositions of Two Oppositely Charged Polyelectrolytes and their Phase Behaviors

2.1 Introduction

When oppositely charged polyelectrolytes are added to a salt solution with the salt concentration below a critical value, the polymers often associate with each other and phase separate into a coacervate phase, dense in polymer, and a supernatant phase, which contains salt ions but little polymer. A phase diagram illustrating this is shown in Fig. 1-1. With increasing salt concentration, the polymer concentration in the coacervate phase decreases while that in the supernatant phase increases. At the critical salt concentration, the polymer concentrations in both phases are the same and above this salt concentration the mixture becomes single-phase and clear.

Early theories of this phase separation gave only qualitative descriptions, but in recent years, more quantitative theories have become increasingly available. It is the goal of this chapter to develop methods to test these theories by providing quantitative data for the compositions of both coacervate and supernatant phases, for both strong and weak polyelectrolytes, at arbitrary pH, and for non-stoichiometric ratios of the two polyelectrolytes. This means that the two polymers cannot be assumed to have the same concentration in each phase, and the salt concentration is not only different in the two phases, but the two ions are not equally concentrated in either of the phases. An example of phase diagrams predicted for a pair of weak polyelectrolytes at two different pH values, is shown in Fig. 2-1. Note that there are five species concentrations in each phase, namely water, positive and negative salt ions, and the two polyelectrolytes. Note also that at the reduced pH of 5 in Fig. 2-1(b), the concentrations of the two poly-ions are very different as are the concentrations of the two small salt ions, in each phase. To date, most analytical work has assumed equimolar conditions at pH near 7, where the two polymers can be taken to have roughly the same concentration in each phase, and the two small salt ions also have nearly the same concentration in each phase. To go beyond this assumption, and to be able to test theories away from neutral pH

or equimolar polymer concentrations, we need to measure the concentrations of all species in both phases. This necessitates the development of novel measurement methods. Here we show and discuss our work in this direction.

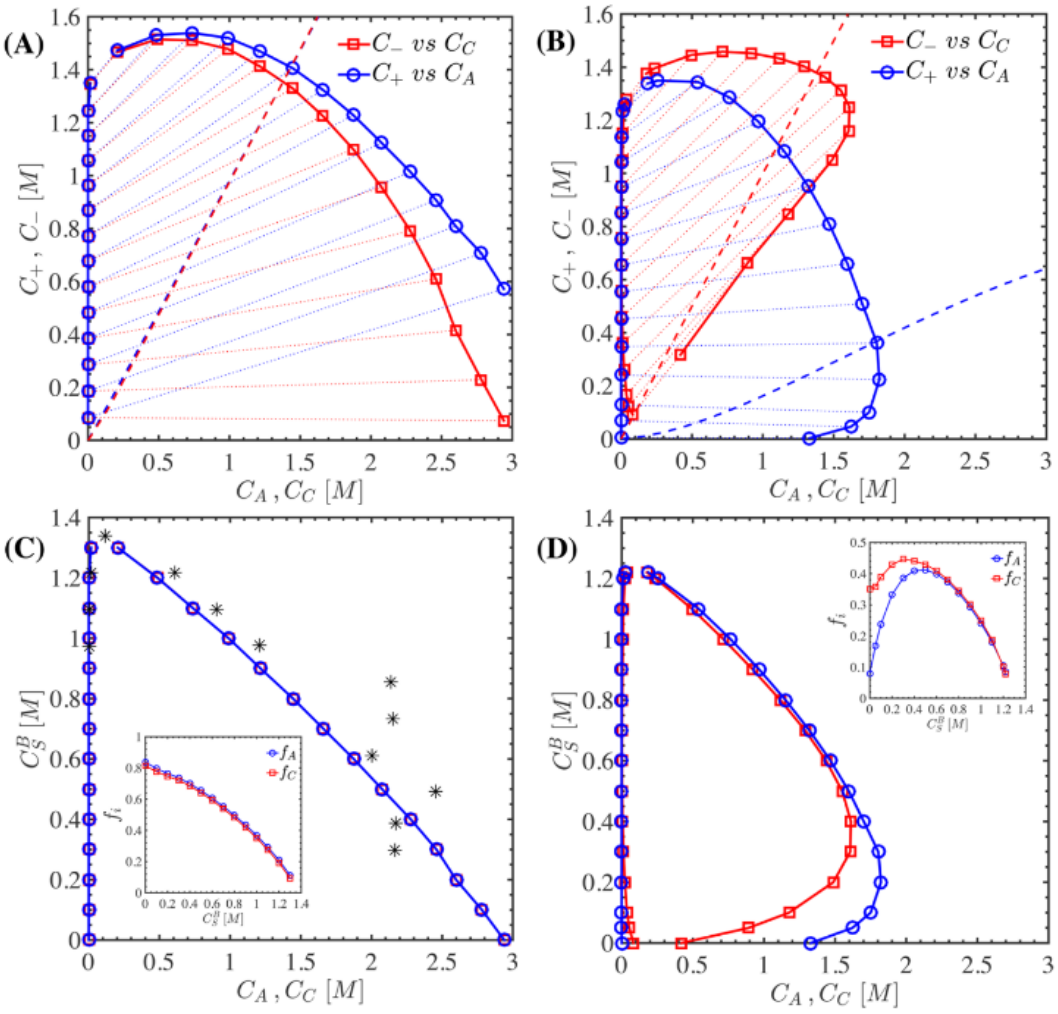

Figure 2-1. Binodal diagrams (see Figure 6 in [1]) illustrating the concentrations of two weakly dissociating polyelectrolytes (PEs) in coexisting phases versus their corresponding counterion concentrations for an aqueous equimolar system at (A) pH = 7 and (B) pH = 5. "C_C" and "C_A" are the concentrations of polycation and polyanion in units of moles of monomer, while "C_+" and "C_-" are the molar concentrations of salt cations and anions, respectively. (C) and (D) correspond to the binodal diagrams in (A) and (B), respectively, where the bulk salt concentration in the stock solutions (assumed to be the same in each) is plotted against the PE concentrations in coexisting phases. Note that circles and squares in (C) are almost indistinguishable. The PE concentration in both stock solutions is fixed at 0.11 M. Experimental binodal data for PAA/PDMAEMA system at pH = 6.5 are represented by stars in (C). The insets show the dependence of the fraction of PE units in the dense phase that are charged and therefore available for ion pairing.

There are five species to measure, namely, the positively charged polymer, negatively charged polymer, salt cation, salt anion and water, in each phase, and the volume of each phase after phase separation also needs quantification. We examined the effects of pH, salinity, and chain length (molecular weight). We first test our method on a strong polyelectrolyte system, polystyrene sulfonate/ poly(diallydimethylammonium) i.e., PSS/PDADMA, in which both polyelectrolytes remain fully charged across a wide range of pH. We use modified methods on a weaker system, PAA/PDADMA, where the polyacrylic acid (PAA) loses charges at reduced pH. In the future, we can use these methods on mixtures in which both polyelectrolytes are weak.

To date, we have developed methods of measuring phase compositions for the strong polyelectrolytes PSS/PDADMA, and the weak/strong mixture PAA/PDADMA, and have acquired preliminary data, which we will compare with the phase diagrams predicted by recently proposed models, especially that of Salehi and Larson [1], to validate and/or modify the theoretical work. We expect in the end to gain a much deeper understanding of polyelectrolyte interactions, thermodynamics, and phase behavior, leading also to the ability to predict transport properties, such as those in Layer-by-Layer assemblies.

2.2 Method

2.2.1 PSS/PDADMAC System

For the PSS/PDADMA system, quantifications of each component are achieved via thermal gravimetric analysis (TGA), conductometry, and proton NMR measurements. PSS and PDADMA polyelectrolyte complexation mixtures are prepared using the method of Wang et al. [2]. Then various volumes of KBr solution are added into the mixture to achieve a fixed known volume, V_{Total}. After phase separation (see Fig. 2-2), the phase volumes of supernatant (refer as "S" in the subscript or superscript) and coacervate (refer as "C" in the subscript or superscript) can be calculated from the readout of graduated tubes and the known total volume of the mixture (see equation 2-1).

$$\Phi_S + \Phi_c = \frac{V_S}{V_{Total}} + \frac{V_C}{V_{Total}} = 1 \qquad (2\text{-}1)$$

Where Φ_S and Φ_c are the respective volume fractions of supernatant and coacervate, and V_S and V_C are their volumes. A graphical summary of our measurement scheme for PSS/PDADMA is

given in Fig. 2-2. The total polyelectrolyte and total salt molar concentrations added into the mixture are known and noted as n_{total}(PEs) and n_{total}(KBr). Water, total polyelectrolyte and total salt concentrations in the coacervate are noted as n^C(water), n^C(PEs) and n^C(KBr), respectively. Water, total polyelectrolyte and total salt concentrations in the supernatant are noted as n^S(water), n^S(PEs) and n^S(KBr), respectively. To calculate the above parameters, the weight of the water, polyelectrolytes and salt need to be measured.

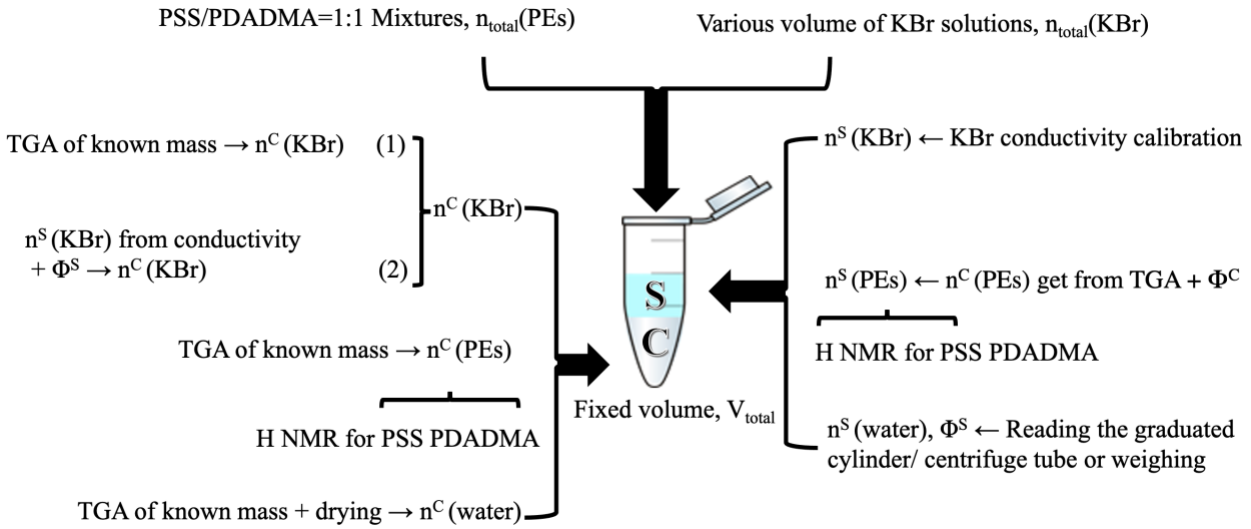

Figure 2-2. Outline of scheme for determining the concentrations of KBr and polyelectrolytes (PEs) in the coacervate (left wing) and supernatant (right wing) phases are given for PSS/PDADMA/KBr system.

The weight of water content in the supernatant and coacervate can be obtained by weighing before and after drying. The weight (percentage) of polyelectrolytes (PSS and PDADMA), and salt (KBr) in the coacervate phase can be measured by TGA of a known mass of the coacervate, by measuring the mass loss over time as the temperature ramps up above melting points. If the water, polymer, and the salt are volatized at different temperatures, the weight percentage of each is determined and mass fractions of the polymer and salt in the coacervate phase can be calculated. Using the phase volumes, and the known masses used to create the original sample, the total masses of polymer and salt in the supernatant phase can be calculated by subtraction. To double check the salt composition in the supernatant, electrical conductometry is measured for the PSS/PDADMA system, where the two oppositely charged polymers are completely dissociated. To double check the polymer composition in the supernatant and to obtain concentrations of individual polymer species, we use quantitative proton NMR.

2.2.2 PAA/PDADMAC System

For the PAA/PDADMA system, similarly, quantifications of each component are achieved via TGA, KCl titration and carbon NMR measurements. While the use of proton NMR to determine separately the concentrations of PSS and PDADMA was pioneered by Schlenoff's group, our use of carbon NMR for PAA/PDADMA is novel, and is used to overcome nonlinearities in the calibration of proton NMR for the PAA/PDADMA system, as discussed below. A graphical summary of our measurement scheme of PAA/PDADMA is given in Fig. 2-3.

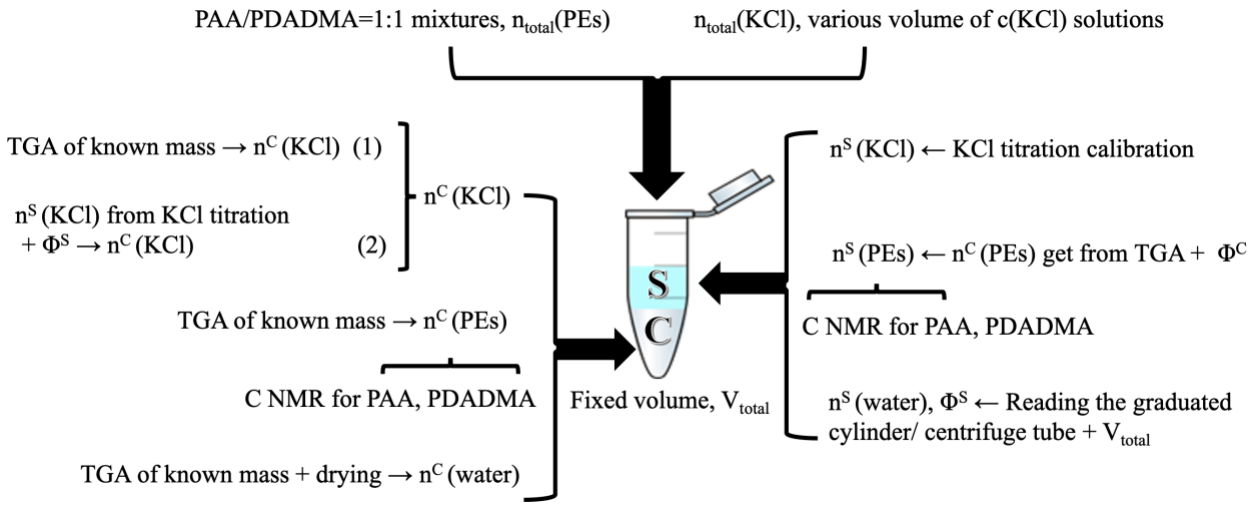

Figure 2-3. Outline of scheme for determining the molar concentrations n^C and n^S of KCl and polyelectrolytes (PEs) in the coacervate (left) and supernatant (right) phases are given for PAA/PDADMA.

The salt species is changed from KBr to KCl when changing form PSS/PDADMA to PAA/PDADMA to minimize the number of species in the system, since for PSS/PDADMA, the bromide salt of PDADMA is used, while for PAA/PDADMA, the chloride salt if used. For PAA/PDADMA, where PAA is only partly dissociated, as discussed below, KCl titration against $AgNO_3$ is conducted instead of conductometry because of the uncertain contribution of hydronium ion to the conductivity, making conductometry an inaccurate method of determining the salt concentrations. Quantitative C NMR is used to obtain concentration of both PAA and PDADMA in both phases, instead of H NMR where only PDADMA can be quantified and not PAA.

2.3 Results and Discussion

2.3.1 Nuclear Magnetic Resonance Spectroscopy (NMR)

NMR was used to quantify each polymer concentration in both phases using a series of standard calibration curves with fixed total polymer mass concentrations.

For H NMR, D_2O is used as the reference with a chemical shift of 4.790ppm. We find that H NMR can quantify the total concentration and the ratio of PSS to PDADMA in the PSS/PDADMA mixture, and the concentration and fraction of PDADMA in the PAA/PDADMA mixture over a concentration range from 1mg/ml to 40mg/ml. The upper limit of H NMR is 40mg/ml due to the saturation of signal. Shown below in Fig. 2-4, as an example, are the H NMR spectra and the calibration curves for PDADMA mole fraction in the PAA/PDADMA system with total polymer concentrations of 2.5mg/ml and 10mg/ml and 0.75M KCl at pH 7. The total concentrations are both below that at which signal saturation occurs.

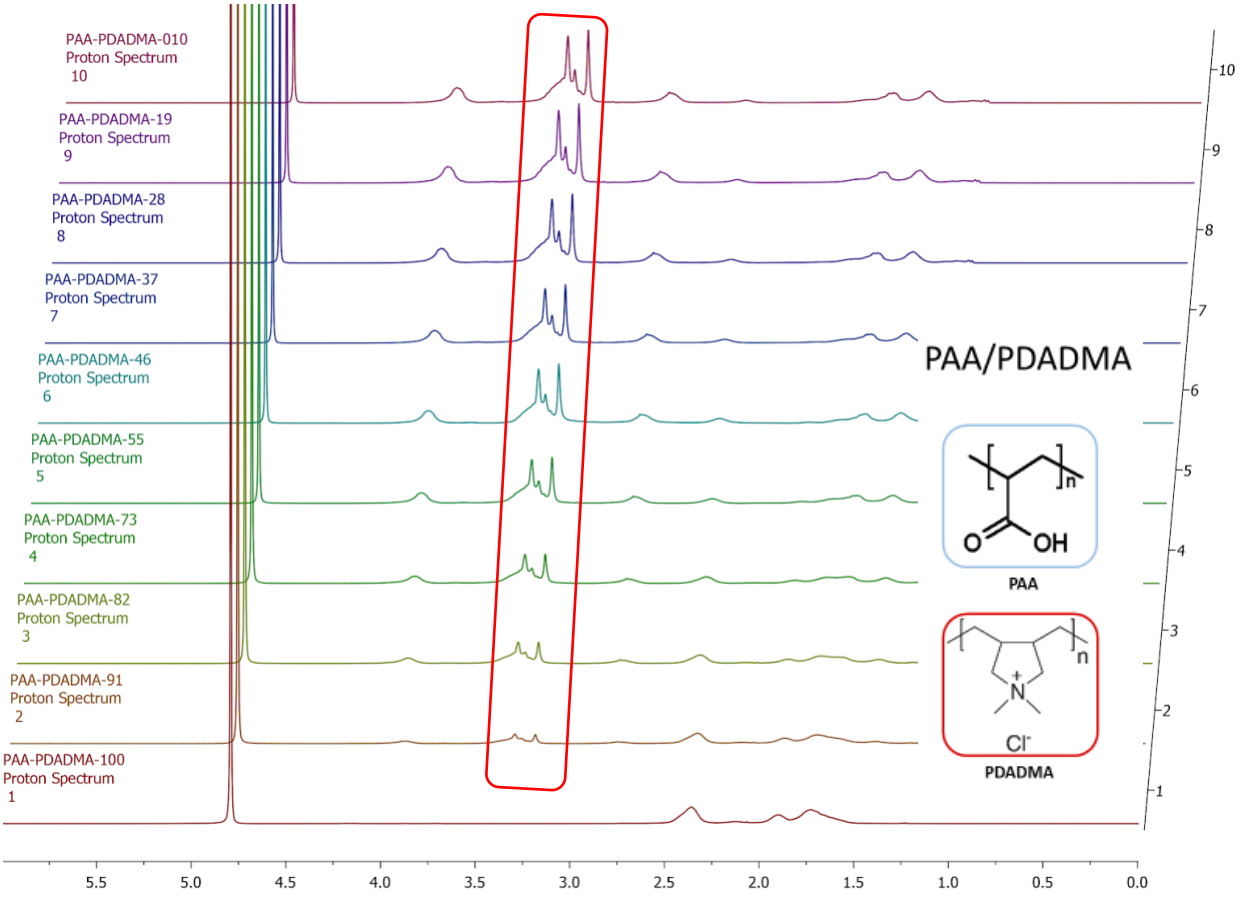

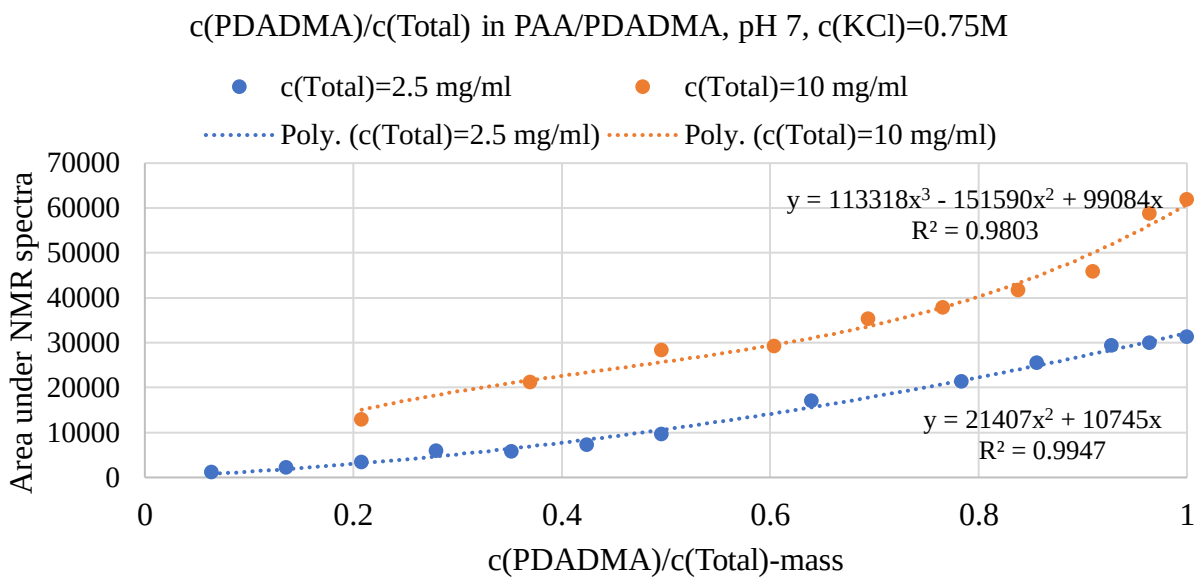

Figure 2-4. (top) Proton NMR spectra for mixtures of PAA/PDADMA with added salt, where the ratio of PAA to PDADMA is varied at total polymer concentration of 10 mg/ml. (bottom) Area under the peaks (3.5-2.99 ppm, in red circle) for 2.5 mg/ml (blue) and 10 mg/ml (orange) total polymer concentration. The results in the lower figure are obtained by integrating the area under all red circled peaks (3.5-2.99 ppm), corresponding to PDADMA peaks. The dashed lines are polynomial fits to the data.

While proton NMR is limited to a concentration of 40mg/ml, C NMR can quantify the concentrations of both PAA and PDADMA simultaneously in PAA/PDADMA mixtures with total polymer concentration ranging from 30mg/ml to 200mg/ml. Shown below in Fig. 2-5 are the C NMR spectra for separate solutions of both PAA and PDADMA and in Fig. 2-6 for four mixtures of these at 200mg/ml total polymer concentration.

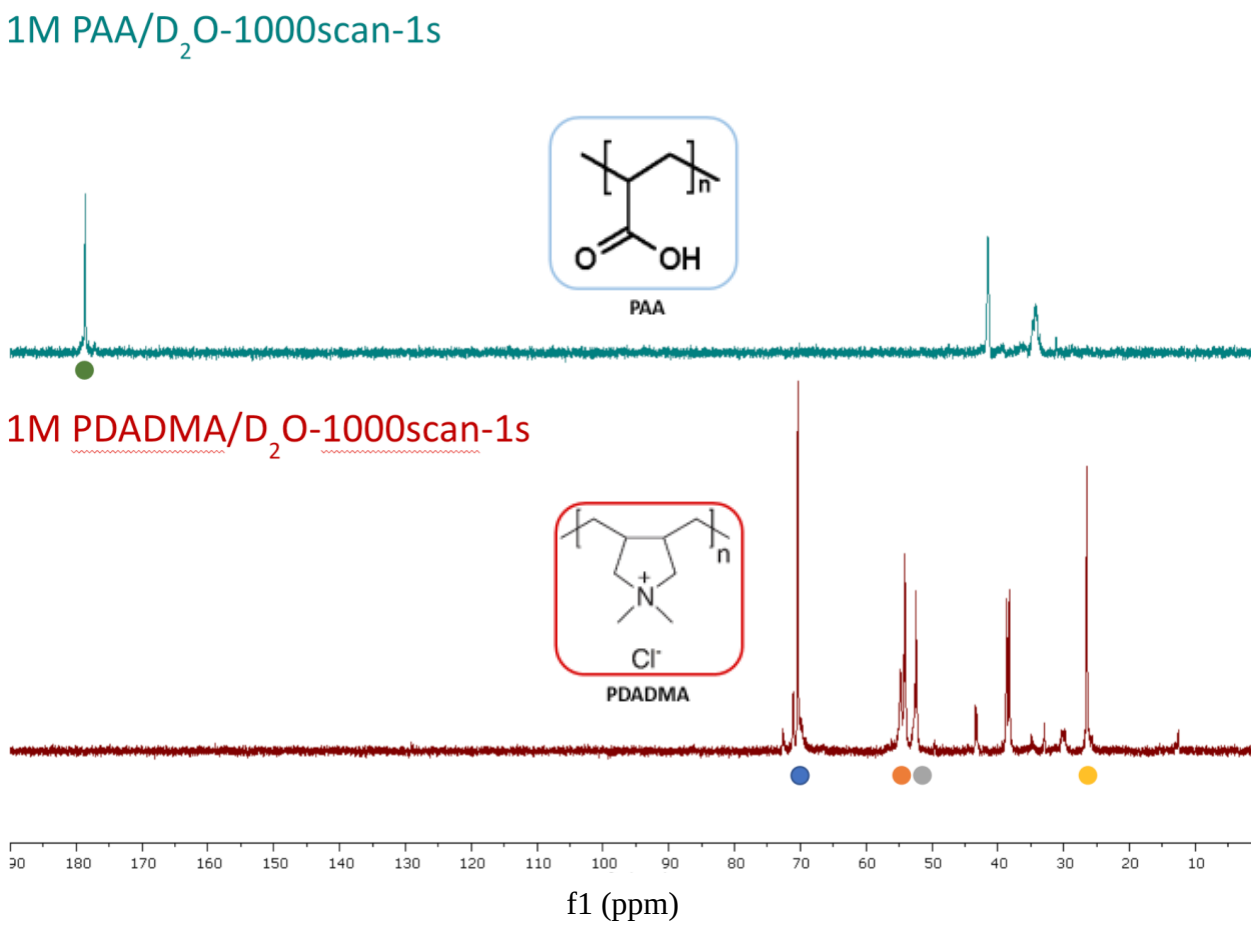

Figure 2-5. Carbon NMR spectra for pure 1 M PAA (top) and for pure 1M PDADMA (bottom) with 1000 scans and delay time (time between each scan) 1s.

In Fig.2-5 (top), the peak above the green point corresponds to the carbonyl carbons in PAA. In Fig. 2-5 (bottom), the peaks above the blue, orange, grey and yellow points correspond to the carbons in PDADMA. All C NMR test were averaged over 1000 scans and 1 s delay time to obtain best signal-to-noise results. These choices provide a suitable compromise between signal quality and run time. In Fig. 2-6, C NMR spectra are reported for four mixtures of PAA and PDADMA, at a total polymer concentration of 200 mg/ml, showing that the peaks corresponding to PAA increase, from top to bottom, as its concentration increases and PDADMA concentration decreases, while the peaks for PDADMA correspondingly decrease. The integrated areas under these peaks are plotted in Fig. 2-7. Note the linearity of these calibration peaks, in contrast to the nonlinearity of the calibration curves for H NMR in Fig. 2-4. The linearity for C NMR results from the weaker sensitivity of the signal to the carbons, relative to the protons. This produces less

interference between the different species, and a linear response with respect to the concentration of each polymer.

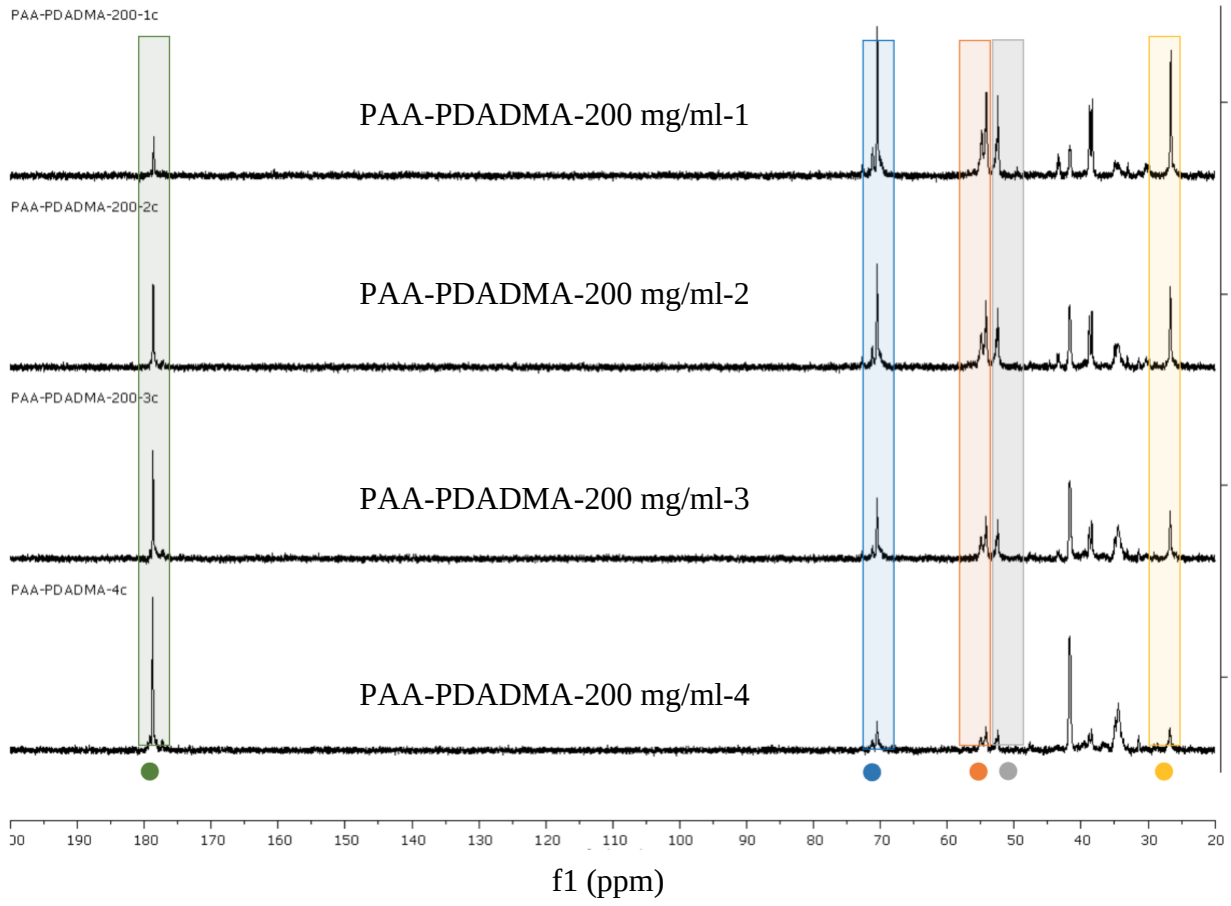

Figure 2-6. C NMR spectra for four mass ratios of PAA/PDADMA at total polymer concentration of 200 mg/ml. The peak on the left corresponds to PAA, while the four on the right are for PDADMA. The four mass ratios can be calculated from the x axis (concentration) of Fig. 2-7.

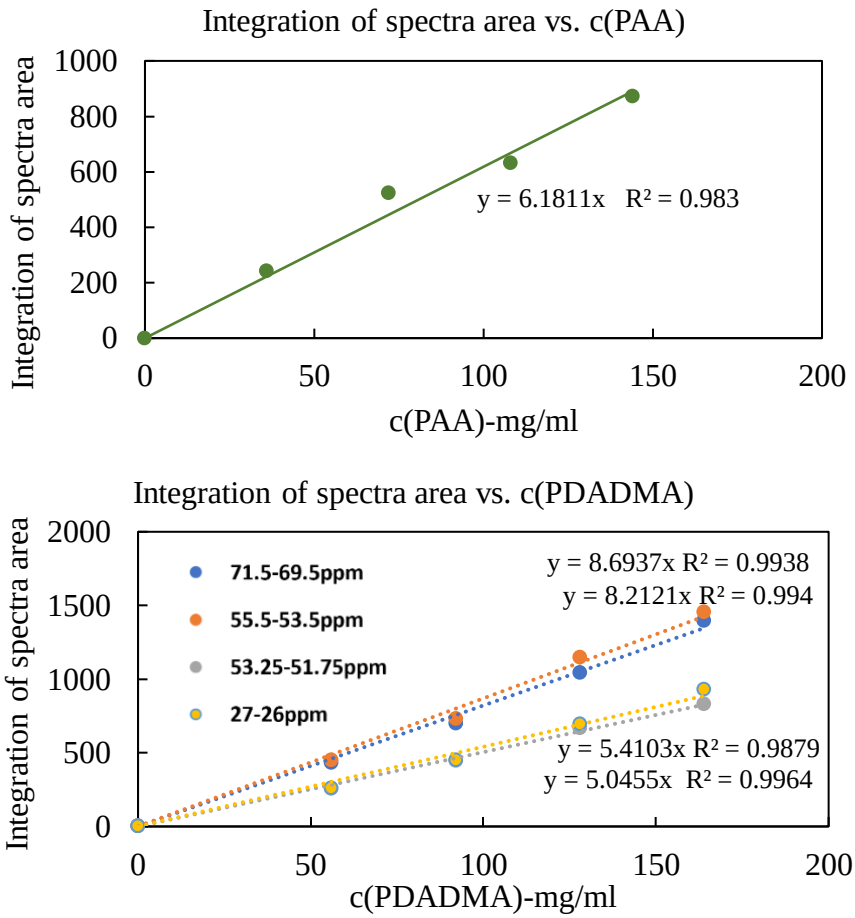

Figure 2-7. Areas under the peaks for the single PAA peak (top) in Fig. 2-6 and the four PDADMA peaks (bottom) in Fig. 2-6 at each of four PAA/PDADMA concentration ratios.

Note in Fig. 2-8 the dependence of the peak areas on salt concentration. We can minimize errors due to this relatively weak dependence by either accounting for the dependence of the C NMR signal on salt concentration when using the calibration curves, or by adjusting salt concentration to a standard value before performing the NMR experiments, so that they are all conducted at the same salt concentration. The linearity of the calibration curves, the low sensitivity to salt concentrations, the ability to measure the concentration of both polymers simultaneously, and the presence of four peaks for PDADMA, are all strong reasons to use C NMR to measure the polymer concentrations in PAA/PDADMA. The only downside is the longer NMR runs required, because of the weakness of the signal. To our knowledge, our work is the first to report the use C NMR to measure polymer concentrations in polyelectrolyte mixtures.

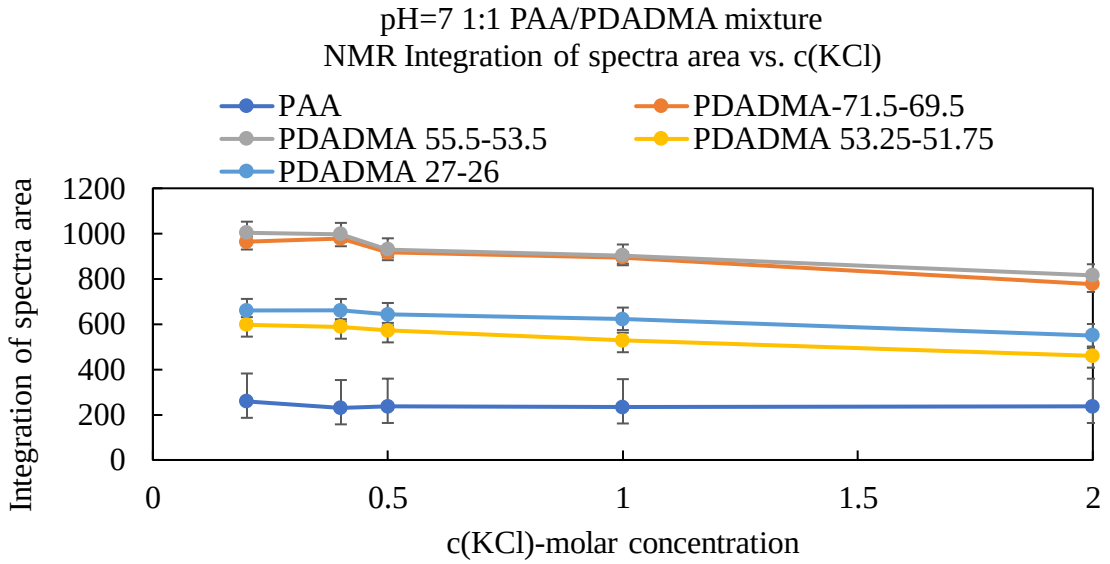

Figure 2-8. Dependence of peak areas from C NMR spectra on KCl concentration. For PDADMA, in the legends at the top, the peaks are identified by the NMR frequency range (in ppm) over which the peaks were integrated.

2.3.2 Thermal Gravimetric Analysis (TGA)

Thermal gravimetric analysis (TGA) was used to obtain weight percentages of residual water, polymer and salt in a given phase. The coacervate samples were initially dried in a vacuum oven at 40 ℃ for 1h before carrying out TGA, and weight loss from drying was measured by the difference in sample weight before and after drying. In the TGA chamber, samples were initially loaded at room temperature and then the temperature was ramped from room temperature to 1000 ℃ at a rate of 20℃/min, producing a typical weight loss curve for a reference sample PDADMA solution shown in Fig. 2-8. The figure shows an initial decrease in weight over a temperature range too low to be attributed to polymer volatilization and so must be attributed to residual hydration water that did not evaporate during the prior drying step. Polymer burns out before 600℃ and salt (KCl) begins to melt and sublime at around 800 ℃ (melting point of KCl: 770℃). The weight percentages of the polymer and of the KCl can be calculated as indicated in Fig. 2-9. Sometimes, there is small residue left in the furnace at the end of the heating ramp, due to charring under an inert atmosphere (nitrogen). This particular TGA analysis shows that the sample contained 40% PDADMA, 52% salt (KCl) and 8% water, by weight. Without the water, the percentages are 43.5% PDADMA and 56.5% KCL. The masses of polymer and salt added to the initial mixture are 48mg

PDADMA (47.52%) and 53mg KCl (52.48%). A second reference TGA scan is shown in Fig. 2-10, with polymer only and no salt in water. From these curves, we conclude that TGA analysis can give us the total polymer and salt concentrations in each phase to within around 10%.

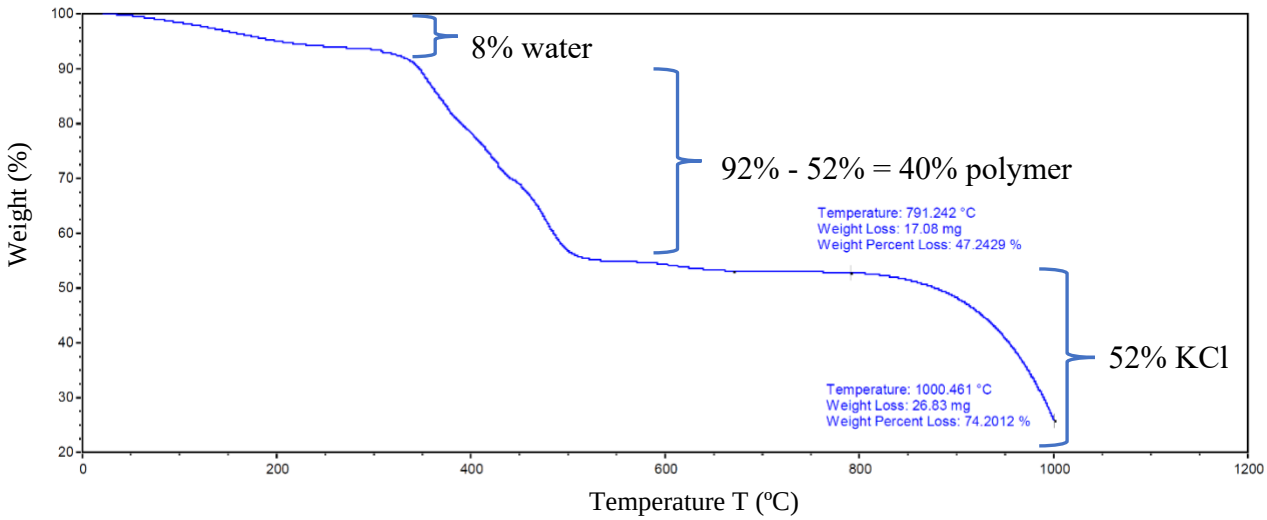

Figure 2-9. TGA weight loss curve at heating rate of 20 ℃/min for PDADMA and salt (KCl) in nitrogen.

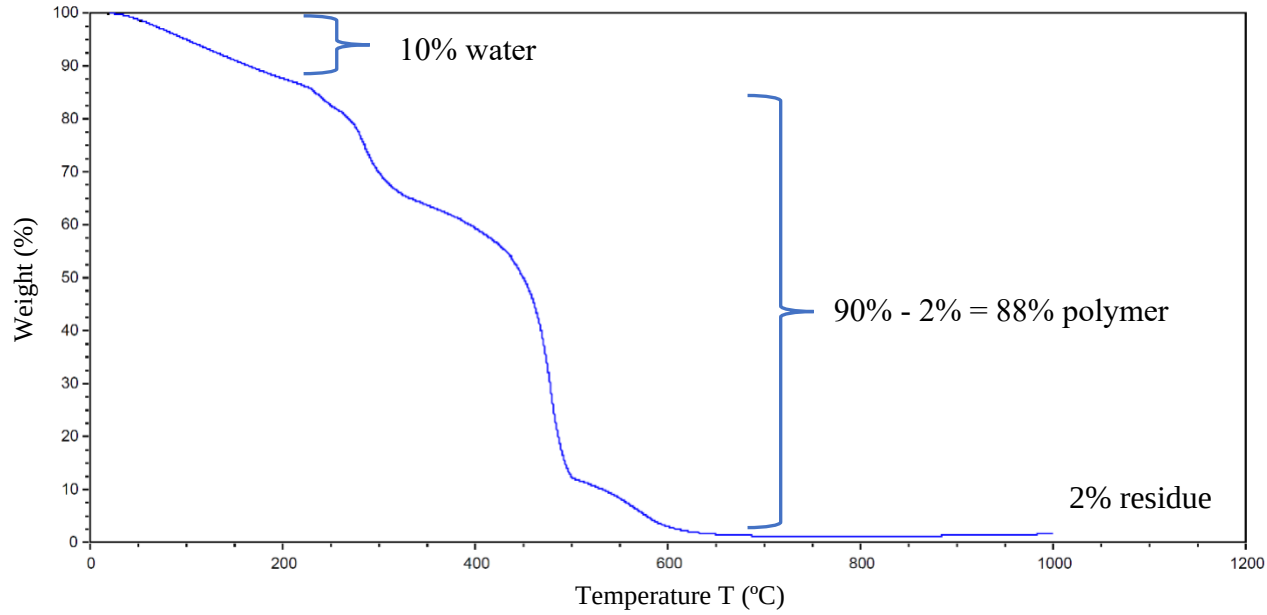

Figure 2-10. The same as in Fig. 2-9, except for a PAA/PDADMA coacervate sample with no salt.

2.3.3 Conductometry

Conductometry was used to quantify the salt ion concentration in the supernatant in the strong polyelectrolyte system PSS/PDADMA with KBr [2]. First the KBr concentrations in dilute solution were measured carefully by conductivity at room temperature and a standard curve developed to convert conductivity to concentration. The method cannot be used when PAA and KCl are used instead of PSS and KBr, because of the uncontrolled contribution of hydronium ions to conductivity due to partial dissociation of PAA and, to a lesser extent, due to the contribution of chloride ions from PDADMA. The calibration curve of conductivity versus added salt, for various concentrations of added PDADMA, is shown in Fig. 2-11. Note that the addition of PDADMA (along with accompanying chloride ions) has a small effect on the calibration curve. With increasing [PDADMA], the error of the calibration curve increases because the chloride ions dissociated from PDADMA also contribute to the conductivity.

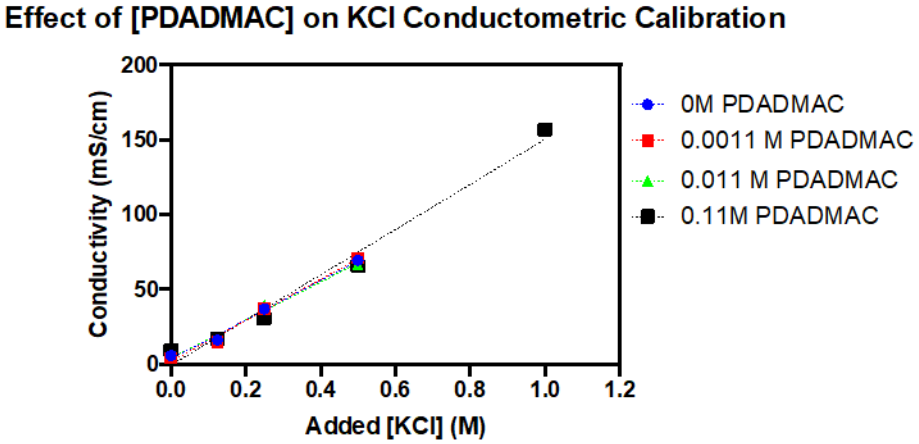

	0M PDADMAC	0.0011 M PDADMAC	0.011 M PDADMAC	0.11M PDADMAC
R square	0.9918	0.9917	0.9875	0.9813

Figure 2-11. Calibration curve of conductivity vs. added salt, for various concentrations of added polymer.

2.3.4 KCl Titration

KCl titration against an aqueous solution of $AgNO_3$ was used to quantify the concentration of chloride ions in the supernatant of the PAA/PDADMA system. This precipitation reactions: $AgNO_3 + KCI = AgCl \downarrow + KNO_3$. Preliminary results are shown in Fig. 2-12. Note that we observed a color change when the precipitation was carried out in air, due to oxidation, which adds to the mass of the precipitate, which degrades the accuracy of the assay. To minimize this error,

daylight, heat and oxidizing agents need to be avoided. These influences account for the large error at the lowest salt concentration in Fig. 2-12. We expect that the accuracy of this method can be improved with practice and care.

Sample	n(KCl)- mol	c(KCl) - M	Error-%
1	0.05	0.1	-15.9
2	0.10	0.2	-2.0
3	0.15	0.3	-2.6
4	0.20	0.4	-5.0
5	0.25	0.5	-4.1

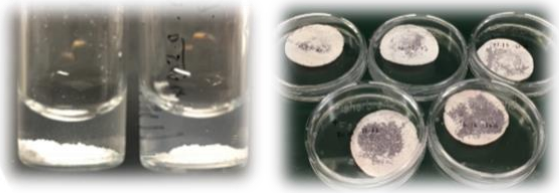

Figure 2-12. (Left) Results of precipitation assay of KCl mixed with AgCl solution, for different standard molar concentrations ranging from 0.1 M to 0.5M of KCl solutions. The errors in the concentration determined from the weight of AgCl precipitate are shown. (Right) AgCl color change due to oxidation is observed.

2.3.5 Phase Re-entry at the Higher Salt Region

Shown below in Table 2-1 are phase volumes of equimolar PAA/PDADMA at various pH values with various levels of added salt. In the Table, V_C is the volume of the coacervate phase measured by the height of the coacervate in a sample tube after sample mixing and centrifugation, and Φ_c is its volume percentage. These results are preliminary steps in our determination of the phase diagrams of this system as a function of both pH and salt. More detailed diagrams are shown in Fig. 2-13.

Table 2-1. 0.5M PAA and 0.5M PDADMA coacervate phase volumes V_C (ml) and volume fractions Φ_c (%) at various pH and salt concentrations ([KCl] unit: M).

	pH 1		**pH 3**		**pH 5**		**pH 6**		**pH 6.5**		**pH 7**		**pH 9**		**pH 14**	
[KCl]	V_C	Φ_c	V_C	Φ_c	V_C	Φ_c	V_C	Φ_c	V_C	Φ_c	V_C	Φ_c	V_C	Φ_c	V_C	Φ_c
0	0	0	0.25	12.5	0.2	10	0.19	9.5	0.26	13	0.40	20	0.50	25	0.60	30
0.2	0	0	0.13	6.5	0.5	25	0.24	12	0.60	3	0.55	27.5	0	0	0	0
0.4	0.18	9	0.13	6.5	0.55	27.5	0.25	12.5	0	0	0	0	0	0	0	0
0.5	0.21	10.5	0.13	6.5	0	0	0	0	0	0	0	0	0	0	0	0
1	0.22	11	0.13	6.5	0.13	6.5	0	0	0.20	10	0	0	0	0	0	0
1.5	0.23	11.5	0.13	6.5	0.13	6.5	0.14	7	0.18	9	0	0	0	0	-	-
2	0.24	12	0.13	6.5	0.20	10	0.13	6.5	0.20	10	0	0	0	0	0	0

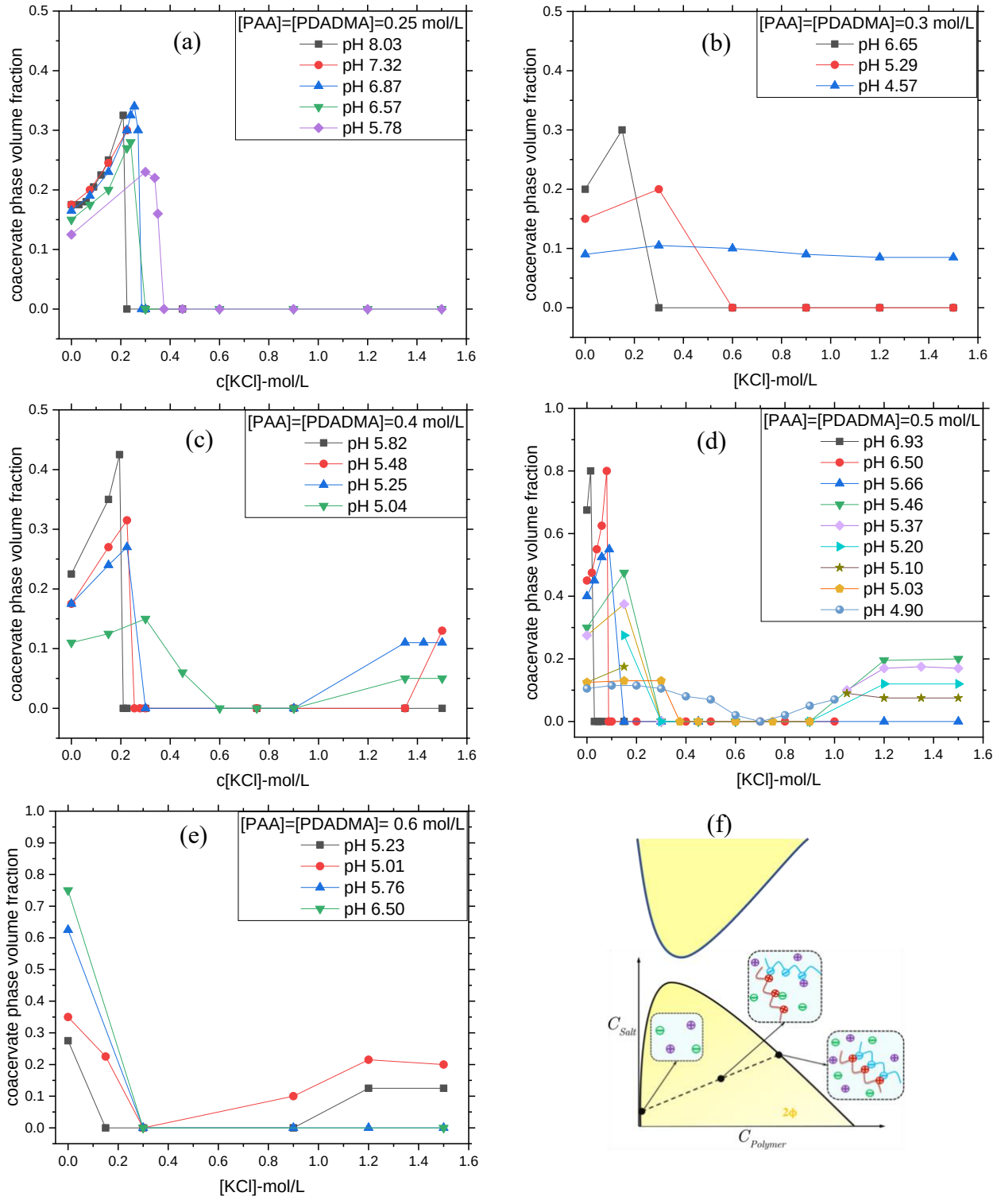

Figure 2-13. Coacervate phase volume fractions as functions of salt concentration (KCl) from 0 to 1.5 M, for various values of pH, and polymer concentrations [PAA]=[PDADMA] (a) 0.25 mol/L, (b) 0.3 mol/L, (c) 0.4 mol/L, (d) 0.5 mol/L and (e)0.6 mol/L. (f) Phase re-entry illustration.

Note in Fig. 2-13, that a non-zero coacervate phase volume fraction is given up to a critical salt concentration, above which the volume fraction of coacervate drops to zero. The salt concentration where this occurs is a lower critical salt concentration above which the solution becomes single phase. We note that in some cases, the maximum phase volume fraction is followed at higher salt concentrations by a lower phase volume fraction before it drops to zero, as seen for example in the purple and blue data in Fig. 2-13(a). In other cases, such as the black and red curves of Fig. 2-13(d), the coacervate phase fraction becomes very high, around 0.8, before seemingly plunging abruptly to zero. While we have a recorded the presence of a single phase as "zero coacervate volume fraction," these cases are more likely situations where the coacervate phase volume expands to 100%, corresponding to a progression along the phase diagram that passes to the left of the critical point, on phase diagram plotted as salt concentration against polymer concentration, as in Fig. 2-13(f). The location of the critical point on such a diagram, and the slope of the tie lines, are important predictions of theories of coacervation, which can be tested by experiments such as these.

In addition, Fig. 2-13(b-e) show that in the pH range 3-14, for salt concentrations above the upper critical salt concentration, two phases again reappear. This implies that in the pH range 3-6, there is both an upper and a lower critical salt concentration, with an intermediate range of salt concentrations over which the polyelectrolyte mixture is single phase. The upper critical salt concentration is typical of strong polyelectrolyte systems for which electrostatics provide the driving force for phase separations, the screening of which, with added salt, leads to a single phase. The presence of a lower critical salt concentration at low pH implies phase separation in that range is driven by non-electrostatic effects and that salt actually increases the driving force for phase separation. PAA on its own phase separate at high salt for a range of pH values [3]. These novel and unusual results shows clearly that we have much to learn about polyelectrolyte phase behavior, and that our methods show great promise in revealing new phenomena and new ways to control coacervation and other phenomena related to it.

2.4 Reference

[1] Salehi, A. and Larson, R. G., A Molecular Thermodynamic Model of Complexation in Mixtures of Oppositely Charged Polyelectrolytes with Explicit Account of Charge Association/Dissociation. Macromolecules 49, 24, 9706-9719(2016).

[2] Wang Q, Schlenoff J. B., The Polyelectrolyte Complex/coaervate Continuum. Macromolecules, 47(9), 3108-3116(2014).

[3] Litmanovich E. A., Chernikova E. V, Stoychev G. V., and Zakharchenko S. O., Unusual Phase Behavior of the Mixture of Poly(acrylic acid) and Poly(diallyldimethylammonium chloride) in Acidic Media, Macromolecules 43, 6871-6876 (2010).

Chapter 3

Review of Coacervate Rheology in Linear Viscoelasticity Region on Time-salt-pH-temperature Superpositions and other Superpositions

3.1 Abstract

The linear viscoelasticity of coacervates formed by oppositely charged polyelectrolytes in salt solution is reviewed, with a focus on time-temperature, time-salt, time-pH, and time-hydration superpositions, and on fundamental relaxation mechanisms. A variety of polyelectrolyte pairs are covered, showing the frequent, but not universal, success of time-salt superposition. Master curves in many cases are similar to those for neutral polymers, including Rouse and reptation theories. However, in some cases, solid-like, as opposed fluid-like, response is observed at low frequencies, especially at low salt concentrations. Some coacervates seem to fit "sticky diffusion" theory reasonably well, wherein relaxation is controlled by the breakage rate of ion pairs; the dependence of the "sticker" lifetime on salt concentration has been explored but is not well understood as yet. It is also possible that local relaxation is not controlled by breakage of ion pairs, but by cooperative, "glassy," relaxation of monomers, salt ions, and water molecules. A compilation and comparison of different data sets and suggested formulas for rheological time constants are presented, and some suggestions are given for future directions. The contents of this chapter are the result of collaborative work with graduate student, Huiling Li.

3.2 Introduction

One of the last remaining fields of polymer science for which the linear rheology remains mysterious is that of coacervates formed by mixing water-soluble polyelectrolytes (PEs) of opposite sign in the presence of salts and water. The rheology of polymer-rich phases formed by such mixtures ranges from hard solid, to soft gel, to liquid, depending on polymer type, molecular weight, salt concentration, and other properties. While there does not appear to be a sharp boundary

distinguishing “coacervates” from “precipitates,” the latter are dense, hard, mixtures of oppositely charged polymers, and are “glassy,” or non-equilibrium, whereas coacervates, also called “polyelectrolyte complexes” (or PECs), are either soft gel-like solids, or viscous fluids that are at thermodynamic equilibrium, or at least close to it. In this review, we focus on coacervates, whose rheology is more readily measured than is the case for precipitates. There are a wide range of uses of these coacervates, ranging from food and personal care products to drug release compounds, underwater adhesives, and others, as reviewed recently by Liu *et al.* [1].

Despite their wide range of applications, and growing interest in their structure and dynamics, physical properties, and rheology, coacervates remain mysterious. Even basic scaling laws, such as the dependence of zero-shear viscosity and relaxation time on molecular weight, and on concentrations of PEs and salts, remain uncertain. The lack of reliable quantitative theories for coacervates, analogous to the Rouse theory of unentangled neutral polymers, and the reptation theory for entangled ones, is a glaring gap. The theory that is closest to playing this role for coacervates is the “sticky diffusion” theory of associating polymers [2], which has been applied to coacervate rheology, but with uneven success, as we will see in what follows. Reasons for the gaps in theoretical understanding include: 1) the rarity of experimental studies on comprehensive series of nearly monodisperse polymers over a wide range of molecular weights; 2) the relative difficulty in controlling and measuring salt, water, and polymer concentrations in the coacervate phase because it is typically prepared by phase separation; 3) sensitivity to ion- and monomer-specific interactions, including PE charge density, monomer sequence, hydrogen bonding, chirality, π–π stacking, etc.[3], thus impeding “universal” scaling laws that transcend specific chemistry; 4) the complexity of the physical phenomena governing coacervates, which includes electrostatics, ion-binding of one PE to another of opposite charge, binding to salt ions, entanglements, and hydrophobic interactions; 5) asymmetries between the two coacervate PEs in the effect on rheology of chain length, charge density, concentration, etc.; and 6) the large number of parameters, including the concentrations and molecular weights of each of the two PEs, concentrations and types of salt, etc. The above list does not even consider the case of charge regulation and pH dependencies of rheology for “weak” PEs, whose charge states are sensitive to pH and chemical environment.

These challenges are slowly being overcome, and many important and provocative experimental and theoretical results are now emerging, as reviewed recently by Sing and Perry [4].

This review nicely organizes the available theoretical approaches to the thermodynamics and structure of coacervates. These include electrostatic "blob" theory, in which the interacting units of the chains are multi-monomer sub-coils of the chain, as described in work by Rubinstein and coworkers [5]. This approach is likely only qualitative for dense coacervates. The case of dense coacervates has been addressed using liquid state theory, which accounts for monomer-scale hard-core and electrostatic interactions, as exemplified in work by Perry and Sing [6] and by Wang and coworkers [7]. Both blob theory and liquid state theory are "generic" in the sense that they use chemically non-specific models in which polymer molecules are treated locally as either random-walk "blobs" or as spherical "monomers," lacking chemical specificity other than size and effective van der Waals and Coulombic charge interactions. Chemical specificity can be provided in an ad hoc way, through assignment of chemically specific interaction free energies and Flory chi parameters between monomers and salt ions, which implicitly account for hydrogen bonding, hydrophobic effects, and other details through data fitting. Such an approach has been taken by Zhang and Shklovskii [8], Olvera de la Cruz and coworkers [9], Muthukumar and coworkers [10], and by Salehi and Larson [11], the latter in collaboration with Friedowitz and Qin [12]. Rigorous, chemically realistic, analyses of coacervate structure require atomistic simulations, as exemplified in work by Sammelkorpi, Lutkenhaus, and coworkers [13]. Such simulations are typically limited in the time and length scales they can access, and the detailed data they provide still need to be interpreted and generalized using more coarse-grained, or ad hoc, theories. Thus, all the above approaches will be valuable in filling out our understanding of coacervate structure in the years ahead. For more details on these methods, the reader is referred to the review by Perry and Sing [4] and the papers referenced above.

This review is directed specifically towards the *rheology* of coacervates, and is intended both to summarize major findings and to focus attention on where progress is most needed. We will focus on the linear rheology of coacervates made from two homo-polyelectrolytes of opposite charge, especially on data that satisfy "time-salt superposition," which suggests some degree of "universality" in coacervate behavior. Readers are also directed to an overview by Liu *et al.* [1]of linear rheology, that also covers phase behavior briefly, as well as block polymer coacervates. There is also some recent work on *polyampholyte* coacervates, in which each polymer contains both a positively charged and a negatively charged block, with dynamics rather similar to that of mixtures of oppositely charged homopolyelectrolytes [14-16]. The review of Sing and Perry [4]

mentioned above, focuses particularly on theories of equilibrium coacervation, but also touches on rheology and other topics of current interest. Ultimately, theories should encompass both equilibrium phase behavior and rheology, since the same thermodynamic driving forces control them both. A validated theory of phase behavior would also allow estimation of the compositional changes in the equilibrium coacervate phase when temperature, salt, or other variables are changed. This would help in interpreting the effect of these variables on the rheology of the equilibrium coacervate phase, including the "shift factors" discussed below.

Given the daunting complexities of coacervate rheology outlined above, a major boost was the discovery of the principle of "time-salt superposition," whereby the linear rheology curves (i.e., G' and G'' versus frequency) for coacervates with differing salt concentrations can be superposed onto a "master curve" by shifting along the frequency axis, and to a much lesser degree along the modulus axis. Time-salt superposition was first revealed clearly in work by Cohen Stuart and coworkers [17, 18], and has since been found in multiple coacervate chemistries, as we will see in this review. However, a major caveat should be borne in mind. Frequently, coacervates are formulated by mixing the PEs with solvent and salt, and allowing the coacervate to phase separate from a supernatant phase that contains not only water and salt, but may also contain one or both PEs. As a result of the phase separation, the salt concentration in the coacervate can differ from that of the original mixture, and there can be differences in water and polymer concentrations as well, and possibly even a change in the ratio of monomer molarities of the two PEs as the overall salt concentration is changed. Consequently, "time-salt superposition" involves superposition of solutions differing at least somewhat in PE concentration as well as in salt concentration. These additional compositional variations introduce vertical shifting along the modulus axis, which is sensitive to PE concentration, and make interpretation of the horizontal shift factors doubtful or complex, since they are affected by PE concentration as well as salt concentration. There may also be doubt about the validity of the superposition itself, if it is carried out over a wide range of salt concentrations with only small overlaps of data. That is, large vertical and horizontal shifts may allow one to stitch together data sets for which failure of superposition would only have become evident if one had used wider frequency ranges. We will show an example of this later in the review. The risk of a misleading "forced superposition" can be counteracted most effectively by using a wide frequency range at each salt concentration. A more efficient method is to use time-temperature superposition to extend the frequency range. The latter method, while useful carries

its own risks, including the possibility of entering a two-phase region unwittingly, as might happen for the PDADMA/PSS, which exhibits a surprising lower critical solution temperature [19].

In addition to these polyelectrolyte-specific issues, the quality of polymer synthesis and characterization is just as important in polyelectrolyte rheology as it is for rheology of neutral polymers. In literature to date, polyelectrolyte samples have usually been obtained from commercial vendors, with higher polydispersities and less certainty regarding synthetic quality than is sometimes the case for more conventional polymers. We have assembled the information on polydispersity available from the publications or supplies, where available, in Table 3-1. Generally, but not always, polydispersities range from M_w/M_n ~1.1 to 1.4. Even where synthesis and characterization of polyelectrolytes are done in-house, with fractionation to reduce polydispersity, scrutiny and replication of experimental results remain important tasks. While this review does not address these experimental realities, readers should be aware that improved sample preparation and characterization will be a critical part of improving our understanding of coacervates and their rheology, and that conclusions drawn from data presented here may need revision as additional samples are studied.

Table 3-1. Degree of polymerization, molecular weight, polydispersity index (PDI) and source of relevant polyelectrolytes mentioned in the review

Reference	Polyelectrolyte	Degree of polymerization	Molecular weight (kDa)	PDI	Source
[3]	PVBTMA	100	213	1.13	Authors' synthesis
	PSS	100	201.7	-	Polymer Standards Service
[6]	PDADMAC	-	289.1	1.3	Sigma-Aldrich
	PSS	-	354.4	1.7	
[17]	PDMAEMA	20, 50, 150, 510	-	<1.2	-
	PAA	10, 20, 50, 150, 510			
[18]	PDMAEMA	17, 51, 150, 527	2.7, 8.0, 23.5, 82.7	1.18, 1.40, 1.04, 1.09	Polymer Source
	PAA	20, 47, 139, 500, 1730	1.5, 3.5, 10, 36, 124.5	1.2, 1.3, 1.15, 1.1, 1.25	Sigma-Aldrich, Polymer Source
[27]	PRE	100, 400	15.5, 60	-	Alamanda Polymers
	PLK	100, 400	16, 66	-	
[28]	PMAPTAC	175, 356, 568, 688, 2112	38.5, 78.6, 125, 151, 466	1.16, 1.13, 1.27, 1.22,1.75	Authors' synthesis
	PMA	141, 250, 329, 756, 838, 2081	15.2, 27, 35.5, 81.6, 90.5, 225	1.03, 1.01, 1.06, 1.03, 1.03, 1.41	
[36]	PDADMAC	-	300	-	Sigma-Aldrich
	IBMA	-	11,82, 196, 410	1.75, 2.6, 3.04, 2.4	-
[43]	PMAPTAC	1020 ,1570, 2370, 3850, 4700	226, 346, 524, 849, 1040	1.05, 1.04, 1.06, 1.06, 105	Authors' synthesis
	PMA	1120, 1280, 2620, 3600, 4780	121, 136, 283, 389, 516	1.08, 1.14, 1.15, 1.05, 1.04	
[50]	PAH	158	14.8	1.04	Millipore Sigma
	PAA	160	15	1.18	AK Scientific
[51]	PTMAEMA	50, 250, 500	27.7 - 28.2, 84.9, 129.4 - 135.5	1.04, 1.05, 1.09 - 1.11	Authors' synthesis
	PSPMA	50, 250,500	16.7, 56.2, 116.8	1.05, 1.1, 1.28	

	PTMAEA	250, 1000, 2000	40.6, 166.7, 388.4	1.21, 1.22, 1.24	
	PAMPS	250, 1000, 2000	69.8, 206.1, 283.5	2.27, 1.23, 1.1	
[52]	PDADMAC	-	100-200		-
	PAA	-	100		-
[54]	PAH	-	120-200		Polyscience
	PAA	-	100		Sigma-Aldrich
[59]	QVP	-	60	-	Sigma-Aldrich
	PSS	-	200	-	
[60]	Poly(NAS)[i]	190	32	1.19	Authors' synthesis
[62]	PDADMAC	970	150	-	Sigma-Aldrich
	PSS	970	200	-	
[63]	PDADMAC	-	400	-	Ondeo-Nalco
	PSS	-	200	-	AkzoNobel

To help the reader, we give in Table 3-2 abbreviations for the PEs (with polycations listed first) reviewed here, along with their pKa values, monomer molecular weights M_0 (without including the molecular weight of any accompanying small salt ion) and literature-reported Kuhn lengths b_K:

Table 3-2. Relevant Polycations/Polyanions and their selected Physical Parameters

Abbreviation	Polycation (or PC)	pKa	M_0 (Da)	b_K (nm)
PVP	Poly (4-vinylpyridine)	3-4.5 [20]	105	2.6[i] [21]
PDMAEMA	Poly (N, N -dimethylamino ethyl methacrylate)	6.1-6.5 [17, 18]	157	2.73, 3.66 [ii] [22] 3.5, 16 [23]
PAH	Poly (allylamineH^+)	8.61-10.28 [24]	57	1.46-2.5[iii] [25]
PLK	Poly (L-lysine)	10.6 [26]	128	0.7[iv] [27]
PMAPTA	Poly [3-(methacryloylamino)-propyltrimethylammonium]	Strong	185	3.0[v] [28]
PVBTMA	Poly [(vinylbenzyl) trimethylammonium]	Strong	176	-
PDADMA	Poly (diallyldimethylammonium)	Strong	126	5.0[vi] [29]
Abbreviation	Polyanion (or PA)	pKa	M_0 (Da)	b_K (nm)
PSS	Poly (styrenesulfonate)	1.22-1.50 [24]	183	3.0[vii] [30] 2.8-12[viii] [31]
PRE	Poly (D, L-glutamic acid)	5[ix] [32]	129	0.7 [iv] [27]
PAA	Poly (acrylic acid)	5-5.5 [18] 4.79-5.78 [24]	72	0.64[x] [33] 0.86-2.52[xi] [25] 6.3 [23] 11.7[xii] [34]
IBMA	Poly (isobutylene-alt-maleate)	6.4 [35]	170	0.68-0.79 [xiii] [36]
PMA	Poly (methacrylic acid)	7.03 [24] 6.4 [35]	86	0.6[xiv] [37]

[i]Evaluated in HCl solution by light scattering using the worm-like chain (WLC) theory.
[ii]2.73 nm is for un-ionized PDMAEMA in methanol, 3.66 nm is for ionized PDMAEMA•HCl.
[iii]Using the WLC relationship and atomistic molecular dynamics, the persistence length varied from 0.73 nm (at 0% ionization) to 1.25 nm (at 100% ionization).
[iv]Measured at 5 wt% polymer concentration without salt by small-angle X-ray scattering.
[v]Assumed by Yang *et al.* [28] because the Kuhn length of a polycation similar to PMAPTA in a PEC in 1 M NaCl was reported to be 3 nm.
[vi]Measured in 0.5 M NaCl solution by light scattering.
[vii]Estimated in 0.5 M NaCl solution by light scattering.
[viii]The persistence length measured by small angle neutron scattering was from 1.4 (in 3M NaBr solution) to 6 nm (without salt).
[ix]Estimated from the Figure 3 in Appel & Yang [32].
[x]Calculated using the freely-joint-chain (FJC) model together with the force-extension curve measured by atomic force microscopy.
[xi]The electrostatic persistence length, calculated according to the WLC relation and full atomistic molecular dynamics simulations, was from 0.43 nm (at 0% ionization) to 1.26 nm (at 100% ionization).
[xii]Measured by small-angle X-ray scattering, for un-neutralized PAA in water at 25°C.
[xiii]The Debye length of IBMA is estimated as 0.68-0.79 nm, which is claimed to be consistent with the Kuhn length of IBMA.
[xiv]Estimated in mercapto and dodecanol solution without salt from the fits of WLC and FJC models using atomic force microscopy.

The review is outlined as follows: Section 3.3 discusses some suggested models of coacervate structure. Section 3.4 describes time-temperature superposition, and Section 3.5 describes time-salt superposition, with multiple examples. Section 3.6 discusses the molecular weight dependence of zero-shear viscosity and terminal relaxation time, while Section 3.7 describes the rheological consequences of large differences in the lengths of polycation vs. polyanion. Section 3.8 discusses time-salt-pH superposition and 3.9 illustrates time-hydration superposition. Section 3.10 shows cases where there is a low-frequency plateau, and Section 3.11 covers available theories for coacervate rheology. Section 3.12 summarizes the main conclusions. References come in Section 3.13.

3.3 Structure of Coacervates

It has long been recognized that a key driving force for polyelectrolyte complexation is the entropy gained by the release of small salt ions from a PE of given charge and replacement of these small ions by many fewer PE chains of opposite charge. Recent theoretical and experimental work suggests that complexation of a pair or a few long, oppositely charged polyelectrolytes occurs even in dilute solutions, due to the small entropy loss caused by binding of a few chains together, relative to the huge entropy gain of the counterions thereby released [38, 39]. Thus, the dense coacervate phase is likely in equilibrium with a supernatant phase containing dilute complexes each containing a few chains. Although coacervation produces close physical association of the PE molecules of opposing charge, the detailed organization of the PE chains within a coacervate has long been a matter of debate and speculation. Michaels [40] suggested both a "ladder model" in which two chains line up, pairing opposite charges like rungs of a ladder, as well as what to him seemed a more plausible "scrambled" model in which multiple polycations crisscross and associate with each polyanion, and vice versa. It is well known that a single long polyelectrolyte in solution takes on an expanded Gaussian conformation due to electrostatic repulsions at low salt, but with added salt, screening of electrostatic interactions causes the coil to shrink down towards a size governed by its "bare" (or charge-free) Kuhn length, where the Kuhn length is the length of a random-walk step size of the chain. Indeed, neutron scattering studies by Schlenoff and coworkers [41] on solutions of poly(styrenesulfonate) (PSS) show, as expected, that the coil size is expanded at low ionic strength but shrinks towards the bare (charge-free) size with increasing added salt, where the bare PSS Kuhn length is around 1.4 nm. In coacervates of PSS with poly(diallyldimethylammonium) or (PDADMA), the ionic strength due to the polyelectrolyte alone is high, and the same group [42] find that the coil size is small and insensitive to added salt concentration, as one might expect. More recent neutron scattering results by Schlenoff and coworkers [43] show that in coacervates of poly[3-(methacryloylamino)-propyltrimethylammonium]/poly(methacrylic acid), (i.e., PMAPTA/PMA), the deuterated PMA chains have Gaussian configurations with Kuhn lengths of 1.5 nm, similar to that of the bare PSS Kuhn length. This evidence supports the "scrambled" model of the coacervate, with chains of both polyelectrolytes taking on Gaussian configurations with Kuhn lengths similar to those of the corresponding uncharged polymers. However, Spruijt *et al.* [23] found that in coacervates of poly(N,N-dimethylamino ethyl methacrylate)/poly(acrylic acid), or PDMAEME/PAA, Kuhn

lengths obtained from radii of gyration measured by neutron scattering were 3.5 nm and 16 nm, for the two different chain lengths studied, and 6.3 nm for PAA. These values are larger than one would expect for bare Kuhn length, but Spruijt *et al*. commented that these values are "upper bounds" due to possible bias from the radii of gyration of long chains selectively segregating to the coacervate. Estimated Kuhn lengths for various polyelectrolytes under different conditions of salinity, pH, and solvent conditions are given in Table 3-2. Even if the configurations of chains in the coacervate are random walks with small Kuhn lengths, the nature of the interactions of the charges on the chains remains in doubt. One limiting possibility is that the charges mix similarly to that of simple salt charges, with opposite charges correlated to reduce spatial variations in net charge and electrostatic energy, while allowing considerable positional disorder to maintain high entropy. This picture is the basis of the Voorn-Overbeek theory of coacervation [44] which ignores the connectedness of polymeric charges, treating them as simple salt ions when calculating their electrostatic interactions.

While this simplistic picture is now largely superseded by theories that more realistically account for chain connectivity, the possibility remains that each polymeric ion sees a "cloud" of neighboring oppositely charged ions or monomers, as opposed to being neutralized by one and only one charge on a neighboring oppositely charged monomer or salt ion, forming a so-called "ion pair" or condensed salt ion. In the latter case, the breakage time of the ion pair is the fundamental event governing the relaxation dynamics of the coacervate. An intermediate possibility, suggested by Colby and coworkers [35] is that oppositely charged chains are paired up for long periods of time as depicted in Fig. 3-1, and that the time constant for reorganization of the coacervate is determined by the rates of formation and breakage of "quadrupolar" local groupings of chains, as depicted in Fig. 3-1. This depiction has the advantage that it accommodates significant differences in spacing of charges on the two chains, with the "wavy" red chain having a wider spacing of charges than the black chain. However, the depiction suggests an extended or expanded conformation of the chains, which seems at odds with at least some neutron scattering data [43]. Lytle and Sing [45] have developed a modification of the ion-pairing picture wherein the binding of one monomer of a PE chain to an oppositely charged chain biases the next monomers on these two chains to bind also. The enhanced probability of binding of the second monomer was expressed in terms of a "transfer matrix" whose probabilities could be deduced from coarse-grained molecular simulations. It is also possible that a more helpful picture might be that of

association of multiple monomers, salt ions, and waters of hydration, whose cooperative motions are necessary for motion of a single monomer, similar to the situation for many glasses, as suggested by some experiments and simulations [13, 43].

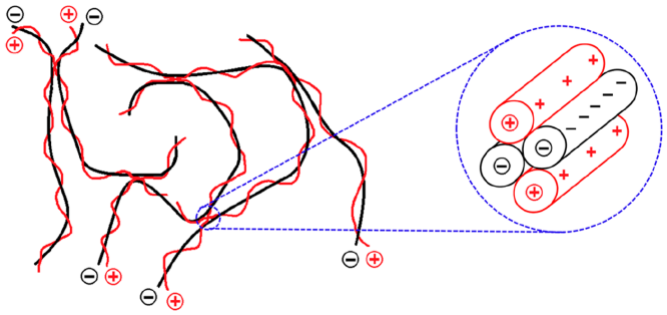

Figure 3-1. Schematic of possible polycation (red) and polyanion (black) conformations in coacervate [36]. Used with permission from Hamad et al. Macromolecules 51, 5547-5555 (2018). Copyright (2018), American Chemical Society.

For better or worse, the detailed structure of the coacervate does not seem to have been of great concern in the development of models for the rheological properties, which are generally of the "sticky diffusion" type, whose rheological predictions are governed by rates of local diffusion. While dependences of these rates on temperature, salt concentration, and other variables can be extracted from fitting the models to experimental data, these dependencies do not define the mechanisms of local relaxation, nor do they even require that diffusion be of the "sticky" type, since any other local mechanism of relaxation, including highly cooperative ones, would give the same rheological phenomena at longer time scales. It can be questioned how well "sticky diffusion" concepts really apply to coacervates composed of two types of polymers. The flexibility of the models to fit rheological data means we can interpret these data without too much regard for either the detailed microstructure or the local dynamics, but, of course, this also limits our ability to use rheology to deduce structure or local interactions. This is a familiar conundrum, in which rheology has exquisite quantitative, but limited qualitative, value. Combined with structural information, for example from scattering measurements or simulations, however, rheology can in principle generate substantial insight into both structure and rates of structural change. In the future the combination of macroscopic rheology and incisive structural probes will hopefully provide a rich picture of coacervate structure and dynamics, from small scales to large. Of primary concern here, however, is the rheological data and their interpretation in terms of rheological models. We therefore proceed directly to a description of the available rheological data, and then to its modeling. We will return to local structure and dynamics in Section 3.11.

3.4 Time-Temperature Superposition

The well-known principle of time-temperature(t-T) superposition is illustrated in Fig. 3-2 for a coacervate of Poly [3-(methacryloylamino)-propyltrimethylammonium], PMAPTA, and Poly (methacrylic acid), PMA, for various degrees of polymerization n_{av}, chosen to be roughly equal for PC and PA. Fig. 3-2 includes results for three different concentrations of NaCl, the lowest being near zero. The different colors index the temperatures used, and for each temperature, "horizontal" and "vertical" shift factors, a_T and b_T, respectively, are employed to bring the curves into superposition on a log-log scale, to form a pair of "master curves" for G' and G'' for each coacervate. The vertical shift factor reflects a change in modulus with temperature and only slightly deviates from unity over the temperature range from -5°C to 65°C. The horizontal shift factor a_T, on the other hand, varies with temperature by over four orders of magnitude for low salt and 1.5 orders of magnitude for 0.3M NaCl, following an Arrhenius dependence as shown in Fig. 3-3 for one of the five pairs of molecular weights.

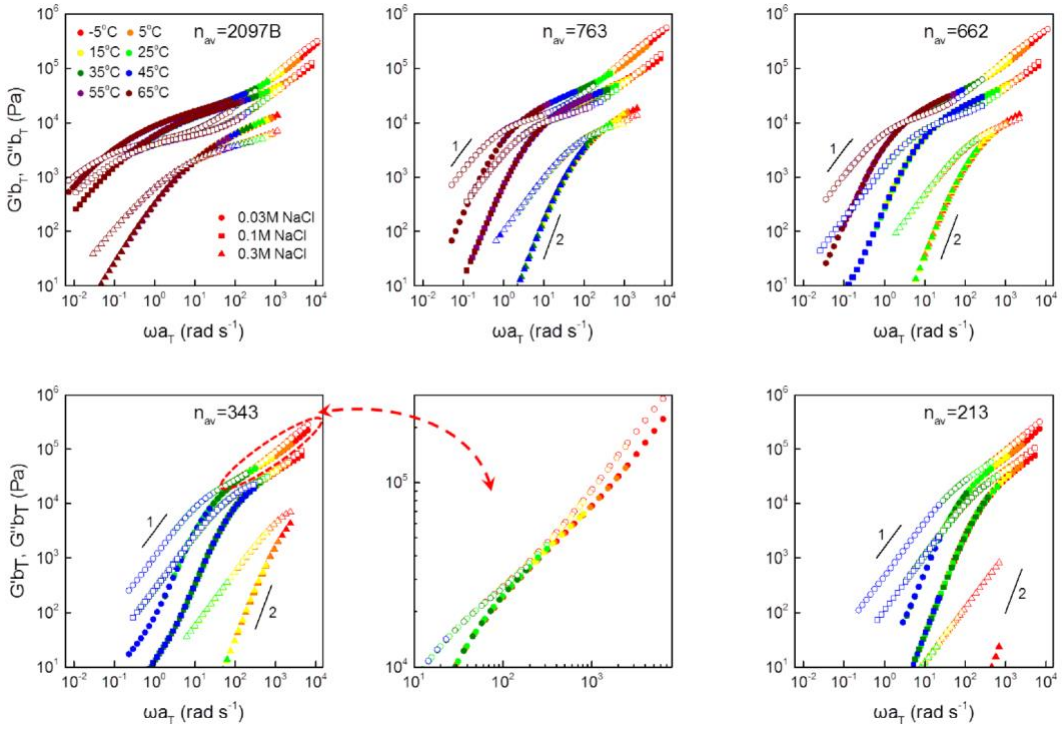

Figure 3-2. Time−temperature superposed storage (G', solid symbols) and loss (G'', open symbols) moduli for coacervates of in-house synthesized PMAPTA and PMA with average degrees of polymerization n_{av} at three NaCl concentrations 0.03 M (●, ○) 0.1 M (■, □) and 0.3 M (▲, △). The horizontal shift factor a_T is given in Fig. 3-3 below, with reference temperature = 25 °C. The vertical shift factor b_T varies only about 10% from unity, and decreases with increasing temperature as expected. The center lower panel magnifies the high-frequency portion of the data for n_{av} = 343 [28]. Used with permission from Yang et al. Macromolecules 52, 1930−1941 (2019). Copyright (2019), American Chemical Society.

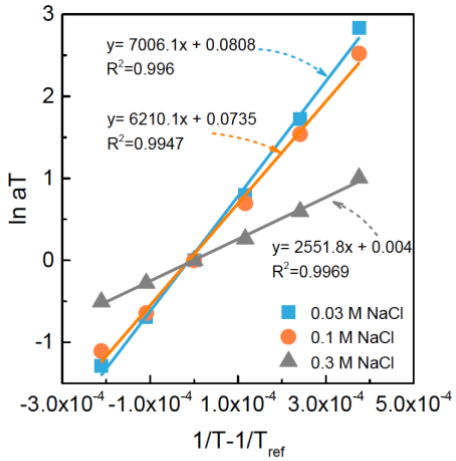

$$ln\left(\frac{a_T}{a_{T,ref}}\right) = \frac{E_a}{R}\left(\frac{1}{T} - \frac{1}{T_{ref}}\right)$$

Figure 3-3. Arrhenius plot of temperature dependence of shift factor a_T for the nav = 2097B sample from Fig. 3-2 at the three salt concentrations, with reference temperature = 25 °C [28]. Used with permission from Yang et al. Macromolecules 52, 1930−1941 (2019). Copyright (2019), American Chemical Society.

The superposition of results at different temperatures indicates that the relaxation processes in the coacervate are the same at each temperature, apart from a rate factor that acts as a "metronome" that uniformly speeds up (or slows down) all processes by the same relative amount as temperature increases (or decreases). The success of the superposition indicates that temperature controls primarily the local friction, but otherwise changes little or nothing about the solution structure or the processes by which relaxation occur. Similar t-T superposition is commonly observed in the relaxation of neutral homopolymers, such as polybutadiene, polystyrene, polyethylene, etc. [46], although deviations from superposition can often be observed at high frequencies and high values of G' and G'' (typically above 10^7 Pa in melts). At these high frequencies, local spatial heterogeneities in modes of relaxation having different temperature dependencies are not sufficiently averaged together to produce a single "mean field" friction [47]. Similar failures of t-T superposition may occur in coacervates if very high frequencies, beyond those reached in Fig. 3-2, are accessed. Interestingly, in heterogeneous polymers such as mixtures of different homopolymers, t-T superposition typically fails [46, 48] presumably because the two polymeric components, even if miscible, are locally segregated enough for the frictional contribution of each to express itself even at modest or low frequency. Given the failure of t-T superposition typical in even miscible blends of uncharged homopolymers [49], it may seem surprising that t-T superposition would hold in a coacervate containing two chemically very

different PEs. One may interpret this as evidence that the two PEs are intimately mixed due to their attractive charge interactions, with both chains "pooling" their frictional response to produce an effective single friction coefficient that reflects the contributions of both chains, at least over the range of frequency for which t-T superposition holds.

Note in Fig. 3-3 that the dependence of the shift factor a_T on temperature follows an Arrhenius form, which is exponential in the inverse of temperature. This, very common, temperature dependence normally reflects relaxation that is controlled by a single activated process, characterized by an "activation energy" E_a that needs to be overcome to allow a single "elementary" step in the relaxation to occur. The value of E_a in an Arrhenius fit is therefore a clue to the key processes that allow relaxation to occur. The Arrhenius form is typical for polymeric melts at temperatures much higher (≈100°C higher) than their glass transition temperature; at lower temperatures within 50-100°C of their glass transition, the so-called "WLF" form is observed for most polymeric melts [46]. (The WLF form is thought to arise from increasingly cooperative relaxation upon cooling and densification, so that there is no single activation energy governing relaxation). It is instructive that the activation energy for the coacervate of Figs. 3-2 and 3-3 decreases dramatically from around 23 k_BT to 21 k_BT to 9 k_BT (corresponding to 58, to 51 to 21 kJ/mol), as the salt concentration increases from 0.03 to 0.10, to 0.30 M. Yang *et al.* (2019) [28] have suggested that the "elementary" step governing coacervate relaxation, in the absence of salt, involves four monomers, as depicted in Fig. 3-4A. In this picture, local movements of a charged monomer require breaking of its physical "bond" with an oppositely charged monomer on another chain. In the absence of salt ions, or of unbound charged monomers, two such bonds must exchange partners in a coordinated fashion [36] to enable "hopping" of a monomer from one chain to another as illustrated in Fig. 3-4A, with a consequent large activation energy. The addition of salt enables the hopping of one monomer to occur independently of its former partner monomer, as illustrated in Fig. 3-4B, with a much lower activation energy. This speculative picture assumes that unbound monomer charges are rare, and that coordinated motions of monomers and salt ions more complex than those of Fig. 3-4 are unimportant. However, more complex exchange processes would give a similar t-T shifting, as long as the mix of underlying basic processes stays the same at other temperatures. Hence, until the activation energy and its dependence on salt concentration are explained quantitatively, considerable uncertainty must be ascribed to any putative mechanism of relaxation.

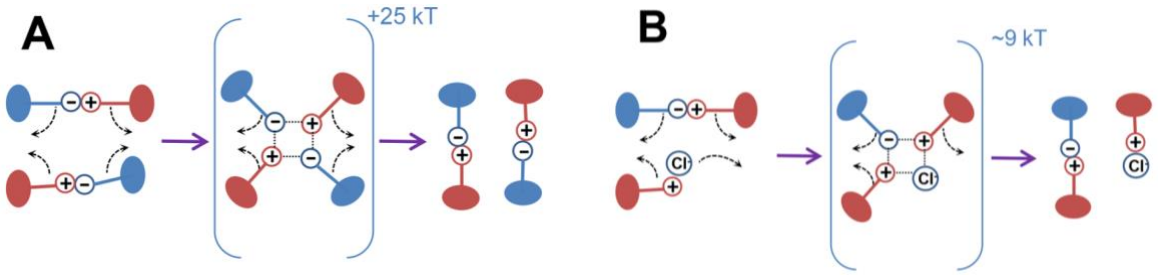

Figure 3-4. Proposed elementary mechanism of viscoelastic relaxation involving polyanion monomers (blue) and polycation monomers (red), without (A) and with (B) enablement by salt ion binding [28]. Used with permission from Yang et al. Macromolecules 52, 1930−1941 (2019). Copyright (2019), American Chemical Society.

3.5 Time-salt Superposition

The first clear demonstration of time-salt (t-s) superposition, shown in Fig. 3-5, was the work of Cohen Stuart and coworkers [18] for PDMAEMA and PAA at near-neutral pH where both PEs are almost completely charged. This work of Spruijt *et al*. covered a range of degrees of polymerization, N= 20, 50, 100, 150 and 510, and salt concentrations, 0.5, 0.75, 1.05, 1.2 M KCl. They plotted curves of $G'_{scaled} = G' /G_c$, and $G''_{scaled} = G'' /G_c$ against $\omega_{scaled} = \omega\tau_c$ with salt-dependent horizontal shift factor τ_c and vertical shift factor G_c. (In Fig. 3-5, the low-frequency limiting power law slopes of 1 and 2 for G" and G' are used to extrapolate these G'' and G' curves until they cross, and G_c and τ_c are the modulus and inverse frequency at this crossing point.) Others have shown t-s superposition for other coacervates including the PMAPTA/PMA coacervates of Schlenoff and coworkers [28] presented in Fig. 3-2, whose t-s superposition is shown in Fig. 3-6. Time-salt superposition typically requires larger vertical shift factors than are used in t-T superposition, in part because the polymer concentration is usually not held constant as salt concentration is changed. For example, in Fig. 3-6, the polymer volume fraction varies from ϕ = 0.298 to 0.203 to 0.154 with salt concentration increasing from [NaCl] = 0.03 to 0.10 to 0.30M. Counteracting this decrease in polymer concentration requires shifting the G' and G'' curves vertically upwards, by almost a factor of two in some cases [28]. Still, the horizontal shift factors are much more significant than the vertical ones, ranging over two decades as shown in the last panel of Fig. 3-6.

While the apparent success of time-salt superposition greatly simplifies our physical interpretation of salt effects on rheology, one should be cautious in assuming that the

superpositions are really as good as they seem. Often master curves spanning 6-8 decades of frequency are constructed from measurements that span only 2-3 decades each, as is evident in the ranges of each colored symbol in Fig. 3-5. Extensive studies of time-temperature superposition in conventional polymer melts have revealed significant deviations from t-T superposition that only become evident when very wide ranges of frequency or time are scanned at each temperature. It is likely that similar deviations from time-salt superposition will also be revealed once wide frequency or time ranges are scanned for coacervates, for example, using creep tests. Even existing data sets, for example in Fig. 3-6 at low frequency, show failures in overlap of data points, which are telltale signs of imperfect superposition. While the usefulness of superposition for semi-quantitative or qualitative analysis makes it worth exploiting whenever possible, the limitations of the method should be kept in mind and efforts should be made to quantify deviations and failures. An example of a likely severe failure that is uncovered by use of wider frequency ranges at each salt concentration will be discussed below in connection with Figs. 3-18, 3-19 and 3-20. Similar caution should be used in the other superpositions discussed below.

In the time-salt master curves of both Spruijt *et al*. [18] in Fig. 3-5 and of Yang *et al*. [28] in Fig. 3-6, the degrees of polymerization (defined as "N" in Fig. 3-5 or "n_{av}" in Fig. 3-6), were chosen to be nearly the same for the two polyions in the coacervate. An exception is in Fig. 3-5e, where the two polyions differed in N by a factor of three. Notice that at the lowest degrees of polymerization, below around 150 in Fig. 3-5a-c, the storage modulus for PDMAEMA/PAA remains below the loss modulus for dimensionless frequencies $\omega\tau_c$ extending at least up to 10^2, while for N around 500, there is a crossover in which G' exceeds G'' and flattens its slope shortly beyond the cross-over frequency. Somewhat similar behavior is observed for PMAPTA/PMA at the highest average degree of polymerization n_{av} in Fig. 3-6, although the flattening is less distinct and requires a higher n_{av} to be observed. This behavior is highly reminiscent of the transition in neutral polymer solutions from unentangled to entangled polymer rheology, with the flattening of the G' curve suggesting a transition to an entanglement network at high molecular weight [46]. For neutral polymers, the transition molecular weight at which entanglements appear is related to the modulus along the plateau. For the data of Spruijt *et al*., the characteristic modulus G_c is reported to decrease from around 10^4 to 10^3 Pa, as N increases to 500, so that, from Fig. 3-5d, one infers a "plateau" modulus of around 10^5 Pa. For the data of Yang *et al*. [28] the "plateau" is at around 2 x10^4 Pa.

If the plateau discussed above is produced by entanglements, its modulus G_0 should be related to the entanglement molecular weight M_e roughly by

$$G_0 = \phi\rho RT/M_e \quad (3\text{-}1)$$

where ρ is the polymer bulk density (i.e., without the solvent), and ϕ is the polymer volume fraction, so that $\phi\rho$ is the solution polymer density; M_e the entanglement molecular weight in the solution, R the gas constant and T the absolute temperature. (The entanglement molecular weight in the solvent-free bulk polymer is designated "$M_{e,0}$."). With a polymer melt density ρ near 10^3 kg/m^3, and $\phi \approx 0.2$, Eq. 1 in the main text, namely $G_0 = \phi\rho RT/M_e$, gives the solution value of M_e near 5 kDa for the data of Spruijt *et al.*, while for Yang *et al.*, it is around 20 kDa. PDMAEMA has a monomer molecular weight of 157 Da, while for PAA it is 72 Da, so that the average is 115 Da. For PMAPTA it is 185 Da, while for PMA it is 86 Da, for an average of 135 Da. Thus, M_e for PDMAEMA/PAA should correspond to around 45 monomers, while for PMAPTA/PMA, it should be around 150 monomers. Usually, the transition from unentangled to entangled behavior occurs at a molecular weight of around two or three times M_e [47] and so should occur at values of N (or n_{av}) around 90-130 and 300-450, respectively, for PDMAEMA/PAA and PMAPTA/PMA. These are significantly lower than the degrees of polymerization at which the plateau becomes evident in Figs. 3-5 and 3-6, respectively, which are around 500 and 2000, respectively. Moreover, the entanglement molecular weight should be related to the concentration ϕ by $M_e = M_{e,0}\phi^{-\alpha}$, with $M_{e,0}$ the entanglement molecular weight in the absence of solvent and α = 1-1.3 [48]. In the data of Spruijt *et al.* [18] the polymer volume fraction ϕ in the coacervate was reported to vary between 0.3 and 0.05, while for Yang *et al.* [28], it varied from 0.3 to 0.15 or so, with the lower values presumably corresponding to higher salt concentration. Thus, the values of N (in Fig.3-5, which is called n_{av} in Fig. 3-6) for hypothetical solvent-free coacervates would be around 20 and 75, respectively, for PDMAEMA/PAA and PMAPTA/PMA melts. The first of these is unusually low, although perhaps consistent with the possibly high stiffness or Kuhn step size of PDMAEMA/PAA. If the "plateau" moduli in Figs. 3-5 and 3-6 have significant contributions from temporary crosslinks due to ion pairs, then the plateau modulus might be significantly higher than that produced by entanglements alone. Note also that in Fig. 3-5d-e, at frequencies below the "plateau" there is an intermediate region of power law relaxation with intermediate exponent

around 0.5, before the terminal region with $G' \propto \omega^2$ and $G'' \propto \omega$, indicating behavior more complex than simple "sticky reptation".

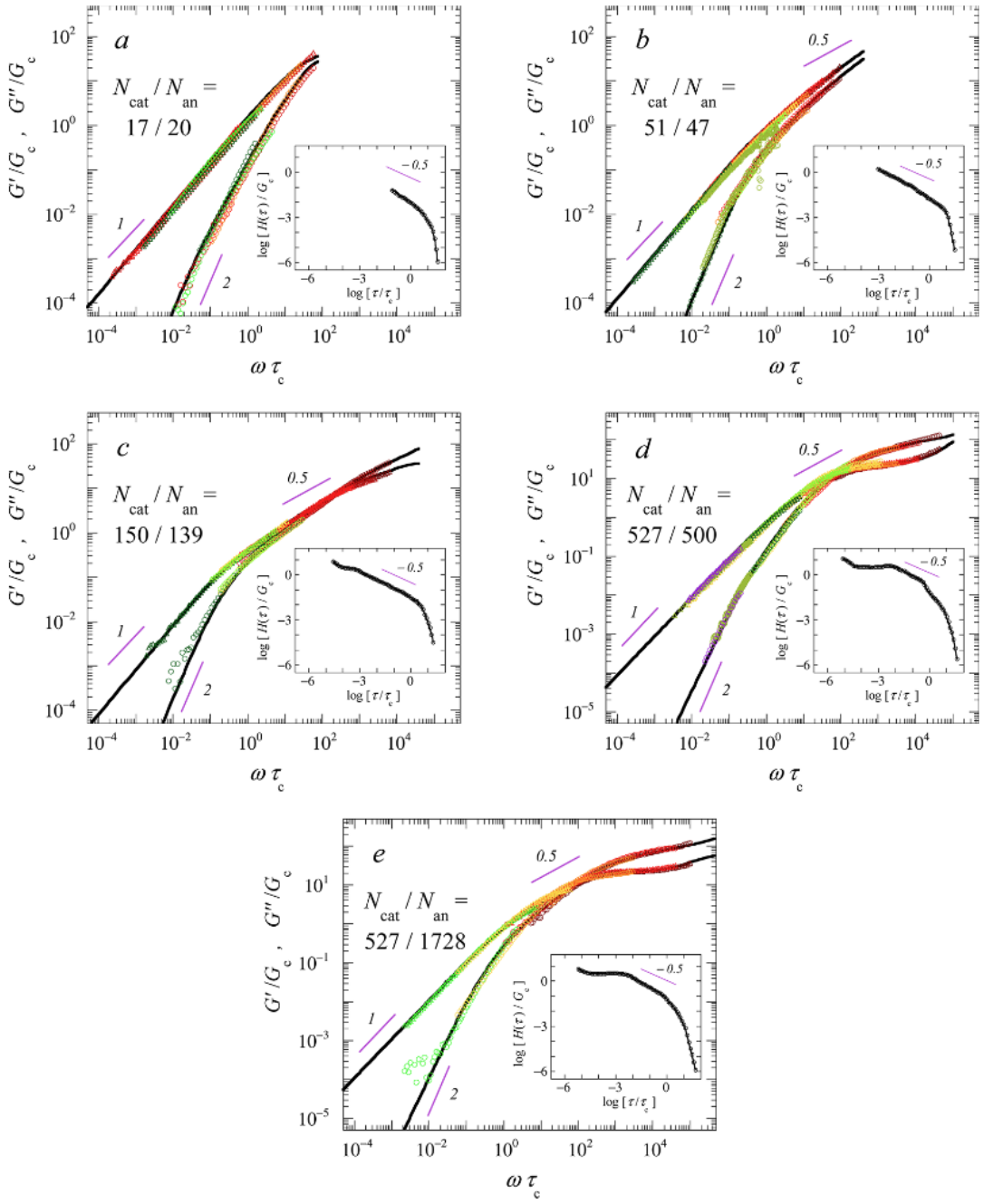

Figure 3-5. Time-Salt frequency-shifted linear viscoelastic curves for PDMAEMA/PAA/KCl coacervates for different polycation/polyanion degrees of polymerization, N_{cat}/N_{an}, given in the legends. The shift factors τ_c and G_c are taken from the inverse frequency and modulus at which G'sand G'' cross each other, when extrapolated from the low-frequency viscous limit. Thus, by definition, at $\omega\tau_c = 1$ and $G'/G_c = 1$, with G_c decreasing from 10^4 to 10^3 Pa as molecular weight increases. The insets give the logarithmic relaxation time spectra. Colors mark data at different salt concentration [18]. Used with permission from Spruijt et al. Macromolecules 46, 1633-1641 (2013). Copyright (2013), American Chemical Society.

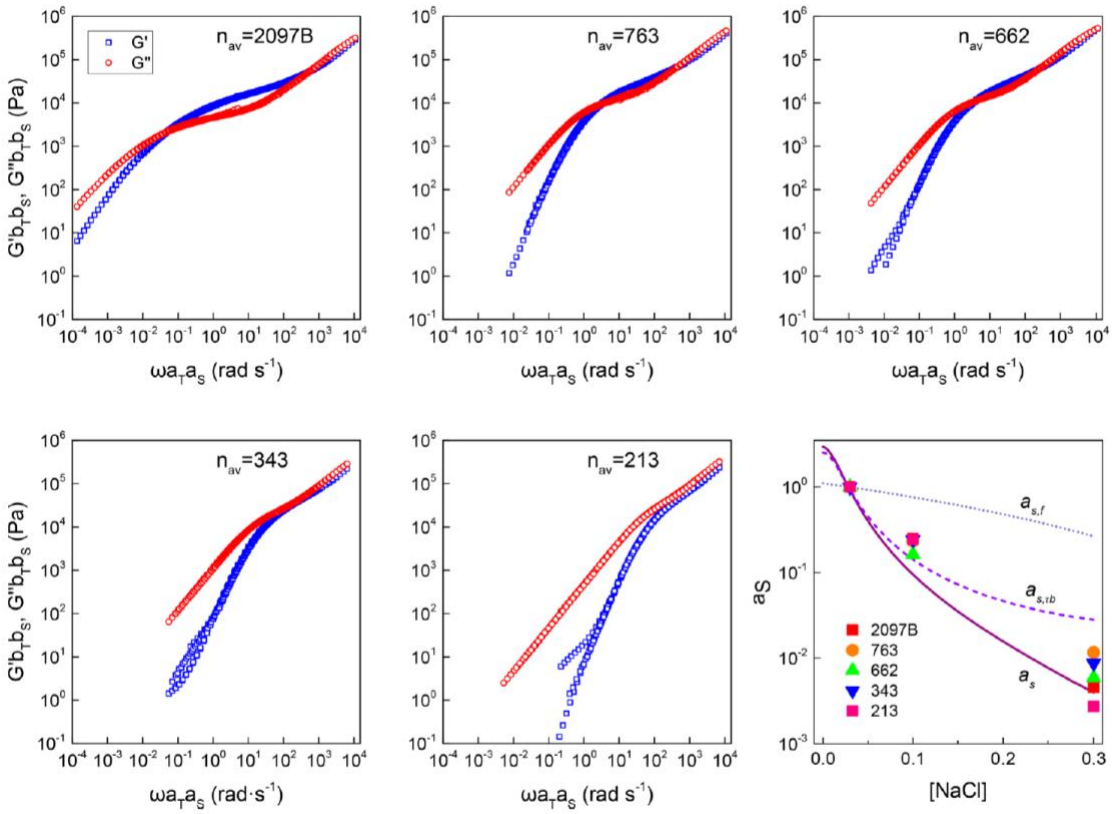

Figure 3-6.Time-temperature-salt superposition obtained for coacervates of in-house synthesized PMAPTA /PMA by further shifting data of Fig. 3-2 by factor a_S along the frequency axis and b_s along the modulus axis, with G' (□); G'' (○). The lower right Figure gives a_S as a function of NaCl concentration for the different average molecular weights. The contributions to a_S are taken to be the product of $a_{S,\tau b}$, due to the sticker lifetime, a_f, due to the fraction of stickers, and a_ϕ, due to changes in polymer concentration. The third of these is estimated as $a_\phi = \phi/\phi_{ref}$ while estimates for the other two are given by Yang et al. (2019) [28]. The "B" in "2097B" indicates that this sample is composed of PEs with "broad" molecular weight distributions of 1.75 for PMAPTA and 1.41 for PMA. The other samples have "narrow" molecular weight distributions of less than or equal to 1.27 for PMAPTA and less than 1.06 for PMA [28]. Used with permission from Yang et al. Macromolecules 52, 1930−1941 (2019). Copyright (2019), American Chemical Society.

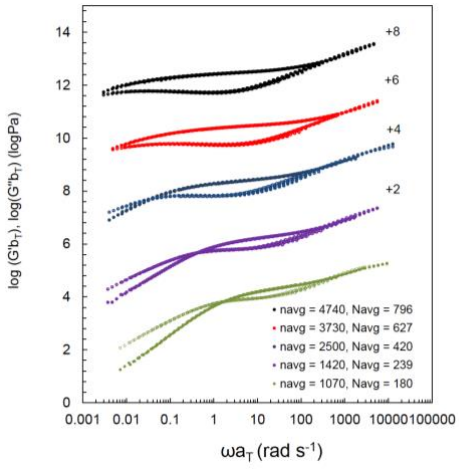

Figure 3-7. Time-temperature superposed G' and G'' for coacervates of in-house synthesized PMAPTA/PMA with 0.01 M NaCl having average degrees of polymerization n_{avg} and numbers of Kuhn steps $N_{avg} = n_{avg}/5.9$ at reference temperature °C. Each curve except the one for $n_{avg} = 1070$ has been shifted upwards by the indicated number of log frequency units (2, 4, 6, or 8) [43]. Used with permission from Akkaoui et al. Macromolecules 53, 4234–4246 (2020). Copyright (2020), American Chemical Society.

Results in Fig. 3-7 for even higher molecular weights of PMAPTA/PMA with n_{avg} up to nearly 5000, at nearly zero salt concentration, show the further development and lengthening of the plateau region, with nearly constant plateau modulus, G_0. The polymers used to acquire these data were also more nearly monodisperse than for those in Fig. 3-6, with $M_w/M_n \leq 1.06$ for PMAPTA and ≤ 1.15 for PMA in Fig. 3-7. (The corresponding values of M_w/M_n in Fig. 3-6 are 1.27 and 1.06, but with 1.75 and 1.41 for the longest chains.) Notice that the high-frequency behavior in both plots, above a shifted frequency of around 100 rad/s, is almost independent of molecular weight. This shows that the fast "elementary" relaxation processes are independent of chain length. The success of time-temperature shifting implies that all slower processes are the result of combinations of these elementary processes throughout the coacervate. Not only is the mechanism of local relaxation of interest, but it is also important to determine how accumulation of these fast local processes leads to slower relaxations and ultimately to complete relaxation of the coacervate at long times.

Very recently, Syed and Srivastava [50] have shown that the relevant "salt concentration" governing the shifting of linear rheology is the total ionic strength of the small ions, including the counterions to the polymer itself. They showed this in a coacervate of PAH and PAA, each of molecular weight around 15 kDa, by changing both the *overall* added salt concentration at fixed PE concentrations, and by changing the *overall* PE concentration at fixed added salt concentration. The "*overall* concentrations" are those of the prepared solution, which then phase separates into a coacervate and a supernatant solution. Changing either the overall salt or overall polyelectrolyte concentration shifts both the composition of the coacervate and the phase volume of the coacervate, where the latter is essentially the position along a tie line of the two-phase envelope. For the compositions studied by Syed and Srivastava [50] the PE concentration changed little with changing overall polymer or salt concentration, and the major difference in all coacervates was simply the concentration of small salt ions. The total ionic strength of both the coacervate and supernatant could thus be varied either through changing the added overall salt concentration or the overall PE concentration. Both methods produced the same master curve when the shift factor

was made to depend on the overall ionic strength of the small ions, both those of the added salt, and the counterions of the PE solution. The shift factor due to both changes in overall added salt concentration, a_s and due to changes in overall polymer concentration, a_p, resulted in a master curve with shift factor that depended on overall small-ion ionic strength, I, as $a_s a_p \sim exp(-4.47\ I^{1/2})$. As alluded to in the introduction, however, it should not be assumed that in general, the effect of salt on PE concentration can be ignored. In some cases, there may be changes large enough to affect the rheology.

3.6 Molecular Weight Dependences of Zero-shear Viscosity and Terminal Relaxation Time

A major clue to understand the long-time dynamics is in the scaling of the longest relaxation time and zero-shear viscosity with chain length. In the PDMAEMA/PAA coacervates of Spruijt *et al.* [18], the longest relaxation time τ was found to scale with the square of average molecular weight at salt (KCl) concentration 0.6 M, from the lowest average chain length of 40 up to the highest of $n_{av} = 10^3$ monomers. A similar quadratic scaling of zero-shear viscosity η_0 was found for salt concentrations in the range 0.5-0.7 M KCl, while a roughly linear scaling of η_0 with chain length was found at 1.0 M KCl. The quadratic scaling of τ with chain length agrees with Rouse theory for unentangled polymers, but the quadratic scaling for η_0 for 0.5-0.7 M KCl disagrees with the linear scaling of η_0 expected for unentangled polymers at constant polymer volume fraction. However, Spruijt *et al.* [18] noted that the polymer volume fraction increased "moderately" with increasing chain length (a range of ϕ in their samples from 0.05 to 0.30 was noted but its molecular weight dependence was not clearly delineated), and perhaps this could explain the shift from linear to quadratic scaling of η_0 with n_{av}. However, the transition to what appears to be an entangled polymer regime is evident in the shape of the G' curve at the longest chain lengths (see Fig. 3-5d-e), and this does not seem evident in the scaling of zero-shear viscosity. Perhaps this is because the entangled regime has not been entered into very deeply, and because changes in the scaling laws of η_0 and τ with chain length are obscured by simultaneous changes in polymer concentration.

For PMAPTA/PMA coacervates, Figs. 3-8 and 3-9 show the dependences of the zero-shear viscosity on average chain length from two studies of Schlenoff and coworkers [28, 43], the first covering a range of n_{avg} up to 2097, and the second reaching a higher value of 4740. (Note that the

conversion of the values of n_{avg} to numbers of Kuhn lengths N is different in Figs. 3-8 and 3-9, with $N = n_{avg}/11.9$ in Fig. 3-8 but $N = n_{avg}/5.9$ in Fig. 3-9. Note also that Schlenoff and coworkers use "N" to denote the number of Kuhn steps in the chain, while Cohen Stuart *et al*. [18] use "N" for the number of monomers, which is "n_{avg}" or "n_{av}" in the work of Schlenoff *et al*. [28, 43]. This difference between the two publications by the Schlenoff group resulted from the authors' re-assessment of the value of the Kuhn length, estimated to be 2 nm in Yang *et al*. [28] but re-assessed to be 1.5 nm in Akkaoui *et al*. [43]. Fig. 3-8 shows a transition from a power-law exponent of around unity to 3.4 in the dependence of zero-shear viscosity on N; the transition occurs at a value $N \approx 30$, which is $n_{avg} \approx 360$ when we convert from N to n_{avg} using the ratio 11.9 mentioned above. In Fig. 3-9 an even steeper power-law of 5.4 is observed for N above 180, which corresponds to $n_{avg} \approx 1000$. The transition from unity to 3.4 is expected based on the transition to the entangled state, which we noted above should occur at $n_{avg} \approx$ 300-450, for the data in Figs. 3-8 and 3-9. The onset of the entangled state thus seems to correspond to a transition to the region of 5.4 power law in Fig. 3-10, and the half-decade wide region with "3.4 power law" marked in Fig. 3-8 then likely just reflects a broad transition from a region with power law near unity to a region with a power law of 5.4. The power law exponent of 5.4, however, is anomalous, since rheology dominated by entanglements should lead instead to a power law of around 3.4 at high molecular weights. Electrostatic interactions, manifested as ion pairs, or other restrictions on polymer local mobility, can certainly slow chain dynamics, but no matter how strong these effects, they should not change the power-law scaling of viscosity with molecular weight, as long as they *act locally*, so that the dynamics of the whole chain are slowed to the same degree regardless of chain length. A change in power law exponent at high molecular weight from 3.4 to 5.4 seems therefore to imply that the electrostatic interactions lead to a chain-length-dependent slow-down in local dynamics. A mechanism for this suggested by Akkaoui *et al*. [43] involves a kinetic coupling of ion-pairing and entanglement dynamics, but this suggestion at present remains untested. We also note the seeming discrepancy between the molecular-weight-scaling behavior of PDMAEMA/PAA of Spruijt *et al*. [18], and that of PMAPTA/PMA of Schlenoff and coworkers. Since the PEs studied by Spruijt *et al*. neither reached degrees of polymerization as high as those studied by Akkaoui *et al*., nor were they as monodisperse, further experimental work will be needed to resolve whether these two systems actually behave differently.

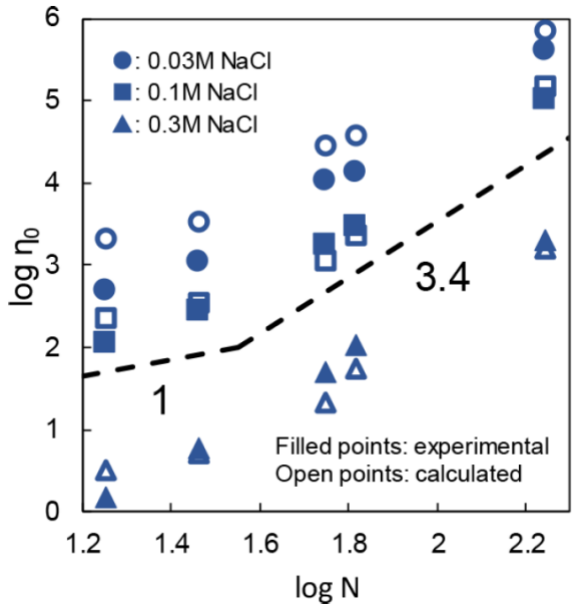

Figure 3-8. Zero shear viscosity η_0 at 25 °C of PMAPTA/PMA PECs as a function of number of Kuhn steps at salt concentrations given in the legend at 25 °C. Here, the number of Kuhn steps N is related to the degree of polymerization by $N = n_{av}/11.9$ where n_{av} is the number of monomers. Filled symbols are experimental, and open symbols are calculated from the product of Rouse relaxation time τ_R and Rouse modulus G_R for $N \leq N_e$ and of plateau modulus G_0 and reptation time τ_d for $N > N_e$, where N_e is estimated as 29 [28]. Used with permission from Yang et al. Macromolecules 52, 1930−1941 (2019). Copyright (2019), American Chemical Society.

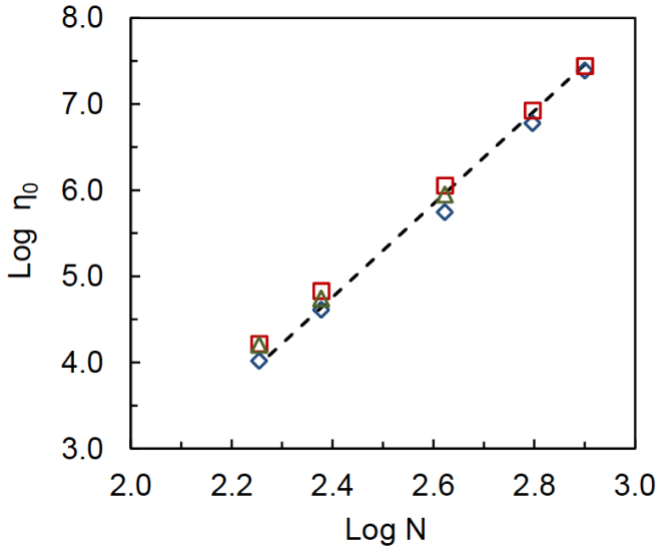

Figure 3-9. Zero-shear viscosity η_0 at 25 °C of PMAPTA/PMA coacervates versus number of Kuhn steps, $N = n_{avg}/5.9$, between 180 and 796, from direct measurements (Δ), from the product $G_0\tau_{rep}$ of measured plateau modulus G_0 and measured longest relaxation time τ_{rep} (◊), and calculated from the product of theoretical expressions for these (□). The dotted line gives the scaling law $\eta_0 \sim N^{5.4}$ [43]. Used with permission from Akkaoui et al. Macromolecules 53, 4234–4246 (2020). Copyright (2020), American Chemical Society.

3.7 Effect of Unequal Degrees of Polymerization

The above results focused on coacervates in which both PEs had similar chain lengths. Results from Spruijt *et al*. [18] in Fig. 3-10 show the relaxation behavior of PDMAEMA/PAA coacervates for which the two lengths are significantly different. Fig. 3-10a shows that increasing the polycation (PDMAEMA) length at fixed length of the polyanion (PAA) greatly slows the relaxation, while the reverse case in Fig. 3-10b shows much less effect of the length of PAA with fixed PDMAEMA length, at least until the PAA becomes very long. This seems to show that the terminal relaxation is dominated by motion of the PDMAEMA, with the PAA serving primarily to impede this relaxation, while not itself significantly contributing to the terminal relaxation until the PAA is very long. This behavior seems hard to explain in terms of a simple ion-pairing model, where release of an ion pair should have equal effect on the local relaxation of each chain, and therefore lead to equivalent behavior, whenever either chain is made longer than the other. On the other hand, for coacervates of PDADMA and poly(isobutylene-alt -maleate sodium) (IBMA-Na) studied by Hamad *et al*. [36], Fig. 3-11 shows that the polyanion, IBMA (pKa = 3.2-3.3) [35], strongly influences the terminal relaxation behavior, differing from the PDMAEMA/PAA system studied by Spruijt *et al*. In very recent work, Liu et al. [51] studied coacervates of cationic poly([2-(methacryloyloxy)ethyl]trimethylammonium) (PTMAEMA) with anionic poly(3-sulfopropyl methacryloyl) (PSPMA) of mismatched lengths, and, as in the study of Spruijt et al. found a somewhat greater influence of the length of the cation on the rheology than of the anion, although not to the degree seen by Spruijt et al. for of PDMAEMA/PAA. The reason for these differing behaviors needs resolution, and a possible reason for this asymmetry in some systems may lie in asymmetry in the Kuhn lengths of the polycation vs. the polyanion, as suggested below in the theory section.

From both Figs. 3-10 and 3-11, we can estimate $G_0 \approx 5 \times 10^4$ Pa, suggesting from Equation (3-1) that $M_e \approx 10$ kDa for both. In Fig. 3-10a the cross over frequency shifts roughly 4-fold for a 3-fold increase in degree of PDMAEMA polymerization from $N = 51$ to 150 and roughly a decade additional increase for a further 3-fold increase to 527, suggesting a quadratic dependence on N for PDMAEMA at long chain lengths, which suggests that the chains are unentangled. Consistent with this, for PDMAEMA, the highest molecular weight, corresponding to $N = 527$, is around 83 kDa, while for PAA, $N = 500$ corresponds to $M = 36$ kDa, so the sample 527/500 in Fig. 3-10a is weakly entangled. For PDADMA/IBMA, the PDADMA molecular weight of 300 kDa is well

above the entanglement threshold, and the dependence of the inverse cross-over frequency on molecular weight M of the polyanion IBMA shown in Fig. 3-12 (right) increases from quadratic to cubic as M increases beyond 100 kDa. This is a factor of 3-5 higher than one might expect from the above estimate $M_e \approx 10$ kDa, since the cross-over should be at around 2-3 times M_e. In addition, the cubic dependence of relaxation time on chain length above M_e differs from the 5.4 power scaling observed for the PMAPTA/PMA discussed above. Thus, the estimated plateau moduli of the coacervates and the corresponding molecular weights at the transition to entanglement-dominated rheology are only very roughly consistent with theoretical expectations. The molecular-weight scaling of relaxation time and viscosity in the unentangled and entangled states are also roughly as expected, with the exception of PMAPTA/PMA, which shows much stronger molecular-weight scaling in the entangled state. (Note, that the molecular weight of PDADMA is 126 Da and of IBMA is 170 Da, giving an average of 148 Da, so that the number of monomers per entanglement is expected to be $N_e \approx 340$. PDMAEMA has molecular weight 157 and for PAA it is 72, so that $N_e \approx 440$.)

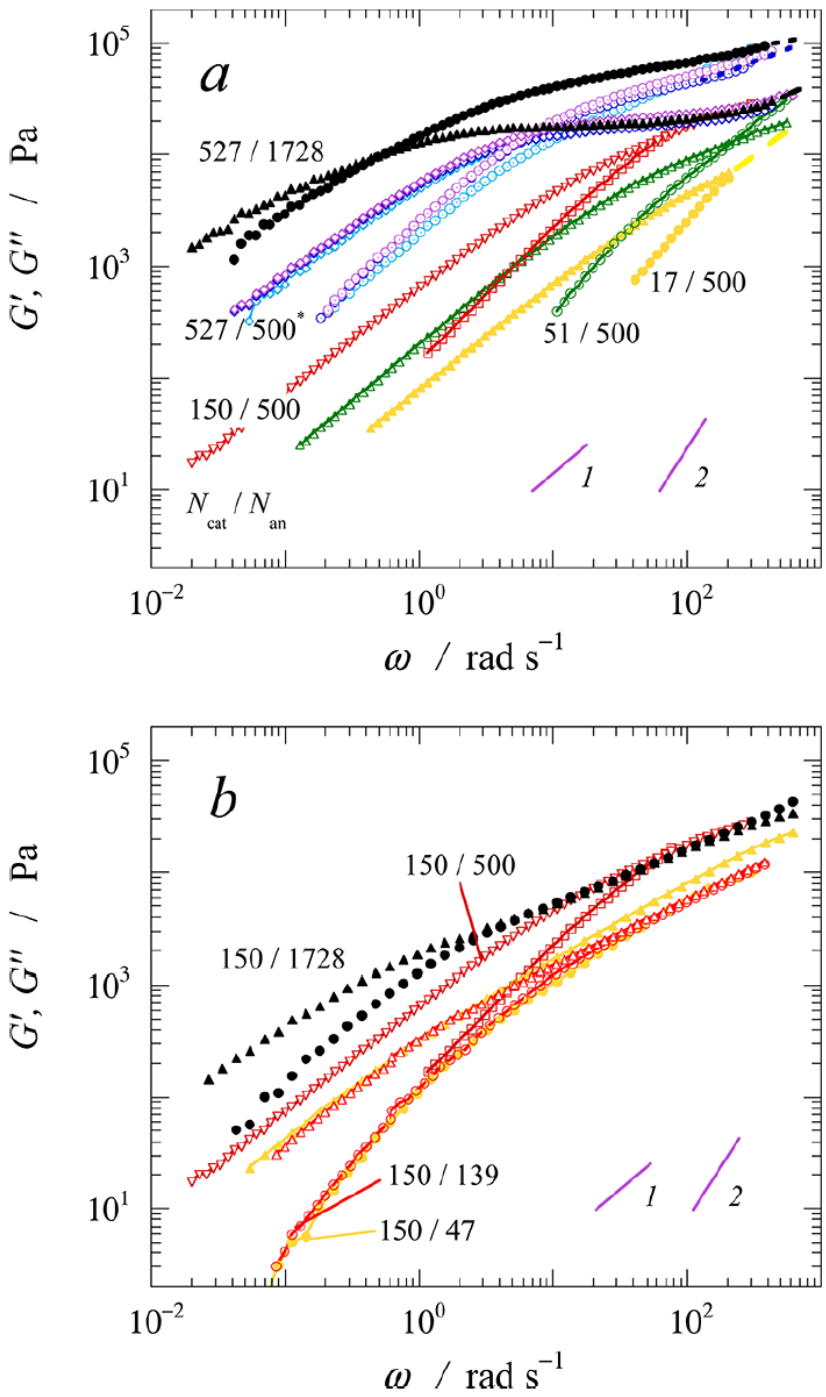

Figure 3-10. Linear rheology of PDMAEMA/PAA coacervates in which degrees of polymerization (N) of each PE varies as shown. In (a), N = 500 for PAA, and PDMAEMA has varying N, except for the black symbols, which has the N values shown and the purple and blue symbols, for which N= 527 for PDMAEMA and PAA has values of 500, 139, 47, and 20, with overlapping curves. In (b), N=150 for PDMAEMA, while N for PAA varies as shown. All results are at 0.70 M KCl at roughly 1:1 monomer mole ratio of the two polymers. The curves with the label "527/500*" denote the cases 527/500, 527/139, 527/47, and 527/20, which overlap [18]. Used with permission from Spruijt et al. Macromolecules 46, 1633-1641 (2013). Copyright (2013), American Chemical Society.

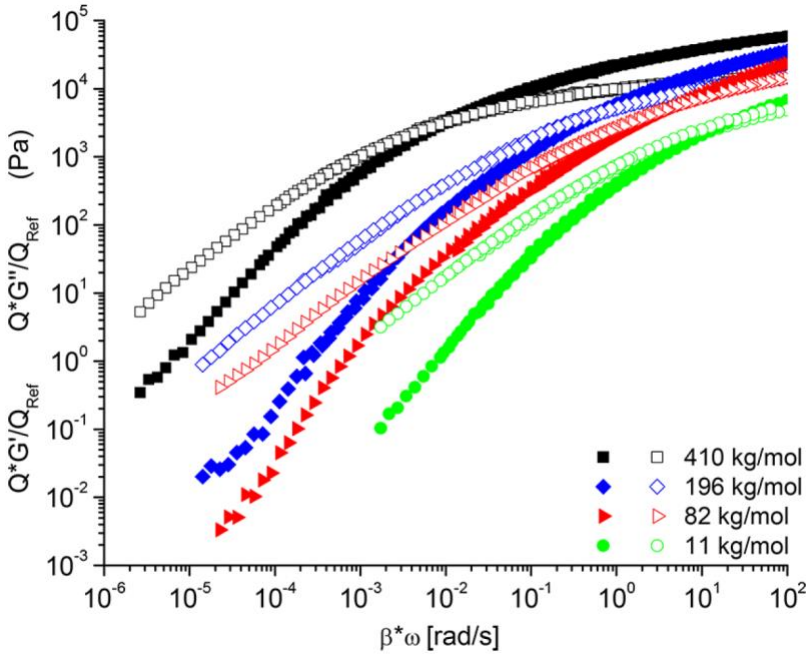

Figure 3-11. Master time-salt superposition curves of G' (filled symbols) and G'' (open symbols) of coacervates of PDADMA and IBMA with the salt-free coacervate as the reference state at 23 °C molecular weight of PDADMAC = 300 kDa, and the molecular weights of IBMA-Na shown [36]. Used with permission from Hamad et al. Macromolecules 51, 5547-5555 (2018). Copyright (2018), American Chemical Society.

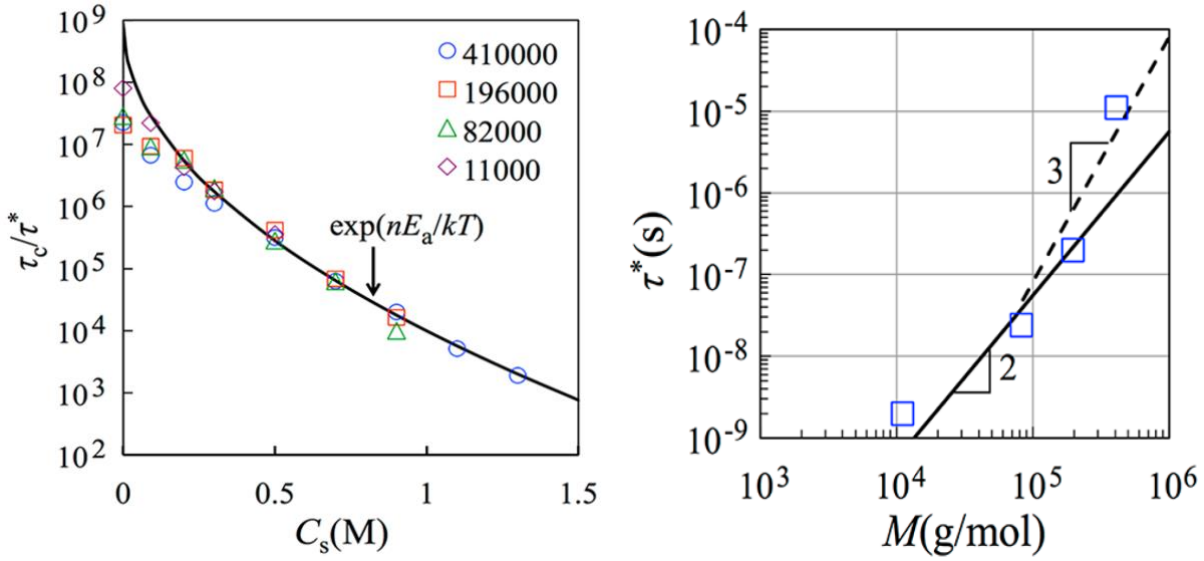

Figure 3-12. (left) Dependence on salt concentration of the cross-over time τ_c rescaled to a common curve by a molecular-weight-dependent time τ^* (M) presented on the right Figure. τ_c is defined as the reciprocal of the cross-over frequency at which G' = G''. The equation for the salt concentration dependence on the left is based on an activated process involving electrostatic interactions, as described by Hamad et al (2018) [36]. Solid curves are based on Equations (3-4) and (3-5) with n = 5, $1/\omega_0 = 10^{-12}$ s, and d = 1.7 Å. Used with permission from Hamad et al. Macromolecules 51, 5547-5555 (2018). Copyright (2018), American Chemical Society.

3.8 Time- Salt-pH Superposition

The work mentioned above was for strong PEs that remain nearly fully charged over a wide range of pH, or for weak PEs at pH values at which both PEs remain fully charged. However, Tekaat *et al*. [52] studied coacervates of PDADMA, a strong PE, and PAA, a weak one, under a range of pH values that led to partial neutralization, or protonation, of PAA. The molecular weights were relatively high, 100,000-200,000 Da for PDADMA and 100,000 Da for PAA, and the coacervate concentration resulting from phase separation seemed not to be reported. Titration curves allowed the charge level of the PAA to be determined as a function of pH and salt concentration, and coacervates were made with the concentration of PAA adjusted upwards to compensate for the reduced charge level, to keep the number of PAA charges equal to the number of charges on the PDADMA as pH was varied. In the absence of salt, PAA became only half charged at a pH around 5.5, while much lower pH was required to achieve similar neutralization with added salt, a phenomenon known as "charge regulation." Coacervates at 1:1 charge ratio made from PDADMA and PAA at various pH values and at 0.25 M KCl are shown in Fig. 3-13a. It is noted in this Figure that the G' and G'' curves shift to the left dramatically when the pH drops below 7, showing a counterintuitive *slow-down* in dynamics for *less-charged* PAA. Remarkably, Fig. 3-13b shows that curves at different pH can be superposed, primarily by shifting along the frequency axis, a phenomenon called "time-pH" superposition, which holds for each salt concentration from 0 to 0.5 M KCl. In addition, time-salt superposition applies to these data as well, allowing a double superposition of data at all pH and salt concentrations into a "super-master" curve, shown in Fig. 3-14. The surprising slow-down in dynamics at reduced PAA charge at low pH in Fig. 3-13 is believed by Tekaat *et al*. [52] to be due to increased hydrophobic interactions between PAA chains made possible by the neutralization of charge. As we will see below, shifting of rheological curves due to hydrophobicity seems to correlate well with the concentration of water in the coacervate, but such a correlation cannot be checked for these data, since water concentrations were not reported by Tekaat *et al*. [52]. In fact, PAA at reduced pH can phase separate from water, depending on salt concentration and temperature [53]. This shows that interactions other than ionic can be important, and even dominate, the dynamics of coacervates.

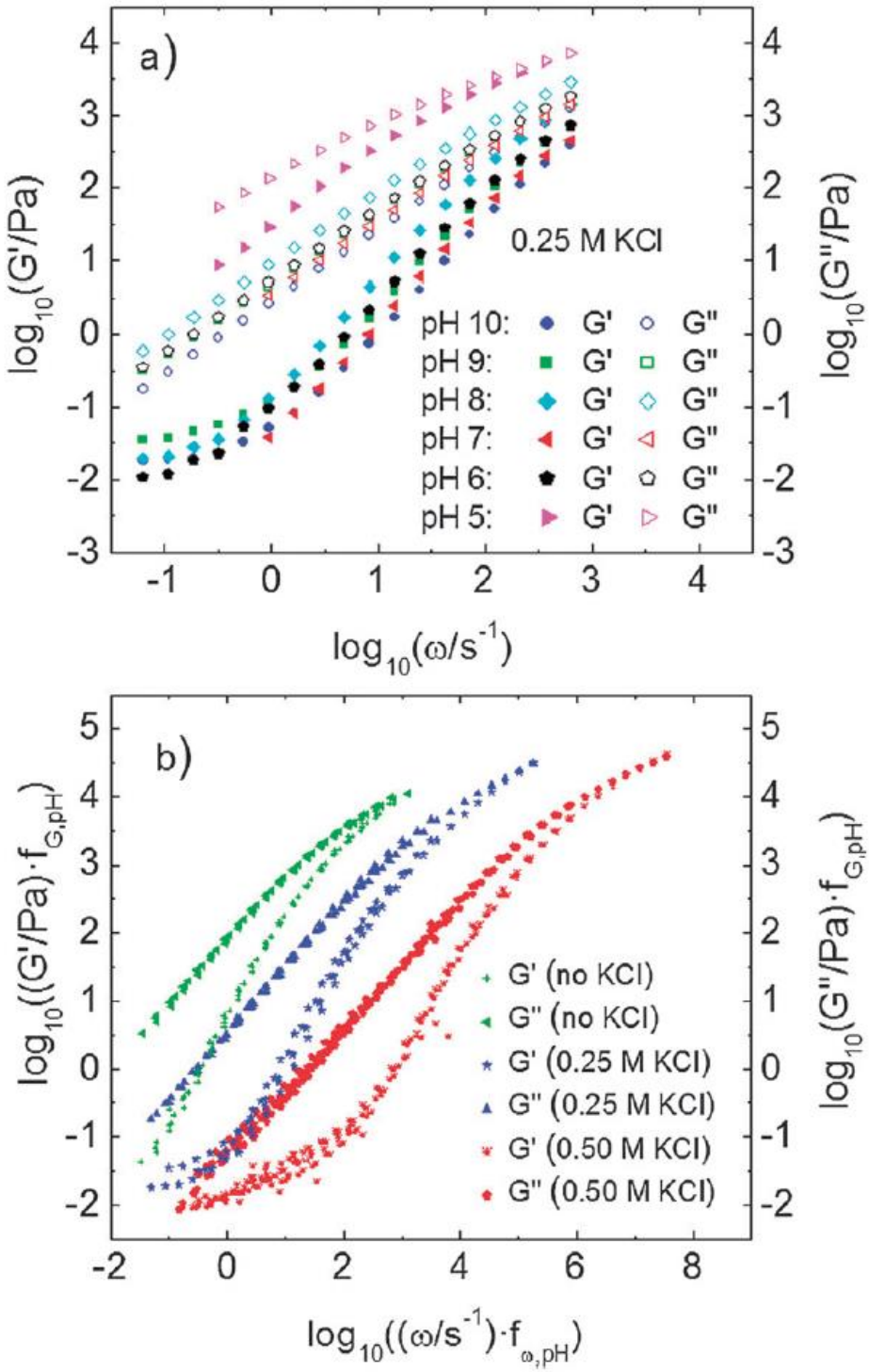

Figure 3-13. (a) pH-dependent storage and loss moduli for PDADMA/PAA coacervates at pH values low enough that the PAA is no longer fully charged at a KCl concentration of 0.25 M. (b) Master curves resulting from time-pH shifting primarily along the frequency axis but with a small vertical shift [52]. Used with permission from Tekaat et al. Physical Chemistry Chemical Physics 17, 22552-22556 (2015). Copyright (2015), Royal Society of Chemistry.

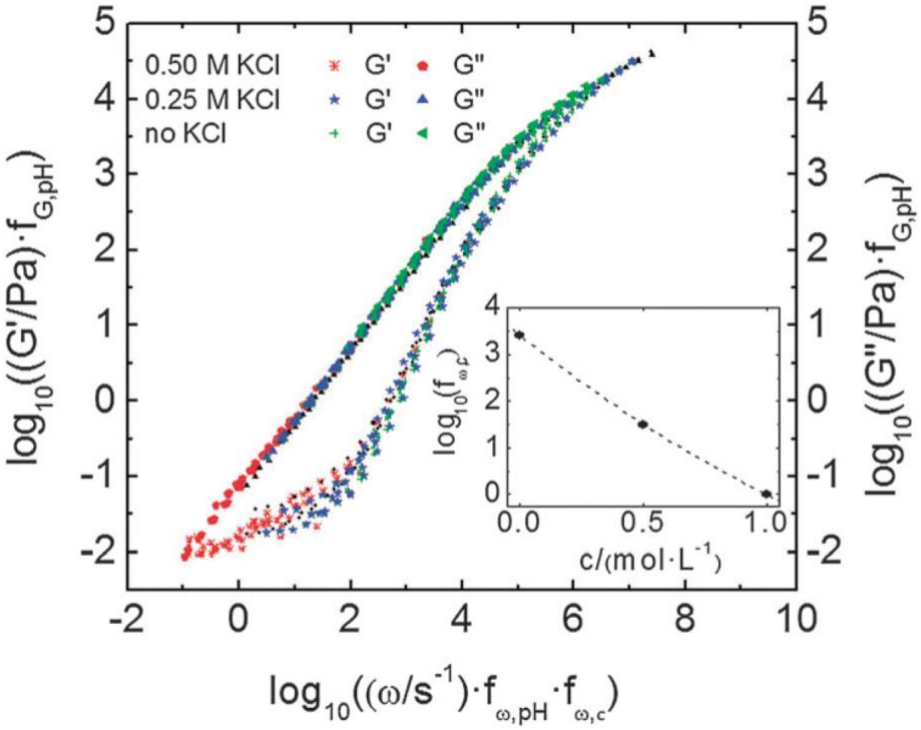

Figure 3-14. "Super master" curve from shifting of master curves of Fig. 3-13b. The inset shows the salt shift factor as a function of salt concentration [52]. Used with permission from Tekaat et al. Physical Chemistry Chemical Physics 17, 22552-22556 (2015). Copyright (2015), Royal Society of Chemistry.

3.9 Time-Hydration Superposition

Lutkenhaus and coworkers [54] recently explored the effect of hydration level on the linear rheology of poly(allylamine hydrochloride) (PAH) and poly(acrylic acid), PAH/PAA, coacervates, where both PEs had molecular weights of around 100 kDa, and found not only time-temperature superposition, but also time-hydration superposition as the hydration level was varied from 13.5 to 35.7 weight%. The superposition is shown in Fig. 3-15, for linear oscillatory extensional flow, yielding a dynamic Young's storage modulus E'. The hydration level was controlled through equilibration of samples at controlled relative humidity (RH) ranging from 50% to 95%, giving the above range of hydration levels. The temperature shift factor had an Arrhenius temperature dependence, with higher activation energies for higher levels of hydration. This is somewhat surprisingly since the sample relaxes faster at higher hydration. For RH between 80 and 95%, E_a = 379 ± 35 kJ/mole, decreasing to 176 ± 20 kJ/mole for 70% RH, and down to 78 ± 57 kJ/mole for 50% RH. The logarithm of the shift factor for hydration, $ln\ a_w$, was found to be linear in the

weight percentage of water present. Thus, water acts as a strong "plasticizer" for the coacervate. The same group [55] found for the same PEs that the inverse "glass transition" temperature $1/T_g$ determined from scanning calorimetry depends linearly on the log of the number of water molecules per ion-pair, with data for different salt concentrations all collapsing onto a single curve. Other, thorough, work by this group, including detailed atomistic simulations for several PC/PA pairs, including PDADMA/PSS, have shown that water plays a central role in the local structure and dynamics of coacervates [13, 56-58]. Connecting such findings to the rheological shift factors, and determining how local structure controls those shift factors, should be a high priority for future work.

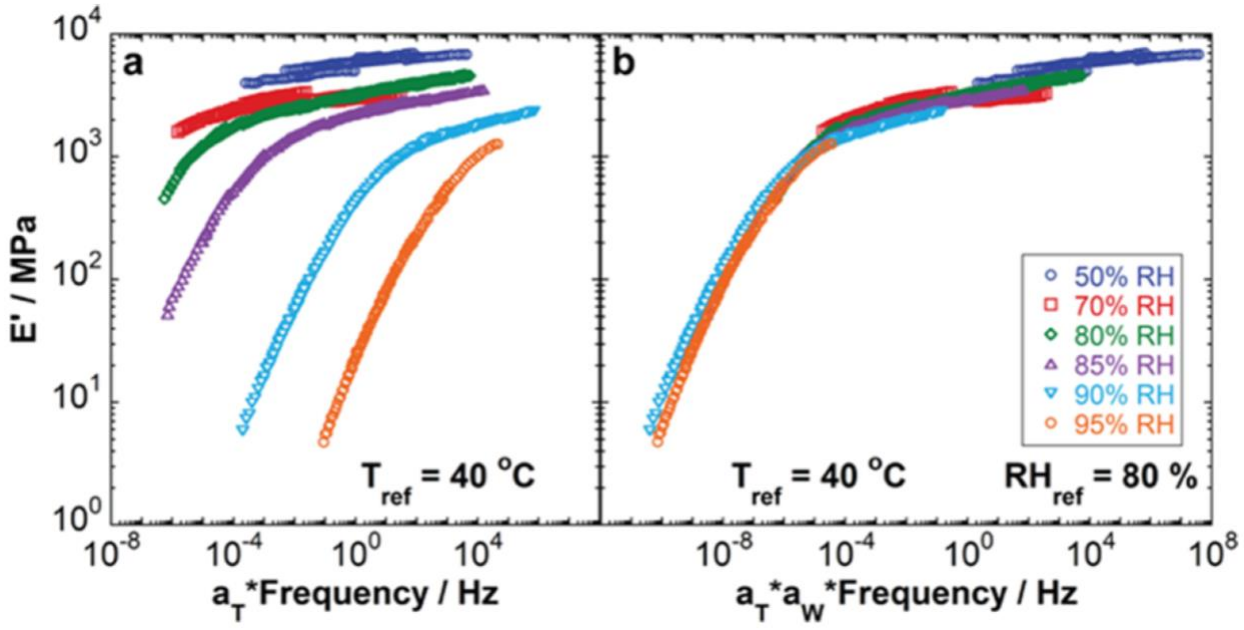

Figure 3-15. (a) Time−temperature master curves of linear viscoelastic extensional storage modulus E' for relative humidity (RH) of 50, 70, 80, 85, 90, and 95% from top to bottom. (b) Time−water "super master" curve from shifting curves in (a) with respect the reference curve with 80% RH and T_{ref} = 40 °C [54]. Used with permission from Suarez-Martinez et al. Macromolecules 52, 3066-3074 (2019). Copyright (2019), American Chemical Society.

A likely similar hydration-controlled relaxation behavior was revealed when PE hydrophobicity was considered explicitly in studies by Shull and coworkers [59]. They quaternized poly (4-vinylpyridine) (QVP) polycations with methyl (QVP-C1), ethyl (QVP-C2) and propyl (QVP-C3) substituents, thus producing polycations with successively higher hydrophobicity but the same chain length and backbone chemistry. These PEs had molecular weights of 60 kDa and

coacervates were made of each of these with PSS, with 200-350 kDa. As expected, and shown in Fig. 3-16a, the more hydrophobic PEs exhibited a higher resistance to swelling with increased salt concentration. The swelling resulting from adding methyl groups onto the QVP side chains is not linear since the swelling curve for PSS: QVP-C3 differs more greatly from those for PSS: QVP-C1 and -C2 than these two differ from each other. Intriguingly, however, a cross-plot of high-frequency modulus G_3* versus swelling in Fig. 3-16b indicates that the effect of the hydrophobicity on the rheology is captured nearly completely by its effect on swelling with water since the modulus versus swelling curves for all three QVP substituents are the same. This seems to be the same phenomenon discussed in the paragraph above, where hydration level was controlled through relative humidity, rather than by the hydrophobic groups on the polymer. The high-frequency modulus (in the MHz range) in these experiments by Sadman *et al*. [59] was measured in a quartz-crystal microbalance that simultaneously measured swelling as a function of salt concentration. The swelling for coacervates with PDADMA, a more hydrophilic polycation, is much greater than for the QVP polycations (Fig. 3-16a), and the modulus versus swelling curve (Fig. 3-16b) deviates somewhat from the curves for the QVP monomers, indicating a lack of universality across all polycations. Sadman *et al*. [59] also examined the effects of various salts, including KBr, KCl, NaCl, LiCl and $CaCl_2$, on the swelling and the modulus, and again found a collapse of data when high-frequency modulus was plotted against swelling. The salt-dependent swelling increases in the order of the salts given above, which tracks their electronegativity and therefore their hydration. The high-frequency modulus is an indicator of "glassiness" of the coacervates, which in principle should be indicative of analogous shifts in lower-frequency rheology, but a precise connection has not been made, since complete rheological curves were not reported. It would be worth finding whether or not the change in salt identity (e.g., KBr, KCl, NaCl, LiCl and $CaCl_2$) can be encompassed in a master curve for all of these salt types. Nevertheless, remarkably, this finding that the effect salt type and concentration work through their effects on water content is very much in line with an extensive body of work by Lutkenhaus [13], Sammalkorpi, and coworkers referenced above, that reveals the key role of water in the local relaxation of coacervates.

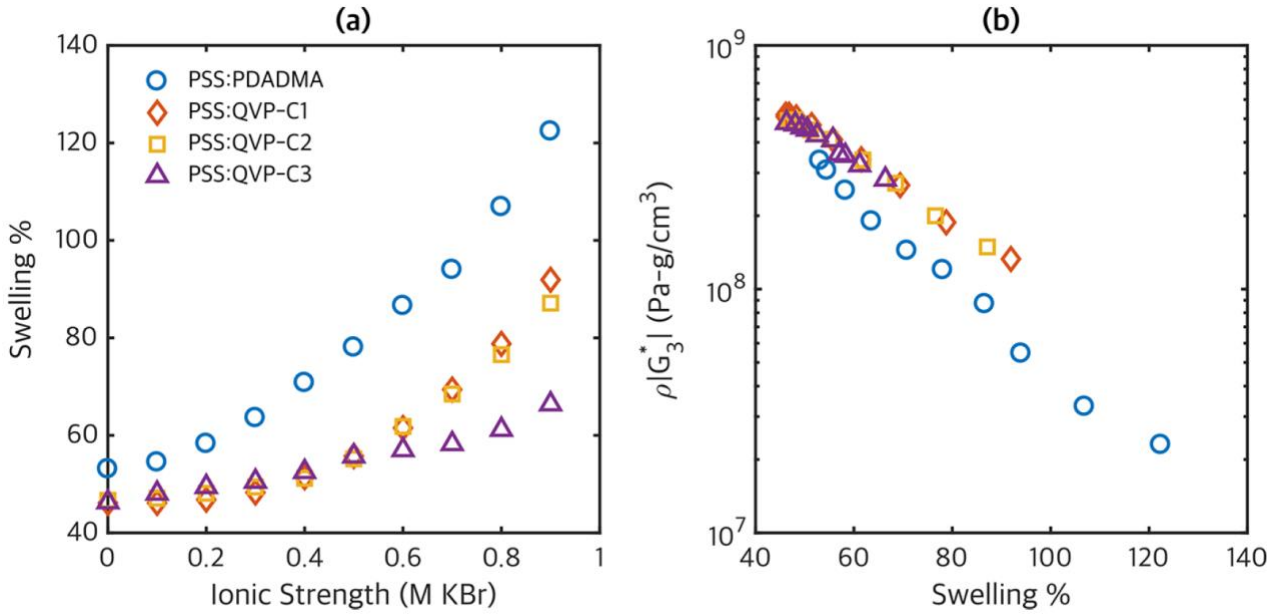

Figure 3-16. (a) Swelling, i.e., water concentration as a percentage of polymer concentration, for PSS: QVP complexes, compared with that for PSS: PDADMA (blue symbols), as a function of KBr concentration measured by a quartz crystal microbalance (QCM). (b) Third-harmonic high-frequency complex modulus measured by QCM plotted against swelling [59]. Used with permission from Sadman et al. Macromolecules 50, 9417-9426 (2017). Copyright (2017), American Chemical Society.

Shull and coworkers [59] utilized time-salt superposition with only horizontal shifts to obtain the master curves for each coacervate given in Fig. 3-17. The shift factors in the inserts to Fig. 3-17 show that the more hydrophobic PEs need higher salt concentrations to form the coacervates within the same modulus range, but once the salt concentration has been shifted, the rheological behaviors remain otherwise nearly independent of hydrophobicity. The curves can also be shifted onto a master curve when temperature is varied. Hence, these coacervates display "time-temperature-salt-hydrophobicity superposition," implying that temperature, salt, and hydrophobicity affect the rate of local monomer diffusion, but otherwise do not affect the long-range coacervate dynamics, which remains that of a simple viscoelastic liquid. The linear rheology is described by a simple expression for the complex modulus, namely

$$\frac{G^*}{G^s} = \frac{(i\omega\tau)^\beta}{1+(i\omega\tau)^{\beta-1}} \tag{3-2}$$

with G^s a high-frequency modulus, τ the relaxation time and β a parameter around 0.42-0.44.

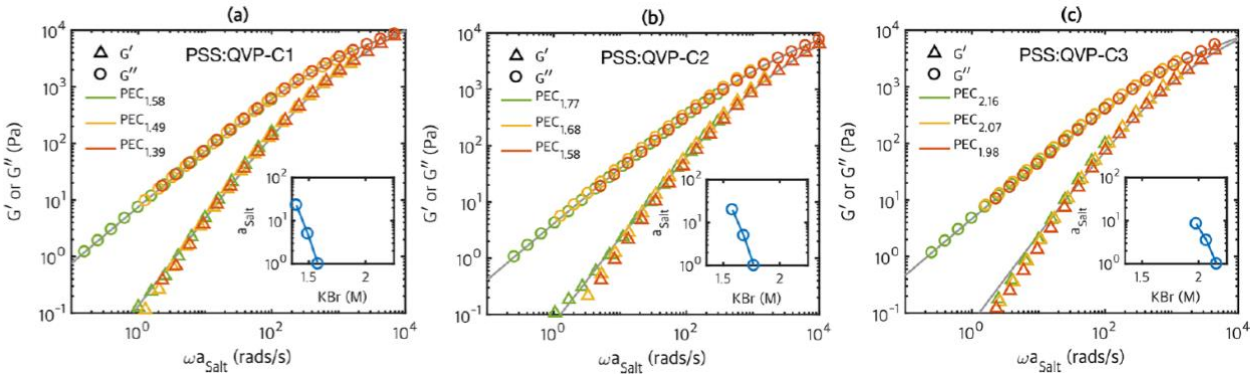

Figure 3-17. Time−salt superposition with horizontal shifting only at 20 °C for (a) PSS: QVP-C1, (b) PSS: QVP-C2, and (c) PSS: QVP-C3. In the designation PEC_x in the legend, x is the molarity of KBr. Curves are shifted with respect to the highest salt concentration in each case [59]. Used with permission from Sadman et al. Macromolecules 50, 9417-9426 (2017). Copyright (2017), American Chemical Society.

Hydrophobicity thus can have an effect on coacervate rheology; however, the importance of the effect seems to be system specific**.** Laaser and coworkers [60] also carried out systematic studies using nonionic monomers copolymerized with both polyanions and polycations in a series of acrylamide copolymers, and saw little effect of the hydrophobicity of the polyion on its rheological response. They speculated as to the cause of this lack of sensitivity, suggesting that an entropic effect may offset the effect of hydrophobicity.

Very recent work by the groups of Perry and Sing [51] also systematically explored the influence of hydrophobicity by comparing the phase behavior and rheology of the coacervates of two closely related pairs of polyions, namely a more hydrophobic methacryloyl-based polymer pair and a less hydrophobic acryloyl-based pair, where the backbones of all polymers are identical except that the former pair has an extra pendant methyl group. The former consisted of poly([2(methacryloyloxy)ethyl]trimethylammonium) (PTMAEMA) with anionic poly(3-sulfopropyl methacryloyl) (PSPMA) while the latter acryloyl-based pair consisted of poly([2(acryloyloxy)ethyl]trimethylammonium) (PTMAEA) with poly(2-acrylamido-2-methyl-1-propanesulfonic acid) (PAMPS). For the same degree of polymerization, the more hydrophobic pair showed a higher modulus and slower relaxation than the less hydrophobic pair, even at a higher salt concentration in the former, but most of this difference could be correlated with the polymer concentration, and thus the degree of hydration, which therefore again appears to be a critical parameter controlling the rheology.

Finally, we note that hydrophobic effects can be very complex. Meng *et al*. [3] found that coacervates made of poly(vinylbenzyl)trimethylammonium chloride (PVBTMAC) and PSS transitioned from a soft solid at zero salt with 90% water content to a stiff gel with lower water content at 2 M NaBr, while transitioning back to a viscoelastic liquid at still higher NaBr. This unusual non-monotonic dependence of stiffness on salt concentration was investigated by X-ray scattering and traced to the formation of hydrophobic domains that opened up upon increase in salt concentration, eventually evolving into a viscoelastic structure perhaps more similar to that of more typical coacervates. These system-specific results dampen hopes for a completely universal theory of coacervate phase behavior and rheology, although theories that encompass important sets of coacervates seem feasible.

3.10 Low-Frequency Plateau Modulus

Note in Figs. 3-13 and 3-14 the appearance of a *low-frequency plateau* in the storage modulus G'. This plateau, with a very low modulus of around 10^{-2} Pa, might suggest a transition to a solid-like gel, rather than fluid, at the lowest frequencies for this coacervate. However, even at the lowest frequencies we see that G'' > G', implying that the response is still predominantly viscous. If the plateau is maintained to arbitrarily low frequency, eventually G'' would drop below G' and the sample would then be characterized as a very soft solid. Note that at zero salt concentration, there is no sign of a plateau, presumably because the frequency was not made low enough. It is also possible that such a low-frequency plateau would be found in other coacervates discussed thus far, if lower frequencies were accessed. Most such data in these Figures do not reach G' values as low as 10^{-1}, let alone 10^{-2} Pa. (However, the data in Fig. 3-11 do show storage moduli this low with little sign of a plateau.) Data for PDMAEMA/PAA by Spruijt *et al*. in Fig. 3-5e [18] show an indication of a leveling off of G' at the lowest frequencies, with G' around 10^{-1} or so. (Note the normalization of G' on the y axis of this plot.) A low-frequency plateau in G' of magnitude between 1 and 10 Pa was also observed in the time-ionic-strength shift factor data of Syed and Srivastava [50]. A weak low-frequency plateau in G' appears in data for coacervates of (poly)-lysine (PLK) and (poly)-glutamic acid (PRE) of Tirrell and coworkers [27] again with G'' > G'. These workers note the possibility that this weak "elastic" terminal response might be a rheological artifact given the weak stress level. Artifacts capable of producing a spurious low-

frequency plateau of low magnitude include transducer torque or calibration limits, heterogeneities or low-concentration "gels," impurities, or high-molecular weight tails in the samples, and "skin" formation on the edge of the rheometer sample due to evaporation.

A much more compelling demonstration of a transition to a solid-like rheological response at low frequencies is found in the studies of Perry and coworkers [61] for a coacervate of PDADMA with molecular weight of M_w = 289,100 Da, M_w/M_n = 1.3 and PSS with M_w = 354,400 Da, M_w/M_n = 1.7 in KBr salt. The concentration of polymer in the coacervate varies with salt but is within the range 0.8 to 1.1 M, which corresponds to volume fraction around $\phi \approx 0.125$- 0.17. Fig. 3-18a shows that within the range 1.0 – 1.6 M KBr, time-salt superposition allows production of a fluid-like master curve similar to that expected for unentangled solutions with near-terminal response at low frequencies. The lack of a clear terminal $G' \propto \omega^2$ behavior may owe to the high polydispersity of the samples. The horizontal and vertical shift factors are plotted in Figs. 3-18 against (b) polymer concentration and against (c) overall salt concentration and (d) salt concentration in the coacervate, which is much lower than the overall salt concentration due to strong partitioning of salt into the supernatant. When the overall salt concentration drops below 1 M, however, Fig. 3-19 shows that the rheology changes to a low-frequency power-law scaling of both G' and G'' with $\omega^{0.3}$, which is "quasi-solid-like" since the exponent for G' is closer to zero (characteristic of a solid) than to 2 (characteristic of a liquid). Note the very large variation of shift factors with salt concentration, especially in Fig. 3-18, including a shift of more than two decades in the vertical shift factor, which is unusually high for vertical shifting. The results are suggestive of a more gradual shift to solid-like rheology below a critical salt concentration.

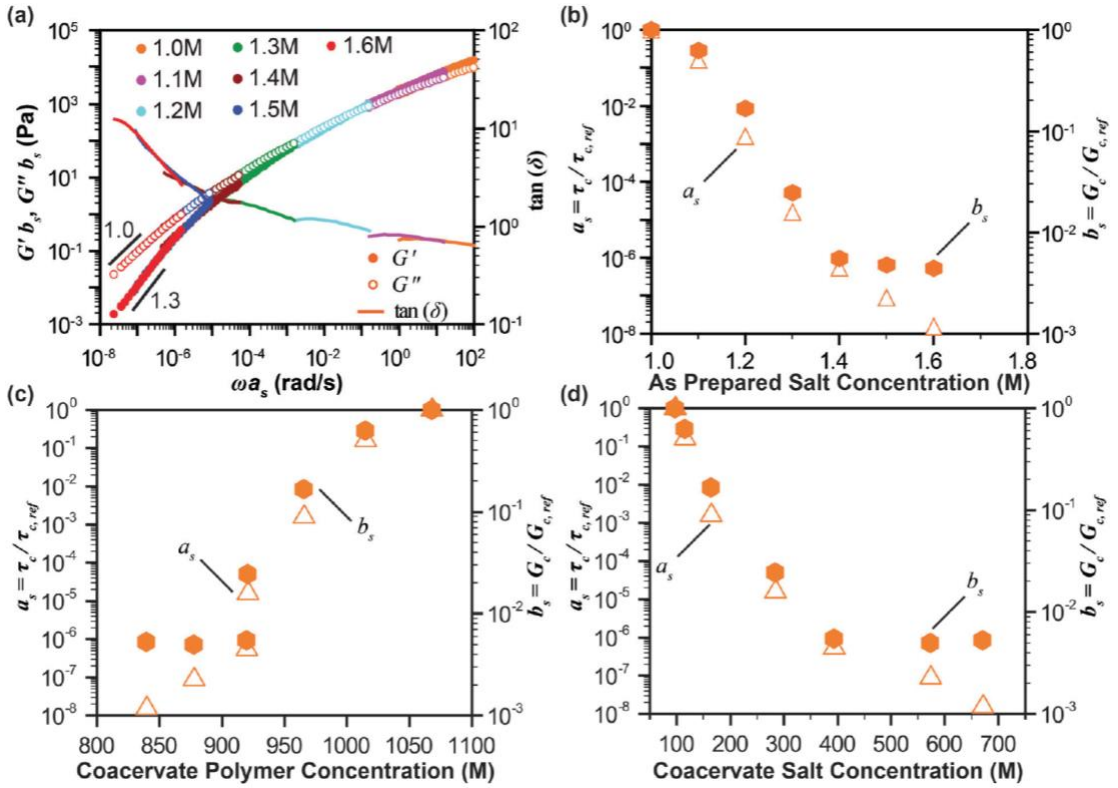

Figure 3-18. (a) Time-salt superposed curves for PDADMA/PSS (with from 1.0 M to 1.6 M KBr), where the given salt concentrations were as prepared in the initial mixture prior to phase separation. (b) horizontal (open triangles) and vertical (solid hexagons) shift factors, a_s and b_s, as a function of the ‘‘as prepared’’ salt concentration. The same shift factors are also plotted with respect to the (c) measured polymer concentration and (d) measured salt concentration, both in the coacervate phase. Note that the monomer and salt concentrations in the lower Figures should be in units of millimolar, mM, not molar M [60]. Used with permission from Liu et al. Soft Matter 13, 7332-7340 (2017). Copyright (2017), Royal Society of Chemistry.

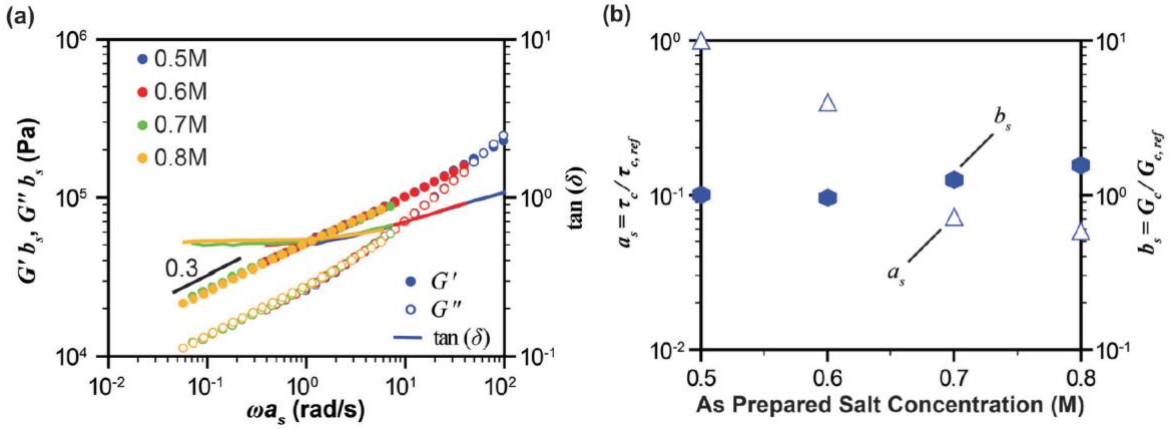

Figure 3-19. (a) Similar to Fig. 3-18, except for lower salt concentrations (from 0.5 M to 0.8 M KBr). (b) Plot of the horizontal (open triangles) and vertical (solid hexagons) shift factors, a_s and b_s, as functions of the ‘‘as prepared’’ salt concentration [61]. Used with permission from Liu et al. Soft Matter 13, 7332-7340 (2017). Copyright (2017), Royal Society of Chemistry.

While the rheological transition to "solid-like" behavior reported above for PDADMA/PSS in KBr seemed to occur abruptly at a particular salt concentration, this transition was revealed to be continuous in the later work of Ali and Prabhu [62]. Fig. 3-20 shows the time-*temperature*-salt superposed G' and G'' curves for PDADMA/PSS coacervates in both NaCl (Fig. 3-20a) and KBr (Fig. 3-20b). Each curve in these Figures is itself the result of a time-temperature (t-T) superposition, allowing data to be gathered over some 5-7 decades of frequency *at each salt concentration*. Achieving a large range of frequencies at each salt concentration is important in revealing the low-frequency break-down in time-salt (t-s) superposition. Notice that at high *reduced* frequencies, in the range 10^2 rad/s – 10^4 rad/s in Fig. 3-20, little deviation can be seen in t-s superposition, but that the deviation becomes huge at lower frequencies. In Fig. 3-18a, on the other hand, also for PDADMA/PSS, the data were taken at a single temperature and data at each salt concentration extended only over two decades. Thus, the data at different salt concentrations barely overlap in Fig. 3-18a. Hence, the "superposition" shown in Fig. 3-18a is evidently only apparent, made possible by shifting both vertically and horizontally and allowing curves to be stitched together despite lacking true t-s superposition. Notice the discontinuities evident in the tan δ curves, where data for different salt concentrations are forced to meet up. Even more telling is the very large vertical shift factors in Fig. 3-18b, which are much larger than is typical in most superpositions. They are also much larger than those shown in the inset of Fig. 3-20b, for a nearly identical system, differing only in that the molecular weights of PDADMAB (PDADMA with bromide ion) and KPSS (PSS with potassium ion) are 150 and 200 kDa, respectively, in Fig. 3-20 from the work of Ali and Prabhu [62], while they are 289 and 354 kDa in the work of Liu *et al.* [61] in Fig. 3-18. The vertical superpositions in the insets in Fig. 3-20 are more modest than in Fig. 3-18, because in Fig. 3-20 curves at different salt concentrations are not forced to superpose except at high frequency. Thus, Fig. 3-20 suggests that t-s superposition should be carried out only when a wide enough frequency range (at least 4 decades) is covered at each salt concentration, ideally obtained by carrying out t-T superposition prior to t-s superposition, or where this is lacking, using a wide range of frequencies at a single temperature. Figs. 3-2 and 3-6 of Schlenoff et al. show cases in which wide ranges of frequencies at each salt concentration are obtained by t-T superposition. While some non-overlapping data at low frequencies in Fig. 3-6 indicates some deviation from t-s superposition, any transition to a plateau in G' at low frequency is very weak at best in these data, even for virtually zero salt concentration.

Thus, the transition from a liquid-like terminal region to a solid-like plateau at low frequency appears to be a non-universal feature of only some coacervates, and when it occurs, does so at low salt concentration. Salt, then, can play two roles; it can both shift act to speed up "sticky diffusion" of the polymer by acting to "plasticize" the ion-pairing, and it can act to break up an otherwise permanent gel-like structure that is manifested at low frequency. The latter role, since it emerges at low frequency, presumably acts on longer length scales than do individual ion pairs and their spacing. The modulus that emerges at low frequency and low salt is as high as 10^2 Pa, which, though higher than observed in Fig. 3-14, nevertheless, using Equation (3-1), suggests a polymer network strand size much larger than the molecular weights of the polymers themselves. However, the data in Fig. 3-20 (left) are for NaCl concentrations of 2.8 M or higher. Shamoun *et al*. [63] also carried out rheological experiments with PDADMA/PSS in NaCl, with roughly similar molecular weights, i.e., 400kDa / 200kDa, as the values used to obtain Fig. 3-20, which are 150kDa /200kDa. Shamoun *et al*. [63] accessed a lower salt range, and observed a much higher low-frequency plateau, one that decreased from 3×10^4 to 1.5×10^4 Pa over the range [NaCl] = 0.1-1.0 M. The results at 1.0 M are shown in Fig. 3-21. These low-frequency moduli are around 2 decades higher than for the Ali-Prabhu data at 2.8 M NaCl in Fig. 3-20. Thus, putting these two studies together, it appears that the low-frequency plateau is sensitive to salt concentration, becoming much higher with decreased salt concentration. Note also in Fig. 3-20 the strong influence of the salt type on the salt concentration at which the transition from liquid-like to solid-like behavior occurs. It is possibly significant that all of the PE pairs showing a low-frequency plateau in G' have been of rather high molecular weight, over 100 kDa up to 400 kDa. Whether the plateau is molecular-weight sensitive, as well as salt-type and salt-concentration sensitive is an interesting question. Some possible reasons for the formation of a low-frequency "gel-like" structure will be suggested in the theory section. For low concentrations of salt, Fig. 3-21 shows that PDADMA/PSS exhibits an interesting transition at high frequency to a "glassy" modulus of 10^7 Pa [63]. This "glassy" modulus remains, however, much lower (by more than an order of magnitude) than the modulus of dense (solvent-free) polymer glasses, and does not show the relatively sharp enthalpy change with temperature upon cooling into the "polyelectrolyte glass." While of considerable interest in its own right, this "glassy" behavior is not the focus of this article, and readers interested in this behavior are referred to work by Lutkenhaus *et al*. among others [13].

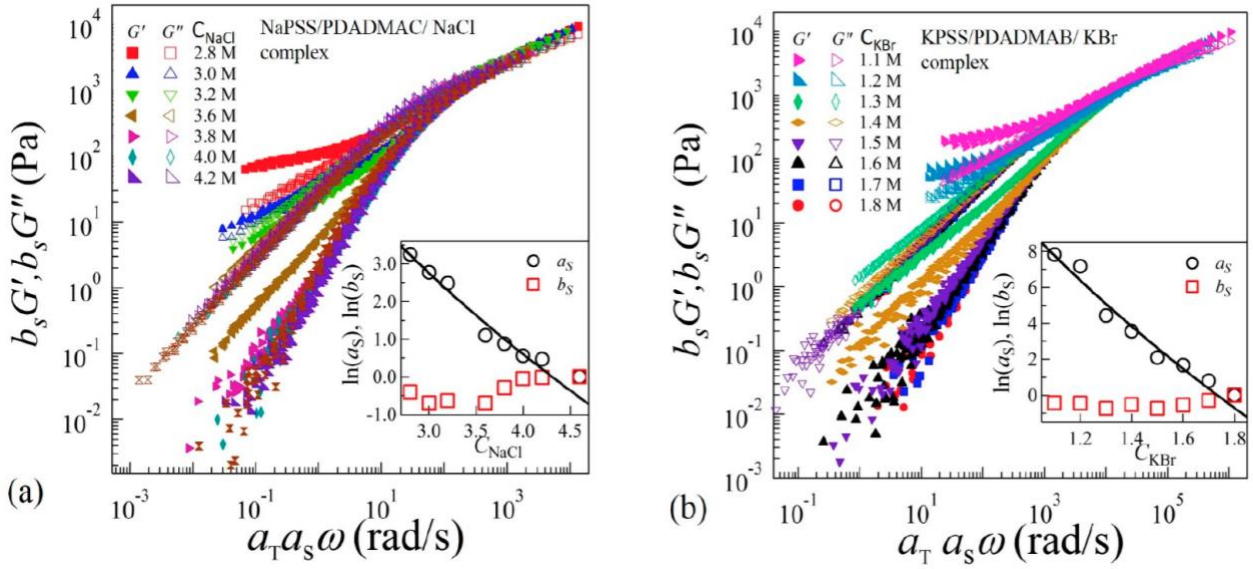

Figure 3-20. Time-temperature-salt superposition curves for coacervates composed of PDADMA/PSS in (a) NaCl, shifted relative to the curve at [NaCl] = 4.6 M, and (b) KBr, shifted to [KBr] = 1.8 M. Insets show horizontal a_s and vertical b_s shift factors [62]. Used with permission from Ali et al. Gels 4(1), 11 (2018).

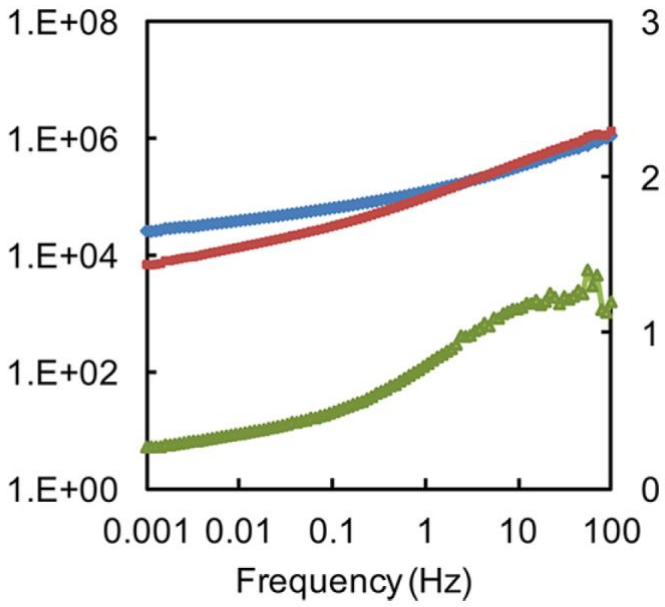

s

Figure 3-21.G′ (blue ◆), G″ (red ■) in units of Pa, and loss tan(δ) (green ▲) for PDADMA/PSS coacervate with 1.0 M NaCl at 30 °C [63]. Used with permission from Shamoun et al. Macromolecules 45, 9759−9767 (2012). Copyright (2012), American Chemical Society.

3.11 Theory

Starting with Spruijt *et al*. [17, 18] the rheological behavior of coacervates has generally been interpreted using the "sticky diffusion" theory of Rubinstein and Semenov [2]. The idea is that monomers on different chains form temporary attractive bonds whose rate of breakage or formation (which are equal at equilibrium) sets the time scale τ_0 for local diffusive motions. Longer-range motions are then identical to that of ordinary polymers, except that all time scales of polymeric relaxation are proportional to this fundamental "stickiness time scale" τ_0. For unentangled polymers, the dynamics are then those of Rouse polymers, with a set of relaxation times given by

$$\tau_p \approx \tau_0 (f/p)^2 \; ; \; 1 < p < f; \; \tau_R = \tau_0 f^2 \tag{3-3}$$

where f is the number of stickers on the chain, and p is the "mode number," which is smaller for the longer relaxation times. The first mode, with relaxation time $\tau_1 = \tau_R$ represents relaxation of the entire chain, while the higher modes, with p > 1, describe a series of harmonics of the primary mode. Modes with higher p represent more localized, and therefore faster, relaxations along the chain. Each relaxation time, including the longest, with p=1, and $\tau_R \propto f^2$, depends quadratically on the number of stickers f per chain. If the chains become long enough to exceed their entanglement threshold, the sticky diffusion model predicts that the longest relaxation time should transition to that of reptation, characterized by the tube disengagement (or reptation) time, which scales as $\tau_d \propto f^3$. These formulas assume that the sticker strength is high enough, and therefore τ_0 is long enough, that sticker breakage time controls the chain relaxation rate, rather than ordinary frictional contacts between chains. For a coacervate containing PEs of opposite charge, the "stickers" can be interpreted as charged monomers that bind ion pairs of opposite charge. If all, or a fixed fraction, of monomers are charged, then the longest relaxation time scales with molecular weight M as $\tau_R \propto M^2$ and $\tau_d \propto M^{3.4}$, which are the same scaling laws as found for neutral polymers in the unentangled, and entangled, limits, respectively. The corresponding scaling laws for the zero-shear viscosity are $\eta_0 \propto M$ and $\eta_0 \propto M^{3.4}$, respectively. In addition, the sticky diffusion theory predicts that the relaxation modes in both limits are the same as for neutral

polymers, with only their overall magnitude, set by τ_0, reflecting the influence of electrostatic interactions.

Thus, if sticky diffusion describes the rheology of coacervates, one expects the linear rheology, reflected in the shapes of the G' and G'' curves, to look essentially the same as for neutral polymers. In addition, there should be a transition, with increasing chain length, from a shape similar to that of the Rouse theory for unentangled chains, to that of the Doi-Edwards theory for entangled chains. A transition from Rouse-like G' and G" curves to shapes consistent with the onset of entanglements can be seen in Fig. 3-6, as the number of monomers increases from n_{av} = 213 to 2097, and in Fig. 3-5 as it increases from around 20 to 500. Curves of similar shape can be found for neutral polymers as molecular weight increases [47]. However, as noted earlier, Fig. 3-9 shows a viscosity scaling law of $\eta_0 \propto M^{5.4}$ for PMAPTA/PMA PEC, which is not explained by any simple local version of sticky diffusion theory. Schlenoff and coworkers suggest a mechanism to explain this scaling based on frequencies of breaking of ion pairing that are correlated to allow a chain to slide through an entanglement [43]. In addition to the anomalous molecular weight scaling of the longest relaxation time, the shapes of the G' and G'' curves are more "smeared out," with less distinctive features, and less clear-cut scaling laws in the low-frequency regime, than for neutral polymers of similar polydispersity. This again suggests that the dynamics and rheology of at least some PECs are not identical to those of melts apart from a stickiness lifetime taking the place of a monomeric friction coefficient. There are also anomalies in the emergence of low-frequency plateaus revealed in Figs. 3-13, 3-14, 3-19, and 3-20, which seem to be as-yet unexplained aspects of the rheology of coacervates.

For data sets that lack these anomalies, such as those of Figs. 3-5 and 3-6, ordinary polymer theories (Rouse and reptation) explain at least qualitatively both the frequency dependencies and molecular weight dependencies of the moduli. This leaves to be explained only the dependences of the fundamental time constant τ_0 on salt concentration, temperature, polymer concentration, and pH (for weak PEs). Of these, the most interesting and distinctive of PEs, is the dependence on salt concentration.

A general expression for the ion-pair breakage time τ_0 based on an "activation energy" E_a for bond breakage on salt concentration is

$$\tau_0 = \frac{1}{\omega_0} exp\left(\frac{E_a(c_{salt})}{k_B T}\right) \quad (3\text{-}4)$$

where ω_0 is a fundamental ion-pair breakage attempt frequency (which is weakly temperature-dependent). The time-salt shift factor a_s is then obtained from the dependence of the time constant τ_0 on salt concentration, which arises from the salt-dependence of E_a. Significantly different expressions for $E_a(c_{salt})$ have been suggested. The first of these is due to Cohen Stuart and coworkers [17] who developed a model for local rearrangement of two pairs of oppositely charged monomers that exchange partners, as illustrated by the four charges in Fig. 3-4 [28]. To pull apart a pair of elementary opposite charges, each of charge magnitude e, in a dielectric medium with dielectric constant ε_r, from a contact separation d out to infinite distance, is simply the electrostatic energy ℓ_B/d. Here $\ell_B = e^2/4\pi\varepsilon_r\varepsilon_0 k_B T$ is the "Bjerrum length" involving the fundamental unit of charge of an electron, e, the dielectric constant ε_r (≈80 for pure water), and the dielectric permittivity in a vacuum ε_0. The Bjerrum length is the length scale at which the electrostatic energy is comparable to thermal energy $k_B T$. However, when salt is present, the charge interactions are screened out at large distances. The simplest theory for screening is based on the linearized Debye-Hückel theory, in which the screening length, based on the salt ions only is the Debye length $\kappa^{-1} = \sqrt{1/(8\pi\ell_B N_{Av} c_{salt})}$, where N_{Av} is Avogadro's number. Thus, electrostatic energy divided by $k_B T$ is cut off at the Debye length and the energy to pull the two charges apart is then $(\ell_B/d - \ell_B\kappa)$. Spruijt *et al.* [17, 18] suggested that n = 2 pairs of such charges must be separated in the transition state between the binding states on the right and left in Fig. 3-4, giving the transition energy as

$$\frac{E_a}{k_B T} = n\ell_B(1/\mathrm{d} - \kappa) = n\ell_B(1/\mathrm{d} - \sqrt{8\pi\ell_B N_{Av} c_{salt}}) \qquad (3\text{-}5)$$

Taking n =2 pairs of charges, and using Equation (3-4), Equation (3-5) can be written as

$$\ln(\tau_0\omega_0) = \frac{E_a}{k_B T} = -2\kappa\ell_B + \frac{2\ell_B}{d} = -A\sqrt{c_{salt}} + B \qquad (3\text{-}6)$$

The Debye length κ^{-1} decreases with salt concentration as $1/\sqrt{c_{salt}}$, giving rise to the dependence shown in the third equality in Equation (3-6), where $A = (32\pi N_{Av}\ell_B^3)^{1/2}$, $B = 2\ell_B/d$, and c_{salt} is in units moles/m^3. (If the concentration units are moles/liter, a factor of 10^3 will need to multiply N_{Av} in the expression for A, as appears in some publications.) The same

argument was made by Colby and coworkers, except they found their results were better fit with a transition state involving *n=5* pairs of ions rather than 2 [36]**.** The derivation leading to Equation (3-6) involves the Debye-Hückel far-field limit of electrostatic interactions, which is valid when charge interactions are weak, but can certainly be doubted when applied to ion-pairs, as discussed below.

Equation (3-6) can be used to predict the time-salt shift factor a_s used to shift the log frequency axis of a rheology curve (such as G') relative to the curve at a reference salt concentration $c_{salt,ref}$. According to Equation (3-6), such curves shift by a logarithmic amount $\ln\tau_0$, so that the time-salt shift factor, relative the reference salt concentration, is given by

$$ln\ a_s\ = -A\left(\sqrt{c_{salt}} - \sqrt{c_{salt,ref}}\right) \tag{3-7}$$

where a_s = 1 at c_{salt} = $c_{salt,ref}$. The predictions of Equation (3-7) are compared in Fig. 3-22a to data for the shift factors from the rheological data of Spruijt *et al*. [18] in Fig. 3-5. Note in Fig. 3-22a that the logarithm of the shift factor seems to fit the square root dependence on salt concentration from Equation (3-7) reasonably well; but because of the limited range of salt concentrations a linear fit does almost as well. The curves shift significantly with different molecular weight, since the characteristic time τ_c is the inverse of the terminal cross-over frequency extrapolated from zero frequency. From the rheological relaxation spectrum, Spruijt *et al*. estimated the lifetime of an ion pair to be around 200 ms at 0.6 M salt, a value very much larger than estimated by Akkaoui *et al*. [43]. The latter give survival time of an ion pair to be around 10^{-8} s, and the hopping time for a broken pair to find a new pair rather than re-forming the original pair to be around 10^{-4} s. These much shorter ion pair lifetimes of Akkaoui *et al*. are much more compatible with the sticky diffusion model, which gives Rouse terminal relaxation times that are a factor of f^2 times the ion-pair hopping time, as discussed in the theory section. The expression for the modulus near the terminal relaxation, which is given by $G \approx k_B T \phi_p f / N b^3$, allows the estimate $f \approx$ 100-1000 for the data of Spruijt *et al*. for degree of polymerization N ≈ 500.

Table 3-3. Literature on time-salt/pH/hydration superposition of coacervates

Refer-ence	Polycation/ Polyanion	Salt	Superposition[i]	t-T fitting form	Low-□ plateau?	Salt shift-factor fitting[ii]
[18]	PDMAEMA/ PAA	KCl	t-s	-	No	$\ln a_s = B - A\sqrt{c_{salt}}$
[36]	PDADMA/ IBMA	NaCl	t-s	-	No	$\ln a_s = B - A\sqrt{c_{salt}}$
[62]	PDADMA/ PSS	NaCl, KBr	t-T-s	WLF	Yes	$\ln a_s = B - A\sqrt{c_{salt}}$
[63]	PDADMA/ PSS	NaCl	t-T-s	WLF	Yes	$\ln a_s = B - A(c_{salt})^{6/5}$
[3]	PVBTMA/ PSS	NaBr	t-s	-	No	$\ln a_s = B - A\sqrt{c_{salt}}$
[59]	PVP/PSS	KBr	t-s	-	No	$\ln a_s = B - Ac_{salt}$
[27]	PLK/PRE	NaCl	t-s	-	Yes	$\ln a_s = B - Ac_{salt}$
[28]	PMAPTA/ PMA	NaCl	t-T-s	Arrhenius	No	$a_s = a_{s,\tau_b} a_{s,f} a_{s,\varphi}$
[43]	PMAPTA/ PMA	NaCl	t-T-s	Arrhenius	No	$a_s = a_{s,\tau_p} a_{s,f} a_{s,\varphi} a_{s,d} a_{s,N_e}$
[54]	PAH/PAA	NaCl	t-T-water	Arrhenius	No	$\ln a_w = B - AW_{H_20}$[iii]
[50]	PAH/PAA	NaCl	t-s-ionic strength	-	Yes	$\ln a_s = B - A\sqrt{c_{salt}}$
[52]	PDADMA/ PAA	KCl	t-pH-s	-	Yes	- (no relevant equation)

[i]'t-T-s' represents time-temperature-salt superposition; 't-pH-s' represents time-pH-salt superposition; 't-T-water' represent time-temperature-water superposition; 't-s-ionic strength' represents time-salt-ionic strength superposition.
[ii]Units of c_{salt} in the table are mol/m^3 (1 mol/m^3= 10^3 mol/L=10^3 M).
[iii]a_W, water shift factor; W_{H_20}, water content in the PEC.

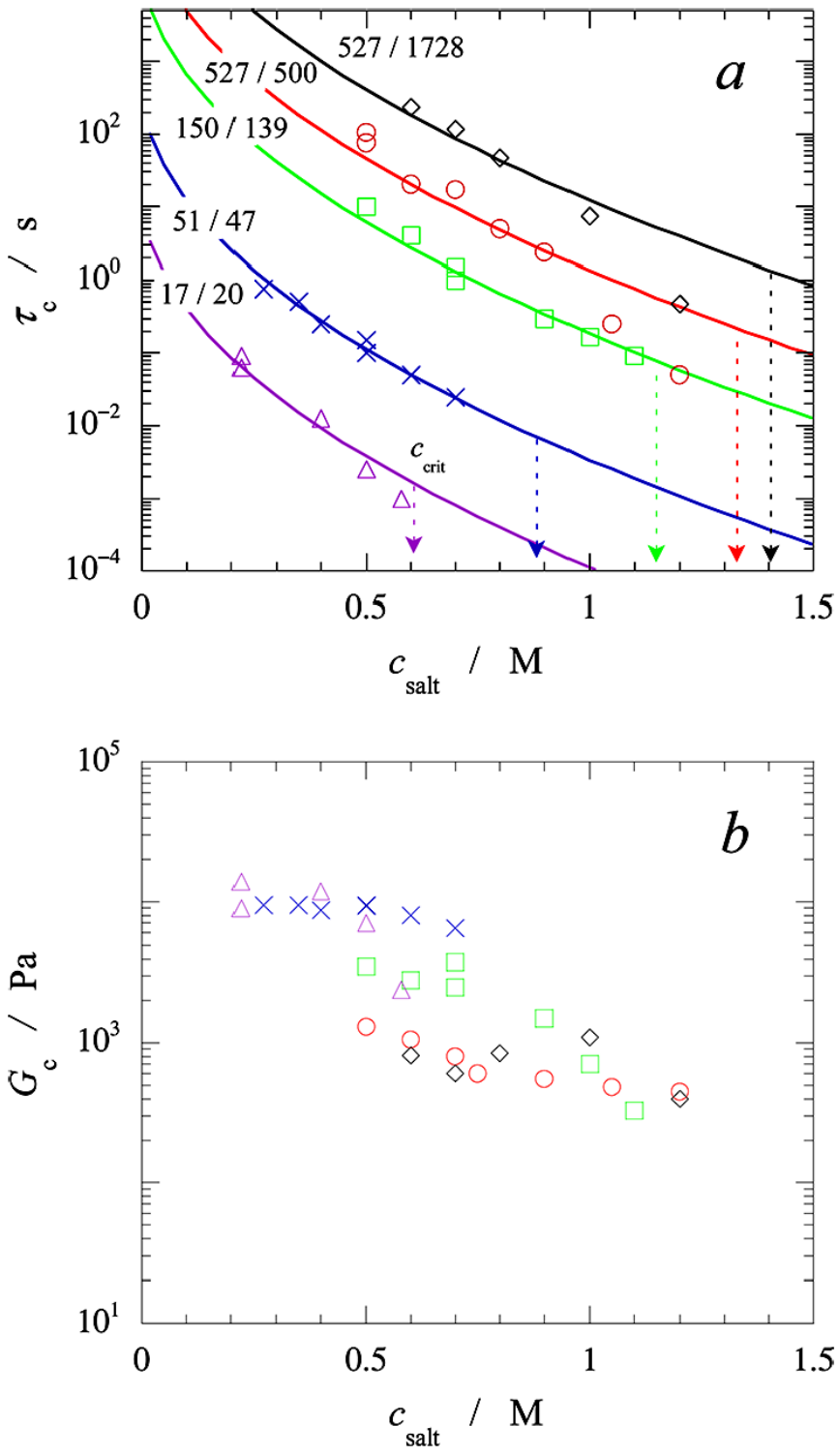

Figure 3-22. Symbols show (a) horizontal and (b) vertical shift factors used to obtain master plots in Fig. 3-5 for PDMAEMA/PAA coacervates with degree of polymerization indicated by matching colors in (a) and (b) with fits in (a) given by Equations (3-4) and (3-5). The vertical dashed arrows in (a) indicate the critical salt concentrations for dissolution of coacervate for each chain length [18]. Used with permission from Spruijt et al. Macromolecules 46, 1633-1641 (2013). Copyright (2013), American Chemical Society.

The shift factor formula of Spruijt *et al*., Equation (3-7), seems successful for shifting their data for coacervates of PDMAEMA/PAA in NaCl, and has also been successfully used by Ali and Prabhu [62] with A = 6.8 ± 0.6 and 23.8 ± 2.5 for their time-salt shift factors a_s for PDADMA/PSS coacervates in NaCl and KBr, respectively. The prefactor A obtained from the fit by Ali and Prabhu is in reasonable agreement with the value calculated from the formula above using the expected value of ε_r = 42 at the reference salt concentration if we take n = 1 and n=4, respectively for NaCl and KBr salts. Meng and Tirrell [3] also report that changes in $ln a_s$ are proportional to $-\sqrt{c_{salt}}$, in agreement with the scaling in Equation (3-6). Hamad *et al*. [36] found the same scaling behavior for PDADMA/IBMA/NaCl, giving a plot of $ln\ a_s$ against $-\sqrt{c_{salt}}$ very similar to that of Spruijt *et al*. shown in Fig. 3-22a. As noted earlier, however, Hamad *et al*. however, found a best fit to the theory in Equation (3-6) by modifying the factor of 2 to 5 pairs of ion s broken in the transition state. This may suggest conformational restrictions that require a few, rather than 2, ion pairs to be broken to allow re-pairing of the freed charged monomers. Thus, a significant body of work is consistent with a scaling law $ln a_s \propto -\sqrt{c_{salt}} + const$, as shown in Table 3-3. We note that Syed and Srivastava [50] varied the total small-ion ionic strength I, and found that the time-salt master curve was a universal function of total ionic strength I for PAH/PAA coacervates, with a constant, A = 4.74, in Equation (3-6), with "I" replacing "[NaCl]," which they interpreted as support for the sticky diffusion model of Spruijt *et al*. [18].

However, not all available papers show this behavior. A linear dependence, $\ln a_s \propto -c_{salt} + const$ has been reported both by Sadman *et al*. [59] for coacervates of quaternized poly (4-vinylpyridine) (QVP) polycations/PSS in KBr solutions, and by Marciel *et al*. [27] for PLK/PRE in NaCl solution. In both cases, this dependence was simply reported as an empirical observation; no theory supporting this scaling has yet been offered. A slight variation from this dependence, namely $ln a_s \propto -(c_{salt})^{6/5} + const$ was observed by Shamoun *et al*. [63]. These different observed formulas for salt shifting are given in Table 3-3.

Even where data is well fit by $ln a_s \propto -\sqrt{c_{salt}} + const$, there is reason to doubt the theory based on the Debye-Hückel approximation, which is a low-salt theory that treats ions as if they are in a diffuse double layer. Not only is the diffuse double layer assumption highly questionable under typical (high) salt concentrations, and high charged monomer concentrations of around 1 M, but the theoretical expression in Equation (3-6) suggests that all monovalent salt ions should give the

same shift factors, and indeed, even the same G' and G'' for the same polymers in different salt solutions. Fig. 3-20, however, shows that this is definitely not true, since the rheology of the same PDADMA/PSS polymers differs greatly between NaCl and KBr solutions. Schlenoff and coworkers have found strong salt-type dependences of phase behavior of coacervates [64], and the same sensitivity should carry over to rheology. Also, if movement of a monomer requires breaking *n* ion pairs, then the coefficient of $\sqrt{c_{salt}}$ is $A = n(8\pi 10^3 N_{Av} \ell_B^3)^{1/2}$ = 5.8*n*, if ε_r = 42, or 2.2*n*, if ε_r = 80) where the factor of 10^3 enters because we use molar units for the salt concentration rather than moles/m^3. Thus, each increase in $\sqrt{c_{salt}}$ by one unit of square root molar concentration increases the shift factor by 5.8*n*, and matching the time-salt shift factor in Fig. 3-22a implies that $n \approx 2$. Similarly, data from supplementary information in Akkaoui *et al*. [42] show a 5-fold change in a_s with a change in NaCl concentration from 0 to 0.2 Molar, again implying that $n \approx 2$, if we use Equation (3-6).

Thus, some support of Equation (3-6) might be drawn from agreement of the fitted value of the prefactor A with the predicted value when we take $n \approx 2$. However, as noted above, the number *n* of ion pairs broken during each re-arrangement step has been adjusted by Hamad *et al*. [36] to make the calculated A agree with the fitted one, and so support for Equation (3-6) from this direction is shaky. In fact, the expression for τ_0 in Equation (3-6) depends on temperature as well as salt concentration, through the dependence of $\ell_B = e^2/4\pi\varepsilon_r\varepsilon_0 k_B T$ on temperature and a weaker dependence of the prefactor ω_0 on temperature. If the salt concentration is zero, then the temperature-dependent shift factor a_T is given by the temperature dependence of $B = n\ell_B/d = ne^2/4\pi d\varepsilon_r\varepsilon_0 k_B T$ = 1.4 x $10^{-4} n/d\varepsilon_r RT$, in mks units, using the known values of e and ε_0 and switching to molarity rather than molecular units. If the binding distance *d* is around 1 nm, and ε_r around 44, then $B = 3.1n$ kJ/mole/RT, with RT in kJ/mole. This corresponds to Arrhenius time-temperature shifting with an activation energy of 3.1n kJ/mole. However, the activation energy for time-temperature shifting for PMAPTA/PMA coacervates at near-zero salt concentration reported by Akkaoui *et al*. [43] is 45 kJ/mole, which would require an unreasonable 15 pairs of ions to break for local chain motion to occur. Admittedly, some of the temperature dependence is likely owing to the temperature dependence of the viscosity of water, which can be approximated at around room temperature as Arrhenius with activation energy of around 23 kJ/mole. If the rate constant ω_0 in Equation (3-5) is inversely proportional to the viscosity, this still leaves an

electrostatic activation energy of 22 kJ/mole, requiring around 7 pairs of ions to be broken to explain the temperature dependent shift factor. Moreover, since this number *n* must be the same value for both the salt-dependent and temperature-dependent shifting, and the value needed for salt-shifting noted above is close to 2, much lower than the value of 15 (or possibly 7) needed for temperature shifting, the expression (3-6) appears to make temperature-dependent and salt-dependent shifting incompatible. In addition, Equation (3-6) depends on a theory of coacervation controlled by Debye-Hückel electrostatic fluctuations. The original Overbeek-Voorn theory [44] for the thermodynamics of coacervation assumed that these electrostatic interactions dominate, but recent evidence strongly points towards ion-specific binding as at least as important a factor for typical coacervate concentrations [61, 62]. And if thermodynamics of coacervation is not governed predominantly by Debye-Hückel electrostatics, neither should one expect such electrostatics to govern the rheology.

Perhaps the most telling argument against the scaling $lna_s \propto -\sqrt{c_{salt}} + const$ is simply that this dependence of lna_s on the square root of salt concentration does not fit any of the data sets significantly better than does a simpler linear fit, $lna_s \propto -c_{salt} + const$, and for some of the data sets in Table 3-3, the square root rule is significantly worse. This is demonstrated in the Table 3-4, where all data sets discussed in Table 3-3 are fit by both square root and linear scaling rules using linear regression, and the goodness of fits, measured by the statistical values of R^2, are compared. Like many of the others, the data sets of Spruijt *et al*., have such a modest range of salt concentration that both scaling laws fit the data with an R^2 value of 0.96 to 0.99, with each scaling law showing a better agreement for a portion of the data sets. For some of the data sets of Marciel *et al*. [27] and Hamad *et al*. [36], the square root scaling is clearly inferior to the linear scaling, with R^2 values as low as 0.82 for the former, and values of 0.96 or above for the latter. Thus, data fitting gives no reason to prefer the square-root scaling law over a linear one for any of the data sets, and in some cases the square root fit is not favored. It should also be pointed out that recent coarse-grained molecular simulations that contain electrostatic interactions between polyions and small ions, but use only soft, generic local interactions spherical polymer beads and ions, do not produce time-salt superposition *et al*. [66]. This suggests that local interactions are critical to an understanding of time-salt shifting, and we should not expect simple arguments based on far-field Debye-Hückel analysis to be of much use.

Table 3-4. R^2 for linear fits of $\ln(a_s)$ as a function of salt concentration (c) and as a function of $c^{1/2}$ from published data listed in Table 3-3.

Reference	polycation/polyanion	N_{cation}/N_{anion}	R^2 for $ln\ a_s \sim c$	R^2 for $ln\ a_s \sim c^{1/2}$
[3]	PVBTMA/PSS	100	0.9352	0.9518
[17]	PDMAEMA/PAA	510	0.9911	0.9862
		150	0.9848	0.9802
		50	0.9711	0.9858
		20	0.9962	0.9926
[18]	PDMAEMA/PAA	527/1728	0.9862	0.9734
		527/500	0.9818	0.9704
		150/139	0.9914	0.9977
		51/47	0.9872	0.9894
		17/20	0.9923	0.9801
[27]	PLK/PRE	400/400	0.9662	0.8248
[28]	PMAPTA/PMA	2097B	0.9996	0.9011
		763	0.9944	0.9963
		662	0.9895	0.9989
		343	0.998	0.9817
		213	0.9995	0.9755
[36]	PDADMA/IBMA	1856/1898	0.9898	0.9588
		1856/907	0.9947	0.9068
		1856/380	0.9944	0.8883
		1856/51	0.9663	0.9288
[43]	PMAPTA/PMA	3730	0.9818	0.978
[52]	PDADMA/PAA	930/1400	0.9954	0.9724
[59]	QVP-C1/PSS	612/1136	0.9979	0.9970
	QVP-C2/PSS		0.9946	0.9934
	QVP-C3/PSS		0.9777	0.9758
[62]	PDADMA/PSS	970/970	0.9484	0.9604
	PDADMA/PSS		0.9544	0.9562

Some of these considerations have led the Schlenoff group to discard relating the time-salt shift factor to dilute electrostatics governed by the Debye length. Instead, they start with a fundamental frequency of hopping, related to the rate ν_T at which ion pairs break. If this is enabled by a salt ion displacing a like-charged monomer from a monomer of opposite sign, then ν_T will be related to the salt ion diffusivity $D_{i,PEC}$ in the coacervate via

$$D_{i,PEC} = \frac{\nu_T d^2}{6} \tag{3-8}$$

where d here is the hopping distance of the salt ion between sites along the PEs, which Akkaoui *et al*. take to be around 1 nm. (This distance is not the same as the distance d used in Equation (3-5), although both are of order 1 nm or so.) From a measurement of the salt diffusivity in the coacervate, a value of ν_T was inferred that ranged from 6 x 10^7 to 1.8 x 10^8 rad/s with increasing salt concentration. The activation energy of this diffusivity determined by measuring the temperature dependence of $D_{i,PEC}$, was around $E_a \approx 20$ kJ/mol, which was then related to the probability p of an un-bound charged site on the coacervate via $E_a = -RTln(p)$, giving $p \approx 2$ x 10^{-4}. The time τ_p is taken to be the time for a single ion pair to be broken, either in the absence of small salt ions, or because a small salt ion displaces the oppositely charged monomer; see Fig. 3-23. Akkaoui *et al*. [43] report a time of around $\tau_p \approx 10$ ns based on dielectric spectroscopy, which is roughly equal to the inverse of the ion hopping rate, i.e., $1/\nu_T$. This time is a factor of *1/p* larger than the breakage attempt time, which is in the picosecond range, and $p \approx 2$ x 10^{-4} is again the fraction of attempts that lead to breakage of the ion pair, which is taken equal to the probability that a charge site in the coacervate is not bound by salt ion or an oppositely charged monomer. The longer, rheological, time scales are then taken to be proportional to τ_p, and also depend on the number of charge groups f on the chain and on the volume fraction ϕ of PE in the coacervate, the distance d between charged monomers, and the number of Kuhn steps N_e in an entanglement segment. All of these factors can be dependent on salt concentration, and thus Akkaoui *et al*. interpret the salt dependence of the shift factor as a product of shift factors from each of these sources, $a_s = a_{s,\tau_p} a_{s,f} a_{s,\varphi} a_{s,d} a_{s,N_e}$; see Table 3-3. This notional product of dependences does not yield any simple expression for the shift factor, such as $lna_s \propto -\sqrt{c_{salt}} + const.$ However, as noted above, it is likely that the success of this square-root expression is fortuitous. If so, resolution of the source of the salt shift factor will require careful measurements of local dynamics using NMR or other sensitive experimental methods, or use of molecular dynamics simulations.

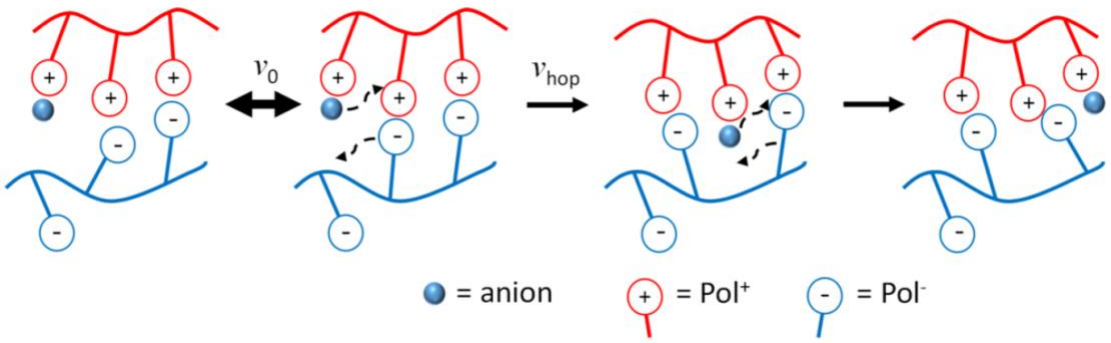

Figure 3-23. Illustration of displacement breakage of ion pairs by migration of a salt ion. Here ν_0 and ν_{hop} are the attempted and actual hop frequency, where $\nu_{hop} = \nu_T$ [43]**.** Used with permission from Akkaoui et al. Macromolecules 53, 4234–4246 (2020). Copyright (2020), American Chemical Society.

Table 3-5 gives formulas for rheological relaxation times adapted from the Rubinstein and Semenov [2] "sticky diffusion" model by the Schlenoff group [28] where the nomenclature was introduced in the above paragraphs, and l is the number of non-charged monomers between charged ones, with $l = 0$ if all monomers are charged; y is the "doping fraction," or fraction of monomer charges that are bound by a small salt ion rather than by an oppositely charged monomer, and d is the distance between charged monomers. Relaxation times are reduced when ion pairs between polymers are diluted by bound small salt ions. N is the average number of Kuhn steps of polycation and polyanion, assuming that they are similar and τ_b here is the effective or renormalized breakage time, which is the average time between ion-pair re-pairing events. This is presumably much longer than the time for ion-pair breaking, since most such broken ion pairs simply re-pair again rather than create ion-pairing with a different partner monomer.

Table 3-5. Formulas for relaxation times and viscosities adapted by Yang et al. from sticky diffusion theory

	Rubinstein & Semenov [2]	Modification by Yang *et al.* [28]
Sticky Rouse	$\tau_R \sim \tau_b f^2$	$\tau_R \sim \tau_b N^2 (1-y)^2$
	$\eta_0 \sim \tau_b \left(\frac{k_B T}{d^3}\right) N l^{-2} \phi$	$\eta_0 \sim \tau_b \left(\frac{k_B T}{d^3}\right) N (1+l)^{-2} \phi$
Sticky Reptation	$\tau_R \sim \tau_b f^2 \frac{N}{N_e}$	$\tau_R \sim \tau_b N^2 (1-y)^2 \frac{N}{N_e}$
	$\eta_0 \sim \tau_b \left(\frac{k_B T}{d^3}\right) \frac{N^3}{N_e^2} l^{-2} \phi$	$\eta_0 \sim \tau_b \left(\frac{k_B T}{d^3}\right) \frac{N^3}{N_e^2} (1+l)^{-2} \phi$

Yang *et al.* [28] seperated τ_b into two parallel relaxation channels, governed by constants $\tau_{b,i}$ and $\tau_{b,e}$, so that $\tau_b{}^{-1} = \tau_{b,i}{}^{-1} + \tau_{b,e}{}^{-1}$. Here, $\tau_{b,i}$ represents the "intrinsic" relaxation time for PE ion pairs Pol^+Pol^-, and was measured to be in the range 1.0-1.4 x 10^{-4} s. $\tau_{b,e}$, which was reported to be of the order 10^{-7} s, reflects the "extrinsic" relaxation time for Pol^+A^- or Pol^-M^+, where A^- and M^+ are a small salt anion and cation, respectively. As the salt doping level increases, $\tau_{b,e}$ dominates and determines the value of τ_b, thus decreasing the relaxation time for ionic bonds to form or break.

Table 3-6. Formulas for relaxation times and viscosities adapted by Akkaoui et al. from reptation theory

Reptation theory for nonsticky polymers	Modification for sticky polymers by Akkaoui *et al.* [43]
$\tau_e \sim \tau_o N_e{}^2$	$\tau_e \sim \tau_p f_e N_e{}^2 \sim \tau_p (1-y) N_e{}^3$
$\tau_{rep} \sim \tau_e (\frac{N}{N_e})^3$	$\tau_{rep} \sim \tau_e (\frac{f}{N_e})^2 (\frac{N}{N_e})^3 \sim \tau_e (1-y)^2 (\frac{N}{N_e})^5$
$\eta_0 \sim G_0 \tau_{rep} \sim \left[\frac{kT\phi}{d^3}\right] \tau_e (\frac{N}{N_e})^3$	$\eta_0 \sim G_0 \tau_{rep} \sim \left[\frac{kT\phi}{d^3}\right] \tau_p (1-y)^3 \frac{N^5}{N_e{}^3}$

Following up with more recent work, the Schlenoff group [43] adapted entangled polymer theory to the PE "sticky reptation" model, giving time constants in Table 3-6. In this table τ_p is the ion-pair breakage time, f_e is the number of ion-pairs per entanglement segment, f is the total number of ion pairs in the chain, and τ_e is the "equilibration time," or relaxation time of an entanglment segment. Note the power law N^5 for the chain-length dependence of reptation time τ_{rep} and zero-shear viscosity η_0, suggested by Schlenoff and coworkers.

While the relationship between ion-pair "hopping frequency" and the overall rheology of coacervates as interpreted by sticky diffusion theory remains uncertain, the anomalies mentioned above call into question whether sticky diffusion really provides a complete picture of coacervate rheology. The anomalies that are particularly striking in the above discussion include: 1) the asymmetry in changes in relaxation time produced by changing the molecular weight of polyanion vs. polycation, shown in Fig. 3-10; 2) the non-reptation power law of 5.4 in the dependence of viscosity on degree of polymerization N in coacervates with nearly equal values of N for polycation and polyanion in Fig. 3-9; and 3) the existence in a number of coacervates of a low-frequency plateau modulus, implying solid-like rather than liquid-like behavior at low frequency, in Figs. 3-13, 3-14, 3-19, and 3-20.

The first of these "anomalies," that of non-symmetry in the effect of changing the molecular weight of the polycation vs. the polyanion, could be explained by a difference in the hopping distance of oppositely charged monomers upon release of the ion pair. If, for example, the polycation monomer can, because of chain stiffness or other factors, move only a fraction of the distance that the polyanion can move before being bound to another ionic group, then the movement and relaxation of the polycation will be slower than the polyanion, even when the former has fewer monomers than the latter, and the chain length of the polycation will have a greater effect on the relaxation time than that of the polyanion. Since the diffusivity of the monomer scales as the square of the hopping distance, a significant difference in their hopping distances could create a profound asymmetry in their effect on relaxation. We note in this respect that the polycation, PDMAEMA, has a Kuhn length of 2.65 nm in water, while for PAA, it is reported to be only 0.64 nm [22, 33]. This suggests that the much greater rigidity of the polycation may cause it to diffuse much less rapidly in response to loss of ion-pairing than does PAA, consistent with the experimental ion pairing. Whether this explanation is valid will require measurements of local hopping rates either by experiment or MD simulations. But we note that the changes in polycation chain length affect the rheology over the entire measured frequency range in Fig. 3-10a, suggesting that the origin lies in short-range local interactions.

The second and third anomalies are likely not explainable by local motions alone, since their effects are primarily at the long-time scales, and do not show up in the high-frequency rheology. The second anomaly, that of the non-canonical 5.4 power law dependence of terminal relaxation time on molecular weight has been seen only once, and therefore awaits confirmation in some other system or by another lab. The third anomaly, the low-frequency plateau modulus, has been seen repeatedly, and is evidently salt-concentration dependent. While the magnitude of low-frequency plateau is low enough in some cases to suggest that it might be a measurement artifact, in other cases it is easily large enough (~10^2 to 10^4 Pa) to be unambiguously present. While not yet explained, there may be some inspiration to be drawn from neutral polymers with attractive interactions that leads them to form gels in some solvents, as occurs for example for isotactic polystyrene in nitropropane below the theta temperature [67]. A theory for such physical gelation has been developed by Tanaka and Stockmayer [68]. Application of these theories to coacervates has not yet been attempted, but may be a fruitful direction, with the caveat that successful application of such theories must, as a minimum, explain why some coacervates show the low-

frequency plateau and others do not. Beyond qualitative success, much more detailed modeling will be required to see if these ideas have merit, and, if so, to make them quantitative and predictive.

3.12 Summary and Suggestions for Future Work

Several thorough studies of coacervate rheology show the utility of time-salt superposition in coacervate rheology, along with conventional time-temperature superposition, and, in special systems, time-pH, and time-hydration superposition. The ability to shift linear rheology curves onto a master curve upon varying temperature, salt concentration, pH, and/or hydration suggests that these variables control local chain hopping rates, but otherwise do not much affect larger-scale physics. Moreover, the similarity of the rheological curves to those for either unentangled solutions or entangled ones depending on chain length, suggests a rather simple physical picture for coacervate rheology that deviates little from well-known behavior of neutral polymers at the coarse-grained level. Yet, there are several anomalies and exceptions to such a simple interpretation. Many coacervates show signs of a low-frequency gel-like plateau, whose presence and magnitude can depend on salt concentration. When there is a terminal relaxation time, its scaling with chain length can deviate significantly from conventional theory, and the separate dependencies of the terminal time on chain lengths of each of the two PEs, in the single case where they have been measured, show a strong asymmetry, thereby assigning an unequal role for the polycation versus the polyanion. And the dependence of the "stickiness" lifetime of a temporary bond between polycation and polyanion monomer is not well understood, and seems to be highly system specific.

Thus, the linear rheology, not to speak of the nonlinear rheology, of PECs remains an intriguing topic for future research. Clear, detailed, and well-confirmed theories are not yet available, but common features in differing systems that suggest that some broadly applicable theoretical concepts are ripe for discovery and exploitation. Beyond imaginative theorizing, definitive results will likely require more careful rheological experiments to establish the range of validity of the various superposition principles, to establish more clearly which polyelectrolyte systems have a low-frequency plateau modulus that is outside the range of experimental uncertainty, and to explore more widely the effects of different monomer and salt types. In

addition, insightful experiments that probe local dynamics, such as advanced versions of NMR and neutron scattering, as well as accurate atomistic molecular dynamics simulations, should help resolve if and when local dynamics can be regarded as a kind of sticky diffusion governed by breakage of ion pairs, versus cooperative "glassy" dynamics involving multiple monomers and salt ions. High-quality PEs synthesized in nearly monodisperse form over a range of molecular lengths, and studied over a range of temperatures, salt concentrations, and salt types, will also be an essential part of bringing this important field to maturity over the next decade or two.

3.13 Reference

[1] Liu, Y., H. H. Winter, and S. L. Perry, "Linear viscoelasticity of complex coacervates," Adv. Coll. Interf. Sci. Matter 239, 46-60 (2017).

[2] Rubinstein, M., and A. N. Semenov, "Dynamics of entangled solutions of associating polymers," Macromolecules 34, 1058−1068 (2001).

[3] Meng, S., J. M. Ting, H. Wu, and M. V. Tirrell, "Solid-to-Liquid Phase Transition in Polyelectrolyte Complexes," Macromolecules, 53, 7944-7953 (2020).

[4] Sing, C.E., and S. L. Perry, "Recent progress in the science of complex Coacervation," Soft Matter 16, 2885-2914 (2020).

[5] Rubinstein, M., Q. Liao, and S. Panyukov, "Structure of liquid coacervates formed by oppositely charged polyelectrolytes," Macromolecules 51, 9572-9588 (2018).

[6] Perry, S. L., and C. E. Sing, "Prism-based theory of complex coacervation: Excluded volume versus chain correlation," Macromolecules 48, 5040-5053 (2015).

[7] Zhang, P., K. Shen, N. M. Alsaifi, and Z. G. Wang, "Salt partitioning in complex coacervation of symmetric polyelectrolytes," Macromolecules 51, 5586-5593 (2018).

[8] Zhang, R., and B. I. Shklovskii, "Phase diagram of solution of oppositely charged polyelectrolytes," Physica A: Statistical Mechanics and its Applications 352, 216-238 (2005).

[9] de La Cruz, M. O., L. Belloni, M. Delsanti, J. P. Dalbiez, O. Spalla, and M. Drifford, "Precipitation of highly charged polyelectrolyte solutions in the presence of multivalent salts," The Journal of chemical physics 103, 5781-5791 (1995).

[10] Adhikari, S., M. A. Leaf, and M. Muthukumar, "Polyelectrolyte complex coacervation by electrostatic dipolar interactions," The Journal of Chemical Physics 149, 163308 (2018).

[11] Salehi, A., and R. G. Larson, "A molecular thermodynamic model of complexation in mixtures of oppositely charged polyelectrolytes with explicit account of charge association/dissociation," Macromolecules 49, 9706-9719 (2016).

[12] Friedowitz, S., A. Salehi, R. G. Larson, and J. Qin, "Role of electrostatic correlations in polyelectrolyte charge association," The Journal of chemical physics 149, 163335 (2018).

[13] Zhang, Y., F. Li, L. D. Valenzuela, M. Sammalkorpi, and J. L. Lutkenhaus, "Effect of Water on the Thermal Transition Observed in Poly (allylamine hydrochloride)–Poly (acrylic acid) Complexes," Macromolecules 49, 7563-7570 (2016).

[14] Sing, C. E, "Micro- to macro-phase separation transition in sequence-defined coacervates," J. Chem. Phys. 152, 024902 (2020).

[15] Lin, Y., J. P. Brady, H. S. Chan, and K. Ghosh, "A unified analytical theory of heteropolymers for sequence-specific phase behaviors of polyelectrolytes and polyampholytes," J. Chem. Phys. 152, 045102 (2020).

[16] Danielsen, S. P. O., J. McCarty, J. Shea, K. T. Delaney, and G. H. Fredrickson, "Molecular design of self-coacervation phenomena in block polyampholytes," Proceedings of the National Academy of Sciences of the United States of America 116, 8224-8232 (2019).

[17] Spruijt, E., J. Sprakel, M. Lemmers, M. A. Cohen Stuart, and J. van der Gucht, "Relaxation Dynamics at Different Time Scales in Electrostatic Complexes: Time-Salt Superposition," Physical Review Letters 105, 208301 (2010).

[18] Spruijt, E., M. A. Cohen Stuart, and J. Van Der Gucht, "Linear Viscoelasticity of Polyelectrolyte Complex Coacervates," Macromolecules 46, 1633-1641 (2013).

[19] Ali, S., M. Bleuel, and V. M. Prabhu, "Lower critical solution temperature in polyelectrolyte complex coacervates," ACS Macro Letters 8, 289-293 (2019).

[20] Wang, Y., V. Kozlovskaya, I. G. Arcibal, D. M. Cropek, and E. Kharlampieva, "Highly swellable ultrathin poly (4-vinylpyridine) multilayer hydrogels with pH-triggered surface wettability," Soft Matter 9, 9420-9429 (2013).

[21] Yoshida, M., "Solution properties of polyvinylpyridine in acid—II. Solution properties of poly (4-vinylpyridine) in aqueous solution of hydrochloric acid," European polymer journal 33, 943-948 (1997).

[22] Andreeva, L. N., S.V. Bushin, M.A. Bezrukova, T.N. Nekrasova, R.T. Imanbaev, V.D. Pautov, O.V. Nazarova, Yu. I. Zolotova, and E. F. Panarin, "Conformation properties of poly (N, N-dimethylaminoethyl methacrylate) macromolecules in various solvents," Russian Journal of Applied Chemistry 85, 417-425 (2012).

[23] Spruijt, E., F. A. M. Leermakers, R. Fokkink, R. Schweins, A. A. van Well, M. A. Cohen Stuart, and J. van der Gucht, "Structure and Dynamics of Polyelectrolyte Complex Coacervates Studied by Scattering of Neutrons, X-Rays, and Light," Macromolecules 46, 4596-4605 (2013).

[24] Dickhaus, B. N., and R. Priefer, "Determination of polyelectrolyte pKa values using surface-to-air tension measurements," Colloids and Surfaces A: Physicochemical and Engineering Aspects 488, 15-19 (2016).

[25] Cranford, S. W., and M. J. Buehler, "Variation of weak polyelectrolyte persistence length through an electrostatic contour length," Macromolecules 45, 8067-8082 (2012).

[26] Mirtič, A., and J. Grdadolnik, "The structure of poly-L-lysine in different solvents," Biophysical chemistry 175, 47-53(2013).

[27] Marciel, A. B., S. Srivastava, and M. V. Tirrell, "Structure and rheology of polyelectrolyte complex coacervates," Soft Matter 14, 2454-2464 (2018).

[28] Yang, M., J. Shi, and J. B. Schlenoff, "Control of Dynamics in Polyelectrolyte Complexes by Temperature and Salt," Macromolecules 52, 1930−1941 (2019).

[29] Dautzenberg, H., E. Görnitz, and W. Jaeger, "Synthesis and characterization of poly (diallyldimethylammonium chloride) in a broad range of molecular weight," Macromolecular Chemistry and Physics 199, 1561-1571 (1998).

[30] Hirose, E., Y. Iwamoto, and T. Norisuye, "Chain stiffness and excluded-volume effects in sodium poly (styrenesulfonate) solutions at high ionic strength," Macromolecules 32, 8629-8634 (1999).

[31] Spiteri, M. N., F. Boué, A. Lapp, and J. P. Cotton, "Persistence length for a PSSNa polyion in semidilute solution as a function of the ionic strength," Physical Review Letters 77, 5218 (1996).

[32] Appel, P., and J. T. Yang, "Helix-coil transition of poly-L-glutamic acid and poly-L-lysine in D2O," Biochemistry 4, 1244-1249 (1965).

[33] Li, H., B. Liu, X. Zhang, C. Gao, J. Shen, G. Zou, "Single-molecule force spectroscopy on poly (acrylic acid) by AFM," Langmuir 15, 2120-2124 (1999).

[34] Taylor, T. J., and S. S. Stivala, "Small-angle X-ray scattering study of a weak polyelectrolyte in water," Journal of Polymer Science Part B: Polymer Physics 41,1263-1272 (2003).

[35] Sauvage, E., D. A. Amos, B. Antalek, K. M. Schroeder, J. S. Tan, N. Plucktaveesak, and R. H. Colby, "Amphiphilic maleic acid-containing alternating copolymers—1. Dissociation behavior and compositions," Journal of Polymer Science Part B: Polymer Physics 42, 3571-3583 (2004).

[36] Hamad, F. G., Q. Chen, and R. H. Colby, "Linear Viscoelasticity and Swelling of Polyelectrolyte Complex Coacervates," Macromolecules 51, 5547-5555 (2018).

[37] Ortiz, C., and G. Hadziioannou, "Entropic elasticity of single polymer chains of poly (methacrylic acid) measured by atomic force microscopy," Macromolecules 32, 780-787 (1999).

[38] Delaney, K. T., and G. H. Fredrickson, "Theory of polyelectrolyte complexation—Complex coacervates are self-coacervates," The Journal of Chemical Physics 146, 224902 (2017).

[39] Priftis, D., N. Laugel, and M. Tirrell, "Thermodynamic characterization of polypeptide complex coacervation," Langmuir 28, 15947-15957 (2012).

[40] Michaels, A. S., "Polyelectrolyte Complexes," Ind. Eng. Chem. 57, 32-40 (1965).

[41] Markarian, M. Z., H. H. Hariri, A. Reisch, V. S. Urban, J. B. Schlenoff, "A Small-Angle Neutron Scattering Study of the Equilibrium Conformation of Polyelectrolytes in Stoichiometric Saloplastic Polyelectrolyte Complexes," Macromolecules 45, 1016−1024 (2012).

[42] Fares, H. M., Y. E. Ghoussoub, J. D. Delgado, J. Fu, V. S. Urban, J. B. Schlenoff, "Scattering Neutrons Along the Polyelectrolyte Complex/Coacervate Continuum," Macromolecules 51, 4945−4955 (2018).

[43] Akkaoui, K., M. Yang, Z. A. Digby, and J. B. Schlenoff, "Ultraviscosity in Entangled Polyelectrolyte Complexes and Coacervates," Macromolecules 53, 4234–4246 (2020).

[44] Overbeek, J. T. G., and M. J. Voorn, "Phase Separation in Polyelectrolyte Solutions. Theory of Complex Coacervation," Journal of Cellular and Comparative Physiology 49, 7-26 (1957).

[45] Lytle, T. K., and C. E. Sing, "Transfer Matrix Theory of Polymer Complex Coacervation," Soft Matter 13, 7001-7012 (2017).

[46] Colby, J. D., Viscoelastic Properties of Polymers, 3rd Ed. (John Wiley & Sons, New York, 1980).

[47] Graessley W. W., Polymeric Liquids & Networks: Dynamics and Rheology (Tayor & Francis Group, New York, 2008), p. 146.

[48] Dealy, J.M., D. J. Read, and R. G. Larson, Structure and Rheology of Molten Polymers: from Structure to Flow and Back Again, 2nd Ed (Hanser, Cincinatti, 2018), pp. 265-266.

[49] Colby, R. H., "Breakdown of time-temperature superposition in miscible polymer blends," Polymer 30, 1275-1278 (1989).

[50] Syed. V. M. S., and S. Srivastava, "Time–Ionic Strength Superposition: A Unified Description of Chain Relaxation Dynamics in Polyelectrolyte Complexes," ACS Macro Letters 9, 1067-1073(2020).

[51] Liu, Y., C. F. Santa Chalarca, R. N. Carmean, R. A. Olson, J. Madinya, B. S. Sumerlin, C. E. Sing, T. Emrick, and S. L. Perry, "Effect of Polymer Chemistry on the Linear Viscoelasticity of Complex Coacervates," Macromolecules 53, 7851-7864 (2020).

[52] Tekaat, M., D. Bütergerds, M. Schönhoff, A. Feryb, and C. Cramer, "Scaling properties of the shear modulus of polyelectrolyte complex coacervates: a time-pH superposition principle," Physical Chemistry Chemical Physics 17, 22552-22556 (2015).

[53] Ikegami, A., and N. Imai, "Precipitation of Polyelectrolytes by Salts," Journal of Polymer Science 56, 133-152 (1962).

[54] Suarez-Martinez, P. C., P. Batys, M. Sammalkorpi, and J. L. Lutkenhaus, "Time–Temperature and Time–Water Superposition Principles Applied to Poly (allylamine)/Poly (acrylic acid) Complexes," Macromolecules 52, 3066-3074 (2019).

[55] Zhang, Y., P. Batys, J.T. O'Neal, F. Li, M. Sammalkorpi, and J. L. Lutkenhaus, "Molecular Origin of the Glass Transition in Polyelectrolyte Assemblies," ACS Central Science 4, 638−644 (2018).

[56] Zhang, R., Y. Zhang, H.S. Antila, J L. Lutkenhaus, and M. Sammalkorpi, "Role of Salt and Water in the Plasticization of PDAC/PSS Polyelectrolyte Assemblies," J. Phys. Chem. B 121, 322−333 (2017).

[57] Batys, P., Y. Zhang, J. L. Lutkenhaus, and M. Sammalkorpi, "Hydration and Temperature Response of Water Mobility in Poly(diallyldimethylammonium)−Poly (sodium 4-styrenesulfonate) Complexes," Macromolecules 51, 8268−8277 (2018).

[58] Batys, P., S. Kivisto, S. M. Lalwani, J. L. Lutkenhaus, and M. Sammalkorpi, "Comparing water-mediated hydrogen-bonding in different polyelectrolyte complexes," Soft Matter 15, 7823—7831 (2019).

[59] Sadman, K., Q. Wang, Y. Chen, B. Keshavarz, A. Jiang, and K. R. Shull, "Influence of hydrophobicity on polyelectrolyte complexation," Macromolecules 50, 9417-9426 (2017).

[60] Huang, J., F. J. Morin, and J. E. Laaser, "Charge-density-dominated phase behavior and viscoelasticity of polyelectrolyte complex coacervates," Macromolecules 52, 4957-4967 (2019).

[61] Liu, Y., B. Momani, H. H. Winter, and S. L. Perry, "Rheological characterization of liquid-to-solid transitions in bulk polyelectrolyte complexes," Soft Matter 13, 7332-7340 (2017).

[62] Ali, S., and V. M. Prabhu, “Relaxation Behavior by Time-Salt and Time-Temperature Superpositions of Polyelectrolyte Complexes from Coacervate to Precipitate,” Gels 4(1), 11 (2018).

[63] Shamoun, R. F., H. H. Hariri, R. A. Ghostine, and J. B. Schlenoff, “Thermal Transformations in Extruded Saloplastic Polyelectrolyte Complexes,” Macromolecules 45, 9759−9767 (2012).

[64] Ghostine, R. A., R. F. Shamoun, and J. B. Schlenoff, “Doping and Diffusion in an Extruded Saloplastic Polyelectrolyte Complex,” Macromolecules 46, 4089−4094 (2013).

[65] Ghasemi, M., S. Friedowitz, and R.G. Larson, “Analysis of Partitioning of Salt Through Doping of Polyelectrolyte Complex Coacervates,” Macromolecules 53, 6928–6945 (2020).

[66] Andreev, M., V. M. Prabhu, J. F. Douglas, M. Tirrell, and J. J. de Pablo, “Complex coacervation in polyelectrolytes from a coarse-grained model,” Macromolecules 51, 6717-6723 (2018).

[67] Tan, H., A. Moet, A. Hiltner, and E. Baer, “Thermoreversible gelation of atactic polystyrene solutions,” Macromolecules 16, 28-34 (1983).

[68] Tanaka, F., W.H. Stockmayer, “Thermoreversible gelation with junctions of variable multiplicity,” Macromolecules 27, 3943-3954 (1994).

Chapter 4

Low-Frequency Elastic Plateau in Linear Viscoelasticity of Polyelectrolyte Coacervates

4.1 Abstract

A thorough study is made of the dependences on salt concentration and polymer chain lengths of the low-frequency plateau of coacervates of poly (diallyl dimethyl ammonium chloride), PDADMAC, and poly (sodium 4-styrenesulfonate), PSS. The reliability and reproducibility of these measurements are carefully checked by determining the frequency-dependent stress limits of the rheometer through use of reference fluids, and by repeat experiments with coacervates. Long-time frequency sweeps show that coacervates with less salt are more repeatable than those with higher salt. A low-frequency plateau only reliably appears below a critical salt concentration, and the magnitude of the plateau depends strongly on salt concentration and on chain lengths of both polycation and polyanion. It is only present for molecular weight of the PDADMAC polycation higher than 100kDa, but the magnitude of plateau is more strongly influenced by the chain length of the polyanion, PSS. Possible causes of the low-frequency plateau are discussed. The contents of this chapter are the results of collaborative work with graduate student Huiling Li.

4.2 Introduction

Polyelectrolyte coacervates (PECs), which are polymer-rich phases formed by mixing oppositely charged polyelectrolyte solutions, are increasingly applied in coatings, water treatment, personal care products, drug delivery, and other applications [1-4]. Nevertheless, fundamental understanding of coacervate physical properties, micro-structure, and rheology remains limited [5]. While the pace of measurements of the rheology of coacervates has rapidly increased in recent years [6], clear trends are generally found only within a limited set of materials, and typically only within a given laboratory, with little lab-to-lab cross comparisons of data for the same materials. In particular, some coacervate measurements show “liquid-like” terminal behavior at low

frequency [7-8], while others show a "gel-like" behavior [9-14]. At low frequency, the latter are characterized by a plateau or near plateau in G' while the former shows a steep decrease in G' with power-law exponent near the expected "terminal" value of 2, or at least greater than 1. The "gel-like" modulus is often very low (i.e., < 1 Pa), however, leading authors to question whether it lies outside of various sources of error, e.g., the minimum torque, the precision of the phase angle measurement, etc. [9]. In other cases, the plateau is much more prominent and salt-concentration and salt-type dependent [13-14]. In addition, the measurements are typically made on samples extracted following phase separation, wherein a supernatant liquid is removed after mixing, centrifugation, and waiting for equilibration of phase separation. The time periods involved in these steps are often not given, and the order of mixing, when its effect is investigated, is sometimes found to be important [15]. In addition, the samples contain water, making them prone to evaporation or other "aging effects," in addition to possible effects on measurement reproducibility of the rheometer-loading procedure, such as variations in how the sample is pressed into the gap, and how it is trimmed. Careful checks of measurement reproducibility are rarely reported. In addition, most studies are carried out on commercial samples of high or unknown polydispersity. In these ways and more, it is fair to say that rheological studies on polyelectrolyte coacervates are often "not up to the standards" of rheological studies of more conventional polymers, or of single polyelectrolytes.

While we cannot address all of these issues here, we do propose to study in some detail the limits of rheometer accuracy, reproducibility, and robustness with respect to sample mixing, duration of rheological tests, and repeat measurements of the same loaded samples, different sample loadings, repeated sample preparations, and repeated measurements in different laboratories. We find that while typical rheometric methods have been sufficient to establish some generally valid trends already presented in the literature, many samples we report on here show unusual behavior and limited reproducibility that, if not overcome, limit precise comparisons of data on different samples and from different labs. This is especially true of samples that produce low-frequency "gel-like" plateaus. Since these samples are by definition solids, it is perhaps not surprising that such samples are slow to equilibrate and sensitive to preparation conditions.

The polyelectrolyte samples that we chose for this study are ones that are easily available commercially and widely used in previous studies, that have been found to produce a low-frequency plateau under some conditions of salt and molecular weight [14], namely poly (sodium

4-styrenesulfonate) (PSS) and poly (diallyl dimethyl ammonium chloride) (PDADMAC). We note that given the number of samples and repeat runs we made here, we have chosen not to focus on possible issues related to sample polydispersity or purification. Once work establishing "best practices" and pitfalls of coacervate preparation and measurement are addressed, important issues of polyelectrolyte molecular weight distribution, and quality of synthesis, purification, and characterization should be addressed. We simply note here that any problems related to these latter factors in our work is common to the field at large and to most published papers in the area.

4.3 Materials and Methods

4.3.1 Materials

Poly (sodium 4-styrenesulfonate) solutions (PSS) having molecular weights (MWs) of 70kDa (20wt% in water) and 200kDa (30wt% in water), as well as solutions of poly (diallyl dimethyl ammonium chloride) (PDADMAC) with MW <100kDa (35wt% in water), MW 200-350kDa (20wt% in water) and MW 400-500kDa (20wt% in water), were purchased from Sigma-Aldrich. Another less polydisperse PSS (PDI=1.19) was purchased from Scientific Polymer Products, Inc. with MW of 2242kDa in powder state. The molecular weight ranges mentioned above are given by the suppliers. For convenience, we will refer to the PDADMAC materials as "100kDa," "200kDa," and "400kDa," samples, respectively. The materials were used, as has been common, without further purification or characterization. These polyelectrolytes with concentrations of 35 wt%, 30 wt% and 20 wt% in water were diluted to make stock solutions with monomer molar concentrations of 2M, 1.6M and 1.2M, respectively. PSS with MW 2242kDa was prepared at 0.4mol/L by dissolving the powder in water. NaCl stock solutions (5M) were prepared by dissolving crystalline NaCl (Sigma-Aldrich) into water at 25 °C. All water was filtered through a Milli-Q water purification system (Thermo Scientific, MicroPure UV/UF) producing water with a resistivity of 18.1 MΩ·cm at 25 °C.

4.3.2 Coacervate Preparation

PECs were formed by mixing cationic and anionic stock solutions at a 1:1 stoichiometric ratio of monomer repeat units with salt solutions, as shown in Scheme 1. Concentrations and volumes were

chosen to achieve overall polycation and polyanion monomer concentrations of 0.1M each (0.2M total monomer concentration) in the final mixture (but before phase separation). To accomplish this, first, a NaCl stock solution and water were added into an empty centrifuge tube, with volume ratio chosen to achieve the desired final overall salt concentration. This was followed by addition of stock solutions of polyanion, PSS, and of polycation, PDADMAC, respectively. The mixtures were vortexed for 30 seconds after each addition of water, polyanion stock solution, and polycation stock solution, respectively. Note that the mass of the polymer added can vary from the desired value by around -1.3% to 0.5% for PDADMAC and -3.5% to 5.7% for PSS because of limitations in pipetting, including some retention of polymer inside the pipette tips or extra drops clinging to the outside of tips. The final sample (typically 4.8 ml or 48 ml) was centrifuged for 15 minutes at 8,000g (Thermo Scientific, SORALL Legend X1R) after which the sample was left undisturbed for at least five days, long enough that the solution ceased to show any further changes in phase separation or appearance. After this, the supernatant phase was removed, leaving only the coacervate for rheological characterization and storage. Evaporation of water from the sample was minimized by sealing the tube with parafilm tape. Shortly after the supernatant removed, a very thin layer of water would sometimes appear on top of the coacervate phase (usually in the samples with high salt concentration), which though visible is difficult to be removed by pipette due to its tiny amount.

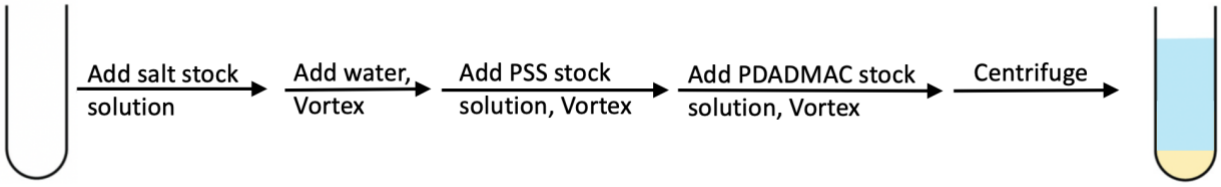

Scheme 1. Preparation process for PDADMAC/PSS/NaCl coacervates

4.3.3 Rheology

All rheology tests were performed on an Anton Paar MCR 702 rheometer using a stress-controlled motor at 20°C. Since some PDADMAC/PSS coacervates are quite stiff, solid-like, gels, a fixture with diameter of 25mm (cone angle 2°) was usually used, rather than cones with larger diameter or cone angle, to avoid high normal stress during setting of the gap, and because of limited coacervate supply. In addition, samples with PDADMAC MW = 400kDa, and PSS MW= 200kDa

containing 2.8M and 3M NaCl, were even stiffer and could not be compressed to the desired gap even with the small-angle 25mm cone; for these, parallel plates with 25mm diameter were used. To minimize evaporation of water within PEC samples during long-time tests, the rheometer Peltier hood was employed and water was used to seal the solvent trap around the bottom plate. The temperature for all measurements was set at 20°C by the Peltier plate and hood setup. Strain sweeps were performed at 0.01, 10, 100 and 628 rad/s to identify the linear viscoelastic region (LVE) of the PEC. Long frequency sweeps were conducted at fixed strains (1%, discussed below) from 628 rad/s to 0.001 rad/s or oppositely, from low to high frequencies.

4.4 Results and discussion

4.4.1 Rheometer Limitations

It is a challenge especially for low-viscosity liquids or soft solids to probe their stress with high resolution at either extremely low frequencies or at the highest frequencies allowed by the rheometer during oscillatory measurements. Thus, the low values of the modulus plateau, around 0.1Pa or even lower, sometimes reported in the low-frequency region of the oscillatory shear of coacervates [9-12], are of questionable accuracy. Theoretically, the lower limit of the modulus, measured in the cone and plate geometry can be calculated from equation (1) given the minimal oscillation torque of 0.5 nNm specified for the Anton Paar MCR702 rheometer. When the strain amplitude is set at 1% (γ= 0.01), the Glower limit is computed to be around 0.016Pa for a cone and plate diameter of 25mm. In the high frequency region, the instrument inertia in the combined motor transducer (CMT) can lead to a measured frequency response of $G' \sim G'' \sim \omega^2$ for weakly elastic materials.

$$G_{\text{lower limit}} = \frac{2*\text{torque}}{\pi*R^3*\gamma} \approx \frac{1.6\times10^{-4}}{\gamma} \text{ (Pa) if R} = 12.5\text{mm} \quad (4\text{-}1)$$

Although the torque limit and the system inertia can in principle be obtained from well-known formulas, other effects, such as surface-tension and other edge effects [16], calibrations, instrument vibrations, sample-loading effects (especially pertinent for soft solids), are difficult to be precisely predicted. These unclear sources of error lead to errors in moduli plateau that can be an order of

magnitude greater than the theoretical torque limit. Thus, here we seek an empirical threshold for the polyelectrolyte solutions based on the experimental results of several reference fluids, including two low-viscosity liquids, namely water and a viscosity-standard oil (APS3, Anton Paar), a viscoelastic single-polyelectrolyte solution PSS (MW=2242kDa, PDI=1.19), and a PDMS reference viscoelastic fluid (AK 1 Million) (see Fig. 4-1). Because the limited volumes of coacervate samples restricted the rheometer fixtures to 25-mm diameter, all measurements on reference fluids presented in the main text were performed on the same small cone and plate at 1% strain amplitude using the CMT transducer, and therefore rheometer limitations established here only apply to this situation. Of course, higher accuracy and lower stress thresholds in frequency sweep tests can be achieved by using larger plates and/or higher strain amplitudes, as seen in Fig. 4-2 for measurements of air with a 50mm plate and in Fig. 4-1 for measurements of standard mineral oil, APS3, with dynamic strain amplitudes.

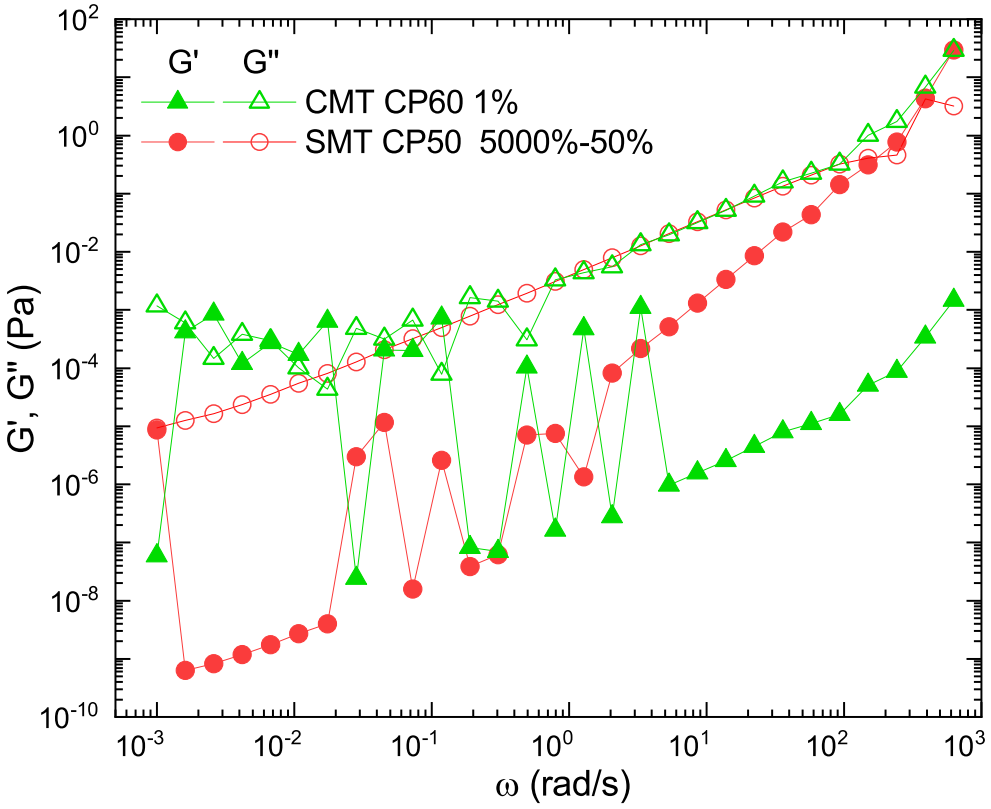

Figure 4-1. Storage (G') and loss (G'') moduli as functions of frequency obtained from the oscillatory measurement of standard oil (APS3, 3mPa·s) using cone and plate with 60mm diameter at 1% strain for the CMT (combined motor transducer) and with strain amplitude ranging from 50% at high frequency to 5000% at low frequency for the SMT (separate motor transducer). Both measurements were performed in the Shetty Lab. Data shows the expected viscous dominated response for the oil over the frequency sweep when using SMT. Noisy moduli values seen in the CMT mode at low frequencies are because torques are close to the resolution limit of the rheometer.

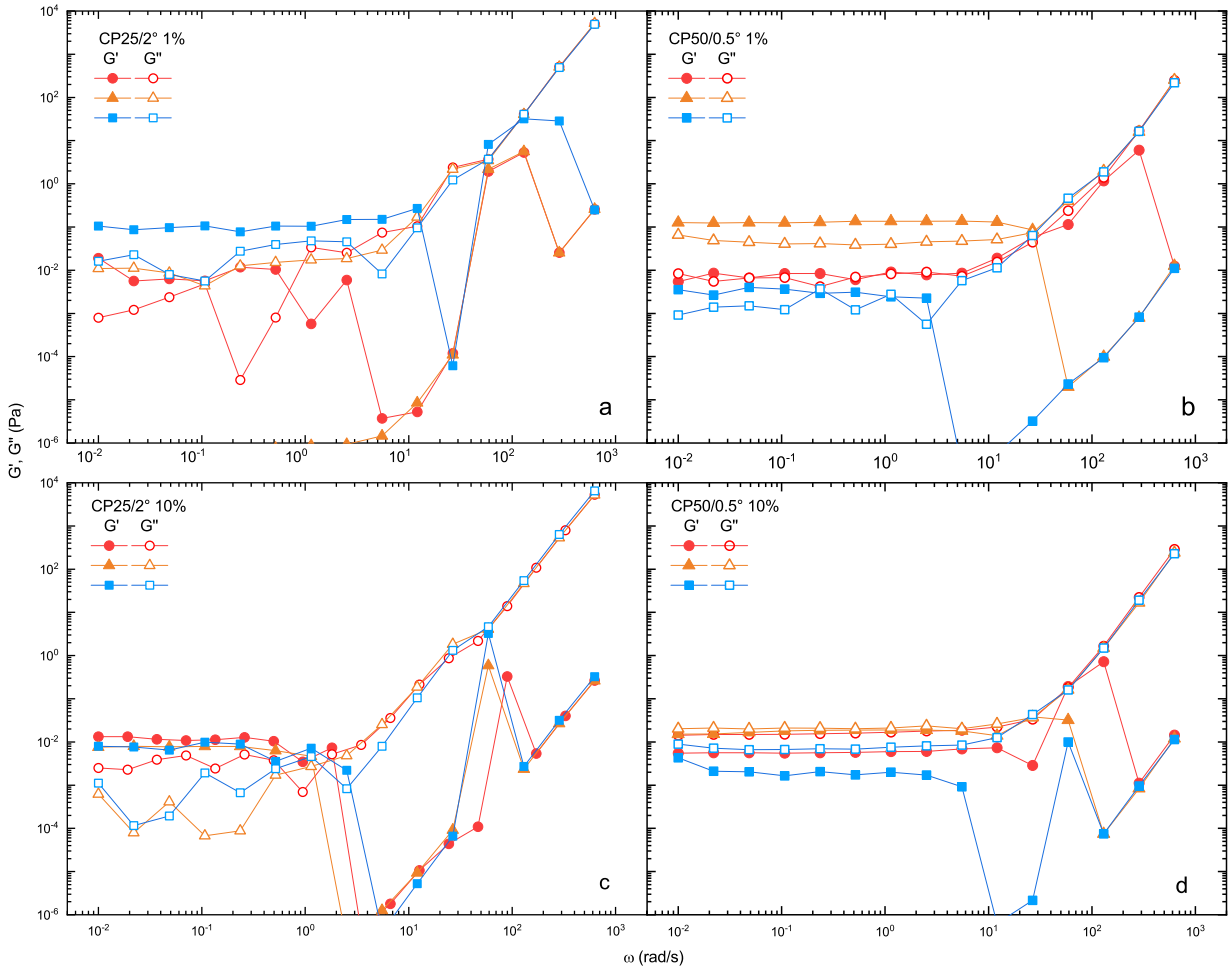

Figure 4-2. Repeat oscillatory measurements of air on (a, c) CP25 and (b, d) CP50 at (a, b) 1% and (c, d) 10% amplitude. Increasing the strain amplitude from 1% to 10% can reduce the noise level of the G' plateau from around 0.1Pa to 0.01Pa for either a 25mm or a 50mm cone-and-plate.

In Fig. 4-3a, three repeat frequency sweeps of water yield G' data roughly following a "plateau" at values up to around 0.2 Pa, over frequencies ranging from 0.01 rad/s to 10 rad/s. These values are ascribable to the instrumental limitations since only noise is expected for G' measurements of water. Note that as frequency increases above around 10 rad/s, power-law increases in G' and of G'' are found, (albeit with several G' data points dramatically lower) which are likely the result of inertia effects on the measurement in the CMT mode because the phase angles of those data points were reported as exactly 90°, which is the value the instrument reports when the angle exceeds 90°, as is expected for data dominated by inertial effects. In addition to the phase angle, the ratio of the sample torque over the electric torque was found to be less than

2%, mostly less than 1%, at high frequency, which also implies that inertia has a strong effect on these measurements. The oscillatory shear data of the viscosity-standard oil (3mPa·s at 20^{o}), which should also have no elastic response, are found in Fig. 4-3b to be similar to that of water, with approximate plateau values G' up to around 0.1Pa. We note that measurements of this same fluid, in larger fixtures at higher amplitudes and a more precise transducer, produce a measurable viscoelastic response, given in Fig. 4-1, that is below the limits established in Figs. 4-3(a, b). Thus, the data points in Fig. 4-3(a, b) are unreliable, as also shown by their lack of reproducibility in repeat runs. Hence, to exclude all noisy and unreliable data, we assign in Fig. 4-3 empirical thresholds for acceptable rheological measurements on the rheometer with CP25 fixtures. These limits are shown as a dashed horizontal line with magnitude 0.3Pa in the low ω region, and a diagonal line with power-law slope around 2.5 in the high ω region. These baselines are further confirmed by the single-component PSS polyelectrolyte solution, which is also observed to have a G' plateau of 0.01~0.1Pa in Fig. 4-3c, contradicting to the literature observation [17], that shows no evidence of a G' plateau for measurements of a similar PSS solution using a large, 60mm diameter, plate. The remaining data points, which are above the threshold lines in Fig. 4-3c, which are mostly G'' points, are comparable to the literature results of single PSS solutions (see Figure 4c in the Ref 17), and therefore deemed reliable.

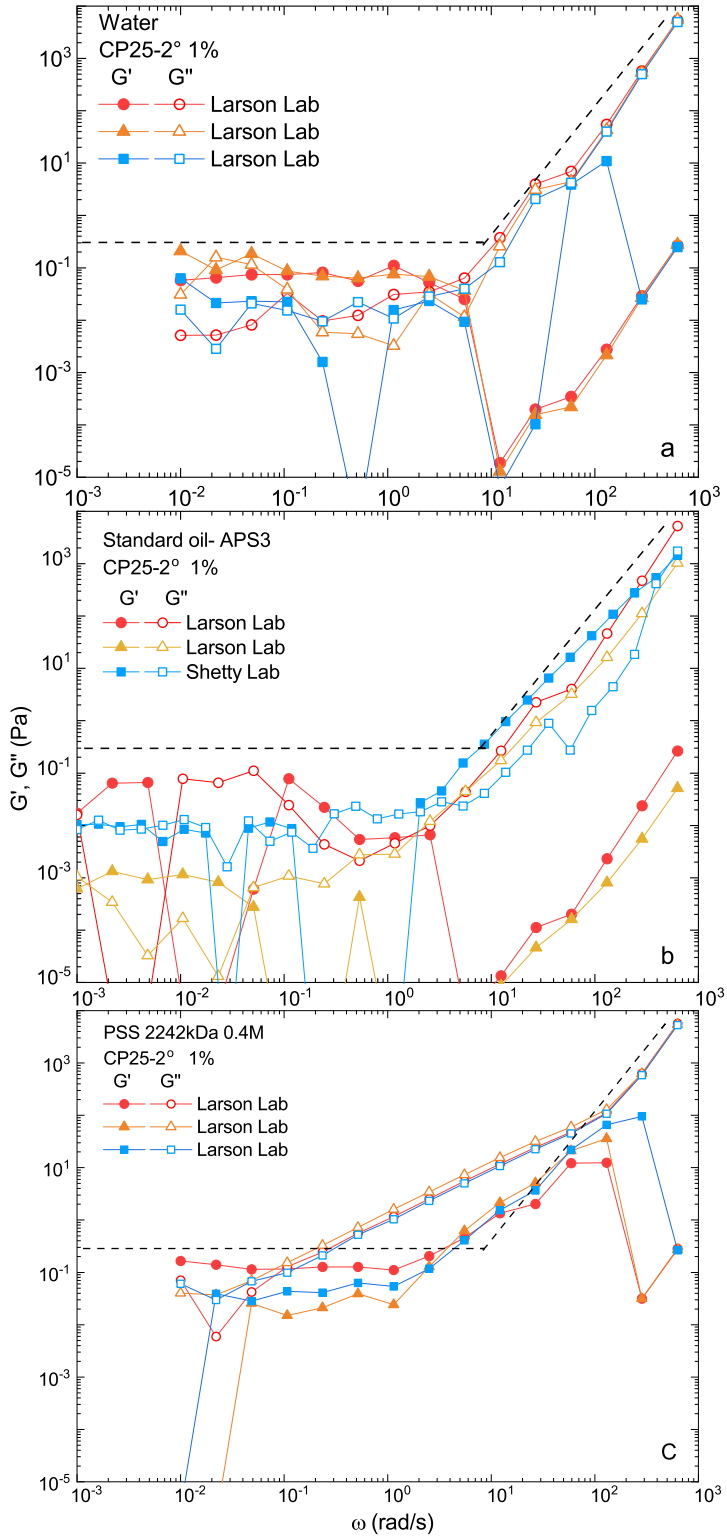

Figure 4-3. Storage (G', filled symbols) and loss (G'', open symbols) moduli as functions of oscillation frequency obtained from repeat measurements of (a) water, (b) standard oil (tested in two laboratories, and (c) polystyrene sulfonate (PSS) solution at an amplitude of 1% strain on identical cone and plate rheometers (Anton Paar Inc) with 25mm fixtures in the Larson and Shetty Labs. Dashed lines are drawn empirically, and identically for all fluids, to exclude data points that are judged unreliable for the standard fluids studied.

The fourth reference fluid, a standard viscoelastic PDMS solution (AK 1 Million, Wacker) yielded typical power-law slopes of G' and G'' in an oscillatory measurement at 1% and 10% strain on a parallel plate with 25mm diameter, as shown in Fig. 4-4, with G' reaching 0.03 Pa at 0.01rad/s below which data become noisy. This is below our cut-off of 0.3 Pa, and close to the theoretical limit of 0.016Pa at 1% strain, indicating that the practical threshold can be sensitive to the materials used, for example, the phase angle at low frequencies as well as the ambient vibrations and other factors.

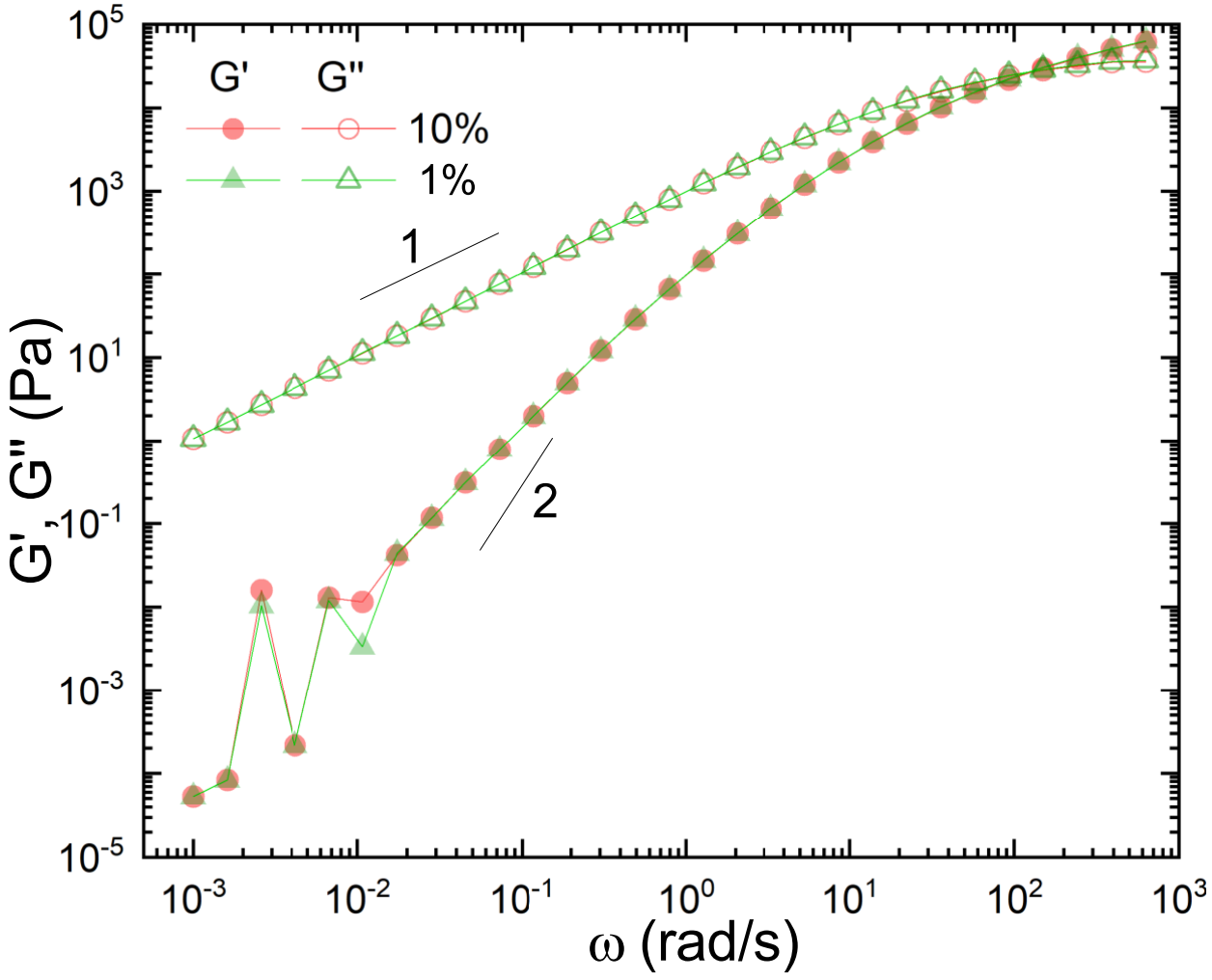

Figure 4-4. Linear shear moduli of standard viscoelastic solution of PDMS with a kinematic viscosity of approx. 1000000 mm²/s (known as "AK 1 Million"), and dynamic viscosity of roughly 103 Pas, as function of frequency tested in Shetty lab (Anton Paar Inc.) on parallel plates with diameter 25mm at 1% and 10% strain amplitude.

4.4.2 Sample Limitations

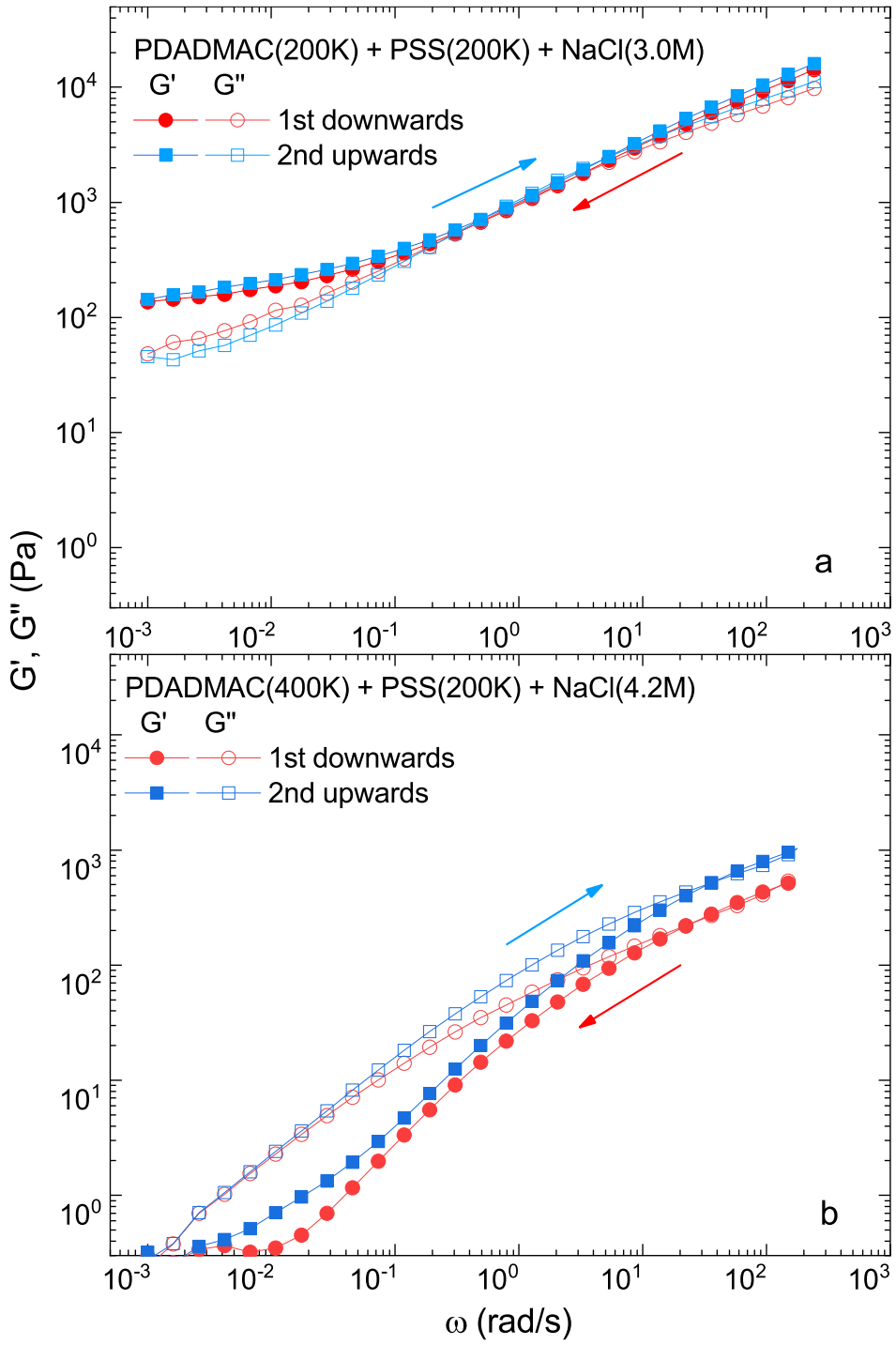

Figure 4-5. Downward and upward frequency sweeps on coacervates of the same loading. Compositions are shown in the legends. Salt concentration refers to the overall concentration before phase separation. Data points below the threshold, 0.3Pa, are omitted for clarity.

In a frequency sweep, the rheological test time increases inversely with the lowest frequency attained. Around 4 hours are required for a sweep from 628rad/s to 0.001rad/s at three points per decade, and 6 hours at five points per decade. Such a measurement duration raises questions about sample constancy and test reproducibility. In Fig. 4-5, samples went through a downward frequency sweep and then an upward sweep with no waiting time between the two runs, taking 12 hours in total. We observe, in this test, that coacervates with less salt, such as the sample with 3M NaCl, were more reproducible than those with more salt, 4.2M, and are not as much affected by the frequency-sweep history. Note that salt concentrations mentioned in this paper refer to the designed salt concentration in the final mixtures before phase separation and the exact salt concentration in coacervate phase could differ from this [18-19]. We note that the more liquid-like coacervates, produced by a higher salt concentration seen in Fig. 4-5b, seem to be more prone to increasing modulus with the time, especially in the high-frequency region. Although we did not observe any direct evidence of it, we cannot rule out that this increased modulus could be the result of water evaporation due to the long time required for obtaining data at low frequencies. We did, however, use a hood to block evaporation and checked for slow changes in modulus by repeating some of the frequency sweeps on the same loading on other coacervate samples, as shown in Fig. 4-6, and found only small changes for most results between the first frequency sweep and the second repeated one.

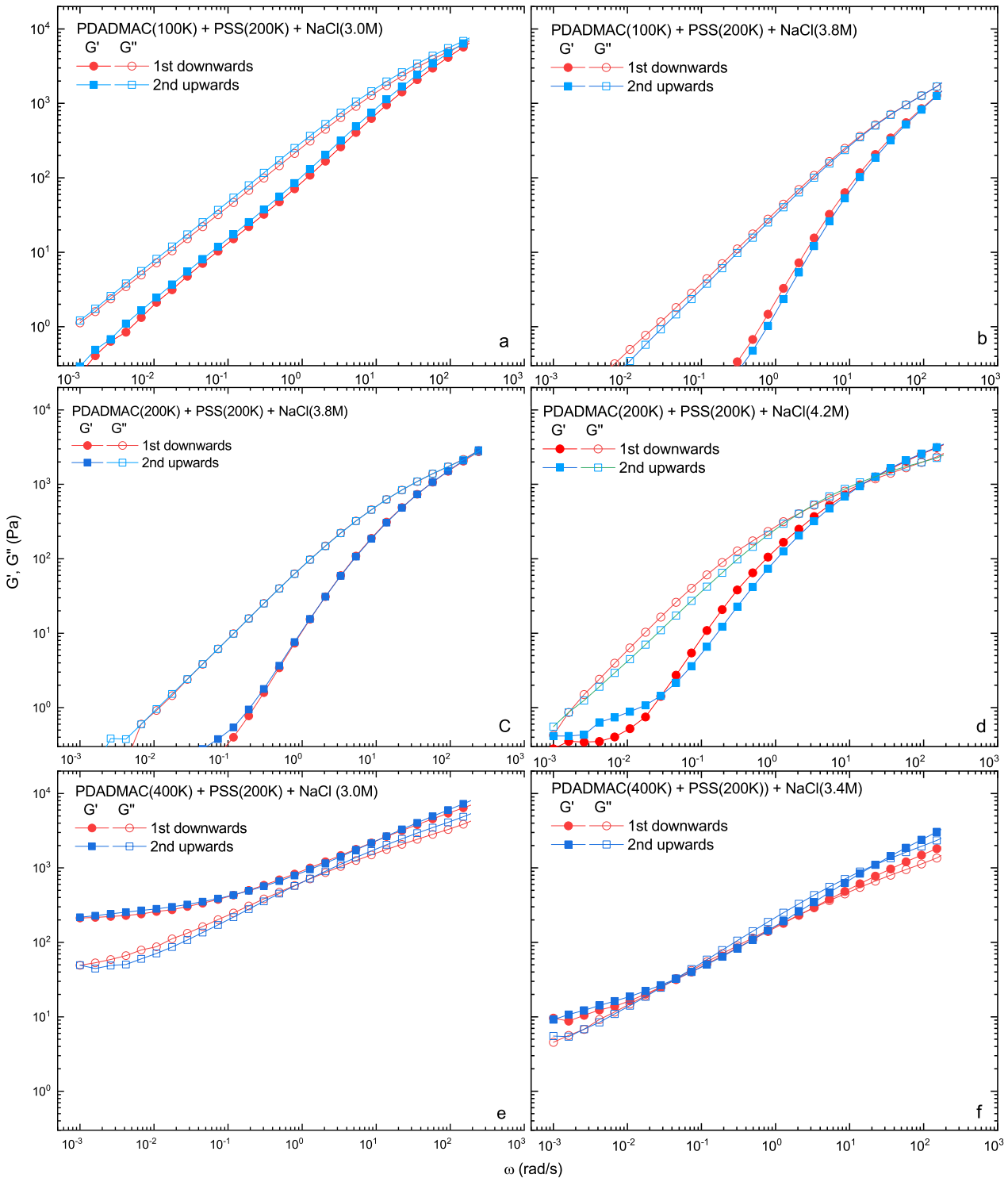

Figure 4-6. Downward and upward frequency sweeps on coacervates (compositions shown in the legend) of the same loading. Samples went through a downward sweep first followed by an upward sweep over a total of 12 hours.

Fig. 4-7 tests the reproducibility against aging of coacervate samples loaded and tested on different dates but identical testing conditions. Coacervates derived from mixtures with a total salt concentration of 3.4M report almost same rheological behaviors even after two-month storage of the sample, shown in Fig. 4-7(a) and (c), while samples prepared with the highest overall salt concentration, 4.2M, exhibited a considerable increase in moduli and change in the shape of the rheological curves. This time sensitivity is probably affected by the hydration level inside the coacervates. Long-time storage could lead either to slow phase equilibrium or, more likely, to some evaporation of water, which can be detected by increased moduli. Thus, there is incentive to finish rheological measurements quickly after sample preparation to minimize changes in hydration level during experiments. Note that in Fig. 4-5(b) and Fig. 4-7 (d), there are storage moduli showing a short plateau window around the threshold, 0.3Pa, at frequencies lower than 0.05 rad/s. These plateaus are doubtful and probably experimental artifacts since they are close to the noise level and thus not taken as low-frequency plateaus. Apart from the above caveats, our investigation of batch-to-batch and lab-to-lab reproducibility of coacervates, seen in Fig. 4-8, reveal quite repeatable measurements not only for liquid-like coacervates but also for gel-like ones, which further demonstrates the reasonable accuracy and reproducibility of our experiments.

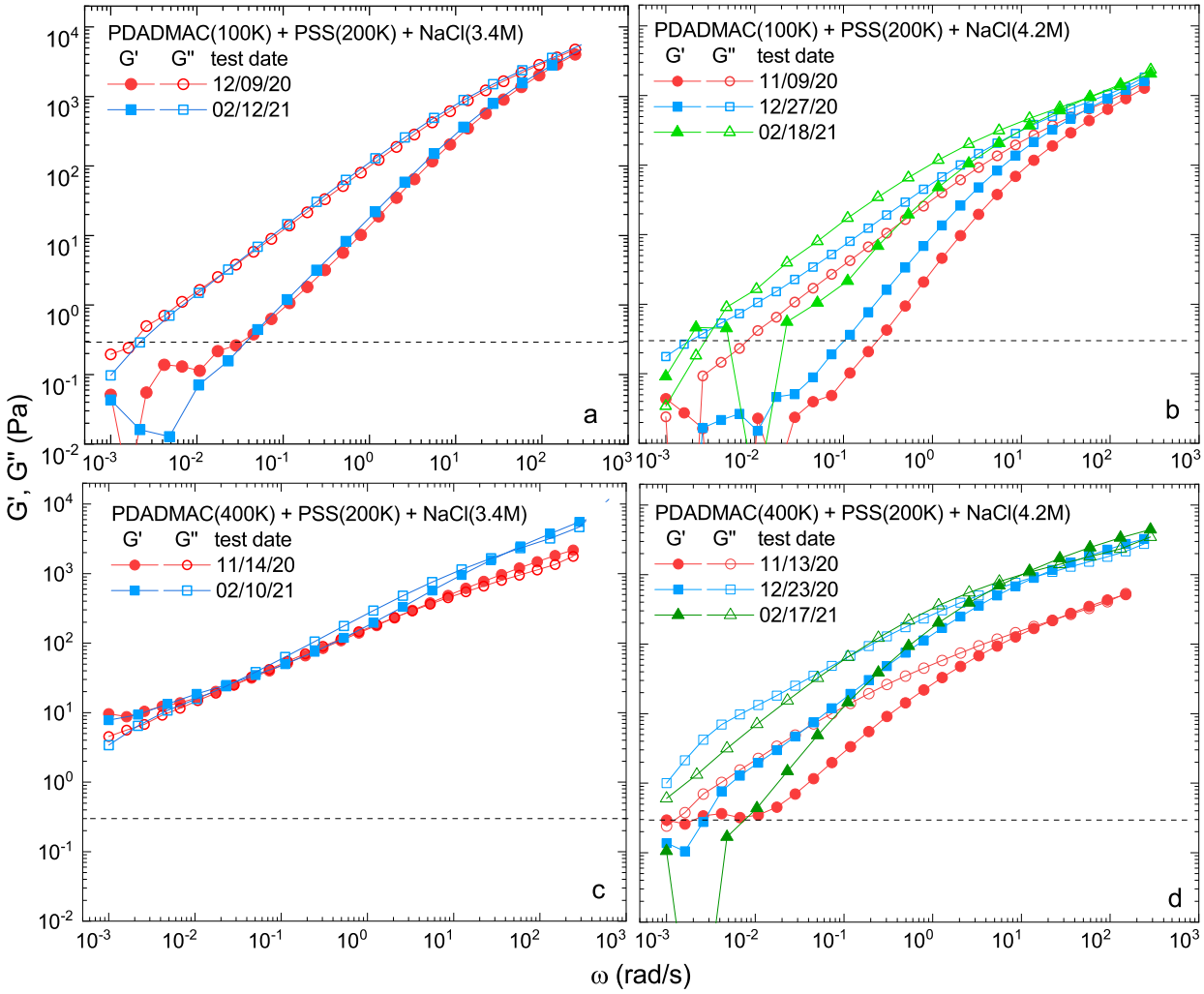

Figure 4-7. Frequency sweep curves of PDADMAC/PSS complexes on different dates with the same PSS chain length (200kDa) but different molecular weight of PDADMAC: (a, b) 100kDa and (c, d) 400kDa. The overall salt concentrations of samples are given in the legend. Any data below the dash line (0.3Pa) is not reliable.

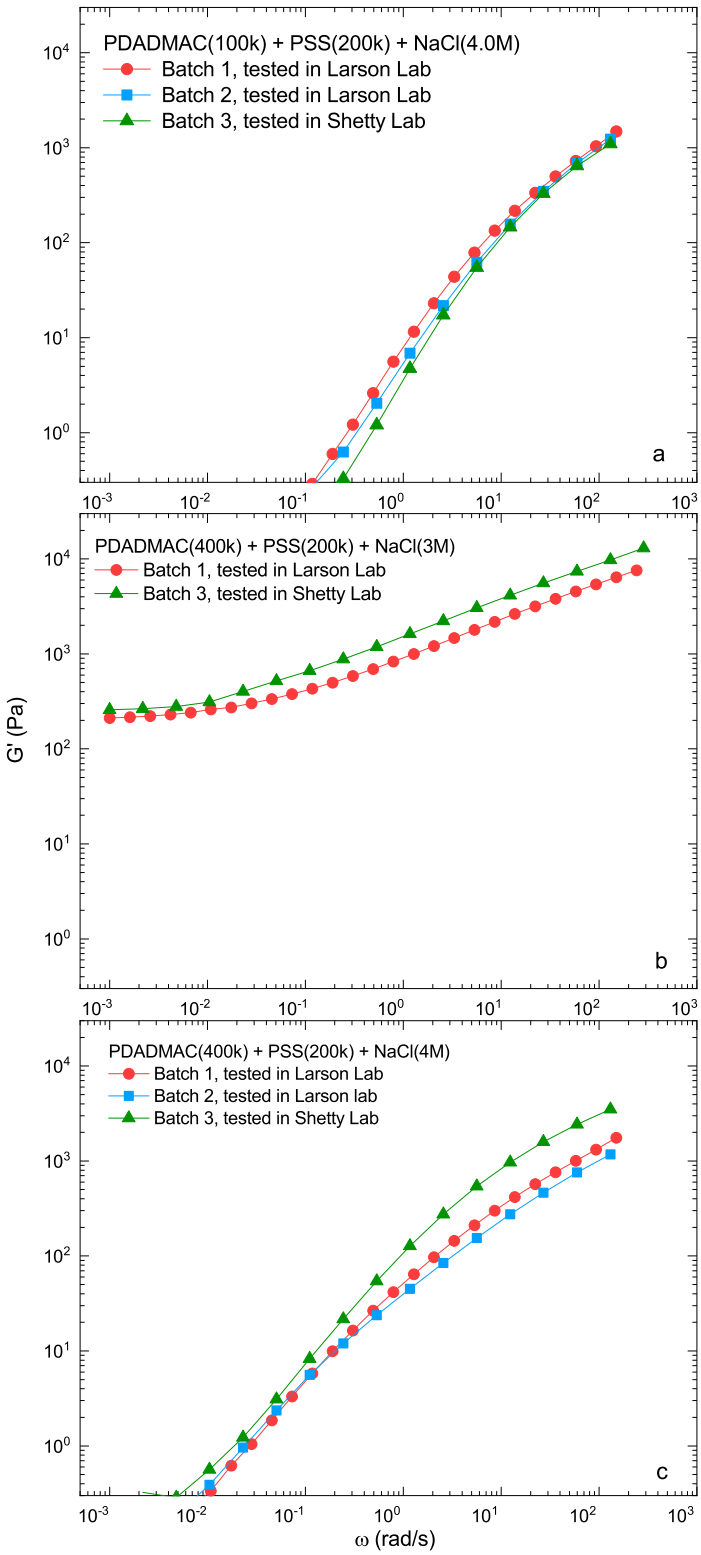

Figure 4-8. Batch-to-batch linear viscoelastic reproducibility of coacervates measured in two different laboratories. Samples from Batch 2 and 3 were prepared through the same stock solutions at the same time, while batch 1 was from earlier stock solutions and prepared six months earlier. Data points below the threshold for reliability, 0.3Pa, are omitted.

4.4.3 Region of Linear Viscoelasticity of Coacervates

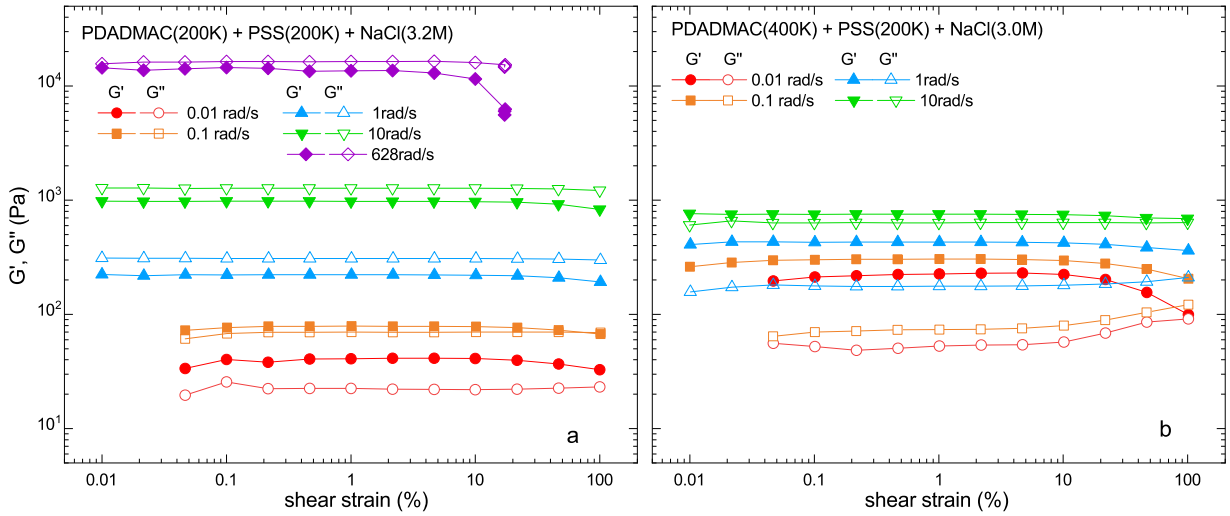

Figure 4-9. Strain sweeps from 0.01% to 100% of polyelectrolyte coacervates at frequencies of 0.01, 0.1, 1, 10, and 628 rad/s. Sample compositions are given in the legends.

The linear rheological values of G' and G'' in oscillatory shearing can only be obtained within the "small-strain" limit, which can be unusually small for polymer gels [20]. The linear viscoelastic region (LVE) is often confirmed by performing strain sweeps at various frequencies, e.g., 1rad/s or 10rad/s. In most cases, the linear region obtained from one or two frequencies is assumed to apply across the whole range of frequencies. However, more caution is required for samples showing gel-like behavior over some frequency range. In Fig. 4-9a, it is seen that at frequencies lower than 10 rad/s, the linear region reaches up to 20%, but fails at 10% strain at 628rad/s. This is consistent with the typical behavior of viscoelastic materials, which show a smaller linear region at higher frequencies. Interestingly, Fig. 4-9b exhibits the opposite behavior in that a smaller range of linear behavior is observed at low frequencies, namely 0.01 and 0.1 rad/s, for which the moduli drop quickly when the strain is increased beyond 10%. Since the strain sensitivity not only limits the linear viscoelastic region, but may also indicate the possibility of strain-induced "damage" or long-lasting changes to coacervate structure, we choose 1% strain as a "safe" amplitude for all frequency sweep measurements discussed below. Such a small strain amplitude and plate diameter, however, limits the accuracy of instruments, especially at low frequencies, and helps set the threshold of 0.3Pa minimum modulus for our reported data.

4.4.4 Effects of Salt Concentration on Polyelectrolyte Complexes

In polyelectrolyte coacervates, salt is commonly treated as a "plasticizer" since it can increase hydration level and screen the electrostatic interactions between ion groups. Changing salt concentrations can shift the G' and G'' curves, while leaving their shape unaffected [7]. Thus, the principle of "time-salt superposition" has been used in the literature to shift curves at high salt concentration to lower frequencies and thereby expand the frequency range of the rheological data, based on the assumption that salt does not change the local relaxation mechanisms, but only adjusts their speed. Time-salt superposition has been verified in multiple polyelectrolyte systems [8, 21].

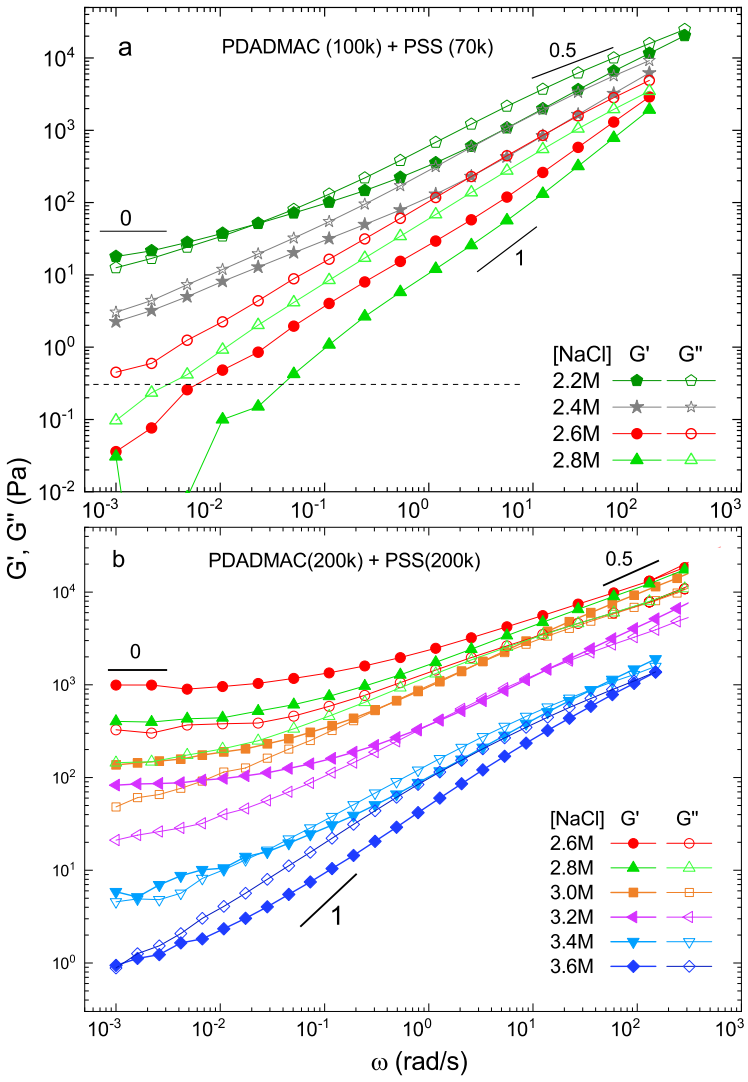

Figure 4-10. Linear viscoelastic curves for PDADMAC/PSS/NaCl coacervates of different molecular weights and salt concentrations, as given in the legends. In (a) the dashed line represents the empirical baseline 0.3Pa, below which the data are not reliable.

However, it has been reported recently that some frequency dependencies cannot be time-salt superposed, especially in the low-frequency region [14]. To study rheological behavior at longer timescales in the coacervate system (PDADMAC/PSS/NaCl), we extend oscillatory shear to a lower frequency than typical, namely down to $\omega = 0.001\, rad/s$, and avoid time-salt superposition. We thereby find in Fig. 4-10 that differences of the shape of the curves become larger at low frequencies, developing a flat region of G' for high molecular weights and lower salt concentrations in Fig. 4-10b. With salt concentration decreasing from 3.6M to 2.6M, in Fig. 4-10b the magnitudes of both G' and G'' increase, and G' is above G'' at all frequencies at the lowest salt concentration, 2.6M. The most notable feature in Fig. 4-10b is that coacervates with salt concentrations of 2.6M, 2.8M, 3.0M, and 3.2M show high storage moduli, ranging from 1000Pa to 100Pa, with relatively low sensitivity to frequency, across two decades of ω from 0.1rad/s to 0.001rad/s. The appearance of a near-plateau at the lowest frequencies indicates that the coacervate has changed to a gel-like material. At higher salt concentrations, 3.4M and 3.6M, in Fig. 4-10b, the coacervate exhibits no clear plateau, but instead an intermediate behavior between liquid-like and solid-like, with $G' \approx G'' \sim \omega^{0.5}$ over most of the frequency range, similar to what Ali & Prabhu reported [14] and similar to other observed gel transitions [22-23]. Here, it is possible that the curve with a slope of 0.5 represents a critical gel point, below which (at higher salt concentration) the coacervates are in the pre-gel regime, and above which (i.e., for less salt) samples are in solid-like gel state. However, the data above and below the transition cannot be separately superposed into two "master curves," one for the liquid and the other for the gel, as can sometimes be done for other gelling systems. We conclude from this that salt not only changes the local rate of chain motion, allowing for shape-independent shifting of G' and G'' curves, but can also produce a gradual structural transition from a liquid-like solution to a solid-like network as salt concentration decreases.

For the same PE system but for shorter chain length, shown in Fig. 4-10a, we did not observe a clear G' plateau at any frequency. However, the 2.2M sample presents fairly flat scaling, $G' \sim \omega^{0.2}$ as well as G' > G'', at low frequencies. It may be possible that a plateau region can be attained if ω could be extended to low enough values, but these are impractical to reach within the time scales we allow for our experiments.

4.4.5 Effects of Chain Length on Low-frequency Plateau

Fig. 4-10 indicates that polyelectrolyte chain lengths, as well as salt concentration, influences the transition to the solid gel state. To examine this in more detail, we prepared samples with different polycation molecular weights, namely 100kDa, 200kDa and 400kDa, and polyanion MWs of 70kDa and 200kDa, leading to six different combinations of the molecular weight of polyanion and polycation. Fig. 4-11(a, d) shows that plateaus are only definite when the chain length of PDADMAC is higher than 100kDa, namely 200kDa or 400kDa, no matter the chain length of PSS. But Fig. 4-11(b, c) shows that the plateaus do not disappear when the PSS MW is lower than 100kDa, namely 70kDa. This seems to indicate that the appearance of a gel-like structure is more dependent on the chain length of the polycation rather than polyanion for this system. Interestingly, the magnitude of the G' at plateau is much more affected by the chain length of the polyanion, PSS. This is shown in Fig. 4-11(b) and (c), where an increase in PDADMAC MW from 200kDa to 400kDa at a fixed salt concentration of 2.8M (green triangle symbols) or 3.0 M (orange square symbols) causes less than a doubling of the G' value, while in Fig. 4-11(b) and (e), at 2.6M NaCl, a five-fold increase in modulus occurs, from 200Pa to around 1000Pa, upon increase in PSS MW from 70kDa to 200kDa. This may indicate that the plateau value, once it exists, is more sensitive to PSS than to PDADMAC MW in this system.

The above observation does not seem to be general, and the opposite influence could be observed if different combinations of polyelectrolytes are chosen. For example, Spruijt and coworkers [8] found that the length of their polycation, PDMAEMA, affected the viscoelastic response more strongly than did their polyanion, while we showed that the length of our polyanion, PSS, has a significant effect on the value of modulus.

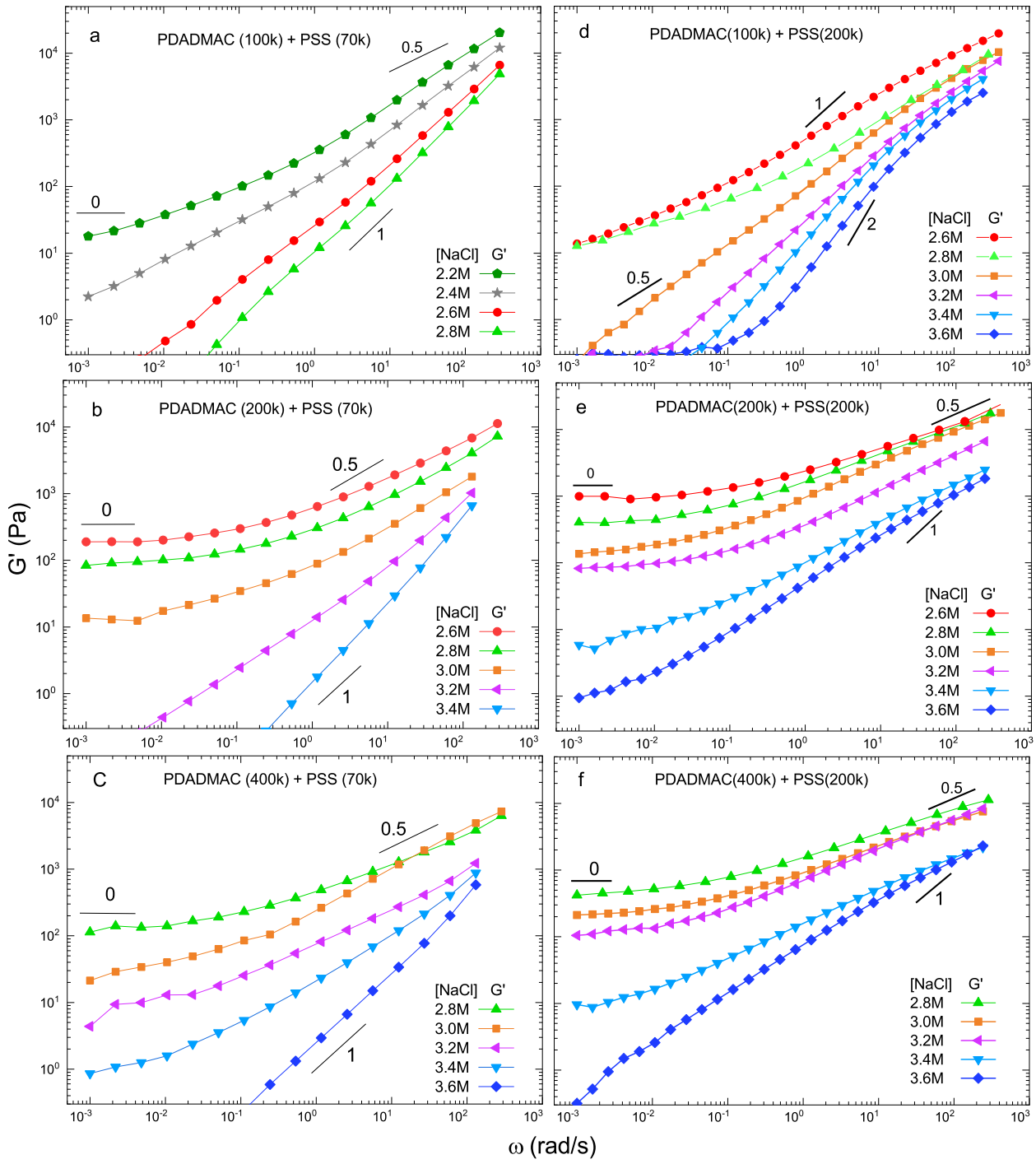

Figure 4-11. Storage moduli for six polyelectrolyte complexes composed of three chain lengths of PDADMAC with (a, d) MW=100kDa, (b, e) MW=200kDa, and (c, f) MW=400kDa, and two chain lengths of PSS with (a-c) MW=70kDa and (d-f) MW=200kDa for various NaCl concentrations, given in the legends. Loss moduli were not shown for the sake of clarity. Storage moduli below the reliability threshold of 0.3Pa were omitted.

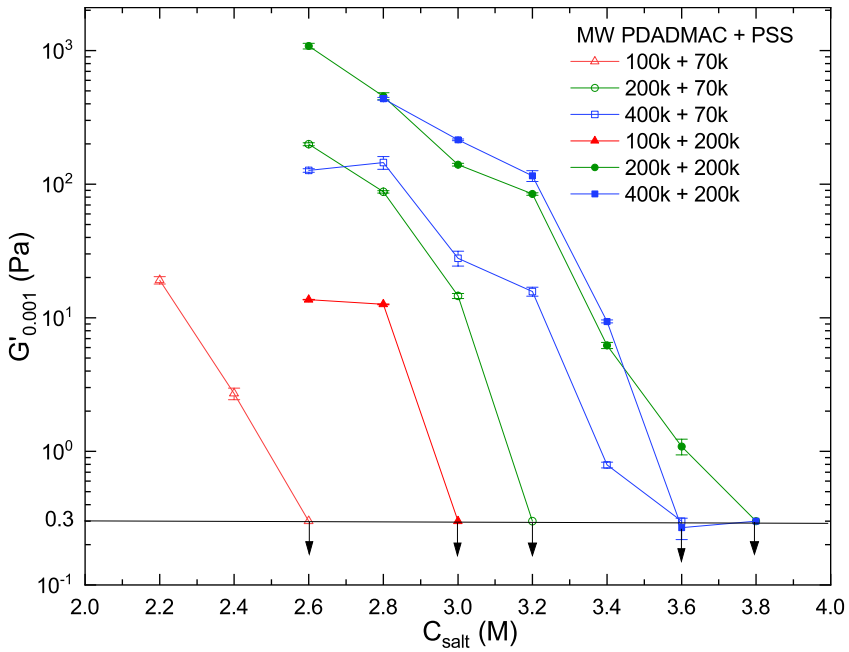

Figure 4-12. Comparison of storage moduli at the lowest frequency of 0.001rad/s as function of salt concentration for six sets of coacervates of different chain lengths, shown in the legend. The cutoff G' is 0.3Pa as discussed above, and so data below this threshold were indicated by a data point on this line and a downward-pointing arrow. Each error bar given was calculated from the repeat runs of long-time frequency sweep of the same loading within 12 hours. Some error bars are covered by the symbols.

Longer polyelectrolyte chain lengths slow the relaxation of the coacervates, while more salt lubricates and accelerates chain dynamics. These effects on chain mobility have been well established in previous work [24-25]. The effect of salt concentration can often be quantified by time-salt superposition [6], which produces primarily a shift of the G' and G'' curves along the frequency axis. However, we also find that both salt and molecular weight affect the presence and magnitude of a low-frequency plateau modulus, an effect which does not follow time-salt superposition. The effects of salt concentration and chain lengths on the storage moduli at low frequency in our work are summarized in Fig. 4-12. The coacervate composed of 70kDa PSS and 100kDa PDADMAC at 2.2M, represented by the left-most red open triangle in Fig. 4-12, has a modulus of around 20Pa, that is similar to that of a coacervate of 200kDa PSS and 100kDa PDADMAC at 2.6M, which is given by the left-most red filled triangle. Both coacervates composed of 200kDa PDADMAC, but with PSS of 70kDa at 2.8M salt (an open green circle) and of 200kDa PSS at 3.2M (a filled green circle), have low-frequency plateau moduli of 100Pa. Note in Fig. 4-12, that the data represented by filled circles/squares can be shifted toward lower salt region to superpose roughly with the data with open circles/squares, especially for data points with

G’ above 10 Pa. It would be worth investigating that whether a model could predict these interesting dependencies of low-frequency modulus plateau on PE chain lengths and salt concentration and identity.

4.4.6 Literature Values of Low-frequency Plateau Modulus

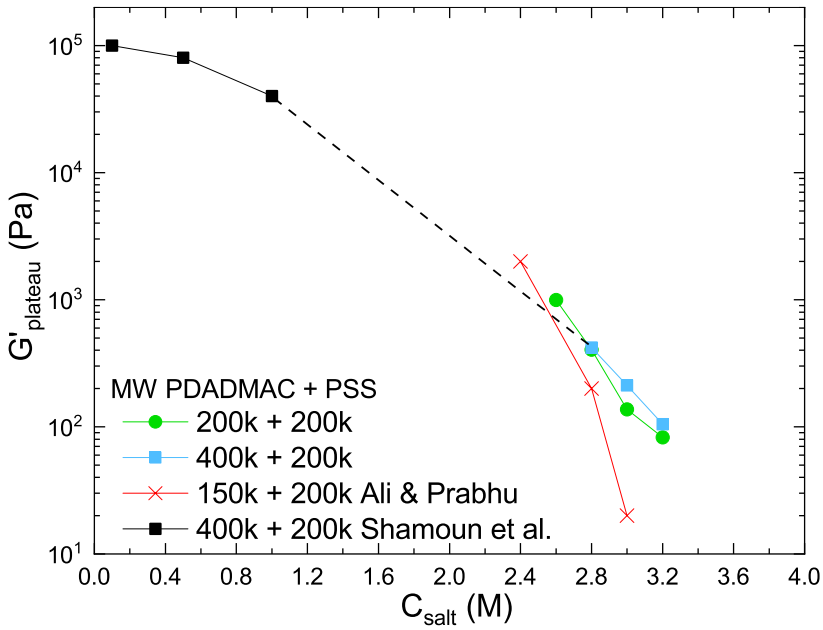

Figure 4-13. Comparison of G’ low-frequency plateau for PDADMAC/PSS/NaCl coacervate complexes as function of salt concentration. Literature data is extracted from Ali & Prabhu [14] and Shamoun et al. 2012[13]. Molecular weights shown in the legend represent the MW of PDADMAC and PSS, respectively.

For coacervates prepared from PDADMAC, PSS and NaCl, Ali and Prabhu [14] previously reported a low-frequency plateau for G’ at frequencies as low as 0.01rad/s, obtained through time-temperature superposition. Fig. 4-13 shows that their samples with 150kDa PDADMAC have slightly lower modulus than ours with 200kDa PDADMAC. The data for three chain lengths of PDADMAC, ranging from 150kDa to 400kDa, show no large increase in plateau modulus. Note that, in our experiments, the low-frequency plateau did not appear for samples with 100kDa PDADMAC over the range of salt concentration considered. It is possible, therefore, that there is a critical chain length of PDADMAC between 100kDa and 150kDa for forming a gel-like structure at long timescale. A much larger plateau was found by Schlenoff group [26], for similar samples to ours, but prepared by adding smaller concentrations of salt (less than 1M) into already-prepared precipitates, rather than through phase separation, as we have done. Despite this difference in

preparation procedure, we find that a reasonable extrapolation of their data to higher salts, leads to moduli consistent with our data set (PDADMAC with 400kDa).

This comparison with literature data reveals that the appearance of a low-frequency plateau is a common and consistent feature of this strong PE system (PDADMAC/PSS). It may be possible that many other pairs of strong polyelectrolytes might reveal a gel-like response at low frequencies if they are studied at high enough molecular weights and low enough salt concentrations. A recent scaling theory by Rubinstein and coworkers [27] attributes the transition from liquid-like to solid-like behavior to an increase in binding free energy between oppositely charged monomers from less than, to greater than, ~1 k_BT. When the solid forms, however, its magnitude is estimated to be of order the density of charged monomers, a value much too high to be consistent with the values we find at high salt concentration.

Theories, simulations [28], experimental results [29] for gel formation in neutral associating polymers [30] might provide clues for developing a predictive theory for gel formation in polyelectrolyte coacervates. The relationship between a low-frequency plateau modulus and the structure and dynamics of associating polymers, including charged polymers, was explored recently by Zhang et al. [31]. Key ideas explored in this work include: 1) the relationship between plateau modulus $G_0 = \rho RT/M_s$ and the density of strongly associating groups, quantified by the average molecular weight M_s of a strand between associating groups, with ρ the mass density of polymer; 2) the transition of charged polymers from a "polyelectrolyte regime" to an "ionomer regime" as determined by average ion spacing along the chain and the product of dielectric constant and temperature with lower values of each favoring the "ionomer regime," in which opposite charges not only pair, but form clusters of multiple positive and negative ions; 3) the existence of a "percolation regime" in which roughly one strong binding site is found on each chain, and the modulus can be arbitrarily small and sensitive to density of binding sites. The formula $G_0 = \rho RT/M_s$ applied to coacervates with typical polymer volume fraction of ~0.3, implies that polymers with M_s ~200,000 Da would have a modulus of around 5 x 10^3 Pa. This implies that many of our coacervates, especially at higher salt concentration, have fewer than one network-forming bonding site per polymer, obviously far less than the number of charges per chain. We also find that the presence and magnitude of the plateau modulus depends not only on salt concentration, but also on chain length, suggesting that the spacing between the strong binding sites is comparable to, or larger than the chain length, so that shorter chains are less likely to form

a percolating network of bound chains than are longer chains. Not only is the number of ion pairs likely to be present in coacervates too large to explain the low-frequency modulus, but their lifetimes are likely too short, based on estimates of ion pair lifetimes by Schlenoff and coworkers [26], among others [6, 8]. In addition, ion-pairing lifetime and its dependence on salt concentration is the basis for explaining time-salt superposition, and the height of the plateau modulus depends on salt concentration and therefore does not obey time-salt superposition.

For these reasons, the low-frequency modulus is likely controlled not by simple ion pairs, but by longer-live aggregates of multiple monomers of both positive and negative charge. Such aggregates are present in ionomers [31], and become more likely when the dielectric constant decreases, as is likely to happen locally within a coacervate with lower amounts of salt and less water of hydration. The transition to the "ionomeric regime" is predicted by Zhang et al. to occur at charge spacings and dielectric constants typical of coacervates, especially if one allows for a broad transition region from the "polyelectrolyte" to the "ionomer" regime as envisaged by Colby and coworkers (see Fig. 3 of Zhang et al) [31]. A picture that might explain that plateau modulus is therefore one in which, in addition to abundant ion pairs, there are aggregates of charged monomers, held together part by a locally high polymer concentration that lowers the local dielectric constant, supporting a locally "ionomeric" environment within the coacervate. The aggregates are likely to be of various sizes and lifetimes, and thus one expects a gradual approach to a plateau as frequency decreases, as aggregates of a range of sizes and lifetimes contribute to the modulus. This is consistent with the gradual broadening of the relaxation spectrum of a coacervate, as salt concentration decreases, eventually leading to a low-frequency plateau, as indicated in Fig. 4-11. Clear fluid-like terminal regimes are largely absent from our data, which instead show intermediate power laws between "liquid-like" and "solid-like" order, tending gradually towards more "solid-like" behavior as the salt concentration decreases. Thus, we picture coacervates that either have a low-frequency G' plateau or have intermediate power law dependences of G' and G'' on frequency as heterogeneous phases with patches of "ionomer-like" material, with low dielectric constant and multiple aggregated charged monomers, with long lifetimes, creating a percolating or near-percolating network structure. We note that this explanation of the low-frequency low modulus of coacervates is consistent with earlier suggestions of a percolated network of chains or domains by Bohidar et al. [12] for coacervates formed by mixtures of charged proteins and polyelectrolytes.

4.5 Conclusion

The rheological behaviors of polyelectrolyte complexes in the low frequency region were revealed more thoroughly and decisively than in previous work, through frequency sweeps down to low frequencies at small strain amplitude, for all six combinations of three commercially available poly (diallyl dimethyl ammonium chloride) (PDADMAC) samples with two poly (sodium 4-styrenesulfonate) (PSS) samples. To obtain reliable data, we determined the limits on experimental accuracy and reproducibility due to rheometer sensitivity, and sample stability against evaporation, aging, and rheometer loading, through repeat tests using two different rheometers, and through measurements on reference standards, yielding clear bounds on acceptable data. We found that coacervates at the highest salt concentrations (close to 4 M) have poor reproducibility, leading to exclusion of these samples from our reported data sets. The formation of a low-frequency plateau and its magnitude are found to be highly sensitive to salt concentration, consistent with previous work. Novel to our work is the finding that it is also sensitive to polyelectrolyte molecular weight, with more rapid increase in its magnitude with increasing length of the polyanion, PSS than of the polycation, PDADMAC. Trend lines of the dependences on salt concentration and chain length are assemble from our data and relevant literature. Why both salt and chain length can, under some circumstances, not only shift the rate of chain motion, but also quench long-range motion into a gel-like response, is a mystery that needs resolution, and a theory to reliably predict it. We suggest that a transition towards a network of "ionomer-like" aggregates might provide a fruitful starting point.

4.6 Reference

[1] Van Haver, L., and Nayar, S., "Polyelectrolyte flocculants in harvesting microalgal biomass for food and feed applications," Algal Research 24, 167-180 (2017).

[2] Wanasingha, N., Dorishetty, P., Dutta, N. K., and Choudhury, N. R., "Polyelectrolyte gels: Fundamentals, fabrication and applications," Gels 7(3), 148 (2021).

[3] Chi, K., Wang, H., and Catchmark, J. M., "Sustainable starch-based barrier coatings for packaging applications," Food Hydrocolloids 103, 105696 (2020).

[4] Borro, B. C., and Malmsten, M., "Complexation between antimicrobial peptides and polyelectrolytes," Advances in Colloid and Interface Science 270, 251-260 (2019).

[5] Sing, C. E., and Perry, S. L., "Recent progress in the science of complex coacervation," Soft Matter 16(12), 2885-2914 (2020).

[6] Larson, R. G., Liu, Y., and Li, H., "Linear viscoelasticity and time-temperature-salt and other superpositions in polyelectrolyte coacervates," Journal of Rheology 65(1), 77-102 (2021).

[7] Spruijt, E., Sprakel, J., Lemmers, M., Stuart, M. A. C., and Van Der Gucht, J., "Relaxation dynamics at different time scales in electrostatic complexes: time-salt superposition," Physical review letters 105(20), 208301 (2010).

[8] Spruijt, E., Cohen Stuart, M. A., and van der Gucht, J., "Linear viscoelasticity of polyelectrolyte complex coacervates," Macromolecules 46(4), 1633-1641 (2013).

[9] Marciel, A. B., Srivastava, S., and Tirrell, M. V., "Structure and rheology of polyelectrolyte complex coacervates," Soft Matter 14(13), 2454-2464 (2018).

[10] Syed, V. M., and Srivastava, S., "Time–ionic strength superposition: A unified description of chain relaxation dynamics in polyelectrolyte complexes," ACS Macro Letters 9(7), 1067-1073 (2020).

[11] Tekaat, M., Bütergerds, D., Schönhoff, M., Fery, A., and Cramer, C., "Scaling properties of the shear modulus of polyelectrolyte complex coacervates: a time-pH superposition principle," Physical Chemistry Chemical Physics 17(35), 22552-22556 (2015).

[12] Bohidar, H., Dubin, P. L., Majhi, P. R., Tribet, C., and Jaeger, W., "Effects of protein− polyelectrolyte affinity and polyelectrolyte molecular weight on dynamic properties of bovine serum albumin− poly (diallyldimethylammonium chloride) coacervates," Biomacromolecules 6(3), 1573-1585 (2005).

[13] Shamoun, R. F., Hariri, H. H., Ghostine, R. A., and Schlenoff, J. B., "Thermal transformations in extruded saloplastic polyelectrolyte complexes," Macromolecules 45(24), 9759-9767 (2012).

[14] Ali, S., and Prabhu, V. M., "Relaxation behavior by time-salt and time-temperature superpositions of polyelectrolyte complexes from coacervate to precipitate," Gels 4(1), 11 (2018).

[15] Wu, H., Ting, J. M., Werba, O., Meng, S., and Tirrell, M. V., "Non-equilibrium phenomena and kinetic pathways in self-assembled polyelectrolyte complexes," The Journal of chemical physics 149(16), 163330 (2018).

[16] Ewoldt, R. H., Johnston, M. T., and Caretta, L. M., "Experimental challenges of shear rheology: how to avoid bad data," Complex fluids in biological systems (pp. 207-241), Springer, New York, NY (2015).

[17] Han, A., and Colby, R. H., "Rheology of entangled polyelectrolyte solutions," Macromolecules 54(3), 1375-1387 (2021).

[18] Ghasemi, M., Friedowitz, S., and Larson, R. G., "Analysis of partitioning of salt through doping of polyelectrolyte complex coacervates," Macromolecules 53(16), 6928-6945 (2020).

[19] Li, L., Srivastava, S., Andreev, M., Marciel, A. B., de Pablo, J. J., and Tirrell, M. V., "Phase behavior and salt partitioning in polyelectrolyte complex coacervates," Macromolecules 51(8), 2988-2995 (2018).

[20] Kavanagh, G. M., and Ross-Murphy, S. B., "Rheological characterization of polymer gels," Progress in Polymer Science 23(3), 533-562 (1998).

[21] Sadman, K., Wang, Q., Chen, Y., Keshavarz, B., Jiang, Z., and Shull, K. R., "Influence of hydrophobicity on polyelectrolyte complexation," Macromolecules 50(23), 9417-9426 (2017).

[22] Adolf, D., and Martin, J. E., "Time-cure superposition during crosslinking," Macromolecules 23(15), 3700-3704 (1990).

[23] Dahesh, M., Banc, A., Duri, A., Morel, M. H., and Ramos, L., "Spontaneous gelation of wheat gluten proteins in a food grade solvent," Food Hydrocolloids 52, 1-10 (2016).

[24] Meng, S., Ting, J. M., Wu, H., and Tirrell, M. V., "Solid-to-liquid phase transition in polyelectrolyte complexes," Macromolecules 53(18), 7944-7953 (2020).

[25] Zhang, R., Zhang, Y., Antila, H. S., Lutkenhaus, J. L., and Sammalkorpi, M., "Role of salt and water in the plasticization of PDAC/PSS polyelectrolyte assemblies," The Journal of Physical Chemistry B 121(1), 322-333 (2017).

[26] Akkaoui, K., Yang, M., Digby, Z. A., and Schlenoff, J. B., "Ultraviscosity in entangled polyelectrolyte complexes and coacervates," Macromolecules 53(11), 4234-4246 (2020).

[27] Danielsen, S. P., Panyukov, S., and Rubinstein, M., "Ion pairing and the structure of gel coacervates," Macromolecules 53(21), 9420-9442 (2020).

[28] Hong, W., Lin, J., Tian, X., and Wang, L., "Linear and nonlinear viscoelasticity of self-associative hydrogen-bonded polymers," Polymer 235, 124301 (2021).

[29] Kreuer, K. & Portale, G., "A Critical Revision of the Nano-Morphology of Proton Conducting Ionomers and Polyelectrolytes for Fuel Cell Applications," Adv Funct Mater 23, 5390–5397 (2013).

[30] Larson, R. G., "The structure and rheology of complex fluids (Vol. 150, pp. 1-663)," Oxford university press, New York (1999).

[31] Zhang, Z., Chen, Q., and Colby, R. H., "Dynamics of associative polymers," Soft Matter 14(16), 2961-2977 (2018).

Chapter 5

Relating 3D Printability of Silicone-based Materials to Rheological Measurements

5.1 Abstract

Direct ink writing (DIW)[1] additive manufacturing with a custom-built static mixer and fine-tip nozzle is used to print polydimethylsiloxanes (PDMS) either mixed with fumed silica or as a two-part commercial liquid silicone rubber (LSR) mixed with polyethylene glycol (PEG). We assess their printability by printing a hollow slump cone, whose print quality is correlated with rheological measurements, including 1) a shear rate up-ramp followed by a down-ramp in shear rate, 2) creep tests at a series of increasing stresses, and 3) oscillatory shear with increasing amplitude well into the nonlinear regime. The PDMS-fumed silica mixtures fail to print even at the highest fumed silica loading used (9 wt%), while LSR-PEG with 4 or 6 wt% PEG prints very well even with low Shore hardness LSR. These large differences in printability of two classes of PDMS materials correlate poorly with the rheological behavior in the up-ramp of shear rate, the creep test, and the large-amplitude oscillatory shearing test. The rheological test that most clearly distinguishes the differences in printability is the apparent yield stress (the current most common *rheological index of printability)* during a down-ramp in shear rate following a previous up-ramp to the maximum shear rate of 1000 s^{-1}, which is similar to the highest shear rate in the print nozzle. The printability of the materials considered here, and quite likely other such materials, depends strongly on their ability to rebuild structure and yield stress quickly after experiencing the high shear rates characterizing its emergence from a narrow nozzle tip. The contents of this chapter are the result of collaborative research with Ph.D. student Matthew Hildner.

[1]Abbreviations:
DIW: direct ink writing
3D: three dimensional
PDMS: polydimethylsiloxanes
LSR: liquid silicone rubber
PEG: polyethylene glycol
PDP: progressive displacement pump
SSM: spiral static mixer
TN: tapered nozzle

5.2 Introduction

Interest in three-dimensional (3D) printing, or additive manufacturing, has grown rapidly over the past decade. In direct-ink-write (DIW) printing, one of several 3D printing processes, a flowable material is extruded through a fine nozzle attached to a print head, which is moved under the control of a gantry to generate 3D printed shapes layer-by-layer [1]. DIW is applicable to a wide range of materials, including silicones, epoxies, urethanes, bio-inks, ceramic pastes, and other suspensions [2-9]. The material choice reflects the desired properties of the final component but must also be "3D printable" or able to be laid down, line by line, at high speed into a pre-programmed, self-adhering, three-dimensional shape that is retained under gravity and other mechanical forces.

The relationship between printability and rheology of the material has been widely recognized. As noted by Corker et al. [4]: "It is generally recognized that a printable formulation must be a shear thinning, yield-stress soft material exhibiting solid-like behavior. The storage modulus (G_0) values must be high to retain the shape, to support its own weight and the layers on top and to span across supports. The 'yield' stress must also be high enough to retain printing resolution as the filament is deposited, but within certain limits to facilitate an easy flow initiation during the printing process." However, Corker et al. also noted that the precise relationship between printability and rheology remains poorly defined, owing to "the diversity of the rheological methodologies," and the "wide range of 'soft materials'" printed.

The material's "yield stress" is the most obvious rheological index that quantifies the ability of the printed object to hold shape against gravity, surface tension, and other forces, at least long enough for drying or chemical reaction to "cure" the material into a permanent final shape. However, the "yield stress" has been measured in a wide variety of ways, and it remains unclear which ones are most relevant to printability. Broadly speaking, "static" yield stresses are measured by starting from a state of rest and increasing strain rate or stress to the point of continuous flow. "Dynamic" yield stress, on the other hand, is measured by inducing flow and then reducing stress to a point close to the point of flow cessation. Precise definitions of "static" and "dynamic" yield stresses have been given in the rheological literature [10-12]; but the tests required to realize these ideals, and give well-defined results for arbitrary materials, are not necessarily the most helpful for the needs of practical 3D printing applications. In fact, as discussed below, a printable material

must meet multiple rheological criteria, and the most relevant ones depend on the printing process and the part to be printed.

In what follows, in Section 5.3, we will first review some of the most pertinent literature that seeks to connect rheological characterization to "printability" using various printing materials, and model printed structures. Then, in Section 5.4, we describe the materials used in our study. This is followed in Section 5.5 by a discussion of the printer and the test geometry. The results follow in Sections 5.6 and 5.7, first the "yield stress" as measured in various rheological flow histories, and then the printing results for the materials chosen for our study and estimates or bounds on the "yield stress" manifested in the printing process itself. We complete Section 5.8 with a discussion of the most relevant rheological predictors of "printability" of our PDMS materials and summarize in Section 5.9. References come in Section 5.10.

5.3 Review of Literature Connecting Rheology to Printability

Researchers in 3D printing have generally improvised definitions of "static" and "dynamic" yield stresses that seemed more pertinent to their needs. The most frequent tests are steady shearing and, even more commonly, nonlinear oscillatory shearing with varying strain or stress amplitude [8, 12]. As an example of the former test, Courtial et al. [14] performed start-up of shearing of a Silibione® LSR 4350 from Elkem Silicones with added polyethylene glycol (PEG) and took the stress at the transient overshoot as the "static" yield stress and the lower, long-time, steady stress as the "dynamic" yield stress. They found values ranging from 1000 to 1700 Pa for the former and 1000 to 1300 Pa for the latter, depending on material composition. They found that all of these materials led to "printable" simple hexagonal towers that slumped less than around 10%; but shapes with significant overhangs showed considerably greater sag, up to 40% or so, which they projected would only become negligible upon increase of their "static" yield up to a value of around 3000 Pa.

More commonly, oscillatory shear has been used to measure yield stresses, usually in a stress sweep [4]. The storage and loss moduli G' and G'' are typically measured starting at a low stress, where the material is in the linear viscoelastic regime; and with increasing stress amplitude, they leave the linear regime, and the apparent G' and G'' both decrease with amplitude. The stress at which this decrease in G' reaches around 10% was called a "yield stress" σ_y by Corker et al.

[4]. At low amplitude the material is solid-like, with G' > G''; but G' decreases with stress amplitude faster than G'', and crosses over it at a stress Corker et al. labelled the "flow stress" σ_f. (An example of this behavior will be shown in our results below in Table 5-3.) Working with graphene oxide suspensions in water, Corker et al. [4] found that "printable" materials had flow stresses of σ_f > 500 Pa, a "flow transition index" of σ_y/σ_f > 20, and a high value of the low-frequency storage modulus. They also assessed the rate of recovery of modulus G' after reduction of strain amplitude from high to low, which is an important measure of the material's ability to hold shape after high deformation rates imposed during printing. However, Corker et al. [4] showed no precise metrics of printed part quality with which the material rheology could be correlated. Feilden et al. [3] and Kokkinis et al. [15] used the same cross-over of G' and G'' as an index for printability but both called it a "yield stress" rather than the "flow stress." Feilden et al. [3] found for their alumina-platelet-containing ceramic paste that a value of this "yield" or "flow" stress σ_f > 500 Pa could be printed into relatively small mechanical parts, such as gears. Kokkinis et al. [15] printed polyurethane acrylate (PUA) oligomers containing alumina platelets with fumed silica as rheology modifier into structures with an overhang having radius of curvature R. This printed overhang failed to hold shape under the action of surface tension γ when $\sigma_f < \gamma/R$; and therefore σ_f needed to exceed around 30-100 Pa to prevent this printing failure. (Note that we here using the same symbol for surface tension as for strain.)

M'Barki et al. [16] defined a "static" yield stress as the plateau stress reached during increase of shear rate in a strain-rate sweep. After attainment of a rate of $\dot{\gamma}$ = 100 s^{-1}, the shear rate was immediately ramped down, and the "dynamic" yield stress σ_y^{Dyn} was taken as the stress when the shear rate had dropped to $\dot{\gamma}$ = 1 s^{-1}. M'Barki et al. found that the dynamic yield stress could be used to correlate the "printability" of stacks of lines, h = 5 mm tall, of an aged Boehmite alumina paste, if both gravity and surface tension were combined into a "printability index" $\Xi = \frac{\sigma_y^{Dyn}}{\gamma R^{-1} + \rho g h}$, with ρ the material density and g the gravitational constant.

Similar to Feilden et al. [3] and Kokkinis et al. [15], Romberg et al. [17] used oscillatory flow to obtain a printability index; but first imposed a stress-amplitude ramp, with frequency 1 Hz, up to a maximum amplitude of 1200 Pa, and followed this by a step decrease in amplitude to 50 Pa, and tracked the recovery of G' with time thereafter. The recovered G' at 0.1 minute and 15 minutes after decrease of stress amplitude, which had values around 5,000 to 15,000 Pa, were

taken as indices of printability. When combined with a theory of buckling, these indices provided bounds on the predicted critical height (up to 60 mm) for gravitational buckling and collapse of a printed tower of various widths from 1-17 mm of EPON 826 epoxy resin filled with 10% clay or silica. Amorim et al. discussed the relevance of a variety of rheological tests for extrusion-based printing of biomaterials, including ones containing biological cells [8].

The above brief review covers a few of the most recent important papers that attempt to connect rheological measurements with 3D printing performance. The review demonstrates progress, but also shows that a large gap remains between current knowledge and a hoped-for "science of printability." If such a science were to be created, rheological measurements of a given material could be used to predict quantitatively the printability of high-quality parts from that material, given a set of printing specifications, such as size and shape of the part, printing-head and nozzle design, and rate of printing. The work still needed to attain this goal is manifest by the range of rheological tests currently used to estimate "printability" and the lack of consensus regarding which ones are most appropriate and why. Studies to date involved a choice of 1) material, 2) printer, 3) printed part, and 4) rheological test; each of which involved multiple choices including geometries, rates, and operating conditions. Few studies share even one of these choices in common with any other study. Although some general criteria for printability have been ascertained, such as the need for a relevant "yield stress" to be high enough to withstand gravitational and surface tension forces, successful correlations to date can only be applied with confidence to a particular material printed by a particular device into a particular geometry. While it seems that some kind of "yield stress" is the most relevant quantity to measure, it remains unresolved whether this should be measured under steady or oscillatory flow, and whether it should be measured during a ramp up of shear, or after a prior high shearing rate. If the latter, it is unclear how high the prior shear rate or stress should be, and how soon afterward the yield stress should be measured.

Overcoming these limitations of knowledge is a huge task that will take contributions from many groups extended over a significant period of time. The main goal of the work reported here will be to study a significant range of printing materials using a wide range of rheological tests, and to compare the resulting rheological measurements with quantified printing outcomes, using a single printing configuration and primarily one standardized printing geometry. We study around a dozen silicone-polymer-based materials, with silicone of different molecular weights, containing

fumed silica or polyethylene oxides at multiple loading levels, intended to impart a suitable yield stress for attaining printability. This class of materials is an important one commercially, and the findings may well be relevant to other classes of yield-stress materials, especially additive-containing viscous liquids. We 3D print these materials all using the same printer at similar printing rates into a standardized geometry, the slump cone, of the similar height, either 20 or 30 mm. We then compare the printability derived from these standard measurements with a wide range of rheological tests, similar to those in the literature and improved in our lab, in an effort to find the most suitable rheological "printability index" for our materials. We consider measures of both "up-ramp yield stress" and "down-ramp yield stress," where the former is measured during upward ramps of rate or stress, and the latter during or after a down-ramp or jump in rate or stress. We consider both shear rate and stress ramps, in both unidirectional and oscillatory flow.

5.4 Materials

5.4.1 PDMS with Fumed Silica

Model liquid silicone rubber (LSR) materials tested are polydimethylsiloxane (PDMS) mixed with fumed silica filler. The CAB-O-SIL® L-90 silica was acquired from Cabot Corporation (lot: 464550). SILASTIC™ SFD-5 (13.5 Pa·s, Approx. Mn = 40,700 g/mol, lot: 8542992), and DOWSIL™ 3-5016 (50 Pa·s, Approx. Mn = 59, 200 g/mol, lot: H050JBR017). PDMS samples were acquired from Dow Performance Silicones. SILASTIC™ SFD-5 and DOWSIL™ 3-5016 are both 100% polydimethylsiloxane hydroxyl-terminated. These PDMS-silica model systems were mixed using a FlackTek speed mixer (model DAC600.2 VAC-LR). The polymers were added to a dental cup with the silica filler. The blend was mixed for 1 minute at 2000 rpm. The sides of the cup were scraped with a spatula and mixed again for 1 minute at 2000 rpm. The blend was de-aired on the dental mixer using the following cycle: 30 s at 800 rpm normal pressure to 3450 Pa (0.5 psi), 1 minute at 1300 rpm at 3450 Pa (0.5 psi), and 30 s at 800 rpm 3450 (0.5 psi) to normal pressure.

Six samples, each with a total mass of 250 mg, were synthesized with the two different PDMS viscosities (13.5 Pa · s and 50 Pa · s) and three different filler weight percentages (5 wt%, 7 wt% and 9 wt%). These six samples are listed in Table 5-1, with numbers corresponding to resin viscosity and filler mass percentage. For example, "S-50-5" refers to the sample with 50 Pa·s

viscosity PDMS and 5 wt% fumed silica filler. Later, two "blank" PDMS samples without any fillers were prepared for comparison with the filled samples, and were given designations starting with "B". Table 5-1 shows the compositions in terms of weight percentages.

Table 5-1.Composition of PDMS/Fumed Silica Model Materials (Unit: wt%)

Designation		B-13.5-0	S-13.5-5	S-13.5-7	S-13.5-9	B-50-0	S-50-5	S-50-7	S-50-9
PDMS (Pa·s)	50					100	95	93	91
	13.5	100	95	93	91				
Fumed silica*		0	5	7	9	0	5	7	9
Total		100	100	100	100	100	100	100	100

* The moisture in the filler is 0.58%

5.4.2 LSR Silicone with PEG

The LSR/PEG 3D printing formulation is based on the method of Courtial et al. [14] for the creation of a 3D printable LSR silicone. The basic procedure is to mix LSR silicone (Silibione® LSR, Elkiem Lyon, France) with polyethylene glycol (PEG) with a molecular weight of 400 g/mol (PEG 400, Sigma Aldrich, St. Louis, MO USA). The LSR silicone is available in various durometers and for this procedure materials with Shore hardness 50A (LSR 4350) and 5A (LSR 4305) durometer LSR were used. The LSR silicone consists of a "Part A" and "Part B" that are designed to be mixed together in equal parts. We used ^{29}Si NMR and TGA measurements on the four commercial LSR materials studied here to estimate the total filler content of each (see Figures 5-1, 5-2 and 5-2 and Table 5-2).

5.4.2.1 LSR Content Assessment - Experiments

NMR. Samples of LSR were dissolved in 99.9% deuterated chloroform ($CDCl_3$) at a concentration of 30 wt.%. 0.03M of chromium acetylacetonate was added as a paramagnetic relaxation agent. A 10 mm diameter Teflon sample tube was used with a 16 mm probe in an Agilent 500 MHz DD2 system at a frequency of 99.29 MHz. A pulse width of 18 μs and a relaxation delay time of 13 s were chosen. The number of acquisitions for each spectrum was 64.

TGA. The samples were analyzed by Thermogravimetric analysis (TGA) using a TA Instruments Discovery Series TGA. Approximately 10-15 mg of sample was heated in a Pt pan. The furnace purge was set with nitrogen at 60 ml/min. and the balance purge with nitrogen at 40 ml/min. Samples were stabilized at 35.0 °C before temperature ramping was started. Then the temperature was ramped at 10.0 °C/min to 950.0 °C. Weight of the sample was continuously monitored to calculated weight retention.

5.4.2.2 LSR Content Assessment - Results and Discussion

As shown in Figure 5-1, in all LSR compositions MQ resin is present. This is indicated by the presence of M unit (Me_3SiO-) on a resin, represented by the broad peak at 11 ppm on a ^{29}Si NMR spectrum, along with the presence of the broad peak from -100 to -120 ppm for the Q unit. In the silicone industry convention, the most common structural units in silicones are referred to as M, D, T, and Q, as depicted in Figure 5-2.

M is a structural unit of $(CH_3)_3SiO_{1/2}$. When it is chemically bonded to a particular environment, the chemical shift of the ^{29}Si nucleus is different. The chemical shift, or the position of the peak distributed along the horizontal axis, provides a signal of what it is attached to. In addition, when it is attached to a resin, the peak is broad, because the resin is a much less defined structure, than a linear polymer. Imaging polymerizing partially hydrolyzed tetraethyl orthosilicate, a mixture of different degrees of condensation and polymerization would be formed. To the contrary, when it is attached to the ends of a linear polydimethylsiloxane chain, the nearest chemically bonded neighbors of M are all the same, and when probed with NMR it produces a sharp peak on the spectrum. With those two pieces of information, which peak belongs to which is known. 5B has both M units on resin and on polymer, as it shows a broad peak centered at 11 ppm and a sharp peak at 7 ppm. Only the sharp peak was labeled on the 5B NMR result, to avoid the graph getting too crowded. For 50 B only broad peak is observed, but no sharp peak at 7 ppm, indicating likely there is resin in it, but no M terminated PDMS polymers. M terminated PDMS polymers usually function as a plasticizer.

“MQ” resin stands for a type of resin mainly consisting of the structural units of M and Q. The predominant silicone content in the liquid silicone rubber compositions is D units, for the polydimethylsiloxane polymer. Other components are present, including M terminal units likely on a linear polymer which shows a sharp peak at 7 ppm, M^{Vi} (Me_2ViSiO-) terminal units with a

peak at -3 ppm for the vinyl functionality on the polymer and potentially also on the MQ resin, and D^H (-HMeSiO-) units with a peak at -35 ppm for the SiH crosslinking agent. The extremely broad Q peak is consistent with the presence of silica also, in addition to MQ resins. These indicate that the liquid silicone rubbers are vinyl end functional linear PDMS blended with side SiH functional siloxanes, and reinforced with a combination of MQ resin and silica. In the lower hardness version, it is possible that a M terminated, non-functional PDMS is added as a plasticizer. This is consistent with the hardness of both.

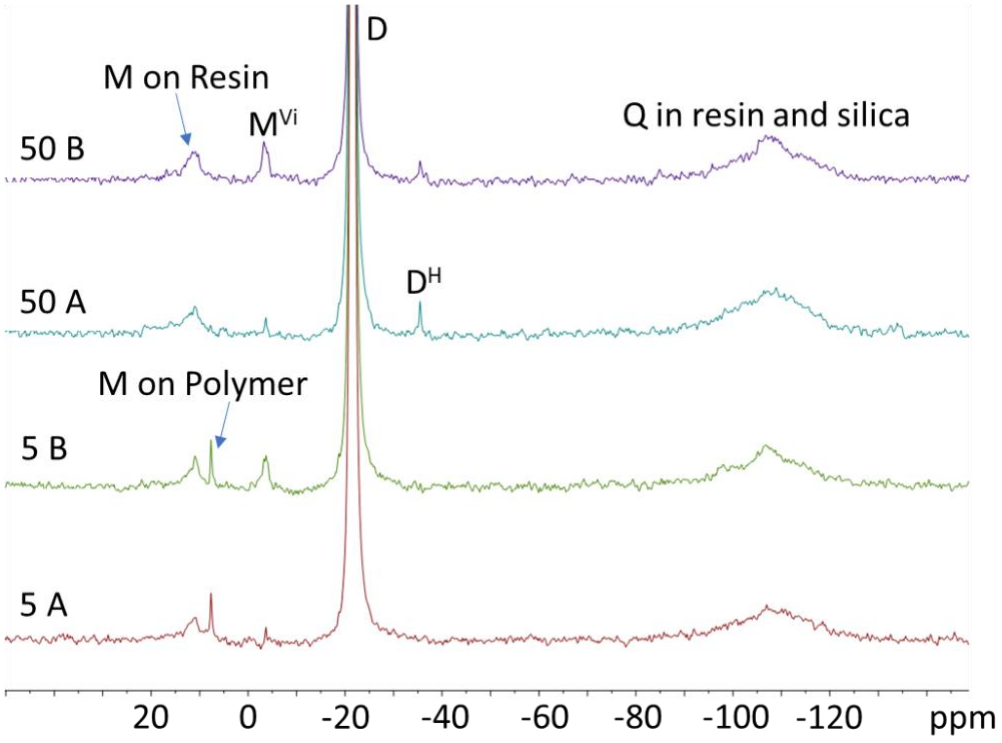

^{29}Si NMR Chemical Shift

Figure 5-1. ^{29}Si NMR spectra of liquid silicone rubbers, part A and part B of the 5 Shore A version (5A, and 5B), and corresponding parts for the 50 Shore A version (50 A, and 50 B).

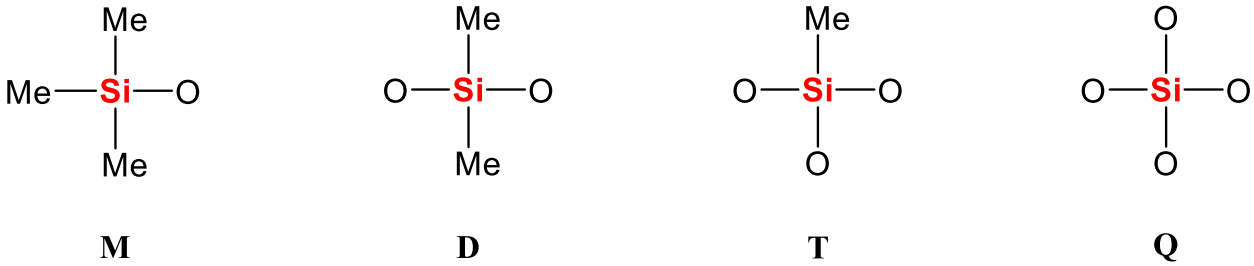

Figure 5-2. Most basic structural units in silicones.

The simultaneous presence of MQ resin and silica makes assessment of filler content more difficult and uncertain, as each interferes with the method better suited for the other. For example, thermal decomposition method or density estimation works reasonably for silica filled PDMS, but does not work well for MQ resin filled PDMS. On the other hand, solution NMR provides useful insight into the ratio of the amounts of Q and D units in a MQ resin filled system, but is much less meaningful for silica filled system. Nevertheless, the amount of mass retained after a thermal treatment still qualitatively corresponds to the filler content in the composition. Figure 5-3 shows the thermogravimetric analysis curves of the four parts of the two liquid silicone rubbers. Table 5-2 also tabulates the final weight retentions of the samples after being heated to 950 °C in N_2. With the large discrepancies of final weight retentions between the A parts of the Shore A 5 LSR and the Shore A 50 LSR, and between the B parts of the two, it is reasonable to conclude that the 50 Shore A LSR contains a much higher level of fillers.

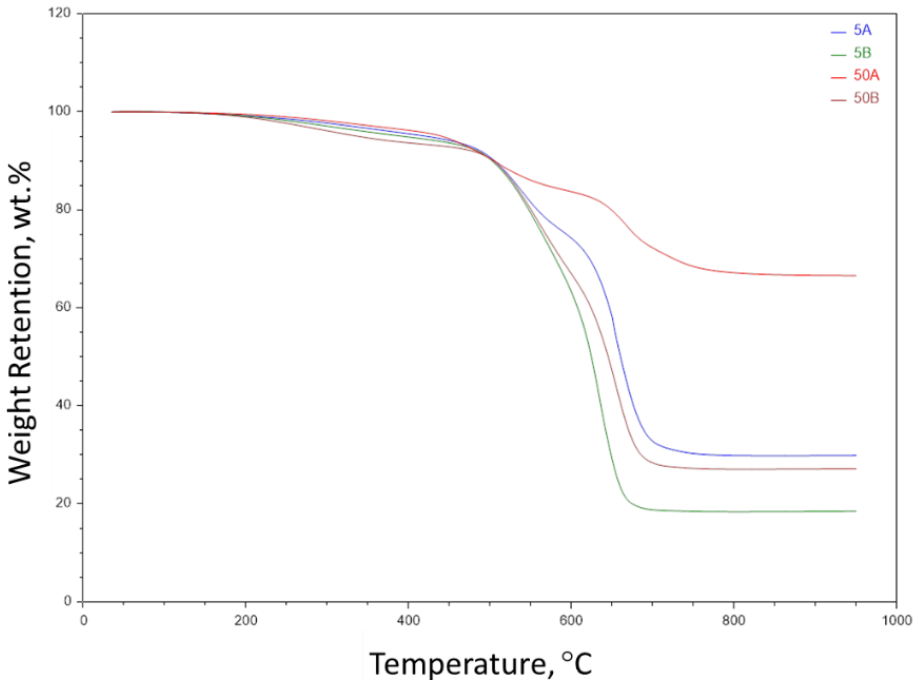

Figure 5-3. TGA weight retention curves of liquid silicone rubber compositions in N_2.

The “filler” is identified as the total of added silica and the “MQ” resin in the LSR, where the latter is a rigid silicone-containing component. It is not possible to determine separately the amount of MQ resin or silica, in this commercial product, without going through a much lengthier analysis. Nevertheless, the amount of mass retained after a thermal treatment still qualitatively corresponds to the total filler content in the composition (see Table 5-2). Since the final LSR

mixture contains parts A and B in 1:1 ratio, the net filler levels of the LSR mixtures can be estimated from the averages over the two parts. Using the measurements in Table 5-2, for the Shore A 5 LSR the total MQ resin plus silica is therefore 20-30 wt% of the total, while for Shore A 50 it is 40-50 wt%.

Table 5-2. Final weight retention of samples heated to 950 °C in N_2.

Sample	Final Weight Retention, %
LSR 5 Part A	28.87 ± 4.14
LSR 5 Part B	18.51 ± 0.12
LSR 50 Part A	66.57 ± 0.54
LSR 50 Part B	27.15 ± 0.09

Note that the 50 Shore A LSR is much more highly filled than is the 5 Shore A one, with some combination of MQ resin and added silica as fillers. As remarked above, the exact amount of fillers, and the ratio between MQ resin and silica, cannot be easily determined because the MQ resin does not decompose cleanly as PDMS does in a TGA temperature ramping experiment, while on a ^{29}Si NMR spectrum the major peak of silica overlaps with that of the MQ resin.

5.4.2.3 LSR/PEG Materials

To prepare the mixed formulations of LSR/PEG, at room temperature the separate LSR silicone components are mixed with a mass fraction (2 wt%, 4 wt% or 6 wt%) of PEG both 1) by hand using a metal stirring rod and 2) by machine using a dental alginate mixer (Alginator, Kerr Corporation, Orange, CA, USA). Results in both printing and rheology are similar for the two mixing methods as shown in Figures 5-4 and 5-5. The combinations of LSR and PEG mass fractions can be seen in Table 5-3. The four samples are denoted as: LSR-50-PEG-2, LSR-5-PEG-2, LSR-5-PEG-4 and LSR-5-PEG-6, with the first number referring to the Shore A hardness and the second number referring to the weight percentage of the PEG.

Table 5-3. Composition of LSR/PEG Materials

Designation	LSR silicone	Shore A Hardness	PEG (wt%)
LSR-5-PEG-2	LSR 4305	5	2
LSR-5-PEG-4	LSR 4305	5	4
LSR-5-PEG-6	LSR 4305	5	6
LSR-50-PEG-2	LSR 4350	50	2

After hand mixing or mixing in a dental alginate mixer, as noted in Table 5-3, each silicone component is transferred to a 30 mL syringe barrel (Quantx 30 mL natural syringe barrel, Fisnar, German Town, WI USA) and degassed for 5 min in a centrifuge (EBA 20C, Hettich Zentrifugen, Beverly, MA USA) at 4500 rpm (average centrifugal radius is approx. 70mm). As mentioned, the rheological and printing results generated by different mixing techniques are similar.

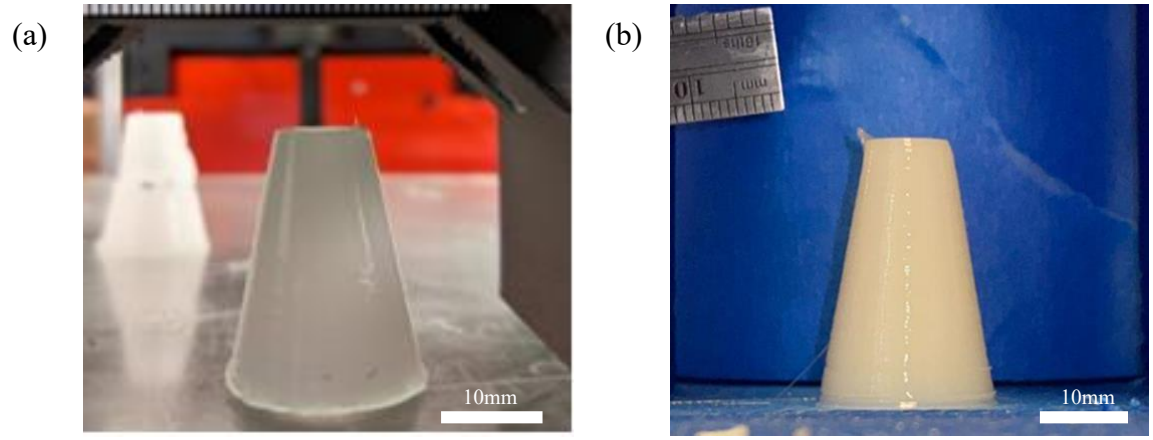

Figure 5-4. 30mm tall slump cones printed with (a) hand-mixed, or (b) machine-mixed LSR-50-PEG-2 materials. Both printing results show no yield.

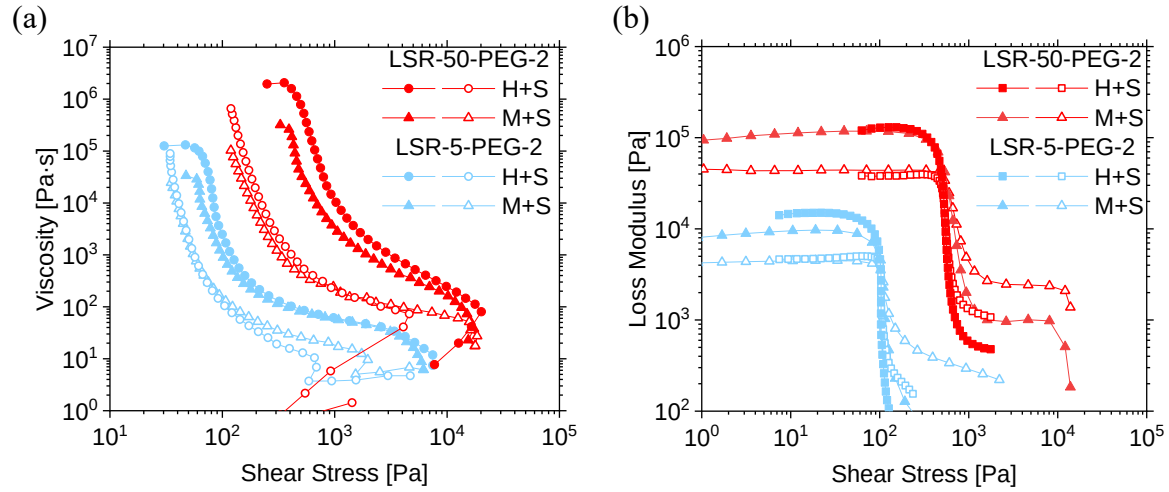

Figure 5-5. (a) Shear rate ramps and (b) strain sweeps results of hand-mixed (H+S) and machine-mixed (M+S) LSR-50-PEG-2 and LSR-5-PEG-2 materials, showing little difference in terms of yield stresses. (All LSR-5-PEG-4 and LSR-5-PEG-6 materials mentioned in the paper were machine-mixed)

5.5 Experimental Methods and Tools

5.5.1 Rheological Measurements

Instrument. An Anton Paar MCR 702 TwinDrive rheometer (Graz, Austria) is used for the rheological measurements in this study. It can rotate both surfaces simultaneously, and in the counter-rotation mode a maximum speed difference of 6000 rpm (100 rps) can be achieved that broadens the shear-rate range for high shear applications. Since this mode was not needed in this study, the shear rate was set by controlling the rotation speed of the upper surface and the torque was also measured on this surface. The torque limit is 230 mN·m, which for the R = 25 mm cone-plate geometry used here gives a stress limit of 8000 Pa, which was high enough for our studies. The cone angle, α, was 2˚ and gap, a, was 0.105 mm. All studies were at room temperature (20˚C).

Deformation histories. The PDMS/fumed silica and LSR/PEG materials were characterized by the following three tests:

(1) *Shear rate ramps*. We first imposed a series of steady shear rates, with the values of the imposed shear rates ramped exponentially from 0.0001 to 1000 s^{-1} with 5 different shear rates imposed per decade over this range, and then ramped back down with the same shear rate spacing. The time duration over which each shear rate in the ramp was imposed was decreased logarithmically from 500 s at 0.0001 s^{-1} to 1 s at 1000 s^{-1}, and this was reversed when the shear rate was ramped down. The ramp up and the highest shear rate were chosen to mimic the shear rate up-ramp in a nozzle flow of a 3D printer with the maximum shear rate experienced by the material in 3D printing being around $\dot{\gamma}$ = 1100 s^{-1} at the tip of the nozzle, shown in Figure 5-7(b). We measured stress as a function of shear rate, giving the viscosity during both upward and downward sweeps. (Data obtained under 0.001 s^{-1} have not been included in the analysis due to instrument limitation.)

(2) *Creep/recovery*. Shear strain was measured after imposition of a constant stress, following by removal of the stress and measurement of the recovered strain. This was repeated for a series of increasing imposed stress values. The stress beyond which strain increased rapidly, and following which recovery of strain was small, allowed an estimate of the yield stress, as discussed in detail later.

(3) *Strain-amplitude sweeps*. For PDMS/fumed silica model materials and LSR/PEG materials, we also carried out strain sweeps. In these tests, oscillatory shearing was imposed at a

fixed frequency of 0.5 Hz (following the procedures of Corker et al. [4]), starting at small strain amplitude in the linear regime, and ramping the amplitude exponentially up with 5 amplitudes per decade until a strain of 1000% was reached, with default duration time at each amplitude set by the rheometer (which advances automatically to the next strain when the moduli attain nearly constant values). Plotting the storage modulus G', which is the component of the modulus that is in phase with the strain, and G'', which is 90° out of phase, against stress amplitude, allows one to define a "flow stress" as discussed later.

5.5.2 Direct Ink Writing Machine

The DIW machine, in Figure 5-6, uses a dual progressive displacement pump (PDP) (Vipro-Head 3/3, Viscotec, Toeging am Inn, Germany) shown in Figure 5-6(a), that can dispense two high-viscosity fluids precisely with rotors forcing fluid through small cavities in a stator. This fluid dispensing method has no pulsing, and the amount of fluid dispensed is directly controlled by the motor rotation [18]. The X and Y positions of the extrusion nozzle on the PDP are controlled on a CoreXY gantry [19-20] by two stepper motors and belts as shown in Figure 5-6(b). The Z position of the extrusion nozzle is controlled by a movable print bed driven by a pair of lead screws attached to stepper motors. The control board is a RAMBo 1.4 (Ultimachine, South Pittsburg, TN, USA). Open-source firmware (Marlin Firmware v1.1.9) controls the DIW system by taking points in the form of G-code and translating them into velocities for the motors.

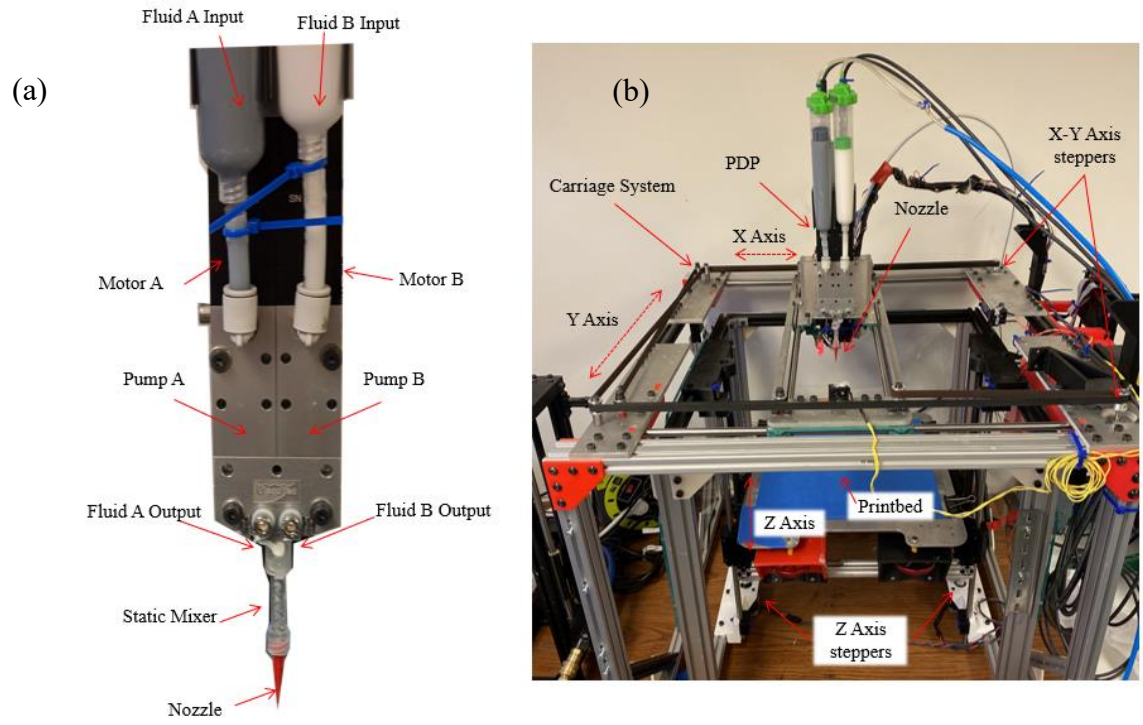

Figure 5-6. Silicone 3D DIW printer: (a) The PDP and (b) gantry

As material flows through the static mixer and tapered dispensing nozzle of the DIW system, it undergoes shear, and the magnitude and duration affect its rheological properties. In the DIW system used in this study, the sources of shear are 1) the static mixer and 2) the tapered nozzle. In both the shear rate, $\dot{\gamma}$, which varies with vertical position in the case of the nozzle, is determined by

$$\dot{\gamma}_{SSM} = K_{g,SSM} Q/(D_{SSM} A_{SSM}) \quad (5\text{-}1)$$

where K_g is the geometry-dependent shear constant, Q is the volumetric flow rate, D is the diameter, and A is the cross-sectional area, in each case of the spiral static mixer (SSM) or tapered nozzle (TN), where A and D depend on position along the axis of the nozzle. For the SSM, $K_{g,SSM}$ = 28 due to its internal elements that induce mixing, and the TN has $K_{g,nozzle}$= 8, the same as an empty pipe [21]. Both the SSM and TN are shown in detail in Figure 5-7(a).

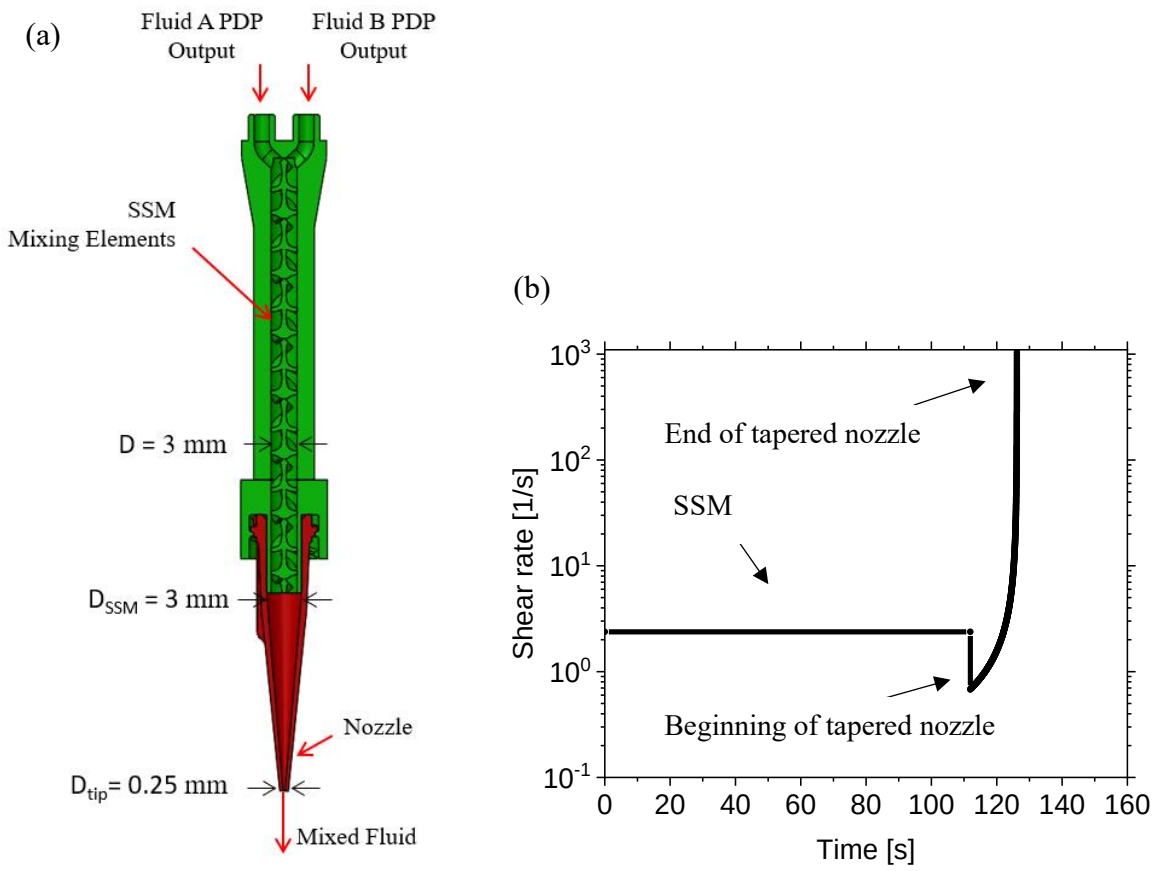

Figure 5-7. (a) Detailed view of the spiral static mixer (SSM) and tapered nozzle (TN) used in the DIW system. (b) Shear rate history in SSM (horizontal line) and in tapered nozzle, (curve for t > 111 s) computed as described in the text.

The area A, 7.06 mm^2, of the SSM is constant so that $\dot{\gamma}_{SSM}$, is constant. By dividing the volume of the SSM, V_{SSM} , by Q , the dwell time, t_{dwell}, that the fluid experiences in the SSM is

$$t_{dwell} = {}^{V_{SSM}}/_{Q} \tag{5-2}$$

The area $A_{nozzle}(x)$ of the nozzle at each position x along its axis is related to its diameter $D_{nozzle}(x)$ by $A_{nozzle} = \pi D_{nozzle}^2(x)$. Since the nozzle is tapered linearly, its diameter decreases linearly from its entry, where it has diameter D_{SSM}, to its tip, where it has diameter D_{tip}. We then can write $D_{nozzle}(x) = \frac{x(D_{tip}-D_{SSM})}{L_{nozzle}} + D_{SSM}$, where L_{nozzle} is the nozzle length. It follows that

the product $A_{nozzle}(x)D_{nozzle}(x) = \pi D_{nozzle}^3(x)$. Using these results and the formula $\dot{\boldsymbol{\gamma}}_{nozzle}(x) = 4K_{g,nozzle}Q/A_{nozzle}(x)D_{nozzle}(x)$, we find that

$$\dot{\boldsymbol{\gamma}}_{nozzle}(x) = \frac{4K_{g,nozzle}Q}{\left(\frac{x\left(D_{tip}-D_{SSM}\right)}{L_{nozzle}}+D_{SSM}\right)^3\pi} \tag{5-3}$$

The time it takes to ramp to the maximum shear rate at the tip of the tapered nozzle can be estimated using the same dwell time equation as is used for the SSM. By combining Eqs (5-1) and (5-3), the shear history of the fluid in the DIW can be generated.

For the printing of DIW slump cones described in this study, Q = 1.8 mm^3/s. The SSM has a diameter D of 3 mm, fluid volume V_{SSM} of 200 mm^3, and K_g= 28, as noted above. As a result, the dwell time of fluid in the mixer is $t_{dwell} = V_{SSM}/Q$ = 111 s, and $\dot{\gamma}$ = 2.3 s^{-1} from Eq. (1). The TN has D_{nozzle} = 0.25 mm, V_{nozzle} = 26 mm^3, and K_g = 8. The area A at the tip of the tapered nozzle is 0.2 mm^2, so that t_{dwell} = 14.4 s and $\dot{\gamma}$ = 1100 s^{-1}. The resulting shear history is shown in more detail in Figure 5-7(b).

5.5.3 Printing of Slump Cone

Definition of geometry. A slump cone test is commonly used to quantify the consistency of concrete, in both lab and field settings [22]. The size and shape of the slump cone allow quick determination of how concrete will hold its shape based on the deformation of the cone. We have created a modified miniaturized slump cone (DIW slump cone), demonstrated in Figure 5-8, based on the ASTM C143 standard, to differentiate the performance of different DIW materials. The DIW slump cone has the same wall angle θ = 10° relative to vertical as the ASTM C143 slump cone, but with reduced 20 mm base and 2.1 mm thick walls (made of seven 0.3mm thick lines). An approximate limiting height of 20 mm is achieved by LSR-5-PEG-4 and LSR-5-PEG-6 (and 30 mm for LSR-50-PEG-2 since this material can withstand higher print heights), while the 2.1 mm thick wall simulates a DIW printing scenario where material strength is important. Most of the PDMS/fumed silica materials slumped so quickly during printing that heights of 20 mm could not be obtained (with the exception of S-50-9 discussed later).

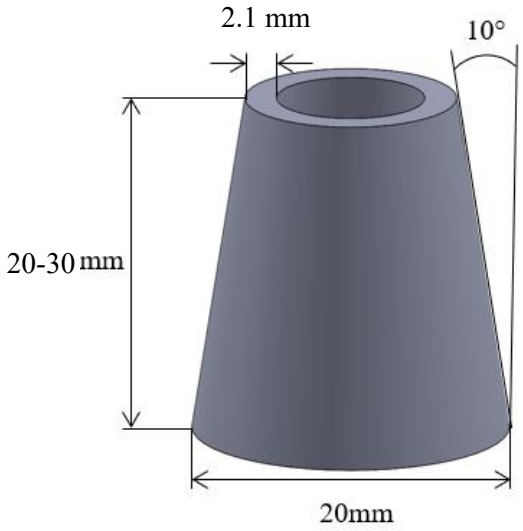

Figure 5-8. Geometry of miniaturized slump cone for DIW printed materials

The ability of slump cone to hold its printed shape provides a metric of the strength of the materials used in DIW, as shown based on an example in Figure 5-9, printed with extra-large layer lines to help visualize this behavior. Note that the DIW material, from the top of the slump cone downwards, transitions from distinct layers, to layers with noticeable compression, to yielded material, where the latter is identified by the distinctive bulge where the wall angle deviates from the original θ = 10°, as seen in Figure 5-9(a) and illustrated schematically in Figure 5-9(b).

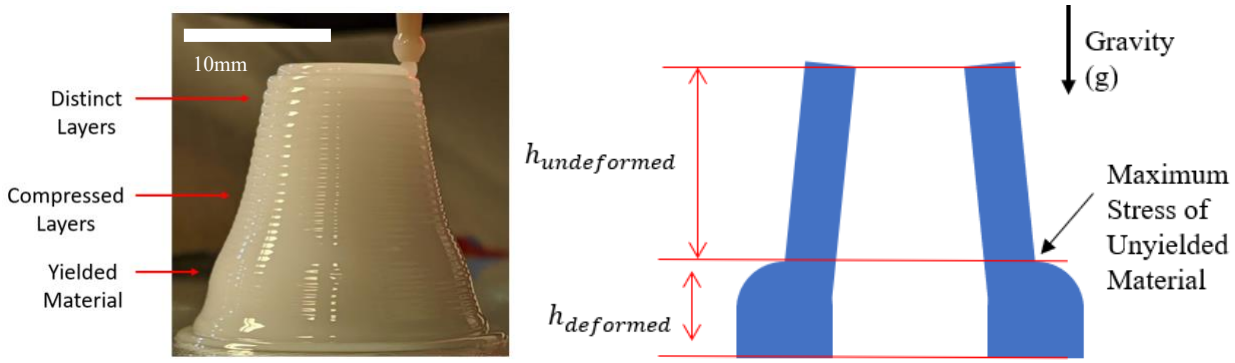

Figure 5-9. (a) DIW slump cone showing yielding during printing. (b) Yielding illustration of DIW material due to gravity.

Yield-stress assessment from slump cone. Printability failure is assessed through material yielding under gravity, identified by the distinctive bulge of the slump cone, discussed above. By measuring the height of the undeformed DIW material, $h_{undeformed}$ above the bulge, the experimental yield stress, σ_y, experienced by the yielded DIW material can be found using:

$$\sigma_y \approx g\rho h_{undeformed} \tag{5-4}$$

where g = 9.8 m/s^2 is the gravitational constant and ρ = 1.07 g/cm^3 is the approximate density of the materials used here. In principle, the right side of Eq. 4 should be divided by cos θ, where θ is the cone wall tilt angle, but since θ ≈ 10°, cos θ ≈ 1, this factor can be neglected here. A larger $h_{undeformed}$ indicates a higher yield strength and thus better performance in DIW applications, where it is expected to hold its 3D shape even though the material is in an uncured state. If a material flows after printing and resembles a puddle, it is considered to have zero yield strength so that $\sigma_y \approx 0$. If, on the other hand, the slump cone shows no sign of deformation, then the σ_y would need to be greater than stress experienced by the material at the base of the slump tower. Thus, σ_y would exceed the value given by Eq. (4), with $h_{undeformed}$ = 20 mm, which is the approximate maximum height of the slump cone printed with the LSR-5-PEG-4 and LSR-5-PEG-6 materials (30 mm for LSR-50-PEG-2). Thus, if there is no deformation at the base of the cone, then σ_y of the material would need to exceed 210 Pa (315 Pa for LSR-50-PEG-2).

Slump Cone Test Parameters. The DIW slump cones are printed at a print speed of 25 mm/s, a print height of 0.2 mm, and a line width of 0.3 mm. Measurement of the undeformed height is performed immediately after completion of printing using the measurement jig shown in Figure 5-10. The measurement of the dimensions of the slump cone is done by aligning the cone in a set position centered underneath a reference scale (305 ME, General Tools and Instruments, Secaucus NJ USA) using a sighting feature on the jig followed by the taking of a picture. Each measurement is then processed using an image processing program (ImageJ) to determine final dimensions using the attached scales in the measurement jig.

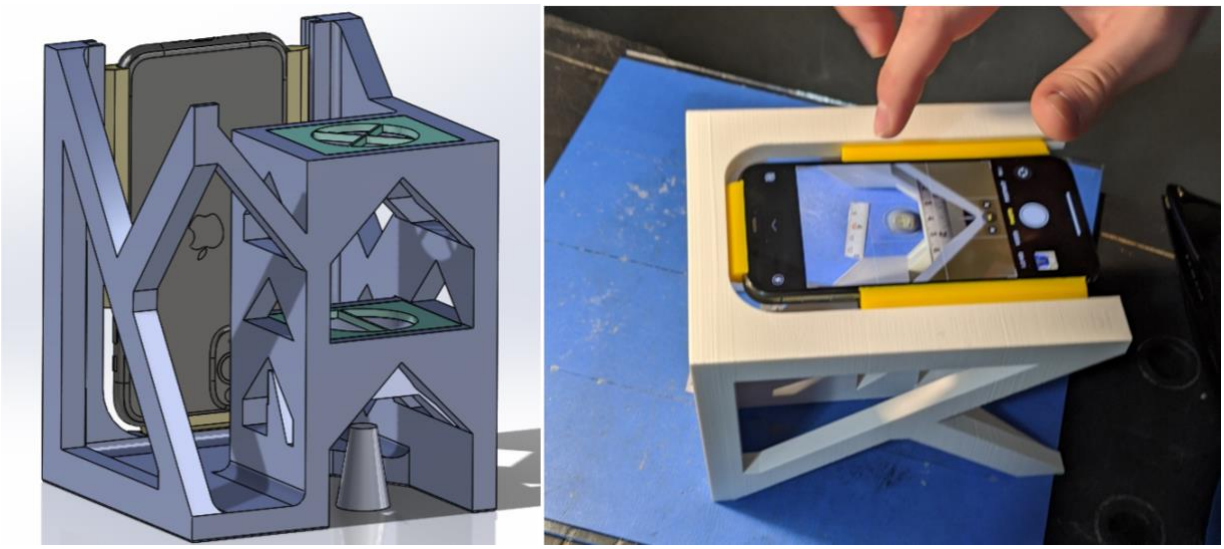

Figure 5-10. Jig for measuring dimensions of slump cones, all measurements are calibrated using the included scales and have a resolution of 0.025 mm.

DIW slump cones. As listed in Table 5-4, a total of 10 DIW slump cones each are printed for LSR-5-PEG-4 and LSR-5-PEG-6 materials because these materials' DIW slump cones could provide a good measurement of the yield strength of the material. One example slump cone was printed each for the LSR-5-PEG-2, LSR-50-PEG-2, S-50-7, S-13.5-7, and S-13.5-9 blends. In the case of the LSR-5-PEG-2, S-50-7, S-13.5-7, and S-13.5-9 materials, printing a tall DIW slump cone was impossible due to immediate failure. In the case of the S-50-9, factors beyond yield strength generated inconsistent results so only a few slump cones were printed. The LSR-50-PEG-2 material had a yield strength significantly greater than what the DIW slump cone used for this study could detect, so only one sample (reaching a stable printing height of 30 mm) is enough to demonstrate its yield strength.

Table 5-4. Materials and their DIW Slump Cones Test Quantity

Materials	S-13.5-7	S-13.5-9	S-50-7	S-50-9
DIW Slump Cones #	1*	1*	1*	3
Materials	LSR-5-PEG-2	LSR-5-PEG-4	LSR-5-PEG-6	LSR-50-PEG-2
DIW Slump Cones#	3*	10	10	3

*DIW slump cones quickly formed puddles due to materials' low yield stresses

5.6 Results and Discussion: Rheology

5.6.1 Shear Rate Ramps

Upward ramps in shear rate with PDMS-fumed silica. During an "upward shear-rate ramp," the shear rate was ramped from 0.001 s^{-1} up to 1000 s^{-1}, as mentioned above. An increasing percentage of fumed silica filler, from 0 to 9 wt%, produces a monotonically increasing viscosity in both 13.5 and 50 Pa·s PDMS, as can be seen in Figure 5-11.

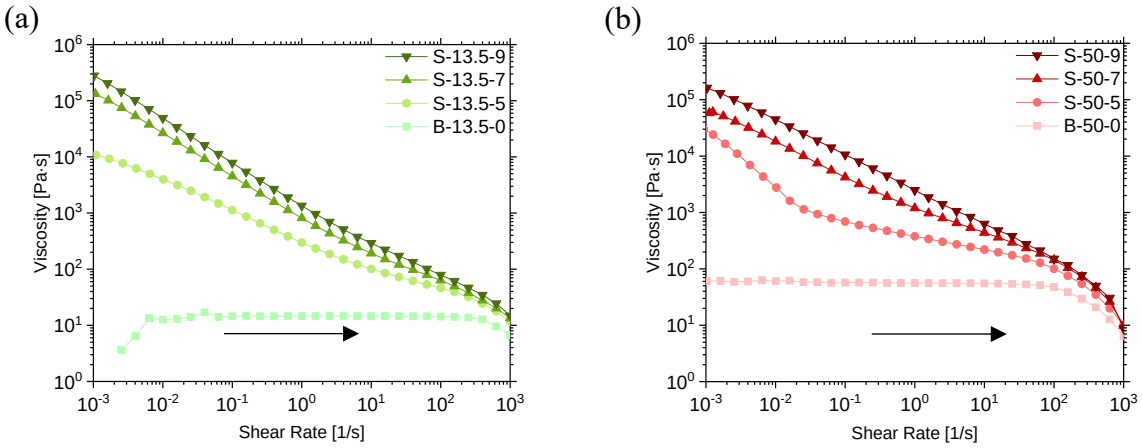

Figure 5-11. Upward shear-rate ramps at various fumed silica filler levels (0, 5, 7, 9 wt%) for samples with PDMS resin viscosities of (a) 13.5 Pa·s and (b) 50 Pa·s. Replicate measurements were performed at least three times and error bars are smaller than markers in this and following graphs.

In Figure 5-12, many of the data in Figure 5-11 are replotted but with each sub-plot having the same filler level (0, 5, 7, and 9 wt%) but varying PDMS matrix. The results show that the viscosity is dominated by the filler level and is insensitive to the PDMS resin viscosity, except for 0 wt% or "blank" samples (designated by "B", and shown in Figure 5-12(a)), which show the expected viscosities of 13.5 and 50 Pa·s. Interesting abrupt changes in power-law slope are observed in some cases (such as in Figure 5-11(b)), the causes of which are not at present known, but are found to be reproducible. As discussed below, the possibility of slippage or other geometry-dependent effects was checked by using other fixtures, and no significant changes in behavior were found.

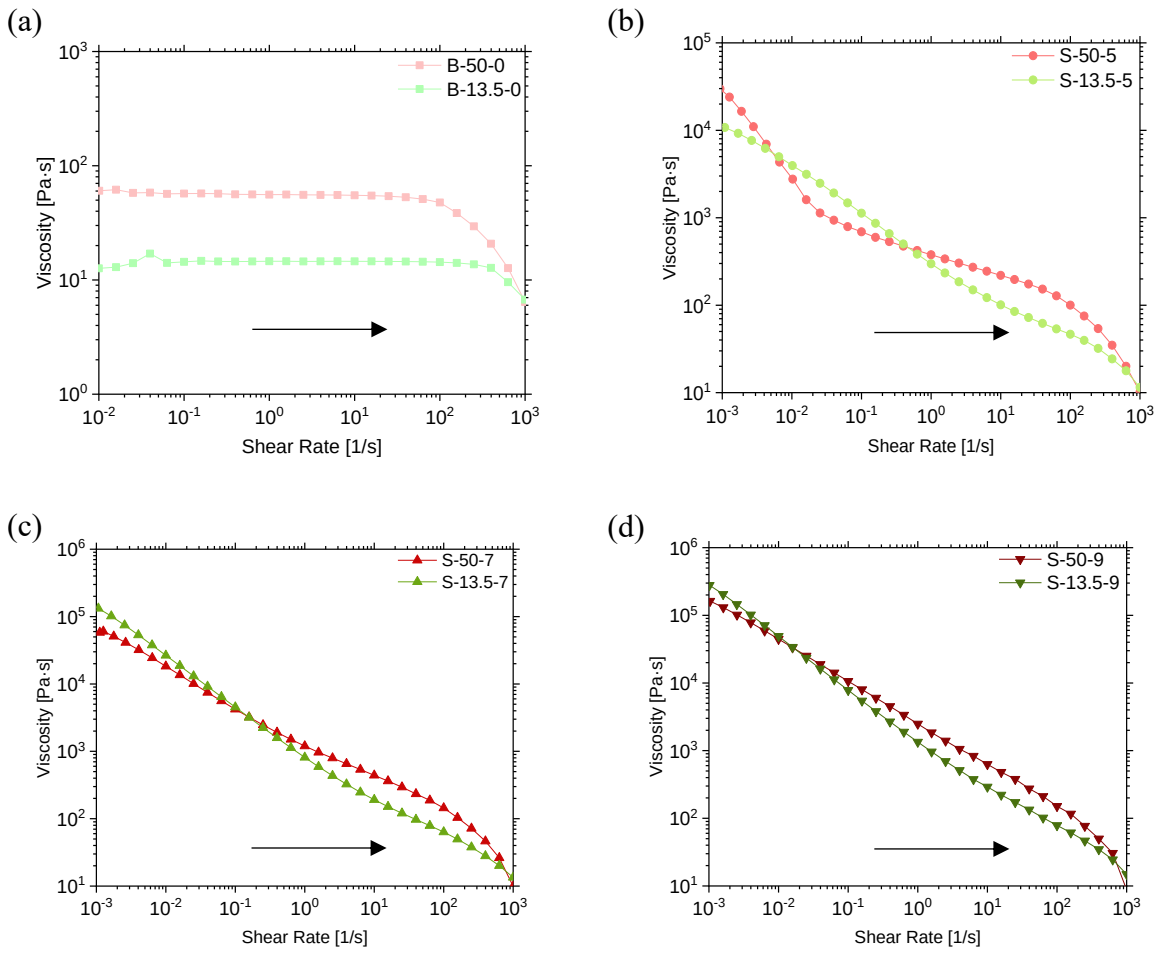

Figure 5-12. Upward shear-rate ramps of different PDMS samples with (a) 0 wt%; (b) 5 wt%; (c) 7 wt%, and (d) 9 wt% fumed silica filler.

Hysteresis in shear rate ramps with PDMS-fumed silica. While the results in Figures 5-11 and 5-12 were obtained in ramps of increasing shear rate, Figure 5-13 shows hysteresis in viscosity when, after reaching a shear rate of 1000 s^{-1}, the shear rate is ramped down from 1000 to 0.001s^{-1}. The "blank" samples with no fumed silica show almost no hysteresis (See Figure 5-14).

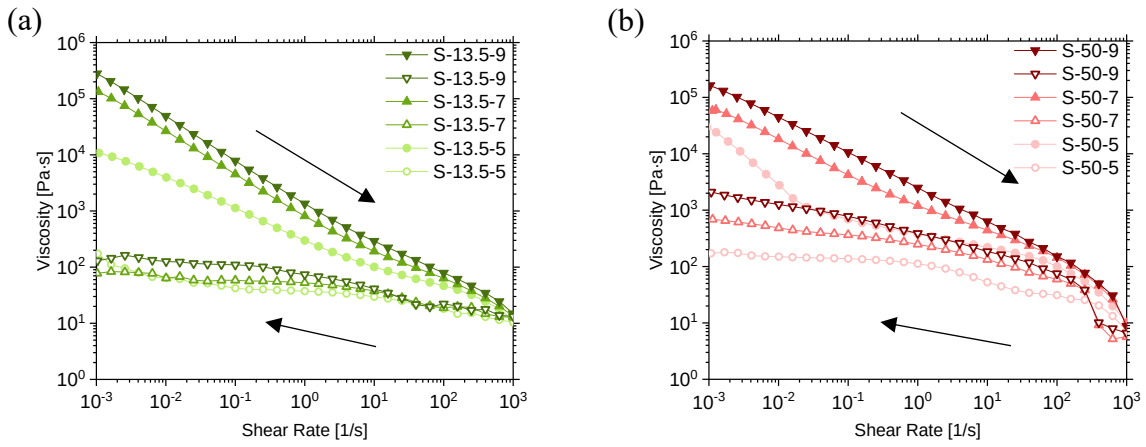

Figure 5-13. Upward and downward shear-rate ramps of (a) 13.5 Pa·s and (b) 50 Pa·s samples at three different fumed silica filler levels, showing hysteresis. In this and subsequent Figures, shear rate ramp-up curves are plotted with solid symbols while ramp-down curves are plotted with hollow symbols. The arrows indicate the directions of shear-rate change.

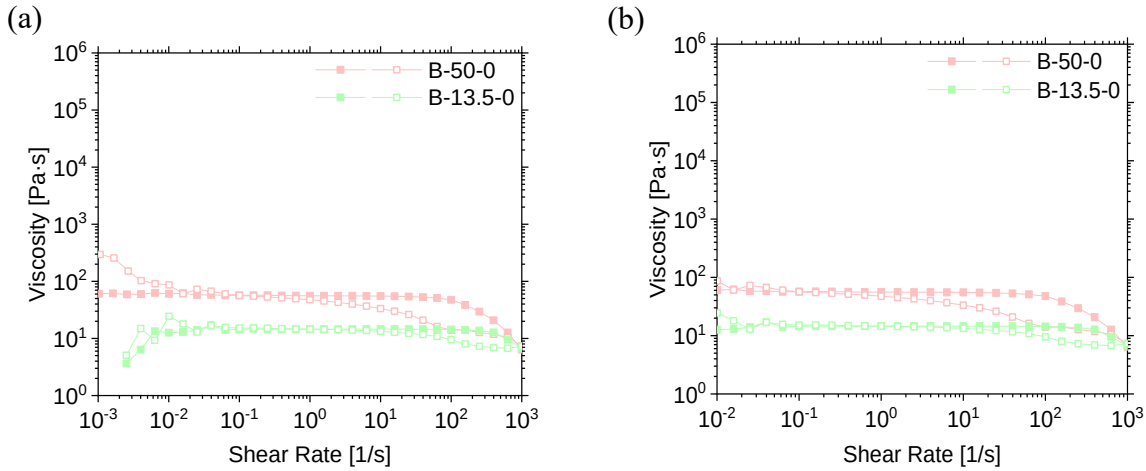

Figure 5-14. Shear rate results of the "blank" PDMS samples with no fumed silica in range of (a) 0.001 – 1000 s^{-1} and (b) 0.001 – 1000 s^{-1}, showing almost no hysteresis.

"Aging" effects with PDMS-fumed silica. Shown in Figure 5-15 are the "1st Runs" plotted with colored symbols, while "2nd Runs" were carried out on the same samples measured again six months later, plotted in black. Little change is seen except for 50 Pa · s samples, with the most pronounced change seen at a low shear rate, but with increased viscosity at the later time for S-50-9, but decreased viscosity for S-50-7, as shown in Figures 5-15(c) and (d). These changes due to aging do not affect our estimates of "yield stress" defined later.

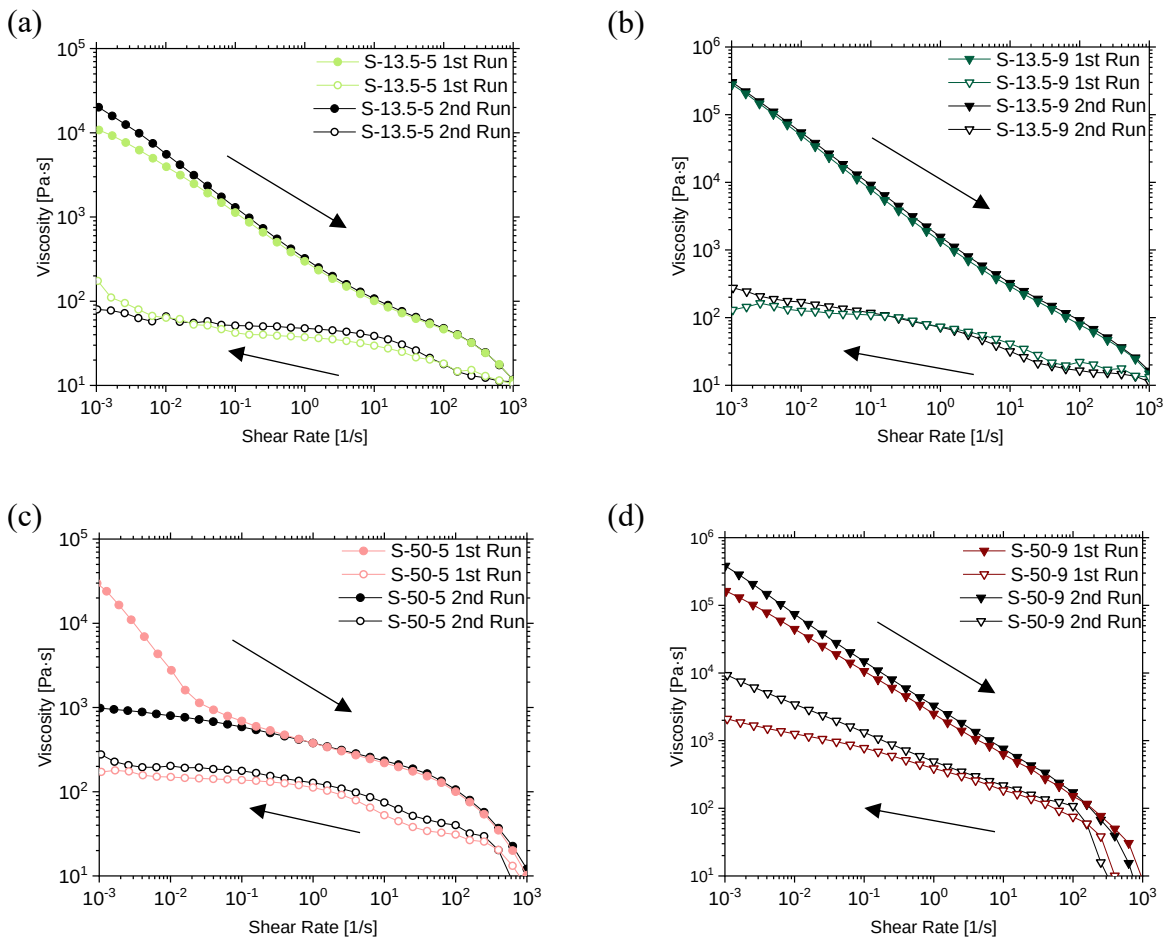

Figure 5-15. Upward and downward shear-rate ramps showing aging effects and hysteresis for samples with (a) 13.5 Pa · s and 5 wt% filler; (b) 13.5 Pa · s and 9 wt% filler; (c) 50 Pa · s and 5 wt% filler and (d) 50 Pa · s and 9 wt% filler. “1st Run” refers to measurements made soon after preparation and “2nd Run" made six months later with the same material.

Hysteresis in shear rate ramps with LSR-PEG. Results of ramp-up and ramp-down shearing on LSR/PEG materials are shown in Figure 5-16. LSR-50-PEG-2 has a higher viscosity over the entire shear rate ramps than the other three LSR-5-PEG samples, and a larger hysteresis. Despite differences in PEG weight percentages, LSR-5-PEG-2, LSR-5-PEG-4 and LSR-5-PEG-6 show little difference in the shear-rate-dependent viscosity.

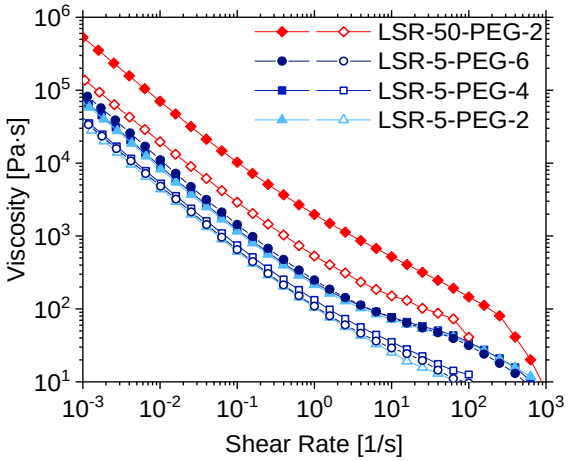

Figure 5-16. Upward and downward shear-rate ramps of LSR/PEG materials with different Shore hardness and PEG wt%; Solid symbols are for upward ramps and open symbols for downward ones.

Replotting of shear rate ramps against stress. To better estimate a "yield stress," we replot in Figure 5-17 the shear-viscosity hysteresis ramps from Figures 5-13 and 5-16 against shear stress rather than shear rate. Note that in the increasing shear-rate ramp, both the LSR and PDMS materials show high viscosities that are nearly independent of shear stress at the lowest shear stresses of around 100-1000 Pa. (The local maximum at low shear rates is likely produced because at the very low shear rates, around 0.001 s^{-1} the strain imposed is not high enough for the viscosity to reach steady state.) Thus, we approximate an "up-ramp yield stress" σ_y^+ as the value of this low-shear-rate stress at the maximum viscosity during increasing shear rate, which is in the range 40-400 Pa for the materials in Figure 5-17. The "down-ramp" yield stress σ_y^- can be estimated as the lowest stress obtained during the ramp-down of shear rate when viscosity is re-building. Figure 5-17(a) shows a steep increase in viscosity during the latter part of the decreasing shear rate, giving reasonably well defined "down-ramp yield stresses" in the range of 30-100 Pa for LSR/PEG materials. But PDMS materials show no distinct vertical upturn in viscosity during the decreasing shear rate; see Figure 5-17(b). Thus, from this test, we estimate $\sigma_y^- \approx 0$ for these materials in this test. Since even the stiffest of these PDMS-silica materials (S-50-9 and S-50-7) show negligible yield stress ($\sigma_y^- \approx 0$) in this test, we take all of them to similarly have a down-ramp yield stress σ_y^- in this test.

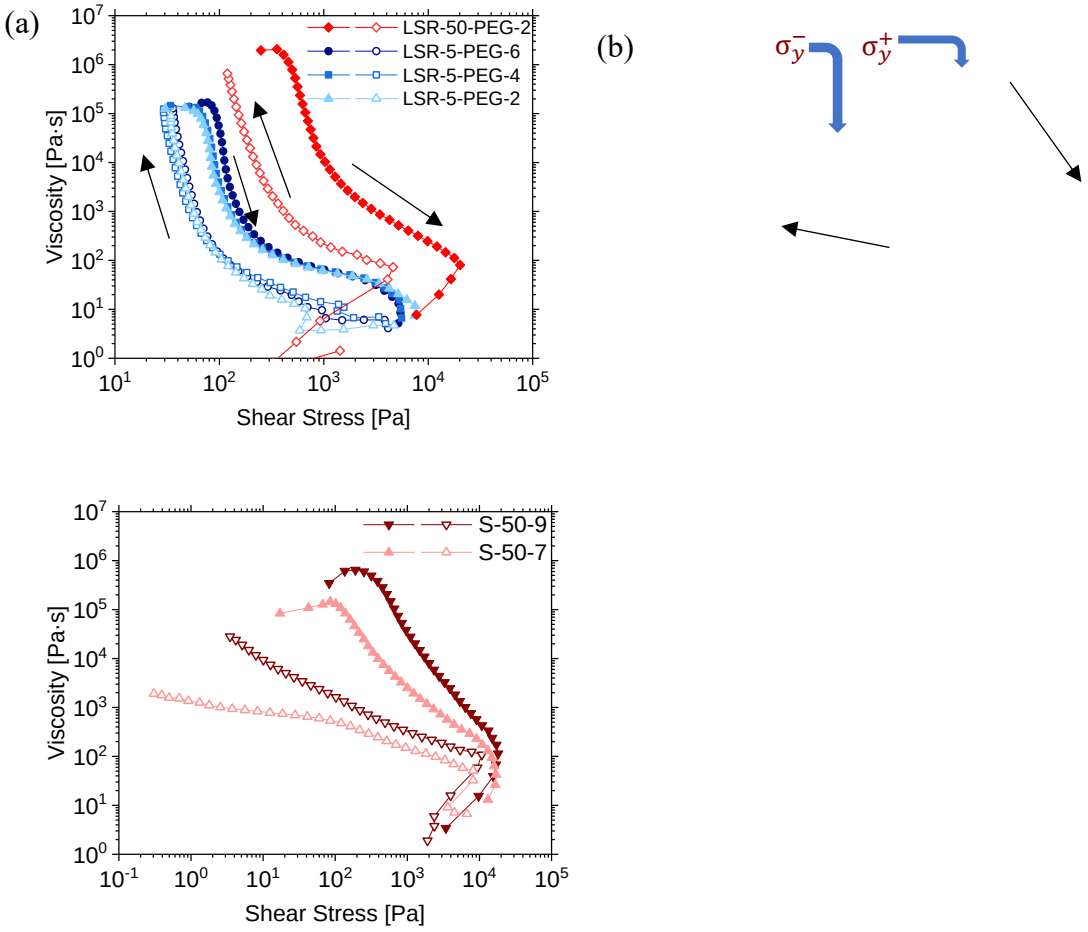

Figure 5-17. Shear rate ramps for (a) all four LSR/PEG and (b) two PDMS-fumed silica materials. Solid symbols represent the ramping up of shear rate and open symbols the ramping down of shear rate.

To test the effect of test geometry and possible influence of wall slip or inhomogeneous deformation, we also use different geometries to perform the shear-rate ramps. For instance, LSR-5-PEG-6 materials were tested by both sand-blasted 50mm parallel plates (gap = 0.213mm) as well as the sand-blasted 25mm cone and plate (gap = 0.105mm) used in all other measurements reported here. The results in Figure 5-18 show similar down-ramp yield stresses, indicating little effect of slippage or edge fracture. Note, however, that at the highest shear rate, there is deviation evident in the return down-ramp, which can be correlated with material temporarily emerging from the sample edge at the highest shear rate in some cases. Such behavior at the highest shear rate can also be seen in the decrease of shear stress during up- and down-ramps in Figure 5-17 at the highest shear rates.

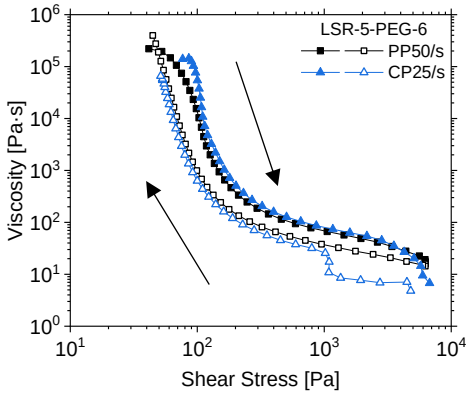

Figure 5-18. Shear rate ramps for LSR-5-PEG-6 using (a) 50mm sand-blasted parallel plate and (b) 25mm sand-blasted cone plate geometry. Solid symbols represent the ramping up of shear rate and open symbols the ramping down of shear rate.

5.6.2 Creep

In creep tests, we hold the stress at a constant value (100-1000 Pa for PDMS/fumed silica samples and 20-1000 Pa for LSR/PEG samples) for 300s, and then unload the stress for 300s and monitor the shear strain recovery. The same sample is subjected to a series of such creep stresses and recoveries, in sequence from lowest to highest. The results of these tests for PDMS/fumed silica are summarized in Figure 5-19, and results for LSR/PEG samples are shown in Figures 5-20 and 5-21.

From these tests, a "yield stress" value (σ_y) is obtained for each material as the maximum stress that can be applied without inducing either a pronounced upturn in the plot of log strain versus log time, or a loss of recoverable strain after removal of stress. To make this definition more precise, we set criteria for yield stress estimation are as follows:

1. *Power-law slope of the creep curve before unloading stress* ≥ 1, *and*
2. *Strain recovery at the end of the creep test* $\leq 5\%$

Since these two criteria give somewhat different values of the yield stress, we give a range of yield stresses in Figures below, with the lower bound set by satisfaction of the first criterion, and the upper bound set by the satisfaction of both criteria. Taking LSR-50-PEG-2 in Figure 5-21(a) as an example, criterion 1 is only met when the stress reaches 800 Pa, as shown by the dashed line, while the strain recoveries after creep tests at 600, 700 and 800 Pa are 8.8%, 4.2% and 1.8%.

Hence, criterion 2 if met for stresses above 600 Pa. Thus, the estimated yield stress for LSR-50-PEG-2 can be said to lie in the range $600 \leq \sigma_y \leq 700$ Pa.

Note in Figure 5-19 that samples with the lowest filler level (5 wt%, 0 wt%) do not show a yield stress, as we have defined it, and for these samples we can set $\sigma_y \sim 0$ Pa. In general, increasing PDMS viscosity (i.e., increasing PDMS molecular weight), or increasing the filler level, leads to a higher yield stress.

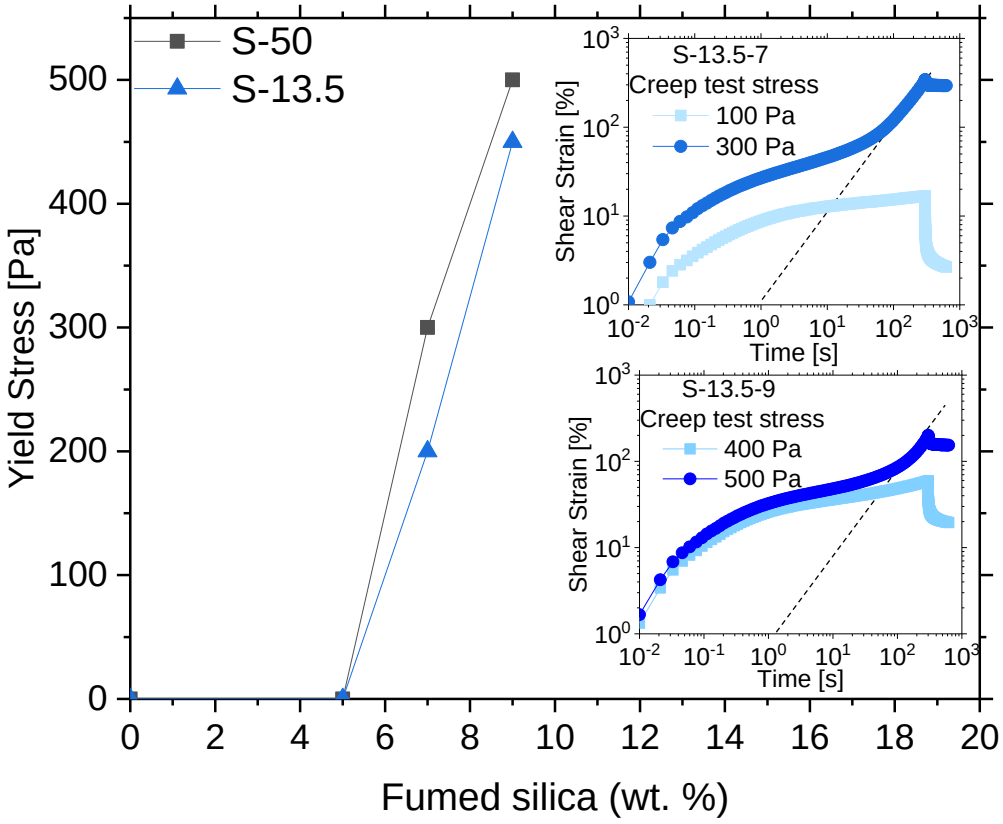

Figure 5-19. Yield stress estimations from creep tests for six model PDMS-fumed silica samples. Inserts show creep tests for S-13.5-7 and S-13.5-9. In this and subsequent figures, the dashed line indicates a slope of 1.

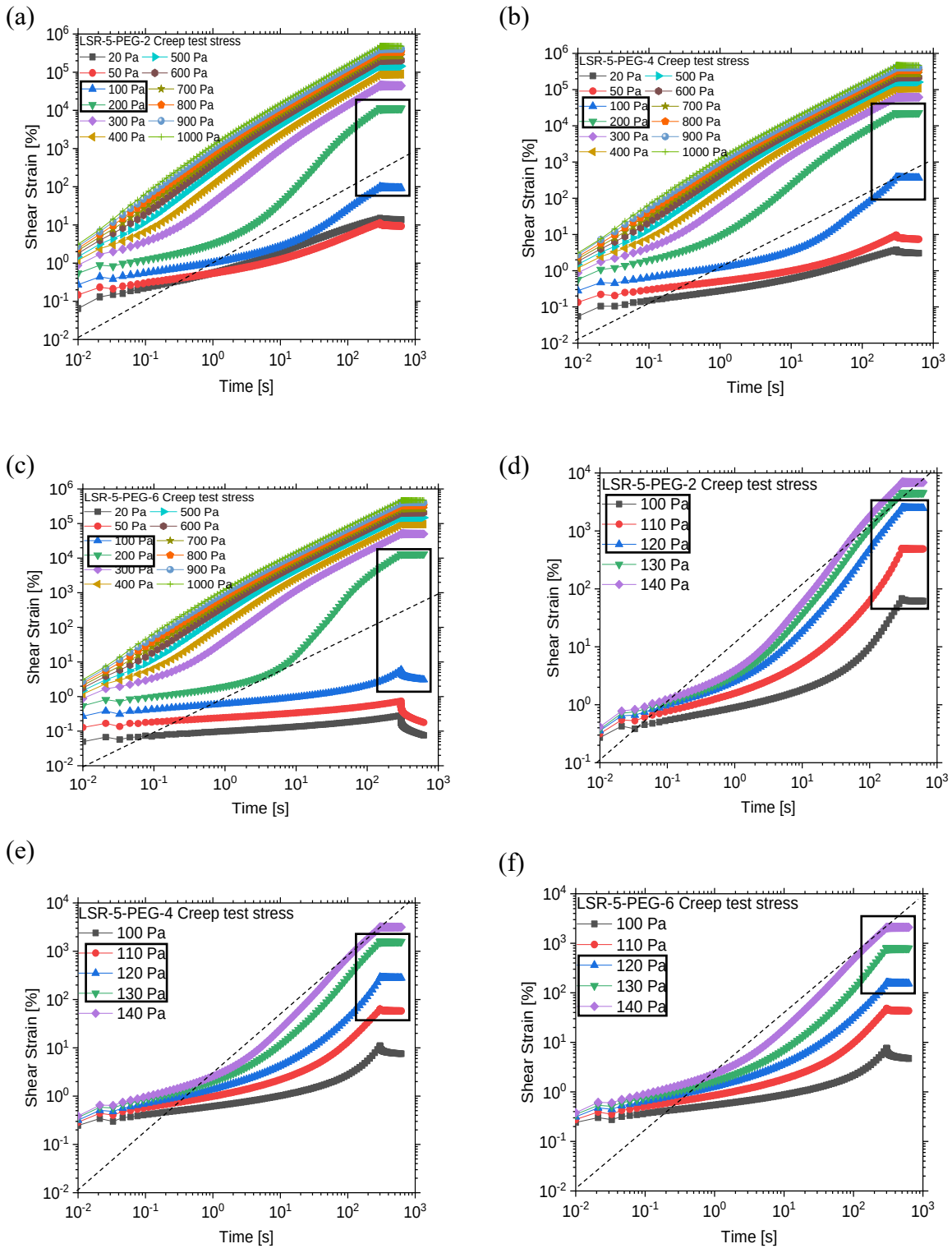

Figure 5-20. Creep tests between 20 and 1000 Pa for (a) LSR-5-PEG-2, (b) LSR-5-PEG-4 and (c) LSR-5-PEG-6 materials. Creep tests between 100 and 140 Pa for (d) LSR-5-PEG-2, (e) LSR-5-PEG-4 and (f) LSR-5-PEG-6 materials. The rectangular box encompasses the final portions of creep/recovery curves that are in the boundary region between yielding and not yielding, as defined in the main text.

Similarily the yield stress estimates are 600-700 Pa for LSR-50-PEG-2, and 100-200 Pa for the LSR-5-PEG series of materials (See Figure 5-20(a-c)). To better resolve the yield stresses for the LSR-5-PEG materials, additional creep tests in the range 100-140 Pa were conducted (see Figure 5-20(e-f)). From Figure 5-21(b), yield stresses thereby obtained are 100-120 Pa for LSR-5-PEG-2, 110-130 Pa for LSR-5-PEG-4 and 120-140 Pa for LSR-5-PEG-6. The small differences between these three ranges are not large enough to distinguish the yield stresses of these samples. Any differences in printability of these samples must therefore be explained using other rheological tests.

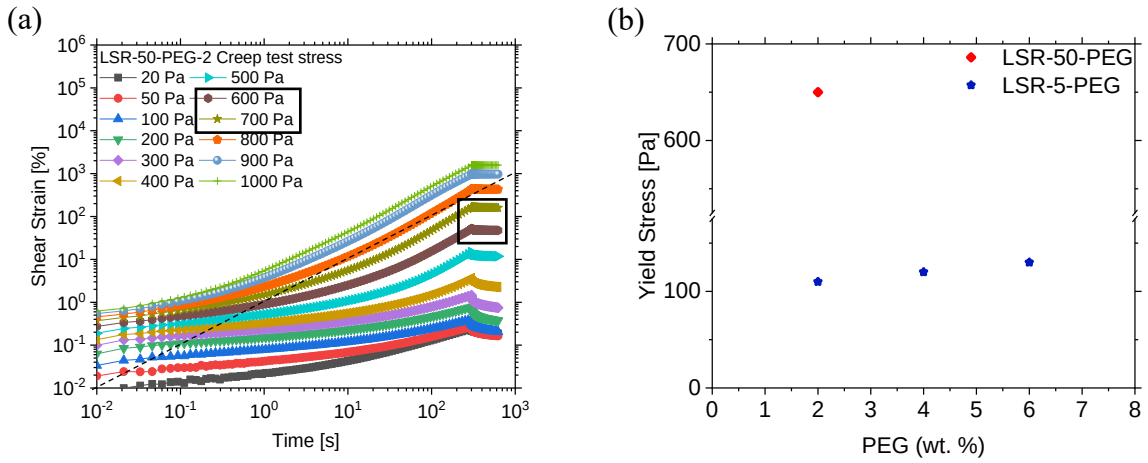

Figure 5-21. Creep tests for (a) LSR-50-PEG-2, and (b) yield stress estimations for LSR/PEG materials. The rectangular box encompasses the final portions of creep/recovery curves that are in the boundary region between yielding and not yielding, as defined in the text.

Creep tests are typically used to measure the "static yield stress," but our samples show continuous slow creep under any stress that we have applied, and so we have used the power-law slope of the creep and the recoverable strain after creep as an indication of a "static" yield stress. Strain sweeps in oscillatory shearing (amplitude sweep tests) or shear-rate sweeps in unidirectional shearing can be used to obtain measures of a "dynamic" yield stress or a so-called "flow stress" in oscillatory shearing as discussed in the summary of literature. Pre-shear at a high shear rate followed by a creep test at a stress lower than yield stress can be used to see if the pre-shear will affect the "static" yield stress.

5.6.3 Strain Amplitude Sweeps

Strain amplitude sweeps were conducted at 0.5 Hz ranging from 0.01% to 1000% strain. Figure 5-22 shows the results plotted against stress amplitude for PDMS and LSR/PEG materials. The yield stress or "flow stress" is defined in this test as the shear stress amplitude at which G' and G'' cross over. Table 5-5 below lists the crossover flow stresses and moduli for eight of the printing materials. The "moduli" given in Table 5-5 are the values at the crossover.

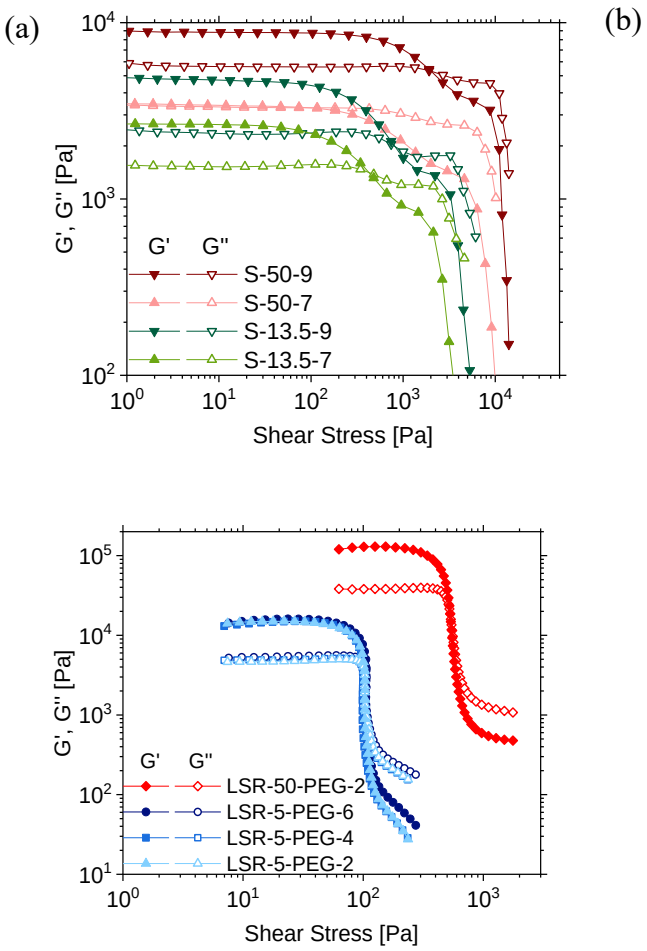

Figure 5-22. Results for strain amplitude sweeps at 0.5 Hz plotted against stress amplitude for (a) PDMS and (b) LSR/PEG materials. Solid symbols represent G' and open symbols G''.

Table 5-5. Flow stress estimates from amplitude sweep tests in Figure 5-22 (Unit: Pa)

PDMS-silica	Modulus	Flow Stress	LSR-PEG	Modulus	Flow Stress
S-13.5-7	1425±45	450±15	LSR-5-PEG-2	3900±50	99±1
S-13.5-9	1950±100	850±45	LSR-5-PEG-4	4300±40	103±1

S-50-7	3275±15	200±5	LSR-5-PEG-6	5760±50	106±1
S-50-9	5400±50	2000±20	LSR-50-PEG-2	18500±150	530±5

5.7 Results and Discussion: 3D Printing

The DIW slump cone was printed using the S-50-9, S-50-7, S-13.5-9, and S-13.5-7 PDMS-silica formulations. The first three of these, as shown in Figure 5-23, showed no ability to build a 3D object and immediately flowed into a puddle following printing. This indicates that the material has an approximate yield strength of ~ 0 Pa for all three of these materials. For this reason, there was no need to print the materials with even lower levels of silica filler (S-50-5 and S-13.5-5), as these have even lower viscosity and yield stress, as our rheological studies have shown.

Figure 5-23. DIW slump cones for (a) S-50-7, (b) S-13.5-7 and (c) S-13.5-9

The S-50-9 PDMS-silica formulation was in some cases able to be printed into a recognizable slump cone, as shown in Figure 5-24, indicating the material has yield strength after being printed. However, due to a combination of batch-to-batch inconsistency, entrapped air, and difficulties loading the material into the DIW system, we were not able to generate consistent results with this material, with complete failure (i.e., an irregular print in Figure 5-24(a) and puddling in Figure 5-24(b)) in some cases. The printed slump cones always showed substantial irregularities even in the best cases, as shown in Figure 5-24(a). Since the best printing produced slump cones without recognizable buckling or flow, we might take the yield stress for this material to be at least as high as the maximum value, corresponding to the maximum print height of 30 mm for the PMDS-silica and LSR-50-PEG-2 materials (where 20 mm maximum height was used for the LSR-5-PEG materials), and use Eq. (4) to estimate that σ_y > 315 Pa. Note, however, that this "yield stress" does not imply a successful printed part, given the highly defective structure obtained, even in the best case. Thus, we acknowledge that the printability "yield stress" for this

material could legitimately be considered to be virtually zero, or as high as 315 Pa, or higher, and we must regard this case as one that gives us an ambiguous printability "yield stress." Note that the much higher viscosity obtained for S-50-9 than for S-50-7 during the down-ramp in shear rate in Fig. 5-17(c) is consistent with the former material's better printability seen in Fig. 5-17(a) compared to the complete failure of printing of the S-50-7 observed in Fig. 5-16(a).

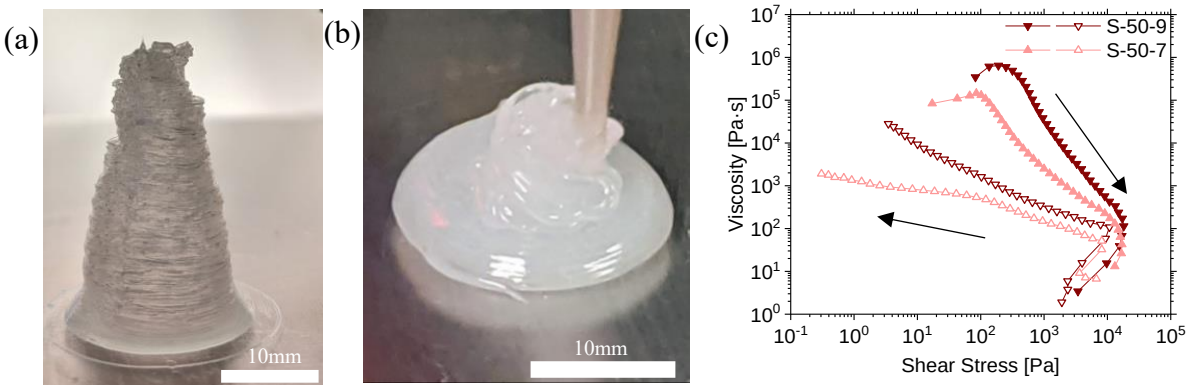

Figure 5-24. (a) DIW slump cone, (b) puddling print (where a wider nozzle is used) for S-50-9 material. This range of behavior changes from a more "successful" printing to a completely failed printing. (c) Shear rate ramps for S-50-9 and S-50-7 materials.

Example slump cones for the LSR-5-PEG-4 and LSR-5-PEG-6 materials can be seen in Figure 5-25. The slump cone for LSR-5-PEG-4, shown in Figure 5-25(c), shows significant bulging around the base of the cone and is noticeably different from that in Figure 5-25(b) for LSR-5-PEG-6, which shows a much more robust structure with only slight bulging at the base and approximates much more closely the schematical slump cone shown in Figure 5-8.

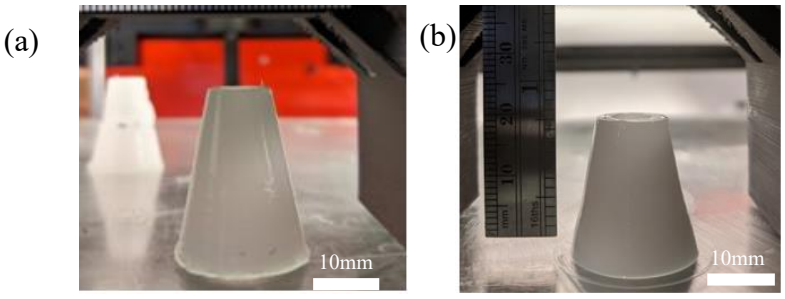

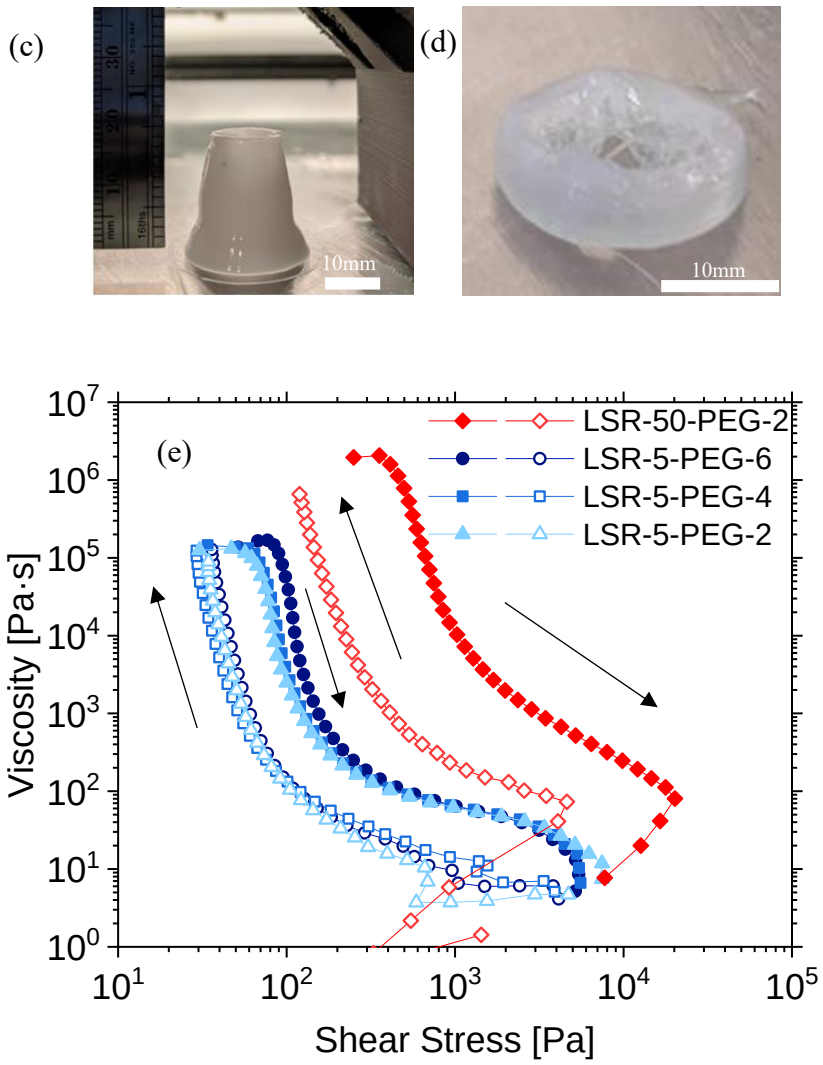

Figure 5-25. DIW slump cones for (a) LSR-50-PEG-2, (b) LSR-5-PEG-6, (c) LSR-5-PEG-4 and (d) LSR-5-PEG-2 materials; (e) Shear rate ramps for four LSR/PEG materials

Using the method described in section 5.5 and Eq. (4), and applied to 10 replicates for LSR-5-PEG-4 and LSR-5-PEG-6 materials, the average yield stresses σ_y extracted from the slump cone tests for LSR-5-PEG-4 and LSR-5-PEG-6 are 135.8± 5.0 Pa and 153.7± 4.9 Pa, respectively, where the errors are standard deviations. In Figures 5-25(d) and (a), slump-cone results for LSR-5-PEG-2 and LSR-50-PEG-2 can be compared, showing the strong influence of the Shore hardness on printability. The LSR-5-PEG-2 fails immediately, forming a puddle during printing, indicating that it had a printing yield stress of ~ 0 Pa, while the LSR-50-PEG-2 could print a slump cone up to a height of 30 mm, indicating a printing yield stress σ_y greater than 315 Pa. The excellent

printing of LSR-50-PEG-2 is consistent with the high viscosity obtained for this material in ramp-down of shearing, as shown in Fig. 5-18(e) by the red open symbols. However, the differences in printability among the LSR-5 materials seen in Figs. 5-18(b)-(d) are not reflected in the ramp-up or ramp-down test results in Fig. 5-18(e), and so other rheological tests seem to be necessary to differentiate the printability of these materials.

5.8 Comparison of Yield Stresses from 3D Printing and Rheology

We now seek to link our rheological measurements to the "printability" of each material. Using the "yield stress" measured in printing and in the various rheological tests as our metrics, we assemble all values obtained, as described above, into Table 5-6. We note that the "yield stresses" extracted from most of the tests fail to correlate with the very poor printability of the PDMS-silica materials relative to the more printable LSR-PEG materials at high PEG loading. In fact, the downward shear ramp, following the upward ramp, is the only one of the tests that correctly predicts printing failure in all PDMS-silica materials, with the possible exception of S-50-9. Recall that S-50-9 printed unreliably, with the best case producing the defect-ridden, slumping, or puddling structures shown in Figure 5-14. The downward ramp for this material likewise produced an ambiguous result, somewhere between a horizontal, or viscous response and a vertical, or yield-stress response, as shown in Figure 5-18(b). Note that the upward shear-rate ramp is particularly poor at predicting printability. The PDMS-silica materials show roughly similar stresses and viscosities as the LSR-PEG materials during increasing shear-rate tests, but these materials are drastically different in the downward shear-rate ramps. *It appears that the downward ramps, after reaching a high shear rate of 1000 s^{-1}, are particularly relevant to printability*. This is perhaps not surprising, since during printing the material must pass through a nozzle with a high shear rate of around 1000 s^{-1}. *The inability of the PDMS-silica materials to rebuild yield stress after this high shear rate appears therefore to be responsible for the failure of this material to print.* The importance of the material's rheological recovery after fast shearing was observed in previous work, including that of M'Barki [16] and Romberg et al. [17], as discussed in the Introduction.

Table 5-6. Estimation of Yield stresses from Rheology and Printing (Unit: Pa)

Materials	From Rheology				From Printing
	Shear ramp		Creep	Amplitude Sweep in oscillatory shearing ("flow stress")	
	Upward σ_y^+	Downward σ_y^-			
B-13.5-0	~ 0	~ 0	~ 0	~ 0	~ 0
S-13.5-5	~ 0	~ 0	~ 0	~ 0	~ 0
S-13.5-7	150	~ 0	200	450±15	~ 0
S-13.5-9	180	~ 0	450	850±45	~ 0
B-50-0	~ 0	~ 0	~ 0	~ 0	~ 0
S-50-5	5	~ 0	~ 0	~ 0	~ 0
S-50-7	85	~ 0	300	200±5	~ 0
S-50-9	190	~ 0	500	2000±20	0-315
LSR-5-PEG-2	45	30	110	99±1	~ 0
LSR-5-PEG-4	50	30	120	103±1	136 ± 5
LSR-5-PEG-6	80	30	130	106±1	154 ± 5
LSR-50-PEG-2	355	100	650	530±5	>315

Both creep and the oscillatory amplitude sweeps showed an appreciable "yield stress" for the PDMS materials containing 7 wt% or 9 wt% fumed silica, and thus neither of these tests provides a reliable indicator of the lack of printability of these materials. Again, this might well be because both the creep test and the oscillatory shear test measure an "upward" yield stress during increasingly strong shearing. Thus, neither of these tests reflects the ability of the material to regain strength following a high-rate shearing. To see whether a creep test could provide a different, and possibly better, measure of printability if performed on a material that has been previously sheared

at a high rate, we show in Figure 5-26 the results of a creep test at 50 Pa after a pre-shear of either 10, 100, or 1000 s^{-1}, with waiting times after the pre-shear of 0, 5, or 20 min. Note that after a low pre-shear rate of 10 s^{-1}, the subsequently imposed shear stress of 50 Pa is not high enough to induce yielding, as measured by the creep strain and recovery afterward, while a pre-shear rate of 100 or 1000 s^{-1} clearly lowers the subsequent "yield stress" to a value below 50 Pa. This is consistent with the very low value of σ_y^- inferred from the down-ramp in shear rate in Figure 5-18(b) for this material. Since the S-50-9 material in Figure 5-26 is the most robust of all the PDMS-silica materials, the others are expected to be even more sensitive to reduction or loss of yield stress following a fast prior flow. *Thus, a key property enabling printability is the robustness of the material to the high shear rate in the nozzle, as measured by its ability to quickly re-grow a significant yield stress following a high rate of shear.*

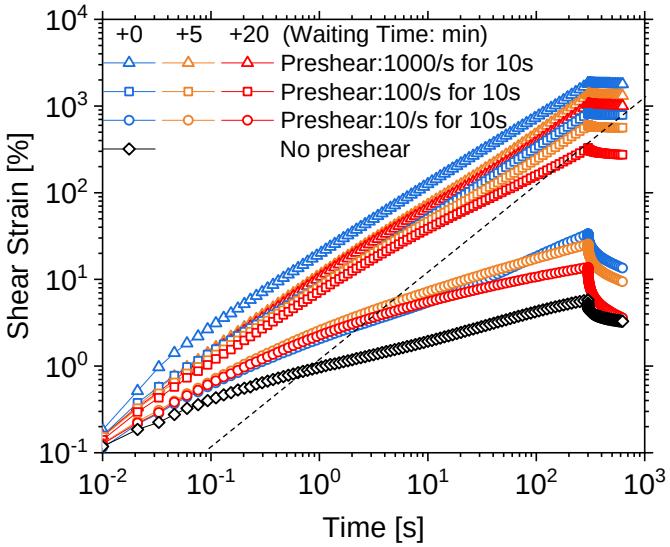

Figure 5-26. Creep tests at 50 Pa for S-50-9 following pre-shear at rates of 10/s (circles), 100/s (squares) or 1000/s (triangles) for 10s, and a wait time of for 0 (blue), 5 (orange) or 20 min (red). The black curve is the reference creep test at 50 Pa without any preconditioning/pre-shearing.

A downward shear ramp or pre-shear prior to measurement of a yield stress therefore appears to be the "most successful" method in identifying the materials that will or will not print. However, the "yield stress" values obtained from the downward shear-rate ramp do not accord particularly well with the yield stress values estimated from printing. Only two of our printed materials, namely LSR-5-PEG-4 and LSR-5-PEG-6, allowed for determination of a definite "yield stress" values that were not either near zero or a lower bound, and these estimated values were

better predicted by the creep and amplitude sweep tests than by the downward shear-rate ramp. Thus, we might infer that a combination of the downward shear ramp and either creep or an amplitude-sweep test might provide the best indication of the "printability" of the materials studied here.

5.9 Summary

We have measured the Direct Ink Write (DIW) 3D "printability" of two series of non-curing filled polydimethylsiloxane (PDMS) materials, the first consisting of resins with zero-shear viscosities of 13.5 and 50 $Pa \cdot s$, and fumed silica concentrations from 5 to 9 wt%, and the second consisting of two-part "liquid silicone rubber" (LSR) of Shore hardness of 5A and 50A with polyethylene glycol (PEG) added at concentrations of 2 to 6 wt%. We printed these materials into hollow "slump cones with 20 mm diameter base, 2 mm thickness and 10° angle, of heights up to 20-30 mm. We assessed the printability by determining whether the printed material could avoid slumping or flowing sufficiently to be printed to the desired height, and, if so, whether or not the cones buckled under gravity. By measuring the height of printed material above any buckling position, and using this height and material density, we estimated the "yield stress" at the buckling position. The printing "yield stress" was then compared to four different rheological measures of yield stress. These are obtained (see Table 5-6) as follows: 1) The shear rate was ramped up to a value (~1000 s^{-1}) typical at the nozzle tip of the 3D printer. The roughly constant stress obtained in the low-shear-rate portion of this ramp was taken as the up-ramp yield stress σ_y^+. 2) After the up-ramp in shear rate to 1000 s^{-1}, the shear rate is ramped down to a very small value (10^{-3} s^{-1}), and a "down-ramp yield stress" is determined as the stress σ_y^- where shear rate reached a near zero value during decreasing shear rate. 3) A series of constant shear stresses were imposed in order of increasing stress and the minimum stress value needed for the material to flow at an appreciable rate and lose the ability to recover significant strain after stress removal is identified as a yield stress. 4) Large amplitude oscillatory shearing is carried out and the stress amplitude at which G' and G'' cross defines a yield stress or "flow stress." We found that the PDMS-fumed silica suspensions were poorly, or not at all, printable, and that this lack of printability was only forecast by method 2) where a yield stress is estimated at low shear after the material had been previously sheared at a high rate, characteristic of flow through the nozzle during 3D printing. The LSR

materials are printable at high PEG loading, consistent with the retention of a reasonably high yield stress in these materials after a previous high shear rate, while the PDMS-silica materials are not printable, consistent with their failure to show a significant yield stress after a previous high shear rate. Thus, DIW printable materials need to not only have a reasonably high yield stress but must be able to rebuild this yield stress quickly following the high shear rate in the nozzle of the printing head. One rheological test capable of assessing this behavior is a shear rate up-ramp followed by a down-ramp, with the yield stress determined at the end of the down-ramp. While this test can discriminate reliably between printable and non-printable materials, quantifying more precisely the degree of printability from rheology and relating it more exactly to the quality of the 3D printing for a given geometry, will clearly require more work, and may require combining the results of multiple rheological tests. The work performed here provides a step towards the goal of developing a rheological testing regimen that reliably predicts the printability of multiple material types in multiple geometries.

5.10 Reference

[1] J.A. Lewis, G.M. Gratson, Direct writing in three dimensions, Mater. Today. 7 (2004) 32–39.

[2] J. Go, S.N. Schiffres, A.G. Stevens, A.J. Hart, Rate limits of additive manufacturing by fused filament fabrication and guidelines for high-throughput system design, Addit. Manuf. 16 (2017) 1–11.

[3] E. Feilden, C. Ferraro, Q. Zhang, E. García-Tuñón, E. D'Elia, F. Giuliani, L. Vandeperre, E. Saiz, 2017. 3D Printing Bioinspired Ceramic Composites, Sci. Rep. 7, 13579.

[4] A. Corker, H.C.H. Ng, R.J. Poole, E. García-Tuñón, 3D printing with 2D colloids: designing rheology protocols to predict "printability" of soft-materials, Soft Matter. 15 (2019) 1444–1456.

[5] S.V. Murphy, A. Atala, 3D bioprinting of tissues and organs, Nat. Biotechnol. 32 (2014) 773–785.

[6] Y. Jin, J. Plott, A.J. Shih, Extrusion-based additive manufacturing of the moisture-cured silicone elastomer, Proc. Solid Free. Fabr. Symp. (2015) 308–318.

[7] L. Hao, D. Tang, T. Sun, W. Xiong, Z. Feng, K.E. Evans, Y. Li, Direct ink writing of mineral materials: a review, Int. J. of Precis. Eng. and Manuf. - Green Tech. 8 (2021) 665-685.

[8] A.S. Wu, W. Small IV, T.M. Bryson, E. Cheng, T.R. Metz, S.E. Schulze, E.B. Duoss, T.S. Wilson, 2017. 3D printed silicones with shape memory, Sci. Rep. 7, 4664.

[9] P.A. Amorim, M.A. d'Ávila, R. Anand, P. Moldenaers, P. Van Puyvelde, V. Bloemen, Insights on shear rheology of inks for extrusion-based 3D bioprinting, Bioprinting, Volume 22, 2021, e00129.

[10] P.C.F. Moller, J. Mewis, D. Bonn, Yield stress and thixotropy: on the difficulty of measuring yield stress in practice, Soft Matter 2 (2006) 274-283.

[11] D.C.H. Cheng, Yield stress: a time-dependent property and how to measure it, Rheol. Acta 25 (1986) 542-554.

[12] R.G. Larson, The structure and rheology of complex fluids, Oxford Univ. Press, New York, 1999.

[13] F.A. Morrison. Understanding rheology, Oxford Univ. Press, New York, 2001.

[14] E.J. Courtial, C. Perrinet, A. Colly, D. Mariot, J.M. Frances, R. Fulchiron, C. Marquette, Silicone rheological behavior modification for 3D printing: evaluation of yield stress impact on printed object properties, Addit. Manuf. 28 (2019) 50–57.

[15] D. Kokkinis, M. Schaffner, A.R. Studart, 2015. Multimaterial magnetically assisted 3D printing of composite materials, Nat. Commun. 6, 8643. https://doi: 10.1038/ncomms9643

[16] A. M'Barki, L. Bocquet, A. Stevenson, 2017. Linking Rheology and Printability for Dense and Strong Ceramics by Direct Ink Writing, Sci. Rep. 7, 6017.

[17] S.K. Romberg, M.A. Islam, C.J. Hershey, M. DeVinney, C.E. Duty, V. Kunc, B.G. Compton, 2021. Linking thermoset ink rheology to the stability of 3D-printed structures, Addit. Manuf. 37, 101621.

[18] A.R. Avdeev, A.A. Shvets, I.S. Torubarov, Investigation of Kinematics of 3D Printer Print Head Moving Systems, Lect. Notes in Mech. Eng., Springer, Cham. (2019) 461–471.

[19] I.E. Moyer, CoreXY, (2012). http://corexy.com/theory.html.

[20] J.F. Lea, H. V. Nickens, M.R. Wells, Progressing Cavity Pumps, in: Gas Well Deliquification. 2003, pp. 383–403.

[21] E.L. Paul, V.A. Atiemo-Obeng, S.M. Kresta, Handbook of Industrial Mixing, John Wiley & Sons, 2003.

[22] ASTM International, ASTM C14s / C143M-20, Standard test method C143: slump of hydraulic-cement concrete, (2020). https://doi:10.1520/C0143_C0143M-20.

Chapter 6
Conclusion and Future Work

6.1 Polyelectrolyte Phase Behavior

We have developed quantitative methods of measuring phase compositions for the strong polyelectrolytes PSS/PDADMA, and the weak/strong mixture PAA/PDADMA, and have acquired preliminary data, which provide approaches to compare with the phase diagrams predicted by recently proposed models to validate and/or modify the theoretical work. We expect eventually to gain a much deeper understanding of polyelectrolyte interactions, thermodynamics, and phase behavior, leading also to the ability to predict transport properties, such as those in Layer-by-Layer assemblies.

The presence of a lower critical salt concentration at low pH implies phase separation in that range is driven by non-electrostatic effects and that salt actually increases the driving force for phase separation. These novel and unusual results shows clearly that we have much to learn about polyelectrolyte phase behavior, and that our methods show great promise in revealing new phenomena and new ways to control coacervation and other phenomena related to it.

6.2 Rheological Characterization of Polyelectrolyte Coacervates

The linear rheology of PECs remains an intriguing topic for future research. Clear, detailed, and well-confirmed theories are not yet available, but common features in differing systems that suggest that some broadly applicable theoretical concepts are ripe for discovery and exploitation. Beyond imaginative theorizing, definitive results will likely require more careful rheological experiments to establish the range of validity of the various superposition principles, to establish more clearly which polyelectrolyte systems have a low-frequency plateau modulus that is outside the range of experimental uncertainty, and to explore more widely the effects of different monomer and salt types. In addition, insightful experiments that probe local dynamics, such as advanced

versions of NMR and neutron scattering, as well as accurate atomistic molecular dynamics simulations, should help resolve if and when local dynamics can be regarded as a kind of sticky diffusion governed by breakage of ion pairs, versus cooperative "glassy" dynamics involving multiple monomers and salt ions. High-quality PEs synthesized in nearly monodisperse form over a range of molecular lengths, and studied over a range of temperatures, salt concentrations, and salt types, will also be an essential part of bringing this important field to maturity over the next decade or two.

The formation of a low-frequency plateau and its magnitude are found to be highly sensitive to salt concentration, consistent with previous work. Novel to our work is the finding that it is also sensitive to polyelectrolyte molecular weight, with more rapid increase in its magnitude with increasing length of the polyanion, PSS than of the polycation, PDADMAC. Trend lines of the dependences on salt concentration and chain length are assemble from our data and relevant literature. Why both salt and chain length can, under some circumstances, not only shift the rate of chain motion, but also quench long-range motion into a gel-like response, is a mystery that needs resolution, and a theory to reliably predict it. We suggest that a transition towards a network of "ionomer-like" aggregates might provide a fruitful starting point.

6.3 Relationship between Rheology and Printability is Associated with Yield Stress

We found that the PDMS-fumed silica suspensions were poorly, or not at all, printable, and that this lack of printability was only forecast by shear rate ramp up-and-down method where a yield stress is estimated at low shear after the material had been previously sheared at a high rate, characteristic of flow through the nozzle during 3D printing. The LSR materials are printable at high PEG loading, consistent with the retention of a reasonably high yield stress in these materials after a previous high shear rate, while the PDMS-silica materials are not printable, consistent with their failure to show a significant yield stress after a previous high shear rate. Thus, DIW printable materials need to not only have a reasonably high yield stress but must be able to rebuild this yield stress quickly following the high shear rate in the nozzle of the printing head. One rheological test capable of assessing this behavior is a shear rate up-ramp followed by a down-ramp, with the yield stress determined at the end of the down-ramp. While this test can discriminate reliably between printable and non-printable materials, quantifying more precisely the degree of printability from

rheology and relating it more exactly to the quality of the 3D printing for a given geometry, will clearly require more work, and may require combining the results of multiple rheological tests. The work performed here provides a step towards the goal of developing a rheological testing regimen that reliably predicts the printability of multiple material types in multiple geometries.